UCLouvain
Institute of Mechanics, Materials and Civil Engineering (IMMC)

sck cen
Belgian Nuclear Research Centre

Modeling the impact of potential radioactive releases into the Meuse and Scheldt aquatic systems.

Thesis submitted by

Amit Ravindra Patil

in partial fulfillment of the requirements for the degree of

Doctor in Engineering Science

Thesis Committee

Supervisors	Prof. Eric Deleersnijder	UCLouvain
	Dr. Jonathan Lambrechts	UCLouvain
Jury Members	Dr. Fabricio Fiengo Perez	Aquafin. Belgium
	Prof. Sandra Soares-Frazao	UCLouvain
	Prof. Benjamin Dewals	ULiege, Belgium
	Prof. Marilaure Grégoire	ULiege, Belgium
	Dr. Katrijn Vandersteen	SCKCEN, Belgium
President	Prof. Renaud Ronsse	UCLouvain

Louvain-la-Neuve, December 2024

Thanks

I would like to express my sincere gratitude to all those who participated in this journey and believed in me.

A warmest thanks to Dr. Fabricio Fiengo Perez for believing in my potential and giving me the opportunity to pursue this Ph.D., which has been an incredible journey of learning and growth. I am deeply indebted to Prof. Eric Deleersnijder for his unparalleled and continuous support throughout my Ph.D. journey, standing by me through thick and thin. I would also like to extend my sincere thanks to Dr. Jonathan Lambrechts for his invaluable help and guidance during this period. Last but not least, I would like to express my heartfelt gratitude to Prof. Ronghui Ma, my mentor during my Master's studies, for introducing me to the fascinating field of Computational Fluid Dynamics (CFD). This journey would not have been possible without that crucial first step.

I would like to acknowledge Prof. Sandra Soares-Frazao, Prof. Benjamin Dewals, Prof. Marilaure Grégoire, Dr. Katrijn Vandersteen, and Prof. Renaud Ronsse for graciously accepting to be members of my Ph.D. thesis committee. I deeply appreciate the valuable time you dedicated to carefully reading this manuscript, as well as your constructive remarks and suggestions, which have greatly contributed to its improvement.

I am also grateful to SCK CEN and UCLouvain for providing the necessary resources and financial support to carry out my research. My sincere thanks go to all my colleagues at SCK CEN and UCLouvain, with whom I had the pleasure of working. A special mention to Dr. Sweeck Lieve and Dr. Johan Camps for their invaluable guidance during the final years of my Ph.D.; your support has been most appreciated. Thank you to Dr. Nele Horemans for her assistance in all matters related to the Ph.D., from reviewing my work to offering various pieces of advice. I am also thankful to all the BIS group members at SCK CEN for their interactions, encouragement, and well wishes throughout this journey. Additionally, I would like to acknowledge the SLIM team; it has been a pleasure collaborating with such brilliant minds. A special thanks to Dr. Insaf Droui for her support on the SLIM and for accompanying me during visits to UCLouvain. My fellow Ph.D. students at BIS, with whom I shared an office, also deserve a big thank you for making this journey a little less solitary.

I would like to extend my deepest gratitude to my wife, Snehal Kadge, for her unwavering encouragement and tireless support, as well as the many adjustments she made to help me through this Ph.D. Without her, this journey would have been much more challenging. I am equally grateful to my parents for their constant encouragement and support, and to my sister, Sanjana, for all the joyful conversations that brightened my days.A special mention to my newborn son, Swadaksh Patil, who has brought immense joy and a new perspective to my life during this final phase of my Ph.D.

Last but not least, I am thankful for all the friends I made along the way, and the memorable moments we shared, which I will cherish for years to come.

I would like to express my deepest gratitude once more to everyone who has been part of this journey. I will always treasure the memories of our shared experiences.

Contents

CHAPTER 1

Introduction

> I know that I know nothing.
>
> — Socrates.

Since water bodies are subjected to sunlight and carry basic nutrients, they not only develop and sustain an ecosystem within the water but are also crucial for terrestrial organisms. Thus, the water with which man is concerned is neither pure H_2O in the chemical sense nor biologically sterile. It is best regarded as a biological material, with nutrient composition and concentrations varying depending on the watershed's geology and ecology (IAEA (1971)). If no human intervention occurs; this state persists until the river enters an estuary and loses its identity as a freshwater system. However, increased human activity (such as agriculture and industries) can alter the composition of the water. Consequently, certain aquatic systems provide water that is used repeatedly, with each use affecting the water quality, which is generally to the disadvantage of the ecosystem. More often than not, the amounts of toxins released into water might become a determining factor for the good status of the water system.

The nuclear energy industry is no different from any other industry and radionuclides can be released by nuclear power plants, research laboratories and medical/hospitals. During normal operations, radioactive materials are contained and controlled very effectively, and it is only the small residue of

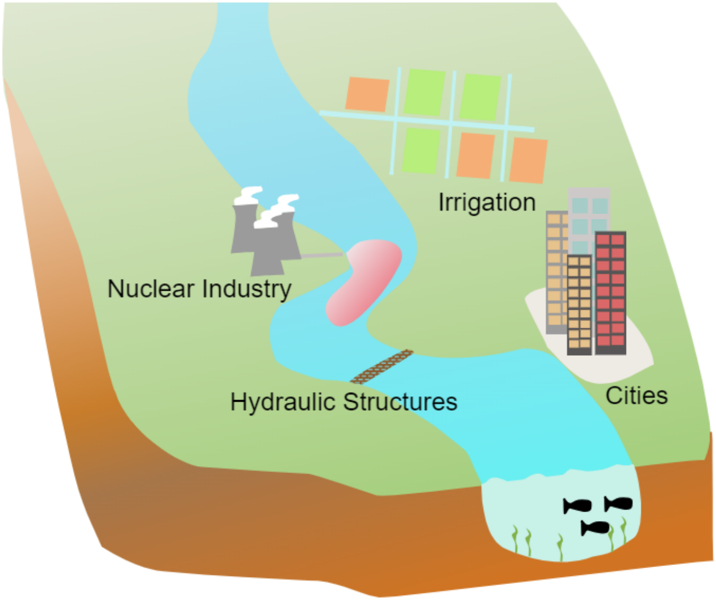

Fig. 1.1: Effects of radioactive waste released into aquatic systems by the nuclear industry on the environment and public health.

radioactive materials in the effluents of installations using or producing them that is released to the environment. Therefore, the waste discharge of radioactive material can be safely absorbed without risk of damage to man or the environment. But uncontrolled and long term discharges, will have severe, and enormous environmental, health and socio-economic consequences. Because of this, most of the nuclear-capable countries have established relevant national authorities to monitor these industries and be prepared in the event of an imminent threat.

Even though the radionuclide effluents from the nuclear industry are highly monitored and subject to strict norms, the fate of such radionuclides following their releases becomes unknown and mainly depends on the unique characteristics of an aquatic system. The radioactive wastes are subjected to various natural processes that begin to dilute, disperse, deposit, and re-concentrate all or part of the radionuclides. The key aspect, however, is the movement of water that can distribute the radioactive materials invariably during the course of its flow. Thus, uncontrolled releases from a remotely located nuclear installation can have a significant impact on populated areas placed along rivers, estuaries, or even the sea (Figure 1.1). The waste radioactive materials can then reach man directly (direct irradiation) or indirectly (ingestion of polluted food or water) and subject him to radiation exposure. Hence, it is not only important to understand how radionuclides are transported in these systems, but a quantitative understanding of these processes can also be crucial for making sound decisions for emergency responders.

Emergency responses to accidental or, in some cases, intentional releases of radionuclides would therefore require specific information (such as affected areas, etc.) to assist emergency response managers in taking action. Direct measurements can provide some information, but predictive information requires a mathematical model (Park et al. (2017)). Radiological transport models are tools designed for generating and organizing information in support of emergency response. As soon as an emergency event has been detected, model results can support a real-time evaluation of the actual situation during and following the incident, and even more importantly, they can provide prognostic information as a basis for protective actions. Computerized decision support systems are the response to these needs (Hofman et al. (2011b)). During the last decade, advances in computational capacity and numerical methods have made it possible to generate this information almost in no time. However, developing such process-based models mostly depends on specific characteristics of the aquatic systems under consideration. Human settlements and industry have increasingly controlled aquatic systems and modified their natural course. Due to the level of complexity of the flow through highly regulated water systems, sophisticated models are needed in order to solve water quality problems such as the distribution of radionuclides.

1.1 Past Nuclear Accidents: What have we learnt?

Exposure to radionuclides is a source of genotoxicity in species, may that be terrestrial or even aquatic (Kesäniemi et al. (2019)). The unit of radioactivity of a given radionuclide is defined by Becquerel (Bq), i.e., equal to one atomic decay per second. Numerous human activities, such as nuclear energy generation and its water treatment, have contaminated many locations across the world. The accidents at Chernobyl (Ukraine, 1986) and Fukushima (Japan, 2011) nuclear power plants (NPPs) are perhaps the most notable sources of radioactive contamination in the natural environment. The accident at the Chernobyl NPP Reactor 4 released more than 9 million terabecquerels (TBq), while the Fukushima Daichi releases were around 1 million terabecquerels to the environment. High levels of radioactivity were observed within a 30–50 km (4,300 km^2) radius of explosions at both accident sites, necessitating the establishment of an evacuation zone to prevent exposure. In the recent event of Fukushima, it was discovered that even those living beyond the evacuation zone (<30 km) had levels of radioactivity that might exceed 20 mSv dosage within a year. As a result, the occupants had to be evacuated; however, this happened only two months after the accident. This evacuation plan reduced the radiation exposure to public health by a factor of 10 (for a detailed study, refer to UNSCEAR (2020)). But it was quite evident that improved emergency preparedness would have further reduced public exposure (Park et al. (2017)). Therefore, continuous efforts have been made globally to enhance nuclear safety and emergency response.

The management of aquatic systems following a radioactive release can pose additional risks to public safety. In the wake of an accident, these heavily contaminated aquatic systems could transport these contaminants further outside the evacuation zone, affecting many more residents. For instance, it was estimated that approximately 30 million Ukrainians had been impacted by radionuclides from the contaminated water since the Chernobyl accident (Zheleznyak et al. (1992)). In fact, a higher concentration of radionuclides was found in tap water in the Tokyo metropolitan area, which was 200 km from the Fukushima plant (Murakami and Oki (2014)). Such contamination, however, not only impacts the drinking water supply but also the food production in these regions that is consumed by the locals. Hence, understanding the transport of these radionuclides through the aquatic system becomes an important element for the improvement of emergency responses.

1.1.1 Aftermath of Chernobyl disaster: Pripyat-Dnieper River

On April 26, 1986, the most catastrophic nuclear accident in history happened at the Chernobyl nuclear power plant's unit 4, where two large steam explosions destroyed the reactor. The subsequent burning of the graphite moderator resulted in the continuing emission of radiation for ten days. Approximately 50% of the ^{131}I and 30% of the ^{137}Cs were released from the reactor core (IAEA (2006a)). The most serious consequences, though, were caused by exposure to short-lived radionuclides, especially ^{131}I, which resulted in many thyroid cancers (Gavrilin et al. (2004)). The impacted areas for the radioactivity were the consequence of the wind direction and rainfall patterns at the time of release. Although the Chernobyl evacuation zone had the highest radioactive deposition, much of Europe experienced considerable fallout. However, deposition was largest in the three countries that lie within the Dnieper River basin (Belarus, the Russian Federation, and Ukraine) (IAEA (2006c)).

The Chernobyl nuclear power plant is part of the unique aquatic ecology of the Prpiyat-Dnieper river-reservoir systems. It is situated on the bank of the Pripyat River, 20 km upstream of its point of inflow into the Kiev reservoir and 13 km away from the confluence with the Dnieper River. Even though surface water systems in many parts of Europe were affected, the majority of fallout was deposited in the catchment of the Pripyat River, which was eventually transported to the Dnieper River-reservoir system. The initial radionuclide concentrations in this river water were relatively high compared to other European rivers and the safety standards for radionuclides in drinking water. The Pripyat River at Chernobyl had the highest radionuclide concentration, with ^{131}I activity up to 4440 Bq/L and ^{137}Cs at 1591 Bq/L (Kryshev (1995)). However, within the first few weeks after the accident, activity concentrations in river waters declined rapidly because of the physical decay of short-lived isotopes. In long term, the long-lived ^{137}Cs and ^{90}Sr comprised the major components of the contamination of aquatic ecosystems. This caused temporary rises in activity concentrations during floods of the Pripyat River that raised severe concerns in places that drew water from the Dnieper cascade, where, even after more than 10 years, the radiocesium activity due to bioaccumulation in fish is still relatively high.

Some twenty million people in the Ukraine were exposed to radionuclides in the water of this river between Kiev and the Black Sea through drinking water, irrigation and fishing (Onishi et al. (2007)). It was estimated that during 1986-1992, the collective dose (EED) resulting from 8 million people drinking the Dnieper River water was 216 manSv and 19 million people consuming fish with 100 mSv and irrigated food products with 513 manSv, for a total of 829 manSv through aquatic pathways. Among all, the irrigation pathway was clearly the dominant pathway. The total aquatic pathway contribution constitutes about 7% of the total collective dose of 11,832 manSv from all pathways (Voitsekhovitch et al. (1994)). Even though the aquatic pathway contributes only a small amount of the total dose, the migration of these radionuclides outside the exclusion zone affected more people over time. Therefore, remediation efforts, especially for fresh water systems, need to be such that they are contained within the evacuation zone. In the case of the marine systems, the closest to Chernobyl are the Black Sea and the Baltic Sea — both several hundred kilometers from the site. The radioactivity concentration in these seas was relatively low, thanks to the large dilution in marine systems (IAEA (1998)). However, it was apparent that the Dnieper River system had the capacity to transport the radionuclides to such a long distance (Jonsson et al. (1999)).

1.1.2 Aftermath of Fukushima disaster: The Pacific Ocean

The Fukushima Dia-chi nuclear power plant (FDNPS) is located on Japan's Pacific coast, in the northeastern Fukushima prefecture, approximately 100 kilometers south of Sendai. The facility, operated by Tokyo Electric and Power Company, was initially designed to have six reactors, but only 1-3 were operating during the disaster. Explosions resulting from the buildup of pressurized hydrogen gas occurred in the outer containment buildings enclosing reactors 1 and 3 on March 12th and 14th, respectively. A third explosion occurred on March 15th in the building surrounding reactor 2. Consequently, radioactive material was released to the atmosphere from FDNPS over an extended period.

This accident, because of its coastal location, was the first major nuclear power station accident in which significant amounts of radioactive material were released into the marine environment. Firstly, a large proportion of the releases of radioactive material into the atmosphere were dispersed over and deposited on the surface of the Pacific Ocean. Secondly, highly radioactive water leaked from a trench outside Unit 2 and caused the direct release of radioactive material into the ocean. Compared to the Chernobyl accident, in which dispersion of radioactive material released to the atmosphere and its deposition over sea surfaces resulted in a maximum concentration of ^{137}Cs in the sea of 2,400 Bq/m^3, direct releases into the ocean as a result of the FDNPS accident led to peak concentrations three to four orders of magnitude higher (UNSCEAR (2020)).

Monitoring of some radionuclides (^{131}I, ^{134}Cs and ^{137}Cs) started on 21st March 2011, after the detection of radioactive material in seawater at a few points in the coastal area around FDNPS. The total amount of ^{137}Cs directly discharged during the period of 12 March–30 April 2011 in the ocean was estimated to be 4 PBq, with an additional deposition of similar magnitude (5 PBq) for the atmospheric fallout into a wider area of the western North Pacific during the first days after the NPPs' explosion (Behrens et al. (2012)). While for ^{131}I it was much higher with 13 PBq of discharge into the ocean and around 100 PBq by atmospheric releases (UNSCEAR (2020)). The percentage of the total release of ^{137}Cs to the atmosphere that was deposited on the surface of the Pacific Ocean has been estimated at around 80% (Hirose (2016)). In comparison, the Chernobyl accident released just about 7% of the ^{137}Cs into the aquatic environment. Furthermore, the radionuclide dispersion from the atmosphere, deposited mostly by precipitation, was incorporated into surface waters. Consequently, radionuclides have been detected in drinking water and foods in Fukushima and other prefectures in Japan.

Fukushima City had the highest values of radiation exposure from surface water contamination, including major cities like Tokyo and Osaka that were not in the evacuation zone. The contribution of the effective dose from ^{131}I to total radionuclides was higher than that from ^{134}Cs and ^{137}Cs. The drinking water contributed the highest thyroid equivalent dose due to ingestion of ^{131}I in Fukushima City, followed by vegetables. The average equivalent doses due to ingestion of ^{131}I for adults were 2700 μSv in Fukushima City, 370 μSv in Tokyo, and 16 μSv in Osaka. In fact, some local governments, including the Tokyo Metropolitan Government, distributed bottled water to protect the health of citizens, particularly infants, against the high concentrations of ^{131}I detected in drinking water (Murakami and Oki (2014)). This was, however, only after 5 days of the accident that a high level of radionuclide concentration in tap water was detected. While the fish consumption contaminated from the Pacific Ocean within the evacuation zone was stopped immediately after the accident. Even though Japan had the SPEEDI (System for Prediction of Environmental Emergency Dose Information) model, but was not available until after 2 weeks, leaving many people exposed to radiation. As a result, the Fukushima disaster has prompted the development of data sets for the emergency response to potential accidental radionuclide releases from nuclear power facilities (Park et al. (2017)).

1.2 Numerical modeling for radionuclide transport

Mostly the assessments of radioactivity doses to humans and non-human biota rely on measurement data and model outputs. An evaluation of the consequences of radionuclide discharge into aquatic systems, however, cannot always be based on measurements taken at a few locations. This would necessitate the installation of a comprehensive monitoring system, which is often incapable of predicting the fate of radionuclides and may leave emergency responders guessing. Furthermore, in order to design efficient monitoring systems, it will require knowledge regarding the advective properties of such systems. This is where mathematical models can help by filling in the gaps and providing helpful knowledge on the fate of radionuclides and also the aquatic hydrodynamics. In fact, it is widely recognized that the abundance of data that these models can provide is even more important in an emergency. Since the nuclear accidents, particularly after Chernobyl, several models have been developed over the years and are still evolving. The evolution is owing to the fact that these models involve a complicated web of interacting processes that control the migration of such toxic substances and the current computer capacity has made the use of those models feasible. Therefore, the International Atomic Energy Agency (IAEA) has spent considerable resources on developing projects to improve such models, that includes VAMP (Validation of Model Predictions) program in 1988 and the most recent is the MODARIA-II (Modeling and Data for Radiological Impact Assessments) project, launched in 2016 (Periáñez et al. (2019)).

Hydrodynamics play a significant role in the transport of radionuclides in aquatic systems. This is because it is the driving force behind the advective behavior of an aquatic system that determines how long contaminants can stay in the system or at a certain location. Therefore, the development of a model will depend on the nature of the hydrodynamics of the aquatic system under consideration. For instance, in rivers, the dominant flow component is typically horizontal, which can be adequately represented by resolving one-dimensional flow currents. On the other hand, estuaries and seas exhibit more intricate flow patterns that necessitate resolving two-dimensional flow currents for accurate modeling. Since the Chernobyl nuclear accident, mathematical models for radionuclide transport in rivers received significant attention that can be easily solved by one-dimensional approach. To name a few, the RIVTOX model was used to solve the problems of the Ukrainian river after the Chernobyl accident (Zheleznyak et al. (1992)), MARTE was used in the Loire River (France), Techa River (Russia) and the behavior of ^{226}Ra in the Huelva estuary (Spain) (Monte et al. (2008)), and CASTEAUR was used in the Rhine River (France) (Duchesne et al. (2003)). However, with increased computational power, several other models were also seen in studies for large areas, such as the sea and even estuaries. Marine transport models got further attention after the Fukushima nuclear accident in the context of the Pacific Ocean. Among the various studies, Kawamura et al. (2011) simulated the spreading of ^{131}I and ^{137}Cs using the Lagrangian model SEA-GEARN released from the Fukushima nuclear power plant and Regional Ocean Modeling System (ROMS; Shchepetkin and McWilliams (2005)) to simulate the behavior of ^{137}Cs released from the reactors off Fukushima (Tsumune et al. (2012)).

Typically, a radionuclide transport model would require the inclusion of at least two components: the hydrodynamic model and the radioactive transport model. However, a sediment model, can sometimes be included, depending on the geochemical property of the radionuclide. The hydrodynamic model is the component that provides detailed description of the water flow in the systems, with this information the rest of the components can determine the pollutant transport. The transport model describes two main processes: advection and diffusion.

The most simplistic approach for describing the pollutant transport (e.g., radionuclide) is the box model. In these models, the area under consideration is divided into a number of large boxes or compartments. These boxes are interconnected according to average water circulation patterns, and it is assumed that the transport of dissolved radionuclides between boxes is formulated according to Fick's law across the compartments. Box models are well suited for assessments of radionuclide dispersion involving large spatial and temporal scales (thousand kilometers; years to decades). Some recent examples of box models are POSEIDON-R (Bezhenar et al. (2016)) and models developed in NRPA (Iosjpe et al. (2009)).On the other extreme are the most detailed and complex models that solve Navier–Stokes equations and the mass conservation equations to calculate the water circulation in the area of interest (Figure 1.2) and pollutant transport. The level of detail of the model can be selected according to the dominant mechanism and processes identified in the water system. For example, the one-dimensional approach is feasible for rivers where the assumption of homogeneous water flow and pollutant concentration across the river section are valid while the tridimensional approach considers that both variables change at each position of the cross section such is the case for deep lakes or ocean. However, a two-dimensional approach is also possible, specially in shallow water systems where the variation of both variables along the vertical can be neglected. Compared to box models, this approach has the advantage of generating detailed and realistic water circulation results (Vyzikas (2014)). Nonetheless, it's use demands a much heavier computational resources

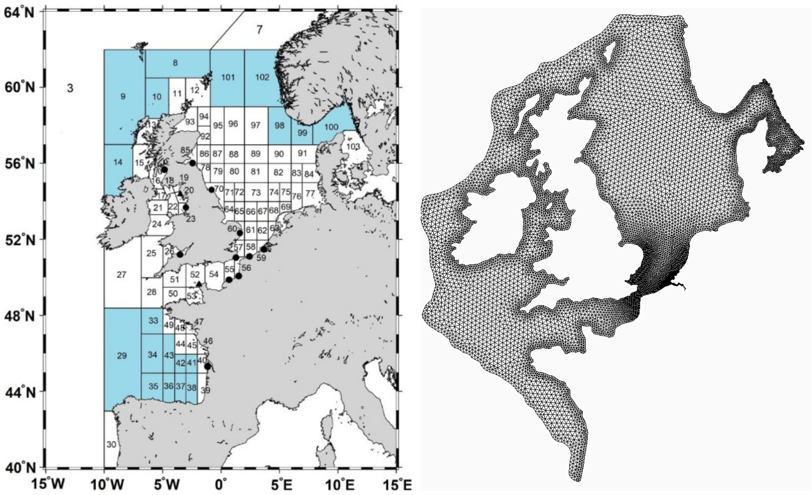

Fig. 1.2: The box model (POSEIDON; figure from Maderich et al. (2018)) defines box structures based on the water current characteristics and estimates water fluxes between them, in contrast numerical models use nodes defined in unstructured triangular mesh, that can describe the complex geometry of coast, is used to solve the Shallow water equation .

than that required by the box model, making it particularly appropriate for short-term studies or small study cases.

Since the Navier-Stokes equations in either form (one-dimensional or two-dimensional) are non-linear hyperbolic equations (Lax (1973))), it is not possible to find an exact solution; instead, one must approximate the solution by using different numerical techniques that differ from one another depending on the nature of the problem to be solved (e.g., solution of smooth or sharp fronts). For a continuous problem (in the case of natural river flow), several classical numerical approaches have been applied, such as the finite difference method (Godunov and Bohachevsky (1959); Chung (2002)), finite volume (FVM) (Anastasiou and Chan (1997); Moukalled et al. (2016)) and finite element methods (FEM) (Gallagher et al. (1978); Hirsch (1978)). Each method presents its advantages and limitations, that depends on the complexity requirement. For example, the finite difference scheme is favored for its simplicity, making it helpful for simple geometric flow (one-dimensional river flow); however, additional transformation will be required for complex geometry such as the sea, in which case other schemes can be implemented without additional modifications. Further details about approaches used in different types of numerical methods and their applicability can be found in Tu et al. (2023). Aside from classical methodologies, various alternative numerical techniques, such as the discontinuous Galerkin finite element method, have shown potential in hydrodynamics (Lai and Khan (2012a), Caviedes-Voullième et al. (2020)) and are regarded as the combination of FVM and FEM methods.

Due to the time and spatial dependence of these equations, space and time discretization become necessary. Therefore, appropriate domain discretization (be it one-dimensional or two-dimensional) will ensure a better representation of the flow and transport in the study area. This is because the discretization of the computational domain affects the numerical accuracy since these equations are solved by numerical approximation. In two-dimensional space, the domain is often divided into either structured elements, unstructured triangles, or quadrilateral elements, which form the mesh. The regularity of structured mesh does simplify mathematical formulation, but it has two significant limitations: first, the resolution variability and second, the ability to capture domain boundaries, particularly for the coast, channels, and tributaries (Tan (1992)). The triangular unstructured mesh (Figure 1.2) is a perfect solution for the cited shortcomings of the structured mesh, but not without increased computational cost. Alternatively, adaptive and moving meshes have the ability to adjust mesh refinement in order to decrease computation costs (Tu et al. (2023)). Therefore, the choice of mesh will primarily be based on the characteristics of the aquatic system and the desired accuracy.

1.3 Impact assessment: What will it tell us?

Impact assessments are typically derived from the calculation of doses. Dose quantities and units can be expressed in a variety of ways depending on the nature of the assessment, either to evaluate stochastic (likelihood of developing long-term health effects at low doses) or tissue reaction (impairment occurring above dose thresholds) (ICRP (2021)).The unit Sievert (symbol Sv) represents the equivalent biological effect for the deposition of a joule of radiation energy in a kilogram of human tissue and is often coined in terms of mSv (one thousandth of Sv).It assesses the stochastic health risk posed by radiation exposure, specifically the likelihood of acquiring radiation-induced cancer and genetic damage. Sieverts are used to express quantities such as equivalent dose, effective dose and collective doses, which consider both external and internal radiation exposure. Equivalent doses are based on absorbed doses to an organ, whereas effective doses are estimated for the entire body (tissue-weighted sum of the equivalent doses in all specified tissues and organs of the body). The equivalent dose in Sieverts is calculated by multiplying the radiation weighting factor representing relative biological effectiveness of radiation (taking account of different biological effects) and energies of radiation. While collective doses are based on the radiation doses received by a population and are expressed in man-sieverts (manSv). The sievert is essential in fields such as dosimeter and radiation protection. Gray (symbol Gy) is another unit for absorbed dose and is defined as the quantity of radiation energy deposited on certain material (1 Gy = 1 J/kg). However, the effect of radiation exposure on the body varies depending on the type of radiation. For example, 1 Gy (1 J/kg) of alpha radiation is 20 times more lethal than 1 Gy of gamma. Therefore, one Gy of gamma absorbed dosage equals one Sv of equivalent dose, and one Gy of alpha absorbed dose equals twenty Sv of equivalent dose. Gy is hence suitable unit for indicating the limits for organ/tissue dosages to avoid tissue reactions)

The effective dose, denoted by the unit Sievert, is commonly used to justify and optimize protective actions. To give a perspective, the mean exposure to natural radiation, sometimes referred to as background radiation (cosmic rays, natural radionuclides, etc.), for humans is around 1 mSv/yr (NRC (2006)). Although it is widely assumed that such amounts have no effect on humans, very little is known regarding the health consequences of low-dose radiation exposure, even up to 100 mSv. This is because the thoroughly studied individuals for the determination of the health effects of ionizing radiation are mainly the survivors of the Hiroshima and Nagasaki atomic bombs with radiation exposure above 100 mSv (Figure 1.3). Therefore, due to the lack of good quality data for low radiation doses, the health effects are typically extrapolated from the graphs developed from these studies (Picano and Vano (2011)). The four dotted curves that shown in Figure 1.3 for doses less than 0.05 Sv are called, from top to bottom, (A) supra-linearity, (B) linear (C) linear-quadratic, (D) hormesis. The hormesis, in particular, covers the potential possibility that very low levels of radiation could actually be beneficial by "training" the immune system to fight cancer. To put these findings (shown in Figure 1.3) into context, approximately 1 person in 100 would be predicted to acquire cancer (solid cancer or leukemia) from a dose of 0.1 Sv above baseline (NRC (2006)). In comparison, approximately 42 of the 100 individuals would be expected to develop solid cancer or leukemia from other causes.

At dose levels of about 100 to 4000 mSv, excess cancers have certainly been observed in Japanese atomic bomb survivors. In the case of in utero exposure (exposure of the fetus during pregnancy), excess cancers can be detected at doses as low as 10 mSv (Schüz et al. (2017)). For the radiation doses at which excess cancers occur in the Hiroshima and Nagasaki studies, solid cancers show an increasing rate with increasing doses that is consistent with a linear association. In other words, as the level of exposure to radiation increased, so did the occurrence of solid cancers. The effects, however, can also be distinguished between short-term health effects that occur after exposure to high radiation and long-term radiation exposures, which can occur with low radiation exposure as well. It was fairly evident from the bomb survivors that the appearance of chronic ailments was imminent following long-term exposure. Consequently, the International Commission of Radiation Protection (ICRP) established a safe limit for lifetime exposure of 100 mSv (i.e., 1 mSv/year) to the general

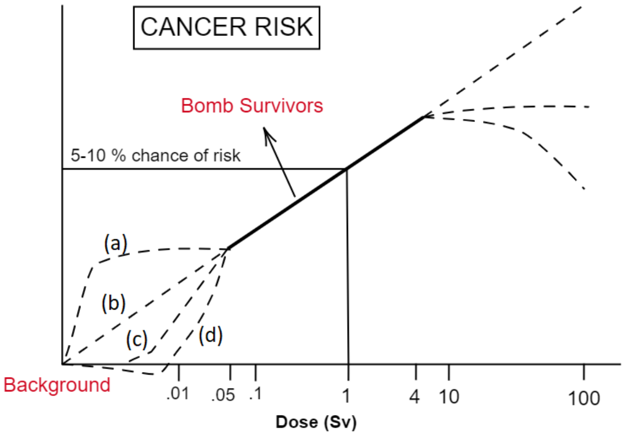

Fig. 1.3: The dose-effect relationship between radiation exposure and cancer (adapted from (Picano and Vano (2011)). The solid line indicates conclusive evidence for doses above 50 to 100 mSv. The dashed line indicates the dose range with absent or inconclusive evidence.

public from all pathways. In regards to water quality, according to the European directive for drinking water, the total indicative dose (TID) from all radionuclides should not exceed 0.1 mSv/year. This results in a limit of radioactivity concentration for drinking water below 10000 Bq/m^3 year-round. However, in emergency exposure situations, the International Commission on Radiological Protection (ICRP) recommends a reference level range of 20-100 millisievert (mSv) effective dose and that above 100 mSv will require protective measures (ICRP (2009)).The International Atomic Energy Agency (IAEA) standards for emergency response specify limitations of 10 mSv per year for the consumption of food, milk, and water, with 2000 Bq/kg and 3000 Bq/kg operational intervention levels for ^{137}Cs and ^{131}I, respectively (IAEA (2016)).It is worth mentioning that these limits are set to provide respondents time to take corrective actions. As a result, it is 10 mSv rather than 100 mSv to ensure that those people who have not been evacuated would still not receive a total dose greater than 100 mSv per year. Nonetheless, the ICRP further adds that reference levels below 20 mSv may be suitable for the response to scenarios having low predicted exposures. Hence, in the wake of an accident, exposed individuals should be subjected to frequent screening for radiation, even below the reference level, to monitor for long-term stochastic effects. Thus, analyzing the immediate impact on the population can assist emergency workers in making better decisions about future remediation.

1.4 Geography of nuclear power plants with its aquatic systems in Belgium

Currently, Belgium has two nuclear power plants: the Doel Nuclear Power Plant and the Tihange Nuclear Power Plant. The first one is located in the port of Antwerp on the left bank of the Scheldt estuary, which houses three active pressurized water reactors with a combined capacity of 1916 MW. The second NPP is located in Huy on the right bank of the Meuse River and includes two active pressurized water reactors with a combined capacity of 1992 MW. The fact that both NPPs in Belgium are situated on the banks of the Meuse and Scheldt aquatic systems makes this scenario unique. It is reported that very low-level radioactive effluents are discharged into these aquatic environments that are monitored by the regulatory authorities (FANC (2022)). Additionally, the French nuclear power station Chooz, which lies close to the Belgian border, is also built on the banks of the Meuse River, which flows downstream into Belgium. The Borselle plant, another NPP close to the Belgian border, is located in the tidally influenced Scheldt estuary of the Netherlands and has the ability to carry the radionuclide plume upstream from the estuary. Therefore, Belgium is essentially vulnerable to two more nuclear power plants in neighboring countries, both of which have the potential to alter the water quality in the Belgian territory and therefore affect the environment and the water availability for human consumption. Figure 1.4 depicts the locations of these nuclear power reactors that are housed close to the Meuse-Scheldt Aquatic System.

The Meuse River, with a length of 905 km (Beckers et al. (2013)l), flows through France and Belgium before reaching the North Sea via the Netherlands, as illustrated in Figure 1.4. Belgium accounts for about 185 kilometers of the overall length and habitats around 6 million people. Freshwater in nature, the Meuse River collects runoff from a vast upstream basin spanning approximately 35,000 km^2, of which 16,670 km^2 are situated upstream of Liege (Lambert et al. (2017)). The majority of this basin is situated in Belgium's Walloon province, and the low mountain range of the Ardennes is where it gets the most precipitation. The river has significant temporal variability in its flows, ranging from extremely high flows during wet winter times to very low flows during dry summer periods because it is primarily rain-fed (Ward et al. (2008)). The Meuse River that flows in Belgium is mostly canalized, the water is highly regulated by weirs and dams, and the river banks are further consolidated.

The Meuse River in Belgium provides water to the canal system via a complicated interaction that includes an open connection at Monsin (Liege) and many locks and supply channels near Maastricht. It connects with the Scheldt River through a connected network of canals (Campine canals) at the port of Antwerp. The largest canal in the network is the Albert Canal, connecting the Meuse River in Liege to the Scheldt River, through which more than half of all commodities in Belgian waterways are transported. In fact, the Albert Canal

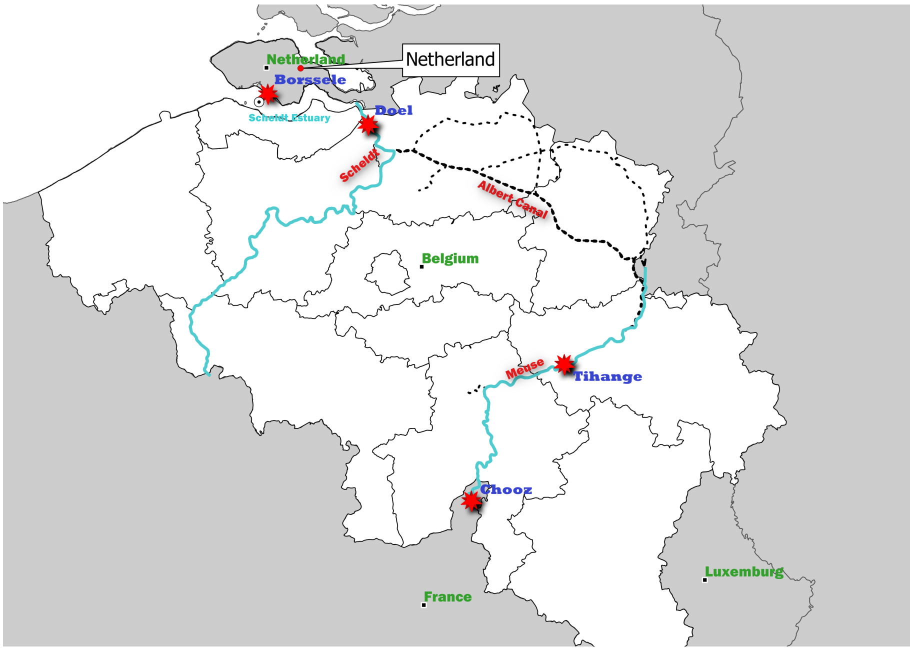

Fig. 1.4: Location of the Nuclear Power plants in Belgium and the neighboring countries that are located on the banks of Meuse-Scheldt aquatic systems

also plays an important role in the supply of drinking water that has been fed by the Meuse River (Bertels and Willems (2022)). Therefore, the Meuse River becomes a critical source of drinking water and for continuous navigation in Belgium. It provides water for drinking, irrigation and recreational activities to more than half of Belgium's population, necessitating the need to conserve and monitor the water quality.

The Scheldt estuary is a large-scale estuary in the south-west part of the Netherlands. The total length of the Scheldt River, including estuary, is about 350 km; the tide penetrates up to the city of Ghent in Belgium (about 180 km from the mouth). The mouth of the estuary is connected to the North Sea. The river receives upstream flows from a catchment area of about 21,800 km^2, which has a rather low gradient (Charriau et al. (2009)). The part of the river influenced by the tide is referred to as the Scheldt Estuary (Figure 1.4) and comprises the saline (salinity = 30–10) western Scheldt from the estuarine mouth to the Dutch/Belgian border (68 km), followed by the brackish estuary (salinity = 10–1), and farther upstream by the tidal, freshwater river system (Arndt et al. (2007)). The tidal wave is semidiurnal and propagates within a complex network of tributaries (Dijle, Zenne, Kleine Nete, Grote Nete). The tidal influence extends up to Ghent (170 km), where the wave is blocked by the presence of weirs. The tidal wave generated in the North Sea is significantly amplified in the Scheldt estuary. The mean tidal amplitude increases from 2 m at the coast to around 5 m in the Scheldt River and even in tributaries. The flow of the Scheldt River is generally small, while tidal motions in the estuary are large, producing a fairly good mixing of fresh and sea waters. However, seasonal variations in freshwater tend to influence salinity in the river and, to some extent, the Belgian coast. Although saline water is not usable for drinking, the Scheldt supports several industrial activities in and around Antwerp. Moreover, the unpredictable variations in salinity tend to limit the number of species capable of adapting to these rigorous conditions, making them unique. Though it contains relatively few species, the abundance and biomass of organisms are usually very high and serve as important life-support systems for human beings (Day et al. (2022); Costanza et al. (1993)).

1.5 Motivation of the Thesis

The Fukushima and Chernobyl nuclear industry disasters showed the risks associated with radioactive releases (IAEA (2006b) UNSCEAR (2021)). Therefore, as the Meuse River and the Scheldt are transboundary water systems, it is required to report not only to the national authority but also to the neighboring countries when radioactivity levels increase due to drought or accidental releases. Data collection during such events is crucial for determining the impact on humans and the environment (Hofman et al. (2011a)). However, the spatial and temporal variability of the release and the complexity of radionuclide transfer within the environment make it extremely difficult to gather all the necessary information, and very often, additional information is obtained by having recourse to model simulations (Monte et al. (2005)).

1.5.1 Objectives

Currently, there is no specific tool to determine the flow dynamics and fate of radionuclide transport in these river basins, which encompass four nuclear power plants (Figure 1.4) along their banks. Hence, the nuclear waste effluents released into rivers can traverse a long pathway and can be distributed invariably along these water basins, and their effect on the water and their dependent organisms cannot be investigated. For instance, if there is an accidental spillage in Tihange or Chooz power stations, the harmful radionuclide effluents can flow through the Meuse, Albert Canal, and port of Antwerp, merge with the Scheldt River, and then spread all over the estuary, which can lead to large health and socio-economic risks for the inhabitants. Currently, we have large capabilities in regard to the computational power for solving many complex equations for a mathematical model over a large space and time domain.

The main objective of this research is to develop a state-of-the-art methodology for the assessment of the impact of radioactive releases on the water quality and environment that can be used to simulate the current (routine releases) situation and for the prognosis of possible accidental radioactive releases. The main goal of the thesis is:

- To develop a reliable model for the Meuse and Scheldt basin to evaluate the distribution of radionuclide effluents and the radioactivity levels.
- To simultaneously represent the flow from river to the sea (including canals and estuary) and thereby extending the SLIM (Second Generation Louvain-la-Neuve Ice Ocean Model) model to incorporate hydraulic works.
- Multiscale hydrodynamic model to represent the flow in the Scheldt estuary, rivers and the European continental shelf.
- To translate simulation results to impact assessment criteria such as dose to human.

The assessment methodology developed here must be flexible enough to integrate the transport dynamics of several water systems, such as inland rivers, estuaries, coast and the sea, in one package. Moreover, it must be capable of providing simulation results that are in-line with the observations. The model for the Scheldt-Meuse River basin can then be used as a decision support tool (DST) for the assessment of possible environmental risk from routine and accidental releases.

1.5.2 Radio-logical Impact Assessment in Meuse-Scheldt Aquatic systems

To achieve these objectives, we use an adapted version of the SLIM model (Second Generation Louvain-la-Neuve Ice Ocean Model) for the simulation of radionuclide transport in Meuse-Scheldt aquatic systems. The current version of the SLIM uses the DG method on an unstructured mesh to solve the one-, two-, and three-dimensional shallow water equations. Additionally, the model is equipped with a Lagrangian particle component (Saint-Amand et al. (2023)), an age component to perform further diagnosis of residence time of pollutants in the aquatic systems (de Brye et al. (2010)), and a component for sediment transport modeling (Lambrechts et al. (2008)). The SLIM model has previously been successfully applied for the simulation of the hydrodynamics of a number of aquatic environments on Earth, such as the Florida Reef tract (Saint-Amand et al. (2023)), Great Barrier Reef,the Congo River estuary (Vallaeys et al. (2021)) and the Mahakam delta systems in Indonesia (Pham Van et al. (2016)).

Here we represent the radionuclide transport in Belgian rivers, waterways and coast by combining two domains defined by the dominant flow hydrodynamics. In the first, we represent the Meuse River, where the hydrodynamics and transport processes are dominant along the flow direction and the anthropogenic influence (hydraulic structures placed for navigation) plays a significant role. In the second, we represent the Scheldt estuary, the Belgian coast and the North Sea. Here, the water flow and the transport are driven by the tidal hydrodynamics and freshwater influxes. Both domains, the Scheldt and Meuse River systems, meet at the port of Antwerp.

The Meuse River is connected to the Scheldt River via the Albert Canal. The Albert Canal is the main waterway of Belgium, and it is regulated by several locks that make navigation possible. It has been shown that the impact of the water diverted through the Albert Canal from the Meuse River on the Scheldt estuary hydrodynamics is small (Arndt et al. (2007), de Brye et al. (2010),Vanderborght et al. (2007)). The Albert Canal is connected to Scheldt at three different points (Royer sluice, Boudewijn sluice and Zandvliet sluice) and the flow is regulated by means of locks. Due to the operation of the locks, water from the Scheldt River comes into the Albert Canal; however, this phenomenon is not thoroughly understood to the extent that it can be included in the model. Box models were successfully used for simulating the salt intrusion in the Albert Canal (Bertels and Willems (2022)). Box models are powerful tools for the simulation of concentrations, but they provide little information about the spatial distribution of the plume. However, in case of emergency planning after accidental releases of pollutants such as radionuclides, detailed models are needed to simulate not only the concentration but also the location and the extension of the plume. As mentioned before, the Albert Canal does not release freely the water from the Meuse into the Scheldt. But instead, the releases are determined by the traffic vessels along the canal. Due to this reason, we decided to simulate the Scheldt and Meuse separately.

The representation of rivers subjected to the operation of hydraulic structures to divert, rise, or store the water in numerical models requires specific considerations. This is because the presence of these structures introduces a discontinuity in the flow, which is difficult to deal with during the solution of the hydrodynamic equations. The most common approach to represent the influence of these structures is to incorporate stage-discharge relationships into the numerical scheme.

The application to a real-world scenario can bring its own challenges. The stage-discharge relationships, for example, are derived from scaled-physical models developed in laboratories and determined mostly under steady-state conditions. Unfortunately, during the operation, the real structure will work under flow conditions that considerably deviate from those used during the laboratory setup. The implementation of these structures in numerical models demands additional considerations. For example, it is appreciated that, when flow conditions are very close to the limits between two flow regimes, instabilities occur. Therefore, besides a robust numerical scheme, an accurate representation of inter-regime flow conditions and a correct estimation of the flow over the structure are required.

The water flow in the Meuse River and the canal systems in Belgium are highly regulated by a combination of weir systems and lock chambers that play a major role in river flow dynamics. This often reduces the flow velocities in these aquatic systems, allowing for safer navigation.In addition, hydraulic structures often regulate the water that enters canal systems (Campine canal) from the Meuse River. Thus, they play a vital function in connecting river systems to canals. In terms of transport modeling, this is an essential variable to consider when predicting the fate of radionuclides. To this end, additional modules for the simulation of hydraulic structures will be incorporated into the SLIM modeling framework. The main advantage of SLIM is its capacity to deal with abrupt water level changes induced by the operation of structures, owing to its discontinuous formulation. In this thesis, we present a novel numerical technique for representing these structures within a discontinuous Galerkin method.

Estuaries connect inland rivers to the coast. Therefore, estuaries are characterized as saline water that forms a transition region between river flow and the saline sea water. Estuaries are subjected to marine influences such as tides, waves, and the influx of saline water and to fluvial influences such as flow of fresh water and sediments. Depending on the extent of these influences, the estuaries can be classified as high- or low-energy estuaries. High-energy or tide-dominated estuaries are dynamic ecosystems shaped by strong tidal energy at the mouth compared to wave energy. Examples of high-energy estuaries are the Scheldt estuary on the European coast, the Columbia River estuary in the USA, and the Bay of Fundy in Canada. Numerical modeling of such high-energy estuaries is a challenging task because of the strong tidal currents, sharp salinity gradients, and varying length and time scales (Kärnä et al. (2015)). Moreover, simulating strong currents over a complex topography goes beyond the assumptions and capabilities of one-dimensional representation and therefore two- and three-dimensional models are required.

The Scheldt estuary is a large-scale estuary with high-energy tides producing a fairly good mixing of fresh and sea waters. Moreover, the study of the transport of potential pollutants in the Scheldt system represents a domain of multiscale nature that deals with everything from the sea to the shallower environment. The width of the river can extend from 10 m at the upstream reach of the river towards the vast North Sea. This includes the interaction of micro-scale processes such as flow in narrow rivers to macro-scale estuaries to the sea and vice versa due to tidal motion. As a result, any potential release in one of these systems can have an impact on the others. For example, a potential release in the estuary can have an impact on rivers due to the tidal motion.

Hence, while considering radioactive discharges, the multiscale domain of the Scheldt must be taken into account. In this thesis, a new multiscale modeling approach for the transport of radioactive pollutants is used, allowing us to simulate complex systems in order to capture this interaction from river to sea. Moreover, the spatial discretization of the domain must be considered carefully to capture the flow characteristics without significantly raising the computing cost.

The NPPs placed in the banks of these aquatic systems could eventually contaminate them in case of an accidental release. The radioactivity could reach the system through many different pathways. The pathways and the radioactive source term will depend on the nature of the accident and the type of reactor. However, since the known accidents at nuclear power plants (NPPs) are caused by various factors, such as human error or extreme environmental circumstances (earthquakes, floods), it is challenging to forecast them. While risk assessment for radioactive releases from each piece of equipment in a nuclear installation is a cumbersome task. But past accidents provide some insight about the possible magnitude, pathways and source term. Therefore, the scenarios in this thesis for simulating the transport of accidental releases in these aquatic systems are selected, assuming worst-case situations derived from past major nuclear accidents. The worst-case scenario is defined as the most severe possible outcome that can reasonably be projected to occur in a given situation with maximum potential disasters. It is a concept used in risk management and strategic planning. In this context, the worst-case scenarios are defined with low-probability, high-consequences outcomes with the maximum negative consequences.Therefore, even though both level 7 nuclear disasters included boiling reactors, the ones being considered are pressurized water reactors (PWR) because PWR has not been involved in any known nuclear accidents. This can lead to understanding the upper bound limit for the impact of such releases. The pathways considered herein are atmospheric and direct liquid releases, with ^{137}Cs and ^{131}I as the main composition of the source term. In both Fukushima and Chernobyl, NPPs ^{137}Cs and ^{131}I were the major contributors to the radioactive contamination.

Among all, nuclear power plants are by far the largest producers of radioactive waste. Hence, these nuclear power plants are of primary concern, and they are regularly monitored by the national authorities for radioactive control. In the large majority of cases, the radioactivity concentrations are well below the detection limit of the measuring instrument. However, this does not mean that these NPPs do not discharge radioactive liquid wastes. But they are significantly diluted by “cold” effluents from the technical area, and in the case of some radionuclides, the waste is stored in a storage tank to allow it to significantly decay before being released into the water (FANC (2023)). Therefore, routine radioactive releases do not cause any significant impact on this aquatic system, especially in short-term periods. However, those radionuclides that tend to get attached to sediments might show a possible impact that is usually after years of accumulation in deposited sediments that gets resuspended during high flow conditions. Additionally, low flow or drought-like conditions in rivers can sometimes lead to an increase in concentrations for routine releases as a result of limited dilution. Since the model involves considering large systems up to hundreds of kilometers, a long-term simulation is not in the scope of this thesis. The large amount of computational resources involved and the memory required for the storage of results are still limiting factors. Therefore, the impact of routine release for a short-term period during low flow conditions is considered for the simulation. However, the duration of short-term simulation (i.e. of couple months) is based on test simulation for longer periods in order to determine the residence time of the pollutant and thus to optimize the simulation period of the multiple scenarios considered here.

Members of the population could be exposed to various radiation sources, be they external or internal. Here, the concept of effective dose has played an essential role in quantifying such exposure. In cases of releases from NPPs, the estimation of radiation doses to the exposed public is important for the evaluation of the impact of the accident and to guide decisions on appropriate radiological protection countermeasures. In the early stages of a nuclear accident, internal exposures due to inhalation and ingestion of radionuclides are likely to contribute significantly to organ equivalent and effective dose, together with external dose contributions from submersion within the radioactive cloud or plume (ICRP (2012)). Therefore, depending on the nature of water usage in particular aquatic systems, this can lead to different exposure pathways. In this study, we consider radiation exposure due to drinking water, which is more likely in the Meuse River than the Scheldt, but external exposure (bathing) to water on the coast is foreseen for the releases in the Scheldt.

Dose assessments for emergencies require following certain recommendations put forth by organizations such as the International Atomic Energy Agency (IAEA) and the International Commission for Radiation Protection (ICRP). These international standards provide guidance and criteria in terms of levels of individual radiation dose, levels of activity concentration of specific radionuclides, or both. For instance, the IAEA recommends considering an average intake of drinking water per person to be 2 liters per day (IAEA (2016)) and the ICRP recommends a dose coefficient for different exposure scenarios to compute the dose to humans (ICRP (2018)). In this thesis, the doses are estimated based on the simulation results for radioactive concentration from the developed model and the exposure pathways were defined based on the water use. Here, we follow the ICRP recommendations in order to assess the impact and compute the doses for different exposure pathways relevant to the aquatic systems.

1.6 Supporting Publication

Papers

- Patil, A., Perez, F., Lambrechts, J., Draoui, I., Deleersnijder, E., *Numerical Modelling for the Distribution of* ^{137}Cs *and* ^{131}I *in the Scheldt Basin after a Potential Nuclear Accident*, Journal of Environmental Radioactivity, vol. 280, Dec. 2024, p. 107568, https://doi.org/10.1016/j.jenvrad.2024.107568.

- Patil, A., Perez, F., Lambrechts, J., Deleersnijder, E., *Numerical Modelling of the Transport and Impact of* ^{137}Cs *and* ^{131}I *on the Meuse-Campine Canals after a Potential Nuclear Accident*, Journal of Radiological Protection, vol. 45, no. 1, Mar. 2025, p. 011512, https://doi.org/10.1088/1361-6498/adc1db.

- Patil, A., Perez, F., Lambrechts, J., Draoui, I., Deleersnijder, E., Dewals, B. (under review by International Journal of River Basin Management) *Numerical Modelling of Navigable Waterways using a Discontinuous Galerkin Method: Study of Meuse River – Campine Canal flow*

- Patil, A., Perez, F., Lambrechts, J., Draoui, I., Deleersnijder, E., 2022? *Numerical modelling of navigable rivers: influence of navigation structures on the Meuse River flow*, In the proceedings of the 11th International Conference on Fluvial Hydraulics. Presented at the River flow 2022, Taylor and Francis, Kingston and Ottawa, Canada. https://doi.org/10.1201/9781003323037-86.

- Patil, A., Perez, F., Lambrechts, J., Draoui, I., Deleersnijder, E., 2024, *A Multiscale 1D-2D Coupled Model Of The Scheldt Estuary Rivers And The European Continental Shelf*, CoastLab 2024: Physical Modelling in Coastal Engineering and Science, https://doi.org/10.59490/coastlab.2024.692.

Conference Communication

- Patil, A., Perez, F., Lambrechts, J., Draoui, I., Deleersnijder, E. 2024. *Model Development for Assessing the Impact of Accidental Radioactive Releases Into the Meuse River-Campine Canal*, In 34th Society of Environmental Toxicology and Chemistry Europe 34th Annual Meeting, Seville, Spain.

CHAPTER 2

Numerical Modeling of Navigable Rivers: Influence of Navigation Structures in The Meuse River Flow

This chapter is based on the following papers:

Patil, A., Perez, F., Lambrechts, J., Draoui, I., Deleersnijder, E., Dewals, B. (under review by International Journal of River Basin Management), *Numerical Modelling of Navigable Waterways using a Discontinuous Galerkin Method: Study of Meuse River – Campine Canal flow*

Patil, A., Perez, F., Lambrechts, J., Draoui, I., Deleersnijder, E., 2022, *Numerical modelling of navigable rivers: influence of navigation structures on the Meuse River flow*, In the proceedings of the 11th International Conference on Fluvial Hydraulics. Presented at the River flow 2022, Taylor and Francis, Kingston and Ottawa, Canada. https://doi.org/10.1201/9781003323037-86.

Abstract

Flow in navigable rivers is generally controlled by hydraulic structures, such as weirs. The numerical representation of such structures requires special consideration. In this study, we introduce a new numerical technique to represent these structures in a discontinuous Galerkin method. The novel approach is based on the calculation of fluxes in accordance with the stage-discharge relationships of the structures, and without the need to position adjacent nodes close to the structure node. Compared to other methods, the new approach offers more flexibility in terms of node treatment and better stability by reducing sensitivity to flux treatment. The developed model simulates the operation of the structures and enables accurate flow calculations in large navigation systems such as canal networks. The model is demonstrated using a real case study, the Meuse River and its canal network in Belgium. The simulation results are in good agreement with available measurements. The discharge distribution predicted by the model for various flow regimes in the Meuse River and the canals is discussed. Finally, the influence of alternative implementations of the weir operation rules on the computed discharge in the Meuse River is evaluated.

2.1 Introduction

Hydraulic works are widely used to allow navigability in waterways, flood control, irrigation, and numerous other purposes. Nowadays, the majority of shallow water models are capable of simulating water flow in river systems by taking into account the influence of hydraulic structures. However, the implementation of such structures in shallow water models requires specific considerations that depend on the type of numerical method. Hydraulic structures introduce discontinuities in the water surface profile at the location of the structure. Moreover, in the near-field of hydraulic structures, pressure distribution is not hydrostatic (García-Alén et al. (2021), Zerihun and Fenton (2007)). Shallow-water models with hydraulic structures developed so far typically fall into one of the following categories, depending on the method employed for integration of the equations: (1) finite differences (FDM), (2) finite volumes (FVM), and (3) finite elements (Flood-Modeller (2023),HEC-RAS (2017),MIKE-11 (2021),Sobek (2018)). For all the categories, the momentum equation is replaced by the empirical stage-discharge relationships at the structure's location. This approach is regarded as imposing internal boundary conditions on the nodes where the structures are located. IBCs enable to have more flexibility in incorporating different structures (Zhao et al. 1994), including gates and reduce the need for local mesh refinement (Echeverribar et al. (2019)).

The aim of this paper is to present an alternative implementation method where the hydraulic structures are introduced into the model as internal boundary conditions in order to overcome the discontinuity and obtain a solution at these points. This is critical, especially when the main goal is to simulate large river systems that are highly impacted by human activities such as navigation and energy generation (Dazzi et al. (2020)). In classical solution methods, the nodes around the structure location must be as close as possible so that the underlying assumptions of the stage-discharge relationships are still valid. For instance, according to Sobek (2018), neighboring nodes of the structure should be no more than 0.5 m apart. That demands using small time steps to maintain stability around the discontinuity. Hence, these schemes face great challenges in order to obtain fast, accurate and stable solutions.

The discontinuous Galerkin (DG) method is a hybrid approach that combines the finite volume and finite element approaches. It also deals with the weak formulation, but it allows the integration of the equations over each segment (in one dimension) or a cell (in two dimensions) independently. The connectivity of each element with its neighbors is ensured by means of the numerical fluxes that are responsible for the transfer of information between them. In contrast to finite volume methods, a higher order approximation to the solution can be applied over each element and that makes the method less sensitive to the flux treatment done at the element edge (Draoui et al. (2020)). In reference to the incorporation of hydraulic structures for water flow modeling, in the DG method, the discontinuities at the boundaries give the possibility of using an alternative approach to the one used in classical methods. In this paper, the conventional numerical fluxes are replaced by newly formulated fluxes that allow the application of empirical relationships at the location of structures without the drawback of requiring the sections upstream and downstream of the structure to be very close to one another in order to ensure the stability of the solution.

The computational power available nowadays allows simulating not only large and complex systems in either one, two, or three dimensions but also combining them in just a single model. Therefore, an effort has been made to develop and adapt new integration methods for the shallow water equations; one of them has recourse to the discontinuous Galerkin (DG) method. Since the introduction of the DG method by Reed and Hill (1973), further developments have been done in order to deal with shallow water equations (Cockburn et al. (1990), Cockburn and Shu (1989),Kesserwani et al. (2008),Kesserwani and Liang (2011)). Thus far, it has been shown that this method is useful in situations where the level of detail required for the simulation of the systems changes depending on the region (de Brye et al. (2010)), for example, when an inland river systems, estuaries, coast, and ocean are coupled. Additionally, the method has been tested for natural river systems and has demonstrated its capacity to manage highly variable bed topography (Lai and Khan (2012b)), as well as its relevance for channel networks (Neupane and Dawson (2015)). However, the viability of the DG approach for water flow in navigable rivers with substantial discontinuities has yet to be evaluated.

The SLIM (Second generation Louvain-la-Neuve Ice ocean Model) model used here includes different modules allowing to simulate a range of different water environments: the one-dimensional, the two-dimensional, and the three-dimensional modules (Hanert et al. (2023),Ishimwe et al. (2023),Saint-Amand

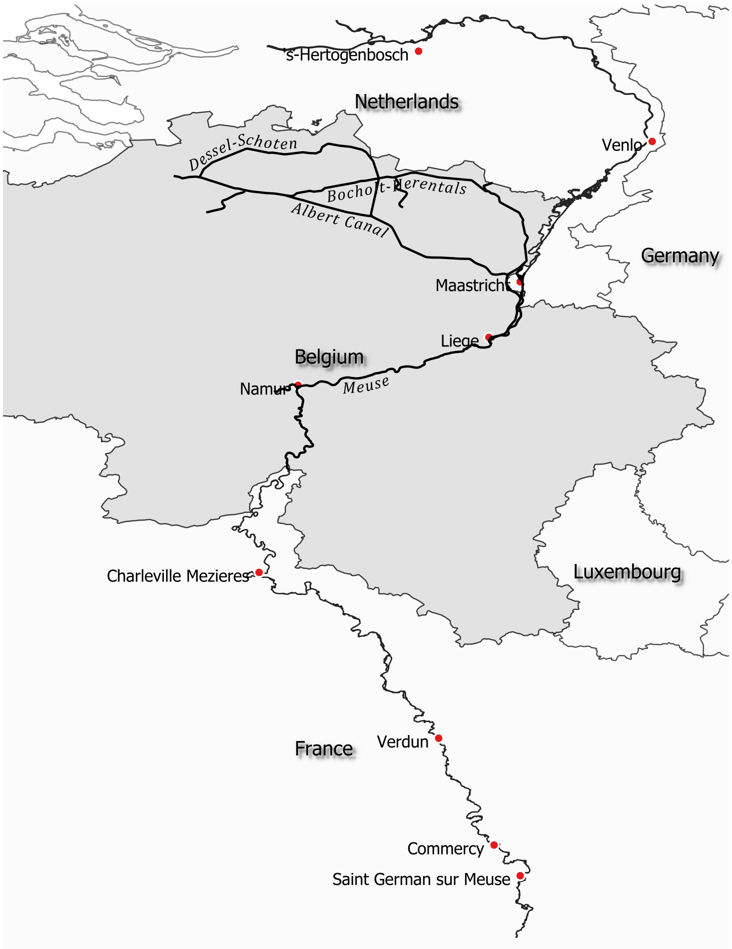

Fig. 2.1: Location map for the flow of transboundary Meuse River in France, Belgium and The Netherlands that is connected to the network of Campine canal in Belgium.

et al. (2023)). When needed, the 1D river model can be fully coupled with the 2D model to represent larger water bodies. Such a framework optimizes the computational resources without compromising the accuracy of the flow simulations. Here, the additional structural modules enable us to simulate the influence of hydraulic structures on the flow. The DG method in the current model has several advantages, including high-order accuracy, more flexibility in choosing the numerical flux approximation, and ease of parallelization, which is especially useful when dealing with large domains. In order to demonstrate the robustness of the proposed method for the incorporation of hydraulic works in this model, the Meuse River and its canal network (Campine Canal) that runs through Belgium are chosen (Figure 2.1). The water flow through it provides a classic case of highly regulated river systems. The structures in this river network are meant to keep a minimum water level that allows continuous navigation year around.

Hydraulic structures used for navigation can play a quite significant role during extreme flow events. Therefore, it is important to be able to adapt the configuration of the structures in real time to avoid flooding. Most of the studies on the Meuse River have focused on the assessment of the impact on flooding of changes in key factors, such as land use and climate changes (Ashagrie et al. (2006),Batlle-Aguilar et al. (2007),Leander et al. (2005),Tu et al. (2005),Wit et al. (2001)). Furthermore, flood inundation maps for communities along the Meuse River have been generated using a two-dimensional shallow water model to assess flood damage (Beckers et al. (2013),Erpicum et al. (2010)) in specific communities of Belgium. However, for such shallow water models in situations like flood simulation, the hydrostatic pressure hypothesis applies everywhere, including across the structure. Hence, while the research done involves modeling flow simulations in specific regions for extreme events, it does not address the influence of hydraulic structures in large river systems such as the Meuse River that includes canal systems.

Among the canals connected to the Meuse River, the Albert Canal is one of the major waterways and sources of drinking water in Belgium. During low flows in the Meuse River, the navigation in the Albert Canal and the water supplies is largely compromised. The operation of locks used for navigation during low periods can lead to a drop in water levels. Therefore, the Belgian agency of navigation has been using models to optimize the operation of these structures during both high and low flows (Pereira et al. (2016)). One of these models is a reservoir-type conceptual model that has been developed to investigate the impact of low flows on water quality under changing climate scenarios (Bertels and Willems (2022)). The existing models simulate the structure in a non-explicit manner as a combination of a sink-source by using a time series of observed discharge. However, this approach restricts the extrapolation for periods where no measurements are available. Therefore, the explicit simulation of the structures is believed to be crucial. In the earlier studies (Pereira et al. (2016)) in this area, diversion structures are considered as fixed structures, which may be a reasonable assumption for low flows. However, in the case of variable flow regimes, a stationary structure will be insufficient to consider flow diversion into the canal. For this, the requirement to make the structure operational is essential.

The aim of this paper is to introduce a novel discontinuous Galerkin approach in order to develop a system capable of reproducing the effect of hydraulic structures on the river flow. For that, we expand the SLIM (www.slim-ocean.be) modeling framework by incorporating additional modules for hydraulic structures. Additionally, a method is used to represent the operation rules of these structures in the river. Such capabilities are developed in order to simulate both low and high flows for large water systems such as the Meuse River systems. We assess the new developments by comparing flow simulations in the Belgian Meuse River and canal systems against measurements. Finally, once the simulation capabilities of the model are demonstrated, it is further used to analyse the impact of the structure's operation on the river discharge and discharge distribution in the canal network. Such large-scale system capabilities, together with process-based models, are crucial for sediment transport and water quality studies.

2.2 Numerical Modeling: Implementation of hydraulic structures

2.2.1 Discontinuous Galerkin Method

Typically, a river has a length relatively greater than its width. This is why a one-dimensional numerical model is appropriate (Hodges (2013)). Such a model solves the shallow water equations ((2.1) and (2.2)) in order to provide water flow variables averaged over each cross-section of the river.

$$\frac{\partial A}{\partial t} + \frac{\partial Q}{\partial x} = s \tag{2.1}$$

$$\frac{\partial Q}{\partial t} + \frac{\partial}{\partial x}(\frac{Q^2}{A} + gI_1) = gA(S_0 - S_f) + gI_2 \tag{2.2}$$

where, Q and A represent the volumetric flow rate and cross-sectional area, s is the source term, t is the time, x is the stream-wise coordinate, g is the acceleration due to gravity, S_0 is the bed slope and $S_f = \frac{n^2Q^2}{A^2R^{4/3}}$ is the frictional slope defined by the Manning formula, R is the hydraulic radius, I_1 is the cross-section first moment and I_2 is the spatial variation of the cross-section width.

This study uses the 1D discontinuous Galerkin method (DG) in the framework of SLIM to solve the shallow water equations. Here, in the momentum equation, $P = \rho g I_1$, $S_0 = \frac{\partial h}{\partial x}$ and $F = \rho g I_2$. These equations in terms of cross-sectional area and discharge are as follows

$$\frac{\partial}{\partial t}\begin{bmatrix} A \\ Q \end{bmatrix} + \frac{\partial}{\partial x}\begin{bmatrix} Q \\ \frac{Q^2}{A} + \frac{P}{\rho} \end{bmatrix} = \begin{bmatrix} s \\ -gA\frac{\partial h}{\partial x} - gAS + \frac{F}{\rho} \end{bmatrix} \tag{2.3}$$

where, h represents the water depth to the deepest point in cross section, $P = \rho g \int_0^H (H-z) b dz$ is the hydrostatic pressure force and $F = \rho g \int_0^H (H-z) \frac{\partial b}{\partial x} dz$

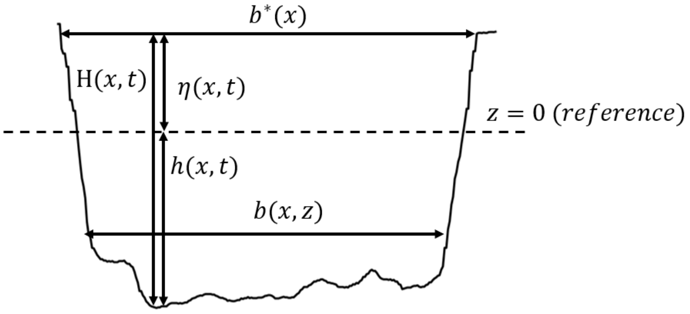

Fig. 2.2: Bed elevation of the river and the notation used to formulate the one dimensional Saint-venant equations for the river cross section.

is the along-flow component of the pressure force resulting from the width variation

S is the slope of the energy line (i.e., the friction induced head loss per unit distance) and the Manning formulation for $S(A, Q)$ is given by:

$$S = n^2 \frac{Q|Q|}{A^2 H^{*4/3}} \tag{2.4}$$

with $H^* = \frac{A}{b^*}$ is the effective depth (simplified form of hydraulic radius), b^* is the free surface width (Figure 2.2) and n is the Manning coefficient.

The conservation equations (2.3) are solved by approximating the solution using the discontinuous Galerkin (DG) method. The main characteristic of this method is that it applies the finite element method for the integration of the shallow water equation at the element level independently. However, this situation leads to multiple solutions at the inter-element interfaces. Therefore, a unique solution is determined by using numerical fluxes (also known as Riemann solvers) as done in the finite volume method approach. Thus, the DG method is normally seen as a combination of both approaches.

To illustrate this method, consider the above Saint-Venant equations in their generalized form:

$$\frac{\partial U}{\partial t} + \frac{\partial F(U)}{\partial x} = S(U) \tag{2.5}$$

where, U is the vector of unknowns with A and Q, whilst the $F(U)$ and $S(U)$ are the fluxes and source terms, respectively. In order to approximate the solution, the computational domain Ω is divided into a set of N_e non-overlapping elements Ω_e (Figure 2.3).

Based on the generalized form, U can be approximated as U_h in the finite dimensional space of polynomials on element Ω_e, with ϕ the set of independent

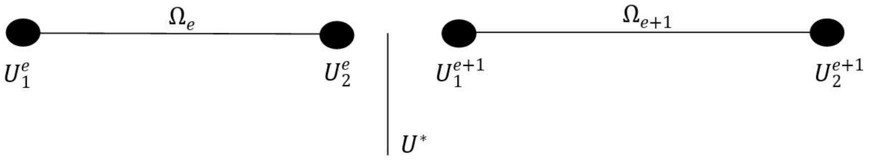

Fig. 2.3: Representation of the nodes in DG method with fluxes for solving shallow water equations and their corresponding symbols used for computation.

shape functions and U_i^e the new unknown nodal values. The approximate solution for each element is written as follows:

$$U|_{\Omega_e} \simeq U_h|_{\Omega_e} = \sum_{i=1}^{2} \phi_i U_i^e \tag{2.6}$$

In the next step the weak formulation is obtained by multiplying equation (2.5) by the local basis functions ϕ. Integrating this over Ω_e we obtain the following element solution:

$$\int_{\Omega_e} \frac{\partial U}{\partial t} \phi_i dx - \int_{\Omega_e} F \frac{\partial \phi_i}{\partial x} dx + [F\phi_i]_{x_e}^{x_{e+1}} = \int_{\Omega_e} S\phi_i dx \tag{2.7}$$

The local boundary term $[F(U)\phi_i]_{x_e}^{x_{e+1}}$ is the term that connects each element Ω_e with its neighbors. However, due to the discontinuous representation, the variables are double valued at the interface between elements. Consequently, it is important to appropriately define a common variable for U. This is made possible by tackling the Riemann problem, whose solution can be used to calculate these variables at a single discontinuity point using the values on the left and right. The description of the problem contains the mathematical character of physical conservation rules. Here, the Riemann problem is defined for the two adjacent nodes U_2^e and U_1^{e+1} of the neighboring elements. In this method, the conservative equations are transformed on the basis formed by the eigenvectors of the Jacobian matrix for the flux $J = \frac{\partial F(U)}{\partial U}$ to obtain the following characteristic form:

$$\begin{bmatrix} \frac{\partial W_1}{\partial t} \\ \frac{\partial W_1}{\partial t} \end{bmatrix} + \begin{bmatrix} \frac{Q_0}{A_0} - \sqrt{\frac{gA_0}{b^*}} & 0 \\ 0 & \frac{Q_0}{A_0} + \sqrt{\frac{gA_0}{b^*}} \end{bmatrix} \begin{bmatrix} \frac{\partial W_1}{\partial x} \\ \frac{\partial W_1}{\partial x} \end{bmatrix} = \begin{bmatrix} -gA\frac{dh}{dx} + gS \\ gA\frac{dh}{dx} - gS \end{bmatrix} \tag{2.8}$$

where A_0 and Q_0 are the mean values between the left U_2^e and U_1^{e+1} nodal values, and W_1 and W_2 are the Riemann invariants. The solution to the Riemann problem for such a discontinuity point lies between the characteristics

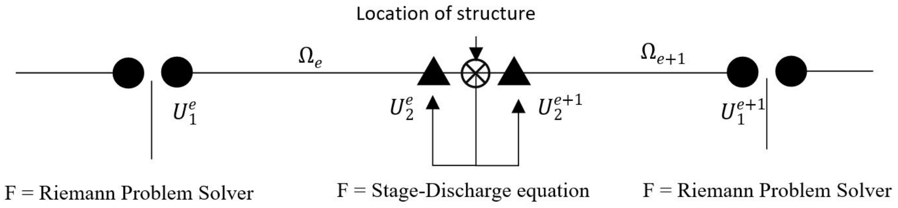

Fig. 2.4: Representation of the nodes in DG method and the treatment of flux by stage-discharge relationships for the imposed discontinuity at the location of hydraulic structure.

of the two eigenvalues (Toro (2009)), and this region is usually known as the star region (U^*). Based on these Riemann invariants, the final solution for the Riemann problem is developed, where the variables of U^* can be determined by the following equations:

$$on \quad \Omega_e : -A^*(\frac{Q_0}{A_0} + \sqrt{\frac{gA_0}{b^*}}) + Q^* = -A_2^e(\frac{Q_0}{A_0} + \sqrt{\frac{gA_0}{b^*}}) + Q_2^e \tag{2.9}$$

$$on \quad \Omega_{e+1} : A^*(-\frac{Q_0}{A_0} + \sqrt{\frac{gA_0}{b^*}}) + Q^* = A_1^{e+1}(-\frac{Q_0}{A_0} + \sqrt{\frac{gA_0}{b^*}}) + Q_1^{e+1} \tag{2.10}$$

Consequently, the term $[F(U)\phi_i]_{x_e}^{x_{e+1}}$ is computed along the element edges. Toro (2009) provides a detailed description and relevance of every term in the Riemann problem method. Refer to Draoui et al. (2020) for a thorough description of the method used to implement the DG method for Saint-Venant equations used in the SLIM Model. For the time integration, we employ the implicit Runge-Kutta scheme that allows flexibility in terms of time step (Iserles (2008),Quarteroni et al. (2007)).

2.2.2 Implementation of hydraulic structures

The DG approach has several benefits when simulating flow and transport in rivers with sudden changes in flow induced by, for example, hydraulic works. Under such conditions, the hydraulic structures in the DG Method can be implemented by imposing a discontinuity at the location of the structure. At this point, rather than employing the typical flux approach in which U* is computed using the Riemann problem solver, a stage-discharge relationship for the structure is employed, as shown in Figure 2.4. Using the stage-discharge relationship, the discharge across the structure is calculated based on the computed area on element Ω_e and Ω_{e+1}. Accordingly, the flux term in Eq. 2.7 is calculated as follows, where the negative sign in the matrix for $F|_{U_2^e}$ is indicative of the flow direction:

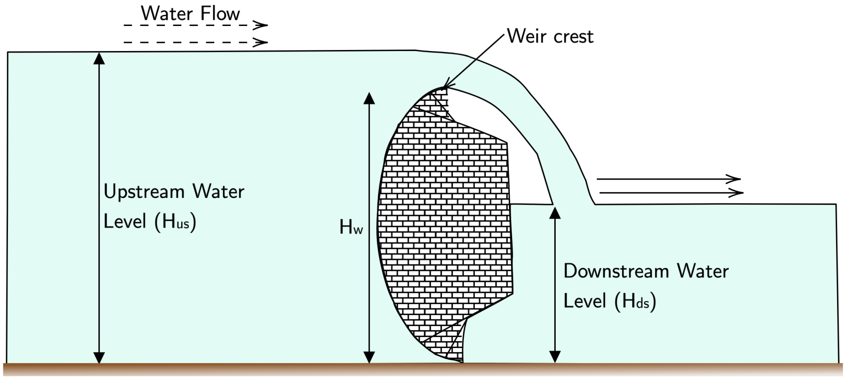

Fig. 2.5: The schematic of the weir in the river and the terms corresponding to the computation of the discharge in the weir equations

$$F|_{U_2^{e+1}} = \begin{bmatrix} Q_{stage} \\ \frac{Q^2_{stage}}{A_2^{e+1}} \end{bmatrix} \quad and \quad F|_{U_2^{e}} = \begin{bmatrix} -Q_{stage} \\ -\frac{Q^2_{stage}}{A_2^{e}} \end{bmatrix} \tag{2.11}$$

where, Q_{stage} is the discharge calculated using the stage-discharge relationship and A_1^{e+1} and A_2^e are the computed areas on the node downstream and upstream of the structure, respectively. The above Eq. 2.11 indicates that the flow across the structure can be entirely based on the water level and velocity observed upstream and downstream of the structure. In this implementation, the classic standard structures and their stage-discharge relationships determined empirically have been incorporated.

2.2.3 Stage-Discharge Relationships

The discharge over a weir is determined as a function of the difference in water levels. Based on the construction of the weir, the relationship between the stage and discharge can vary. Rectangular broad crested weirs are considered in this study, which are most prevalent in river systems. In this type of structure, the expression for discharge will depend on upstream water level (H_{us}), the weir crest level (h_w) and the downstream water level (H_{ds}) (Figure 2.5). Under these conditions, two scenarios are possible. In the first case, the downstream water level is low enough that it has no effect on the upstream flow conditions (free flow condition), whereas in the second case, the downstream water level is high enough to affect the upstream discharge and water level (submerged flow conditions). The equation for weirs is as follows (Bos (1989)):

$$Q_{stage} = \begin{cases} C_1 W(H_{us} - H_W)\sqrt{(H_{us} - H_W)} : \frac{H_{ds}-H_W}{H_{us}} < \frac{2}{3} \quad Free \quad flow \\ C_2 W(H_{ds} - H_W)\sqrt{(H_{us} - H_{ds})} : \frac{H_{ds}-H_W}{H_{us}} \geq \frac{2}{3} \quad Sub \quad flow \end{cases} \tag{2.12}$$

where, C_1 and C_2 = weir coefficient and W = width of the structure (see Figure 2.15 for the width representation). The above Eq. 2.12, when applied to submerged conditions, allows us to connect the upstream water level of element Ω_e to the downstream water level of element Ω_{e+1} across the structures. As a result, no special treatment of the water level is required for the direct implementation in the discontinuous Galerkin method.

In the above Eq. 2.12, the upstream water level must always be greater than the weir crest. However, based on the water levels across the weir, several other conditions have been prescribed to consider particular cases. Firstly, zero flow is computed across the weir if the water levels upstream and downstream are lower than the weir crest. Secondly, if the downstream water level is higher than the weir crest and the upstream water level, the flow direction is naturally reversed. Because the DG method takes information in both directions, it can effectively accommodate such a natural process. However, the difference in water levels yields a negative result in Eq. 2.12 for the structure. If this occurs, the parameters for upstream and downstream water levels in the discharge expression are swapped. Hence, this implementation of weir structures becomes valid for the bidirectional flow of the river.

Underflow gates are widely used to control the discharge from rivers into canals. If the gate opening is unsubmerged or in free flow conditions, then relationship will only depend on the upstream water level and gate opening. If the opening is submerged, the discharge also depends on the submergence depth ($\frac{H_{ds}}{H_{us}}$) (Figure 2.6). The relevant equations for computing the discharge are is represented in Eq. 2.13 (Bos (1989)):

$$Q_{stage} = \begin{cases} CWH_W\sqrt{2gH} \quad where \quad H = H_{us} - H_W : \frac{H_{ds}}{H_{us}} < 0.66 \quad Free \quad flow \\ CWH_W\sqrt{2g3H} \quad where \quad H = H_{us} - H_{ds} : \frac{H_{ds}}{H_{us}} > 0.66 \quad sub \quad flow \end{cases} \tag{2.13}$$

where, H_w = gate opening height and C = the loss coefficient. In the underflow gate, several other possibilities such as submerged weir flow can also occur but is not considered in this study.

2.3 Meuse River Systems

The Meuse River follows a transboundary course in Europe for up to 895 km in distance (Kitsikoudis et al. (2020)). It originates in France and flows through Belgium to reach the North Sea through the Netherlands. The Belgian part

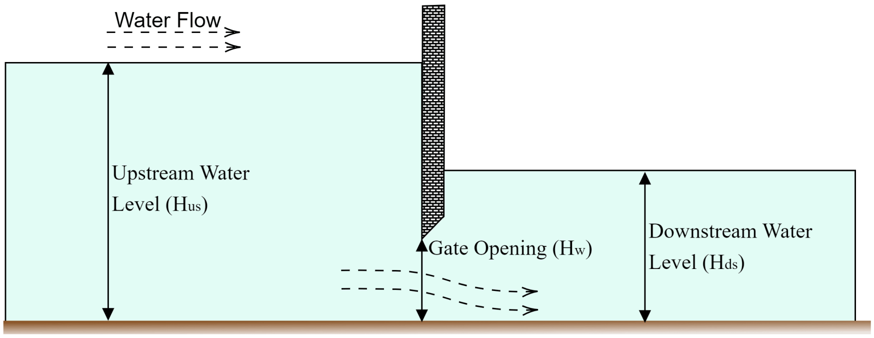

Fig. 2.6: The schematic of the Sluice gate in the river and the terms corresponding to the computation of the discharge in the gate equations

of the Meuse river stretches up to 144 km from Givet at the French border to Lixhe near the Netherlands border (Beckers et al. (2013)) and is one of the great navigable rivers in Europe that connects these countries (Figure 2.7). It is canalized throughout most of its course in Belgium and bypassed by the Juliana Canal in the Netherlands and thereafter it continues as a free flow. The Belgian part of the Meuse River is highly regulated by a combination of weir systems and lock chambers, which play a major role in river flow dynamics. Along the Meuse River in Belgium, there are 15 weirs between Givet and Lixhe. These weirs raise the water level to obtain a sufficient hull for navigation even during dry periods. This also aids in reducing the velocities in the river for safer navigation. Beside the weirs, a lock is placed at the same location, which assists the vessel with vertical movement in order to pass from one river segment to the next.

The Meuse River systems, as shown in Figure 2.7 can be subdivided into three parts: (1) the Meuse River that extends from Givet to Liège and includes all its tributaries. Among them are the Sambre and Ourthe rivers, which have a large catchment area that can contribute a significant influx into the Meuse River, (2) The Dutch part of the Meuse River that starts downstream of the weir of Monsin and ends at the bifurcation of the Meuse River into the Juliana Canal (Figure 2.9b) at Maastricht. At this point, part of the Meuse river is also diverted to the Zuid-Willemsvaart canal that returns to Belgium (Figure 2.7) and feeds the Flemish channels located in the north of Belgium. With a stretch of 46 km in Belgium, the Zuid-Willemsvaart canal exits Belgium at Lozen (Figure 2.7) and continues its flow into the Netherlands and (3) The Albert Canal system that starts downstream of Liège flows into Flanders and discharges its water into the Scheldt Estuary. The Albert Canal connects Antwerp and Liège with a total length of 129 kilometers and six sets

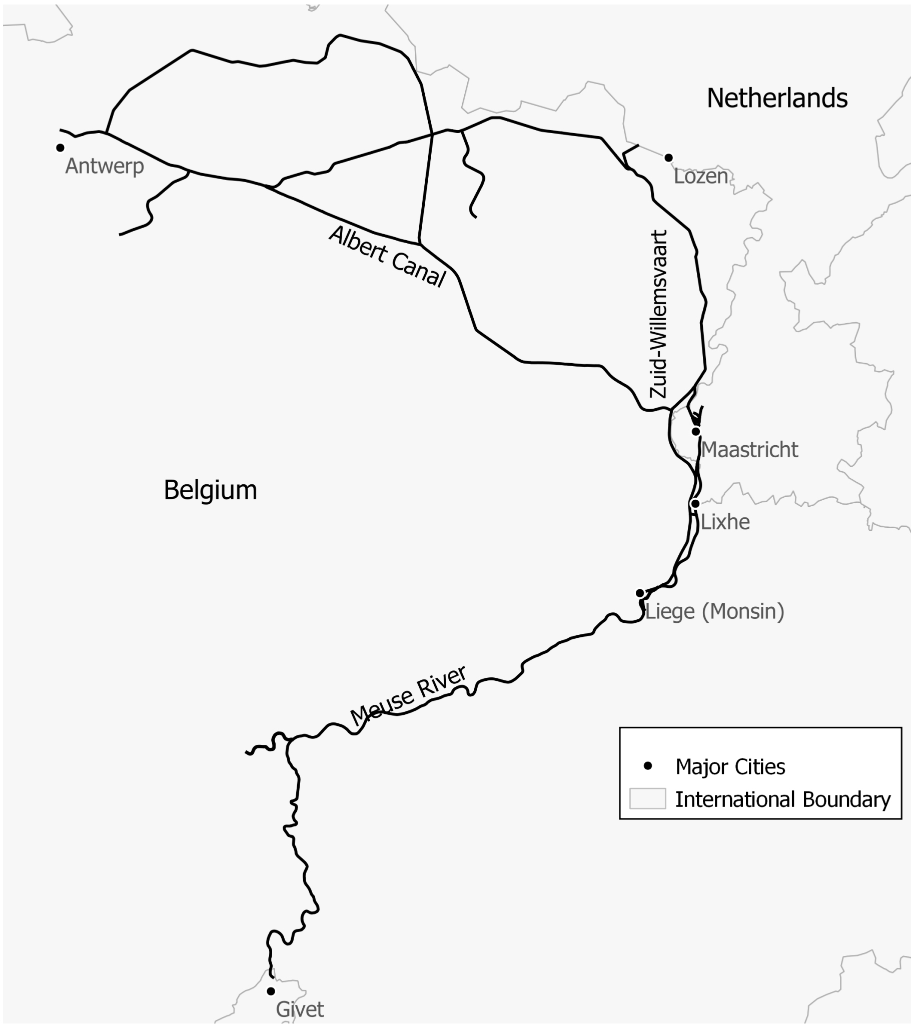

Fig. 2.7: Map of the section of Meuse River and its canal systems flowing in Belgium

of canal locks (Figure 2.10) are installed to overcome the difference in elevation of 56 meters. On the one hand, the distribution of water between the Albert Canal and the Dutch Meuse systems is regulated at Liège by operating the weir located at Monsin. On the other hand, the diversion of the water from the Meuse into the Juliana Canal and Zuid-Willemsvaart at Maastricht is controlled by a weir and an underflow gate, respectively.

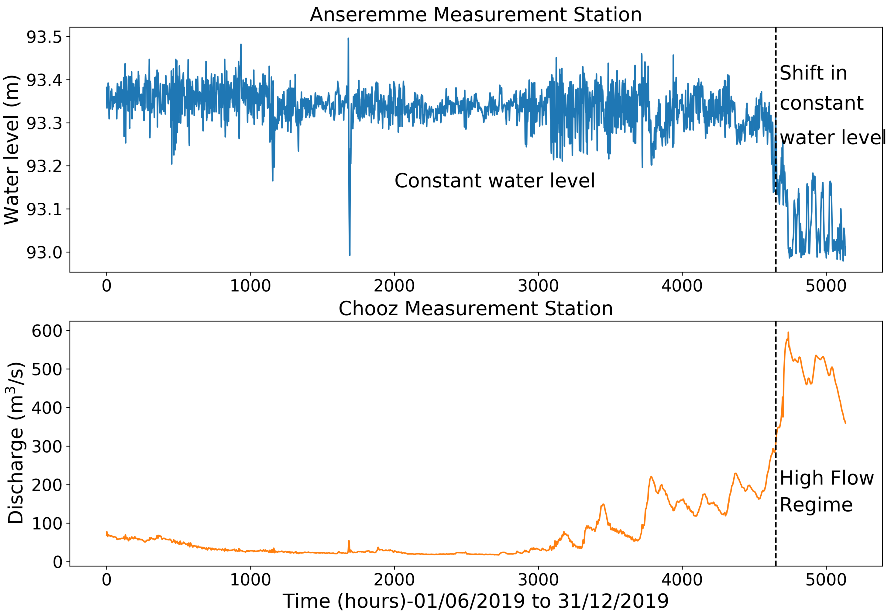

Fig. 2.8: (a) The Measurement data for water level station at Anseremme (Top) and (b) discharge station at the Chooz (Bottom): Representation of the target level maintained in the Meuse River and shift in target level due to change in flow regime.

2.3.1 Structures in Meuse River systems

The weirs in the Meuse River are movable, and they are operated to maintain a target water level in the river. The operation of these weirs is based on feedback from water level measuring stations. Furthermore, the river discharge measurements at Chooz in the upper Meuse and Amay in the lower Meuse are also used as complementary criteria for the operation of the weirs (for locations, see Figure 2.17). If the discharge in the river reaches a certain threshold, the target water level that needs to be maintained is lowered. This can be observed in measurement data; for instance, as seen in Figure 2.8a, the measured water level at Anseremme (about 24 kilometers from Chooz) is lowered from 90.35 to 90.06 meters at around 12th December 2019 (i.e., 4650th hours in Figure 2.8). While at the same time, as seen in Figure 2.8b, the corresponding discharge measured in Chooz has exceeded the 500 m^3/s discharge threshold. This is done in order to prevent the weir directly upstream of the weir under consideration from becoming submerged.

Nonetheless, in specific locations, such as weirs near major cities like Namur and Liège, the weirs operate under specialized rules. The weir at Liège (referred

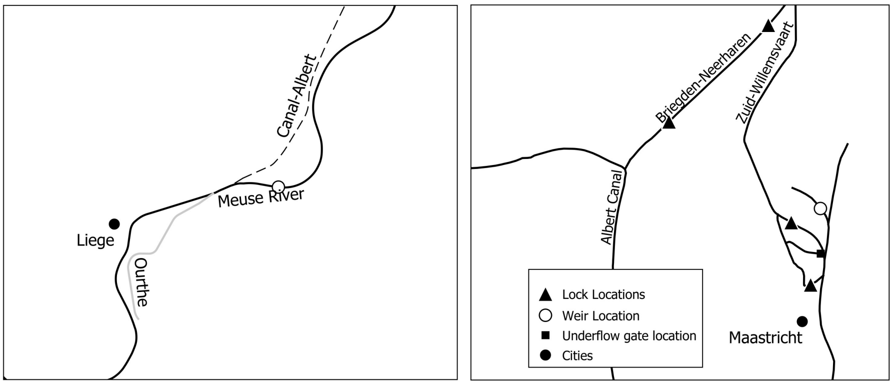

Fig. 2.9: (a) Map for the connection of Albert Canal (Left) and (b) Zuid-Willemsvaart (Right) with the Meuse River and the location of locks and weirs near the connection.

to as Monsin Weir) is placed in the Meuse just downstream of the splitting point of the Meuse and the Albert Canal (Figure 2.9a). This weir has the main function to control the flow into the Albert Canal. However, it also plays a significant role in flooding control in the Albert Canal. The Monsin weir can be lifted to function simultaneously as a weir and an underflow gate. Moreover, the structure can be completely lifted during very high flow events to obtain a more effective flow conveyance and avoid flooding the cities. A similar weir is also present in the river at the bifurcation of the Meuse at Maastricht. At the point of water diversion at Maastricht, a weir is used to keep the water level for navigation and to convey the water through the Juliana Canal. Upstream of this bifurcation on the left bank of the Meuse River, an underflow gate and lock chamber are used to feed water into the Zuid-Willemsvaart canal (Figure 2.9b) and to allow navigation through it.

2.3.2 Lock Chamber in Meuse River and Albert Canal

The lock chambers used in the Meuse River and the Albert Canal aid in the movement of boats through varying water levels. However, to operate the locks in the Albert Canal, a rather stable water level at its entrance needs to be ensured, which is the main function of the Monsin Weir. Since the Albert Canal needs to be navigable year around, its operation can be difficult during dry periods. For this period, a series of Archimedes screw pumps placed beside the lock chamber are used to bring the water used during the movement of the vessel back upstream of the lock.

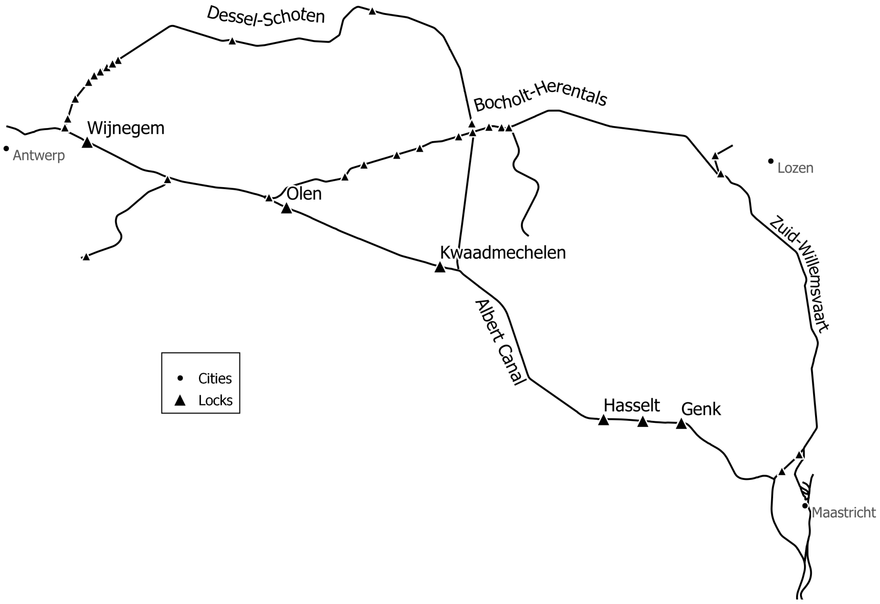

Fig. 2.10: Map for the location of locks in Albert Canal, Zuid-Willemsvaart canal and their interconnecting canals

2.3.3 Structures in Albert Canal and Campine Canals

Figure 2.10 shows the lock chambers present in the Albert and the Campine canals, which in total comprise 28 locks. Among them, the Albert Canal consists of six locks, each bounded at both ends by a set of three lock chambers, as shown in Figure 2.11. The navigation in this canal allows larger vessels than in the other canals of the country. The smaller Campine canals, fed by the Zuid-Willemsvaart canal, are connected to the Albert Canal at four different places, as seen in Figure 2.10. These canals are smaller in size, and navigation is made possible by a single lock chamber. Like the Meuse River, maintaining the water level in these canals is also of vital importance. For this purpose, there are bypass channels constructed across the lock chamber (Figure 2.11) that allow the water to flow continuously once the target water level for navigation is reached at each segment of the canal. For the lock chamber placed in the other Campine Canals, the flow continuity is regulated by the culvert used for filling and emptying the lock chamber.

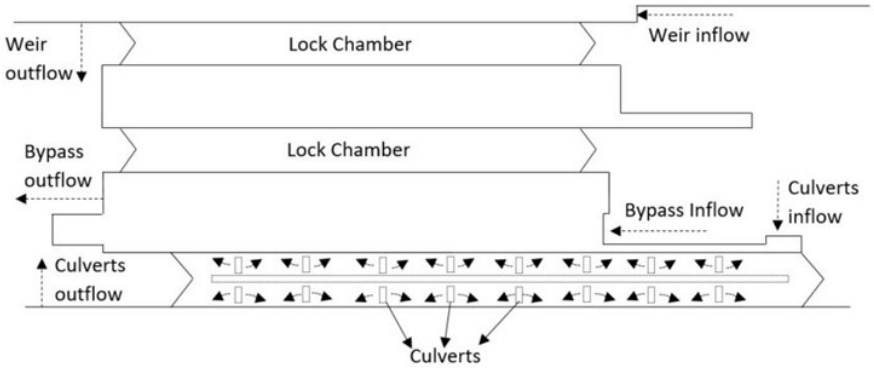

Fig. 2.11: Schematic diagram of a typical lock chamber in Albert canal with illustration of different flows across the Lock chamber to maintain the water level.

2.4 Model Setup

The case study area comprises the Meuse River in Belgium and the canal networks to which it is connected, including the Albert Canal. The 144 kilometers long stretch of the Meuse River considered here runs from the Belgian-French border (at Givet) to Maastricht in the Netherlands . The Meuse River is connected to the Albert Canal and Zuid-Willemsvaart Canal, which are included in the modeling. The former extends over 156 kilometers from the Meuse River to the port of Antwerp, and the latter runs over 46 kilometers from Maastricht to Lozen. Interconnections between these main canals play an important part in water distribution (Figure 2.7). As a result, the canals that connect the Albert Canal, such as Bocholt-Herentals, Schoten-Dessel, Kwaadmechelen-Dessel (Figure 2.10) and Briegden-Neerharen (Figure 2.9b) are also included in the computational domain. A section of the Juliana Canal, just downstream of its connection with the Meuse River, is also represented in the simulations. The domain of the study is shown in Figure 2.12.

2.4.1 Meuse River Model: Setup

The cross-sectional profile of the riverbed is required to solve the Saint-Venant equations. The bathymetric data (multi-beam sonar) was combined with the topography data (LidAR) in order to improve the representation of the riverbanks. This is because the LiDAR's are unable to fully penetrate the water and the fact that sonars are often employed in boats prevents them from covering the banks, as seen in Figure 2.13. The topography, however, can stretch far enough from the riverbanks. As a result, the point in the topography data with the highest elevation within 50 meters of the riverbank was chosen as the

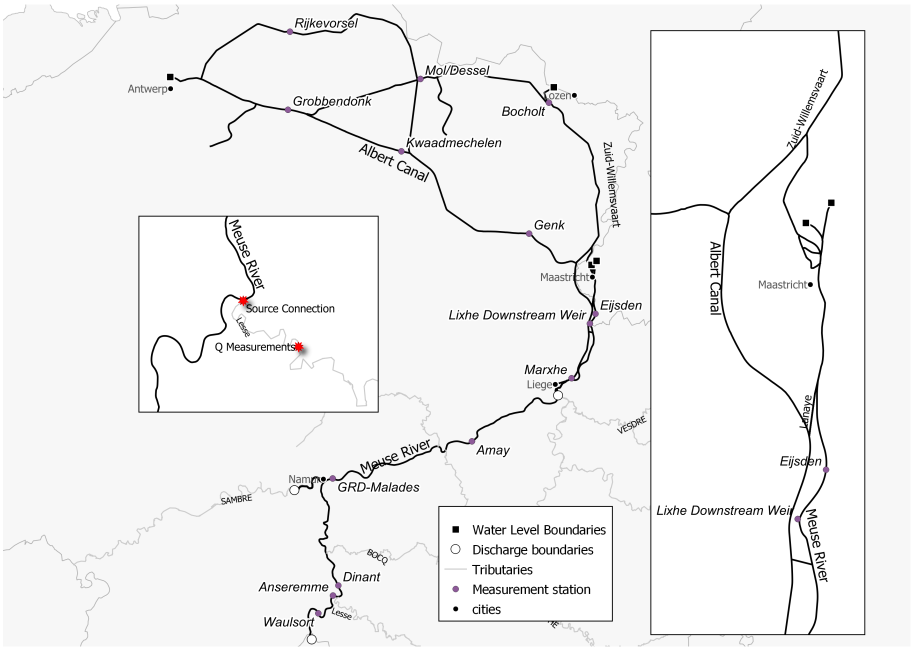

Fig. 2.12: Map of the section of Meuse river and its canal systems flowing in Belgium: The location of boundary condition. The tributaries Sambre and Ourthe are considered in the model with appropriate boundary conditions.

end point for the cross-section profile (Figure 2.13). Later, among the highest point from the left and right of the river, the one with a smaller elevation is considered as the maximum elevations for that profile. An illustration of this is shown in Figure 2.13. These profiles were extracted along lines that were perpendicular to the flow, which were generated based on ortho-photos of the river every 500 meters. Special emphasis is given to the profile's end points in areas with islands, side dykes and regions where canals/tributaries join the river. Discharge at upstream boundaries of the computational were prescribed at three locations, as shown in Figure 2.12:

- at the measurement station of Chooz, which is located close to the French-Belgian border,
- at Ronet on the Sambre river (left-bank tributary of river Meuse)
- and at Sauheid on the Ourthe river.

These rivers are the only tributaries for which bathymetric data are available; hence, they are included in the model up to the first available discharge mea-

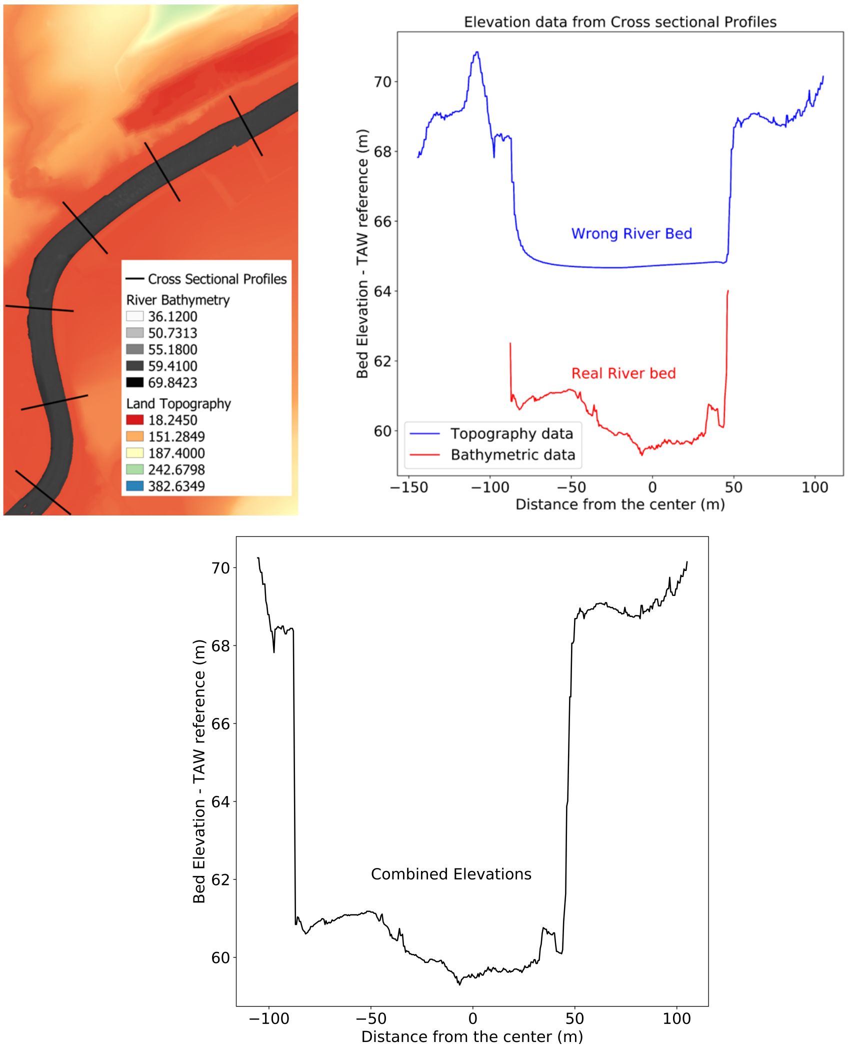

Fig. 2.13: Illustration of the selection of cross-section profile from the bathymetry and topography data: Perpendicular lines drawn on the both data sets (left), cross-section profile for both data sets (Middle), Combined profile (right)

surement point upstream from their corresponding confluence. For the rest of the tributaries, no bathymetric data is available. In order to include the flow delivered by the tributaries, available time series of discharge measured upstream at the confluence with the river Meuse are introduced into the model as source terms at the junction, as shown in Figure 2.12. The stations used for specifying the source terms representing the tributaries are listed in Table 2.1.

Tributaries as source terms	**Measurement station used**	**Distance from the Confluence**
Hermeton River	Hastière Station	2 km
Houille River	Houille Station	7 km
Lesse River	Grendon station	10 km
Molignée River	Warnant Station	5 km
Bocq River	Yvoir station	2 km
Burnot River	Profondeville station	3 km
Samson River	Thon Station	9 km

Table 2.1: The tributaries included in the model as source term with their respective station used as input and the distance of the measuring station from the confluence with the Meuse river.

The discharge measuring station for the tributaries indicated above is sometimes located far from the confluence with the Meuse River. These stations can be up to 10 km away from the confluence, while others are within 2 km. This causes the hydrograph's peak to shift, especially during heavy precipitation events in the catchment basin of these tributaries. The main difficulties during the determination of peak shift are: (1) the difference in discharge magnitude between the Meuse and each of the tributaries and (2) the lack of intermediate stations that could be used to estimate the shift. The available stations for discharge measured in the Meuse River account for the contribution of a large part, that already includes the catchment of most of the tributaries. Therefore, during high flow events, the individual contribution of the tributaries is difficult to define.

For the downstream boundaries, the water levels measured at: (1) Wijnegem station located in Albert Canal, (2) Boergerhan station in Juliana Canal and (3) Lozen station in Zuid-Willemstraat canal were used.

2.4.2 Canal Model: Setup

In the Campine canal, it is considered that the slope of the channels between lock chambers is negligible. This is based on the historical information presented in the reports, where the elevation downstream of a lock chamber is identical to the elevation upstream of the following lock chamber. Moreover, based on bathymetric surveys done for a small segment downstream of Liège,

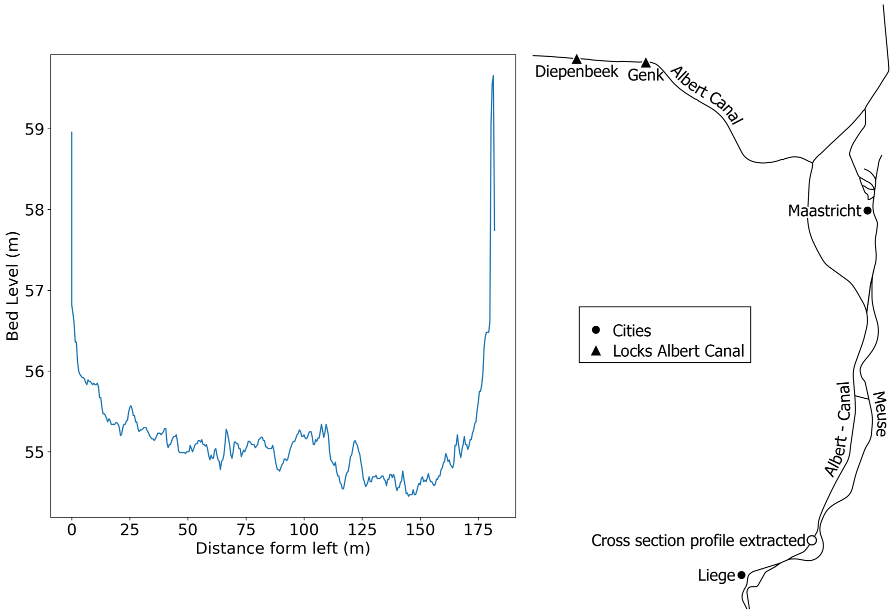

Fig. 2.14: (a) Bed Level elevation in Albert Canal at Monsin (connection with the Meuse river) in TAW reference level (left). (b) Location of the cross-section profile extracted from the Bathymetric data and the Genk lock in Albert canal (right)

we can confirm that the elevation reported corresponding to Genk (upstream of the lock) and the values of the last cross section extracted from the bathymetric data are similar, as presented in Figure 2.14. It is important to emphasize that the distance between Genk and the last cross section available from the survey is located 40 km away. Additionally, due to a lack of precise bathymetry, the cross section of the canals is assumed to be rectangular. For the width of the channel, the ortho-photos were used from "Geopunt Flanders", (2022).

In Albert Canal, other structures, such as bypass channels and culverts used to maintain the water level, are also present adjacent to each lock. Other smaller canals lack bypass channels and rely solely on culverts to keep the water level constant. The dimensions, functioning, and operation rules of these constructions are unknown to the authors. The development of such a sophisticated structural system is a challenging undertaking from a modeling perspective. Since there is a lack of data on how these structures function, it is difficult to establish precisely how each of them would affect the flow. As a result, addressing the unknown factors of each structure independently in the numerical model can result in a variable space with a large number of dimensions that could not be defined adequately. Therefore, we opted to deal with them as single input-output structures, where the different flows (the flow through bypass, culverts and leakage losses) through them are lumped. Here, these structures are implemented as a weir for the sake of simplicity and to further avoid the complications of the simulation of the emptying and filling of the lock chamber. The simulation of the emptying/filling time of the lock chamber requires a smaller simulation time step. The important advantage to simulate lock chamber as weirs is that weirs make possible both regulation of the water level and the control of the discharge flow through the structure.

Downstream of the Belgian-Dutch border, the connection between the Meuse River and the Zuid-Willemsvaart Canal at Maastricht is simulated as an underflow gate. The dimensions of the underflow gate are based on site measurements, and the gate opening is determined to approximate a discharge of 11 m^3/s. Moreover, there will be a steady discharge through the gate because the Zuid Willemsvaart canal lock at Bocholt and the weir at Maastricht control the water level upstream and downstream of the underflow gate, respectively. As a result, the Meuse River is set up to discharge approximately 11 m^3/s of water into the main canal, which is consistent with the reported data (De smedt and Van der beken (1982),Van Steenbergen (2017)).

2.4.3 Operation Rules for the Weirs

The operation of the weirs in the Meuse River is such that the water level upstream remains at a target level, which is determined based on the discharge as discussed earlier. All weirs along the Meuse River are operated according to such operating rules, except for the Monsin Weir, where the target water level remains constant irrespective of the discharge. This is linked to the position of this weir in the direct vicinity of the bifurcation with the Albert Canal. The target water level can be clearly observed in the measurement data (Figure 2.8); the level of the weir crest, on the other hand, cannot be estimated, nor any measurement data is available to the authors. Additionally, as illustrated in Figure 2.15, weirs are divided in the lateral direction of the flow and the radial gates can be operated individually. Thus, it is possible to obstruct the flow in some weirs while passing it through others. If so, no data regarding this operation is available. Hence, we assume that all the gates of the weir are always in operation and the width of these gates are determined using ortho-photos. Due to this data limitation, implementing these operation rules is a difficult task. Nonetheless, based on the observed measurement data the equation 2.14 was obtained in order to compute the weir crest level (h_w). It is also worth noting that the weir height is an assumption as no data is available.

$$h_w = h_m - (\frac{Q}{C_1 W})^{\frac{3}{2}} \tag{2.14}$$

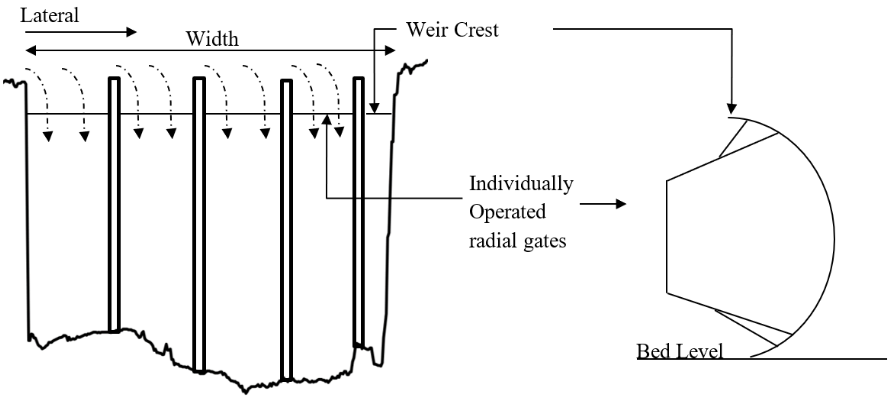

Fig. 2.15: Schematic representation of a typical weir in the Meuse river

where, h_m is the water level that needs to be maintained. This equation is directly derived from the weir equation. Here, if the parameters such as the weir coefficient and width (w) are kept constant, the weir crest will mainly depend on the h_m and the discharge. The constant water level that needs to be maintained can be determined from the measurement data, and the weir crest level can then be controlled solely by discharge. In the model, this discharge is obtained from a node upstream of the weir. In general, these operations rules that are established in the model will allow all the discharge to pass through the weir. This can be seen as an inverse problem where, based on the discharge and water level, the elevation of the crest level is determined. This approach of operating the structures acts as an internal boundary condition for water level.

2.4.4 Calibration Method

In the shallow water equations, the computed flow variables are the cross-sectional flow area and the discharge. Two model parameters must be estimated by calibration. One is the Manning coefficient associated with flow resistance modeling, and the other is the weir coefficient in the stage discharge relationships characterizing the structures. A dependence of such coefficients on flow variability (e.g. hysteresis in the stage-discharge relationship may arguably exist. However, this dependence is only strong for extreme conditions such as low water depth (García (2005)) or flooding (Perret et al. (2022)).

The model is assessed by comparing the numerical results against measured water levels and discharges recorded at gauging stations. Most existing stations record water levels and only a few of them also monitor discharge. The model for the Meuse River is calibrated in two steps. First, the weir coefficients and

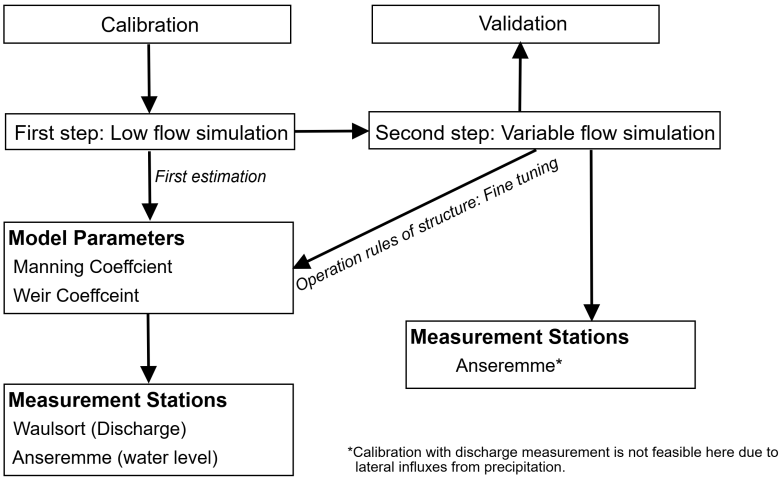

Fig. 2.16: Flow chart of the model setup procedures used to calibrate the considered model parameters using measurement stations.

the Manning coefficients are calibrated for a fixed elevation for the crest of the weirs. This situation happens during low flow periods when the weirs are barely operated, and inflows from the catchment and tributaries are minimal. Time series of water levels and discharges during such periods are used for a first estimation of the value of each coefficient. In this step, the simulated discharges are compared with observations at Waulsort and Anseremme stations (Figure 2.17). In a second step, a longer time series that comprises low and high flow periods is used to further fine tune the coefficients. During this period of time the weirs are operated in accordance with their regulation equations. In this step, the computed water levels are compared to measurements at Anseremme station (Figure 2.22).Figure 2.16 illustrates the flow chart for the steps involved in the method of calibration that is then used for the validation of flow variables at a different period.

The Nash-Sutcliffe Efficiency (NSE) coefficient is used as a metrics for model performance (Moriasi et al. (2007)). In particular cases in which the observations remain almost constant in time (e.g., regulated water level), the performance reported by the NSE coefficient is artificially low, as a result of the definition of this metrics (Morales-Hernández et al. (2013)). Hence, an additional performance metrics is utilized. It consists in evaluating the percentage of simulated data that fall within the 95 % confidence interval of the observations (based on the standard deviation of the observations) (Van Liew et al.

(2003)).

2.4.5 Data Availability

Among the data available, the majority of it consists of data collected by the measuring station for water level and discharge. Besides that, data such as the bathymetry of the river and the description of the canal are also made available by the regional authorities. In this section, all the measured data and the relevant data that is used during model setup, validation and calibration are described.

2.4.5.1 Bathymetric data

The elevation data used to extract the cross-sectional profiles was provided by the 'Service Public de Wallonie' (SPW), the regional authority for the Meuse River. The bathymetric data for the Meuse River were collected using multi-beam sonars and in certain shallow water areas by echo sounders with a resolution of 10 cm, whereas the relief of the flood plains was measured using the airborne LiDAR technique with a resolution of 1m. Unfortunately, a detailed bathymetric information for the Campine canal is not available. However, due to the regularity of the cross-section and the presence of locks, it is possible to construct the longitudinal profile of the canal. This is achieved by using information about the geometric characteristics of locks (FHR (2005)) and high resolution ortho-photos. Table 2.2 shows the bed level elevations described in the literature and are represented in the Belgium elevation reference (TAW - Tweede Algemene Waterpassing).

2.4.5.2 Data usage: Meuse River

In the Meuse River most of the stations that record the water level are situated immediately upstream of the weirs. Additionally, the difference in water levels between upstream and downstream of the weir is sufficiently large enough to prevent submersion of the structure. Therefore, water levels observed at these stations are around a target water level that guarantees navigability along the river. In the case of Lixhe station, the measurements are done (shown in Figure 2.17) directly downstream the last weir used for navigation in the Belgian Meuse. The calibration of the model was done using the measurement of the water level at Anseremme. With regards to the model validation, we compare the simulated water levels against measurements done at Anseremme, GRD and at Lixhe.

The model was also calibrated and validated for discharges. Although five measurement station exist, four of them have sufficient historical data for these purposes. The four stations are: (1) Chooz, whose measurements are used as a boundary condition, (2) Amay, the only station in the upper Meuse, (3)

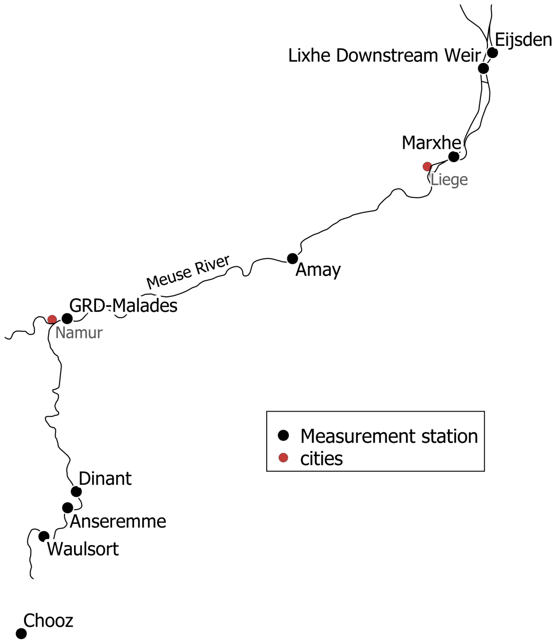

Fig. 2.17: Map of the section of Meuse river flowing in Belgium: The location of Measurement station used in the Meuse river for calibration and validation.

Waulsort, located downstream Chooz and (4) Eijsden, located in the lower Meuse. Though the Waulsort station has a record for short time series, it is selected for the calibration because this was adequate to calibrate the model (e.g. the weir coefficient). The time series for all these measurements in the Meuse river were obtained from “Service public de Wallonie” for Belgium and “Rijkswaterstaat” for the Netherlands. The measurement station used in this study for validation and calibration is shown in Figure 2.17:

2.4.5.3 Data usage: Campine Canal

The Albert Canal, as previously stated, begins at the junction with the Meuse River. The amount of discharge that is fed into the canal is determined by the operation of the weir in Monsin. The discharge required for canal operation has been reported in several publications and is also measured in the Albert Canal at the diversion. Table 2.3 describes the discharge reported by these studies at two different locations. One, at Monsin (Liege: Figure 2.7), where the division occurs and secondly, at Genk, where the first lock in Albert Canal is placed. The discharge in Genk is lower than that in Monsin due to the presence of three lock chambers (Figure 2.12) that allow water to pass through them. With respect to the other side channels that branches from the Meuse River, Table 2.3 also shows the discharge reported by these studies. The literature data on discharge reports single values and therefore they do not take into account the flow fluctuation in the Meuse River. The reported figures, shows discharges that vary within the range of 16 and 25 m^3/s. As a consequence these values are just used to bound the order of magnitude of the discharge (De smedt and Van der beken (1982),FHR (2005),Van Steenbergen (2017)). In the case of measurement data, the Haccourt station, located nearby the bifurcation of the Meuse into the Albert Canal, and Kanne station, which is closest to the Albert Canal's first lock (Genk), both show negative discharges (Figure 2.18). Furthermore, the measurements at these stations show that the discharge can reach up to 100 m^3/s (Figure 2.18), even when the discharge recorded in the Meuse River at Amay station is around 50 m^3/s. This could be attributed to interference's in the measurements taken at these locations (e.g. effect of waves induced by vessels, lock operations) . The influence of lock operation is more significant at the Kanne measuring station, this is because of its proximity towards the lock. As a result of these effects, the direct use of these measurements for calibration and validation is not possible because the model does not include this phenomenon. Nonetheless, the average trend of the time series could give us some insight about the water flow.

Name of the Lock	Bed level Upstream (m)	Bed Level Downstream (m)
Genk	55	44.9
Diepenbeek	44.9	35.8
Hasselt	35.8	24.7
Kwaadmechelen	24.7	14.7
Olen	14.7	4.7
Wijnegam	4.7	0.75

Table 2.2: The bed elevation in the Albert Canal as derived from the study: the elevation represented above are for bed level upstream and downstream of the Lock.

	FHR, 2005	Van Steenbergen 2017	De smedt and Van der beken, 1982
Albert Canal At Monsin	20 m^3/s	25 m^3/s	16 m^3/s
Albert Canal at Genk	9 m^3/s	-	6 m^3/s
Zuid-Willemsvart	-	15 m^3/s	11 m^3/s

Table 2.3: Discharge that is fed to the canal systems by the Meuse River as reported by different studies.

In the Flemish canals as well, it is observed that they exhibit similar behavior as described for stations in the Albert Canal. The interference due to operation in this case is much larger due to its closer proximity to the lock

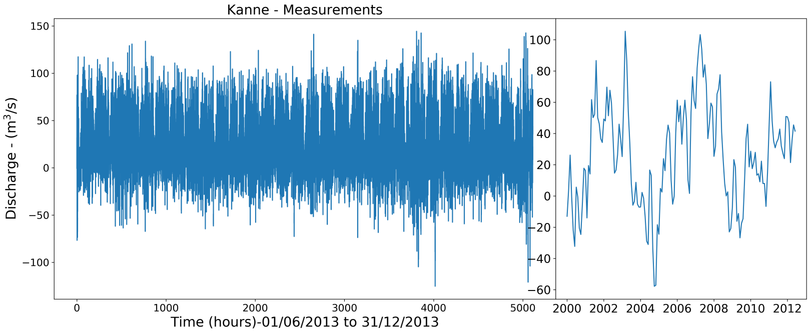

Fig. 2.18: Discharge Measurement data at Kanne (Closest to the Lock) in Albert Canal for the 3 months period (left) and the measurements recorded at this station during low flow in the Meuse River (Right)

chamber. As a result, the measurement data does not provide reliable information on the discharge, whereas previous studies by De smedt and Van der beken (1982) were able to measure an average discharge distribution across the Flemish channel (Table 2.4).

	Bocholt − Herentals	**Dessel − KwaadMechelen**	**Dessel -Schoten**
De Smedt et. al., 1982	9 m^3/s	3.5 m^3/s	2 m^3/s

Table 2.4: Discharge distribution in the Flemish canals as reported by De smedt and Van der beken (1982)

For the water level measurements, the reported data in the literature agrees well with the measurement data. Additionally, in Albert Canal, there are water level measurements taken at Marxhe, which is located immediately after the confluence, as shown in Figure 2.17. Therefore, in order to validate the implementation of diversion structures in the Meuse River for the Albert Canal, Marxhe Station is taken into account. The rest of the canal networks has over 20 water level measurement locations, each positioned just upstream of the lock chamber. Not all of these locations are used for validation; instead, the measurements closest to the confluence within these canals are selected. All the measurement stations used for validation for the water levels in the Albert Canal and the Flemish canals are shown in Figure 2.19.

2.4.5.4 Data availability for the tributaries

Most of the tributaries of the Meuse River lack bathymetric data, except for a small section for the Sambre and the Ourthe River. This makes including

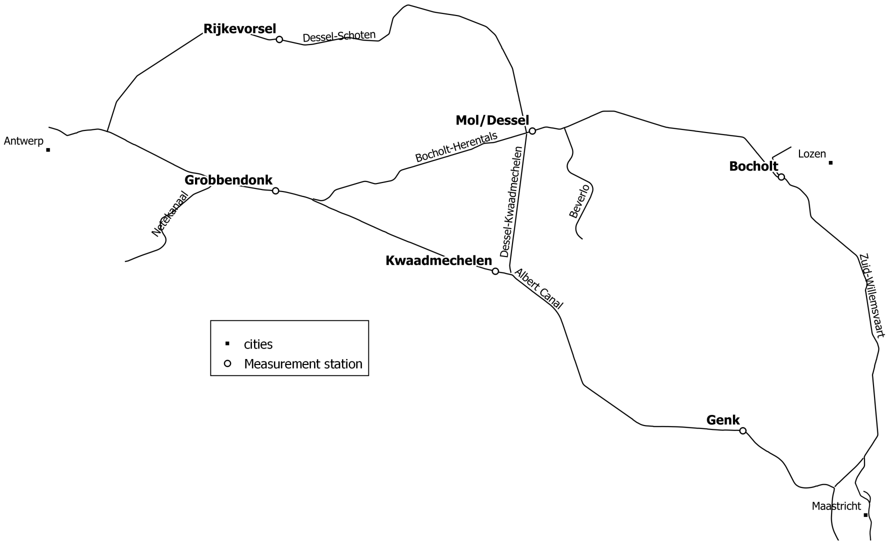

Fig. 2.19: Map of the section of canal systems of Meuse river flowing in Belgium: The location of Measurement station used for validation.

all of the tributaries in the model unfeasible, which is essential for predicting discharge in the Meuse River (particularly during major precipitation events in their respective catchments). In terms of measurement, most tributaries have stations that measure both water level and discharge. However, in the case of the tributaries that lack bathymetric data, the desired station is the one that is near to its confluence with the Meuse River. Such stations are available for the Sambre and Ourthe rivers. In the case of other tributaries, an alternative approach is followed and is described in the setup section.

2.5 Results and Discussion

2.5.1 Meuse Model

Here, the results of model simulation compared to a standard software Mike 11 are shown (section 2.5.1.1), then the results of the two-step calibration procedure introduced in section 2.4.4 are presented (section 2.5.1.2), followed by additional comparisons between computations and observations aiming at validating the model (section 2.5.1.3). An overview of all measured data considered for model calibration and validation is given in Table 2.5. The validation includes several stations along the stretch of the river with different duration's, to illustrate the robustness of the model.

Step	**Station**	**Period**	**Duration**	**Variable**	**Figure**
Calibration	Waulsort	10/05/202-21/05/2021	12 days	Discharge	Figure 2.21
	Anseremme	04/06/2019-31/12/2019	7 months	Water level	Figure 2.22
Validation	Anseremme	01/01/2018-31/12/2018	12 months	Water level	Figure 2.23a
	Grand Malades	01/07/2013-31/12/2013	6 months		Figure 2.23b
	Lixhe	01/06/2013-31/12/2013	7 months		Figure 2.24
Validation	Amay	01/06/2013-31/12/2013	7 months	Discharge	Figure 2.25
	Eijsden	01/09/2017-24/02/2018	6 months		Figure 2.26

Table 2.5: Overview of the observed data considered for model calibration and validation.

2.5.1.1 Comparison with MIKE 11 model

To evaluate the structure implementation in SLIM, the model results are compared to those of the MIKE11 model. The Meuse River domain, which includes three weirs, is used for the comparison up to around 20 km from the French-Belgian border (Figure 2.1). A steady discharge of 105 m^3/s is applied at the upstream boundary and a water level of 91.1 m at the downstream boundary, as measured in Chooz and Dinant (Figure 2.17). The weir heights are computed using the approach outlined in section 2.4.3 for steady state conditions. Figure 2.20 shows the comparison of water level and velocity computed by both models. The current model agrees with the MIKE11 model, demonstrating the validity of the implementation. However, certain velocity differences are noticeable, particularly close to the structures (for instance, at 5 km). This could be attributed to the method these stage discharge relationships are implemented in the numerical scheme. MIKE11 uses finite difference schemes, where the stage discharge relationships are implemented such that, it includes information from neighboring nodes, to compute the flow variables at the structure's nodes (MIKE-11 (2021)). Therefore, neighboring nodes needs to be closer to the structure, whereas in the current model, the discontinuous character of the numerical method guarantees that the nodes adjacent to the structure are always closer. Therefore, the mesh resolution across the structure could be the reason for variation in velocities.

2.5.1.2 Calibration: Meuse Model

As a first step in calibration method described in section 2.4.4, the simulated discharge at Waulsort, and water level at Anseremme is compared to measurements done between May 10 and May 21, 2021 (Figure 2.21). In the second step, the weir coefficient was further improved; here, the results were compared to those of water levels measured at Anseremme between June 4 and December 31, 2019 (Figure 2.22).

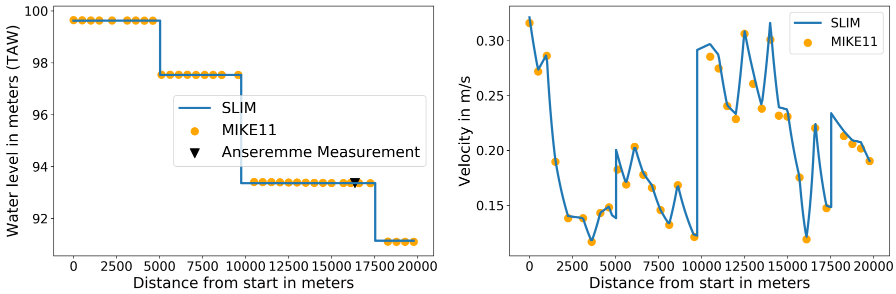

Fig. 2.20: Model comparison in the Meuse River using the hydraulic structure of the developed SLIM model and the traditional commercial model MIKE11 for (a) water level (left) and (b) velocity (right).

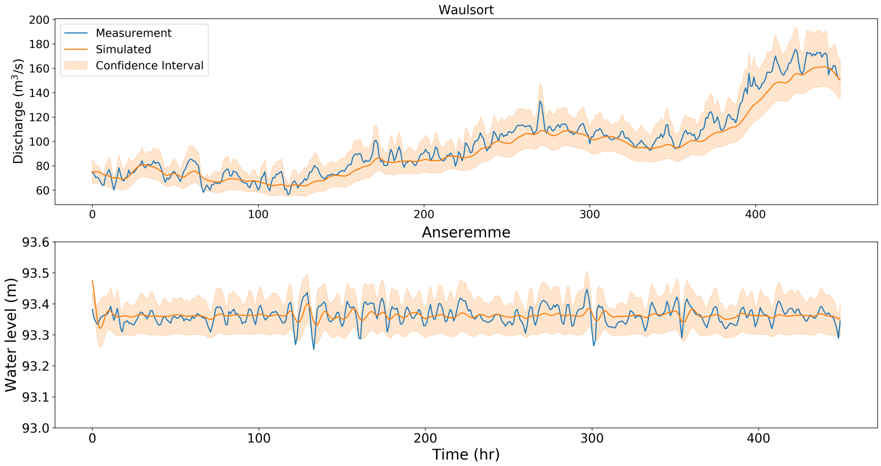

Fig. 2.21: Waulsort discharge and Anseremme water level station: comparison of simulated and measured values with confidence interval for calibration

Figure 2.21 shows a comparison of the simulated and measured discharges at Waulsort and Anseremme. In both cases, the NSE coefficient is equal to 0.94 and the confidence interval covers 99 % of the total simulated data in the first step of calibration. During the calibration, it is observed that lower weir coefficients (< 1.6) result in a rise in water level (greater than measured) due to hold up of the flow. Furthermore, a first estimation of Manning coefficient of 0.033 $sm^{-1/3}$ yielded satisfactory results. It is worth noting that the chosen Manning coefficient for the first estimate is based on the range of coarse sand

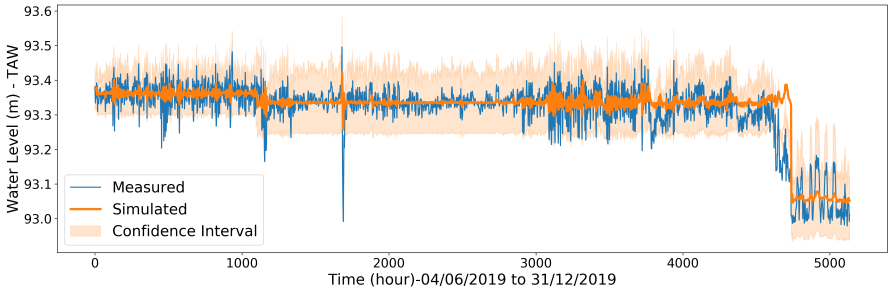

Fig. 2.22: Anseremme water level station: comparison of simulated and measured values with confidence interval for calibration

and gravel bed (Arcement and Schneider (1989)). It can be seen in Figure 2.21, the calibrated results closely follow the main trend of the observation time series. Moreover, in comparison to measured data, the model has a deficit in the cumulative volume of around 1 % (presumably due to surface runoff coming from urban area and inter-catchment not included in the model), which indicates that the model preserves the water volume and provides good prediction in comparison to measured data.

In the second step, the water level between the measurement done at Anseremme and the simulated values are compared (Figure 2.22): the NSE coefficient is 0.74 and a confidence interval with coverage of 96% is achieved. In this step, the weir coefficient is further increased to 1.8 to minimize hold up with respect to high flows. Several Manning coefficients (0.028, 0.03, and 0.033 $sm^{-1/3}$) were applied to fine-tune the coefficients, but no substantial difference in results was seen, hence 0.033 $sm^{-1/3}$ was retained from the first step. Therefore, weir coefficient of 1.8 and Manning coefficient of 0.033 $sm^{-1/3}$ were found to fit best with the measured values (irrespective of high or low flow) and was used in all subsequent simulations. It can be seen (Figure 2.22) that the calibrated simulation closely follows the main trend of the observation time series. However, it does not catch the fluctuations around the mean flow. Precipitation in the inter-catchment basin of the Meuse River, from Chooz to Waulsort, including tributaries, may be a cause of such fluctuations. Moreover, the station being close to the weir and lock chamber can record the waves generated and propagated by the structures, potentially causing the water level to fluctuate.

2.5.1.3 Validation: Meuse Model

In the validation, as described in section 2.4.1, the comparison of simulated water levels and discharge to measurements are presented. The first three fig-

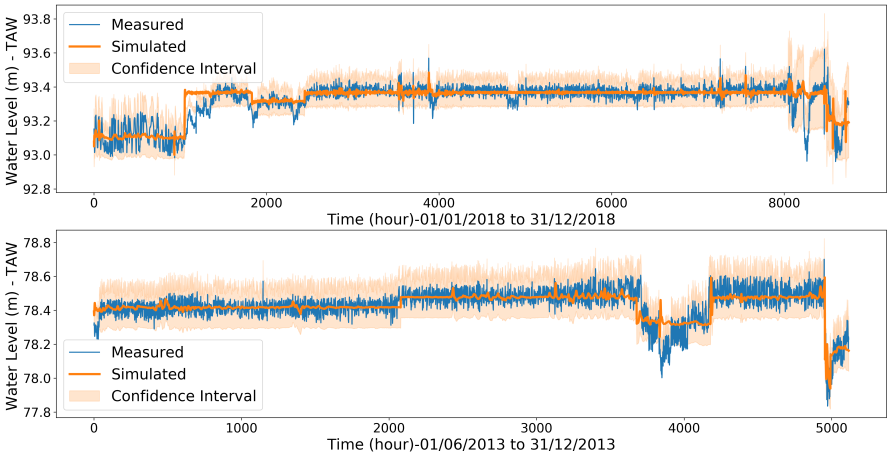

Fig. 2.23: Comparison of simulated and measured values with confidence interval for Validation (b) Anseremme water level station (top) (b) GRD water level station (bottom)

ures (Figure 2.23a, 2.23b and 2.24) show the water levels and last two figure (Figure 2.25 and 2.26) shows the discharge. The comparison of water levels at Anseremme between the model and measured values (Figure 2.23a) has a NSE coefficient of 0.68 and 95% of the simulations are covered by the confidence interval. For the water level comparison at GRD, the NSE coefficient is 0.65, and the confidence interval covers 93% of the simulation (Figure 2.23b). The sudden shift in water level observed, especially in the case of Anseremme (Figure 2.23a: 1000 hour) is because the operations of the weirs, as simulated by the model, are instantaneous, while in reality, the operation of the weir takes place gradually. In the case of GRD, for a period of around 16th November 2019 (i.e., 4000th hour in Figure 2.23b), a difference between simulated and measured water levels is observed. The details behind this behavior are unknown to the authors, but this is most probably due to the operation rules. However, after the lower point of the observations, the model matches again the target level.

The next water level measurement station is located in Lixhe, which is further downstream from the bifurcation of the Meuse River into Albert Canal. The NSE coefficient for the comparison of water levels between the model and measured data is 0.93, and the confidence interval covers 96% of the simulations (Figure 2.24). The behavior water level time series in this station is different from what was observed in rest of the upstream stations. Here, the influence of the operation rules is minimal, and changes are dependent only on the flow.

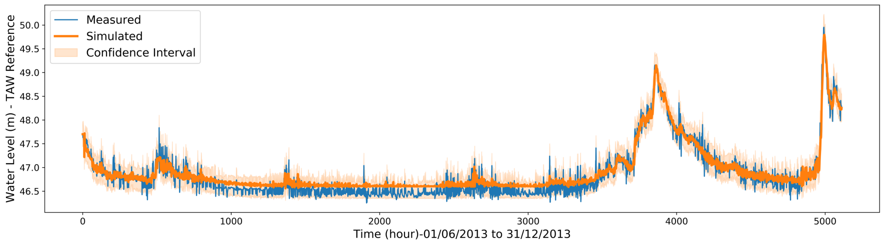

Fig. 2.24: Lixhe water level station: comparison of simulated and measured values with confidence interval for validation

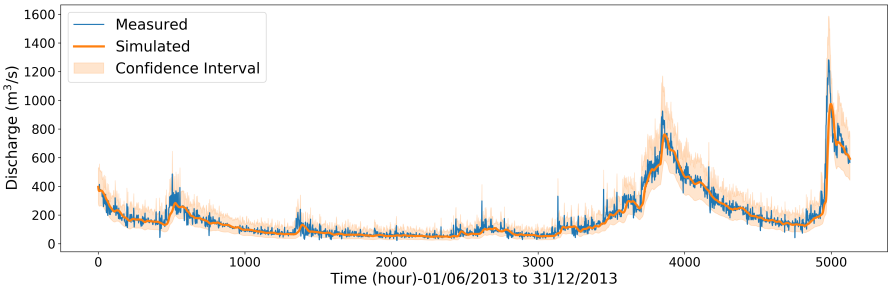

Fig. 2.25: Amay Discharge station: comparison of simulated and measured values with confidence interval for validation.

Therefore, a relatively higher NSE coefficient compared to other two stations are achieved. Moreover, as mentioned in section 2.4.4, the NSE coefficients tend to stay artificially low for time series like Anseremme and GRD.

As discussed in section 2.4.1, in the upper Meuse, Amay is the only suitable station for the validation of discharge with sufficient historical values. The comparison between the simulated and measured discharges for Amay station is shown in Figure 2.25 below: A NSE coefficient of 0.92, a cumulative deficit equal to 4.3% and coverage of 98% were obtained (Figure 2.25). These performance evaluators show a good agreement between simulation and measured flow. However, differences can be seen for some discharge peaks. The primary reasons for this are the inflows into the river during high precipitation events, not only coming from the Meuse catchment but also from the catchment of the tributaries. Moreover, some of the discharge measurement stations are not placed near the confluence of the tributary with the Meuse River but a few kilometers upstream. This makes it difficult to estimate the arrival time of a flood event and thus the contribution to the peak discharges in the Meuse River.

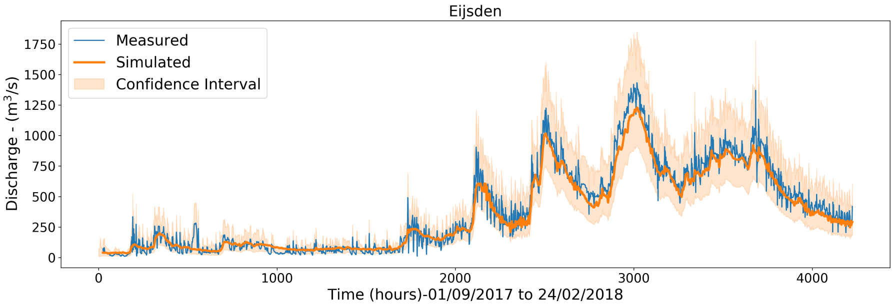

Fig. 2.26: Eijsden Measurement station: comparison of simulated and measured values with confidence interval for validation.

Similar results with an NSE coefficient of 0.96 and 97% coverage can be seen for the comparison of discharge between simulated and measurements done at Eijsden station (Figure 2.26). It can be seen that the representation of the peaks and their arrival time are well simulated by the model. In comparison with Amay station, the model results show better results in Eijsden (since they consider different periods). This further indicates that these differences in peaks are caused by a lack of monitoring stations for the influx of water into the river.

To summarize the model performance Figure 2.27 provides an overview of the NSE values obtained during the calibration and validation steps of the model, while Figure 2.28 reports the portion of computed values falling outside the confidence interval of the measurements.

The NSE coefficients and confidence intervals for the comparison of the simulated and measured values indicates a good model performance. However, the NSE coefficient for measured water levels in Anseremme during validation is lower than that achieved during calibration. This is justified by the fact that the amplitude range of the oscillations is larger, with a mean of 15 cm against 10 cm during the calibration period. While, for the discharge comparison the NSE values are greater than 0.9 and values out of confidence interval increases for the measurements located further downstream the river, primarily due to lack of inputs form the lateral inflows. Although the NSE coefficient by nature tends to undermine the model performance at Anseremme and GRD, values outside of the confidence interval that are well below 7% reaffirm the model's capability. Nonetheless, it is worth mentioning that a NSE coefficient greater than 0.5 generally considered appropriate in hydraulics (Moriasi et al. (2007)).

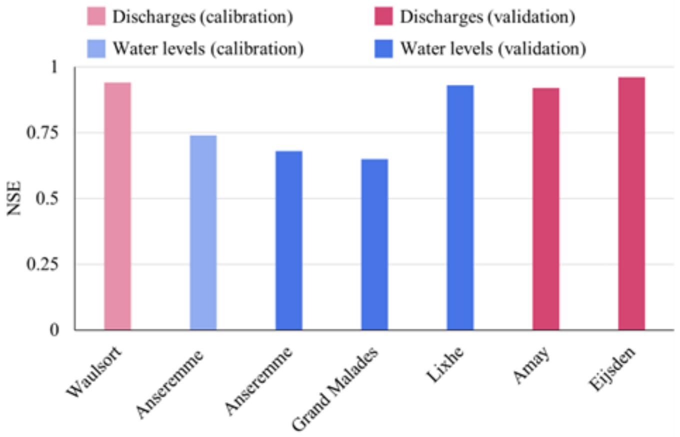

Fig. 2.27: NSE values obtained in the calibration and the validation of the model for the Meuse River

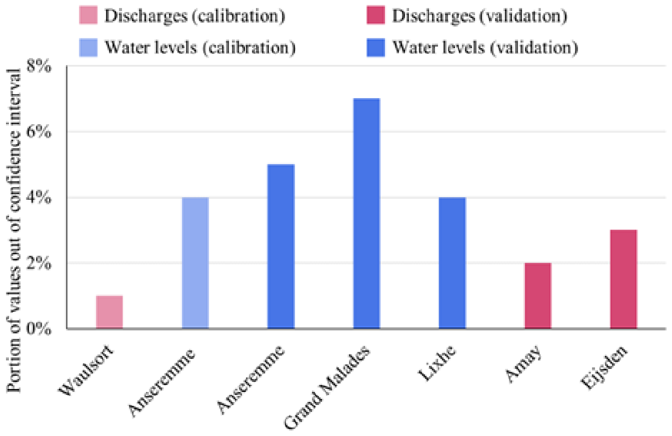

Fig. 2.28: Portion of computed values falling out of the confidence interval of the observations in the calibration and the validation of the model for the Meuse River.

2.5.2 Canal system

In Sub-section 2.5.2.1, the focus here is set on evaluating the performance of the model for predicting the discharge partition between the Meuse River and the Albert Canal, with the aim of validating our implementation of the diversion structure controlling this flow partitioning. Next, computed water levels in the canals are compared to observations in section 2.5.2.2, while section 2.5.2.3 discusses the model ability to reproduce the discharge distribution between various canal branches.

2.5.2.1 Discharge partition between the Meuse River and the Albert canal

For evaluating our implementation of the diversion structure controlling the flow at the bifurcation between the Albert Canal and the Meuse River (Monsin weir), measurements at Marxhe station are considered over a period of six months (between June 1, 2013 and December 31, 2013, as shown in Figure 2.29a). The simulated and measured time series show a good agreement for the water level, with a maximum deviation of 0.12 m. Figure 2.29b compares the simulated discharge entering the Albert Canal to the measured discharges at Haccourt during the same six-month period. Although the discharge measurements show inaccuracies, as discussed in section 2.4.5.3, the simulated results follow the overall trend of the measured time series. Simulated discharge peaks appear fairly consistent with the higher values in the observations, in spite of the presence of high-frequency disturbances in the measured time series. During normal flow in the Meuse River (from 100th until 3000th hour in Figure 2.29b), the simulated discharge in the Albert Canal is between 12 and 31 m^3/s. The differences in the reported data (De smedt and Van der beken (1982),FHR (2005),Van Steenbergen (2017)) for estimated values of discharge all fall within this range. This shows that the simulated discharges are consistent with the values reported in literature. Such model capabilities are made possible thanks to the regulation rules implemented in the model to reproduce the influence of Monsin weir.

2.5.2.2 Water levels

Figure 2.30 displays computed and measured water levels at six stations in the Albert Canal and the Campine canals. The simulated water levels are in good agreement with the measured data. The error magnitudes on the mean value remains below 1 cm at half of the stations (Genk, Kwaadmechelen and Mol), while they reach 2 cm, 5 cm, and 7 cm at stations Rijkevorsel, Grobbendonk and Bocholt, respectively (Table 2.6). Furthermore, the mean values of the simulated results correspond to the value indicated in the FHR (2005).

The fluctuations in the measured water levels differ substantially from one station to the other. In the Albert Canal at Genk, Kwaadmechelen and Grobendonk, the amplitude of the fluctuations reaches 0.30 m, whereas they are about twice smaller (~ 0.17 m) in the other Flemish canals. This difference is consistent with the larger capacity of the lock chambers in the Albert canal (transfer of $\sim 5 \times 10^4 m^3$ per lock operation (FHR (2005)) compared to the locks in other

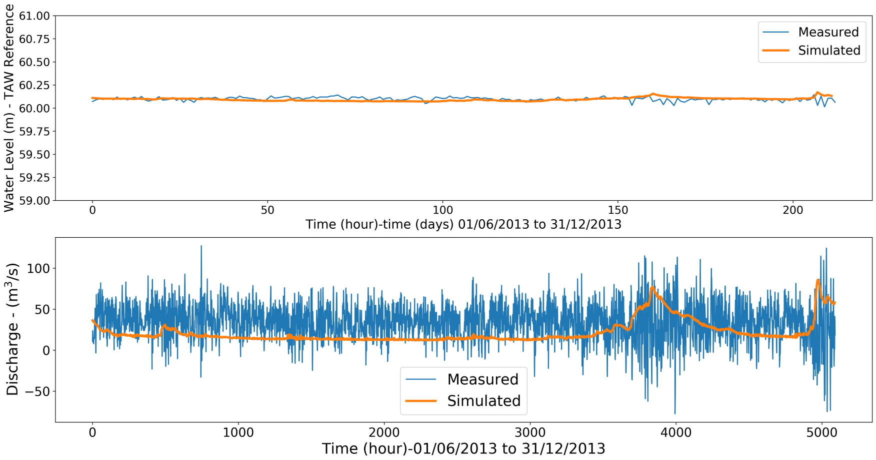

Fig. 2.29: (a) Marxhe measurement station: Comparison of simulated and measured values (top). (b) Simulated discharge into Albert Canal from the Meuse River at Monsin

canals, which is likely to lead to higher amplitudes of the waves induced by lock operations. Again, the simulations do not resolve these waves since individual lock operations are not reproduced in the model, which leads to maximum absolute differences between simulated and measured water levels as presented in Table 2.6.

Station Name	**Measured Mean (m)**	**Simulated Mean (m)**	**Error on Mean Value (m)**	**Maximum error (m)**
Genk	60.093	60.088	-0.005	0.31
Kwaadmechelen	29.69	29.7	0.01	0.29
Grobbendonk	9.718	9.67	-0.048	0.35
Mol	29.705	29.7	-0.005	0.17
Rijkevorsel	29.721	29.7	-0.021	0.15
Bocholt	42.575	42.508	-0.067	0.21

Table 2.6: Mean value for the measured station and Simulated data in mTAW with the mean value and maximum error in meters between both the data

2.5.2.3 Discharge partition between canal branches

The simulated distribution of discharge in the Campine canal connected to the Meuse River is shown in Figure 2.31. The minimum and maximum values of discharge presented in Figure 2.31 corresponds to months from June to August

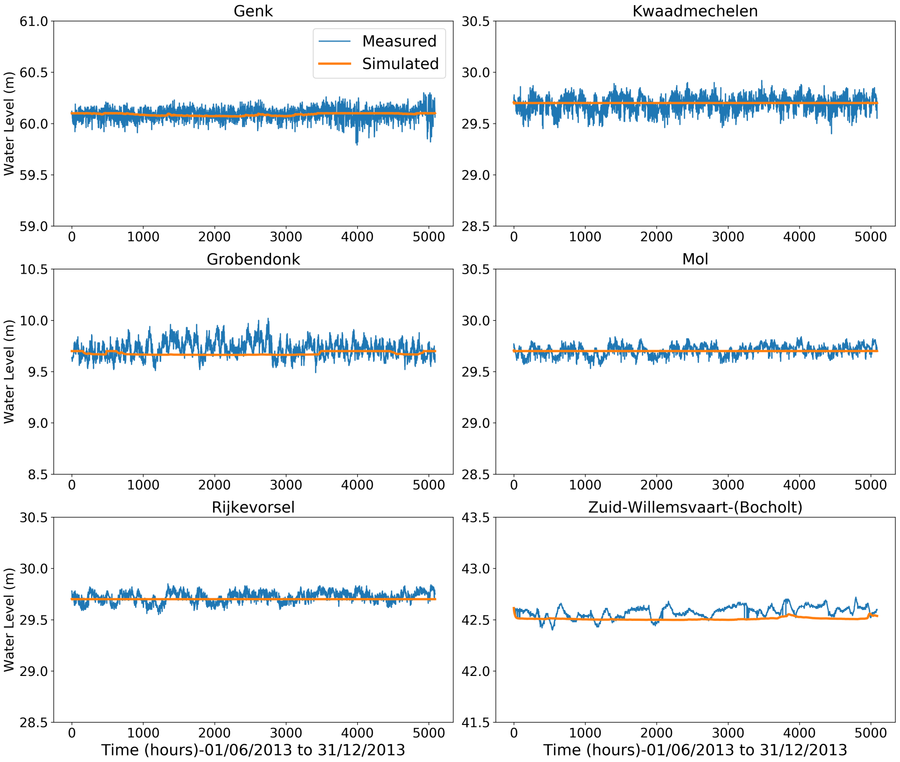

Fig. 2.30: Comparison of simulated and measured values for validation for all water level stations located along the Campine Canal (refer section 2.4.5.3 for locations)

2013. The discharge in the Meuse River shows an average of about 400 m^3/s and a minimum value of 40 m^3/s at Monsin. These simulated values are close to observations reported in a previous study (De smedt and Van der beken (1982)) that are described in section 2.4.5.3.

High discharges in the Meuse River have a significant influence on the flow in the Albert Canal, where the discharge can reach 90 m^3/s (three times the average value), as can be seen in Figure 2.29b. In the Campine canal, the impact is less significant. This is mainly due to the high regulation of the water inflow into the Zuid-Willemsvaart canal through a underflow gate and a weir in Maastricht. In the Dessel-Kwaadmechelen canal (Figure 2.12), during high flow events in the Albert Canal, the flow direction is reversed. The impact is larger here than along the other two canals (Dessel-Schoten and Bocholt-Herentals) connected to the Albert canal because the locks placed along them regulate the flow at the connection.

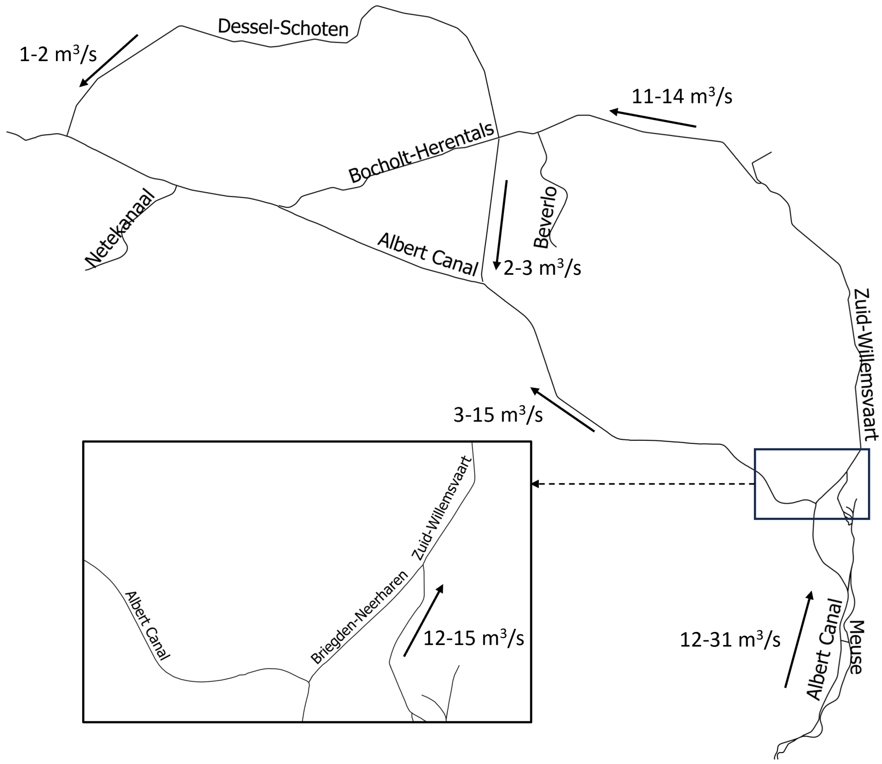

Fig. 2.31: Range of discharge distribution among the interconnected canals with the accurate representation of water levels for June till August 2013

2.5.3 Influence of the modeling of operation rules

Since operating rules of the hydraulic structures along the Meuse River are incompletely documented, their modeling in this study relies on assumptions derived from measured data. However, inferring operation rules from data interpretation remains challenging. Therefore, we test here the sensitivity of modeling results to the operation of weirs in the simulations. Two modeling options were tested. In Scenario 1, the weirs are assumed to be mobile, as they actually are. In Scenario 2, the weirs are assumed to be set at a fixed position, corresponding to the lowest probable value of their crest elevation. Scenario 1 is run first, and the position of the weirs were recorded. Then, the lowest position of each weir was selected to be used as fixed position in Scenario 2. Unlike scenario 1, it is evident that water levels will fluctuate in scenario 2. As illustrated in Figure 2.32b, for scenario 2 the water level at

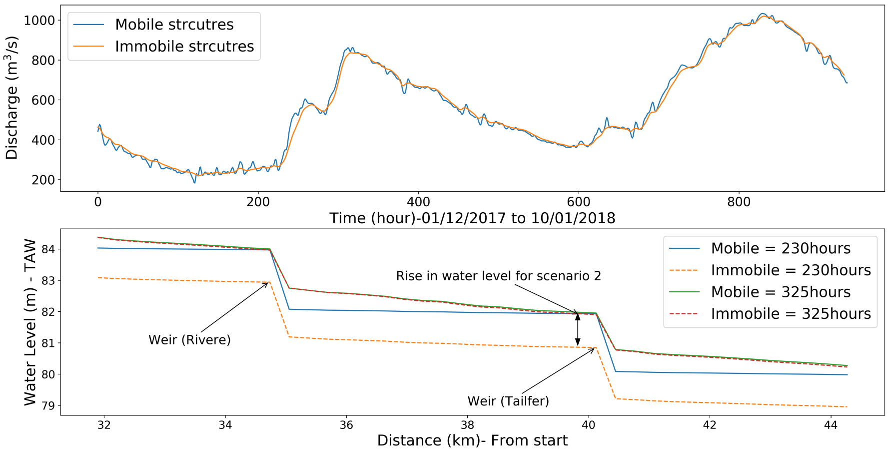

Fig. 2.32: (a) Comparison of discharge for a simulation of mobile and immobile structures in the Meuse River (top) (b) comparison of water levels at two weirs (Rivere and Tailfer) for low discharge (235th hour) and high discharge (325th hour) to illustrate the rise in water levels due to immobile structures and constant water level for mobile structure (bottom).

the weir increases during the rise in discharge (230–325 hours in Figure 2.32a), whereas for scenario 1 it remains constant. However, the impact of this on discharge in the far reach of the river is examined (in this case, near Eijsden). As shown in Figure 2.32a, the time series of discharges are very similar between the two scenarios, suggesting that the operation rules of the weirs have limited influence on the peak discharges in the Meuse River. In Scenario 1, the peak discharge arrives 1-2 hours earlier than in Scenario 2 and the peak discharge is about 15 m^3/s higher than in Scenario 2. In the rising limb of a flood wave (for example, between the 230th and 263rd hours), Scenario 2 lags behind Scenario 1, whereas during the recession part, the results of both scenarios can hardly be distinguished. This is consistent with the stronger backwater effects occurring in the case of fixed weirs (Scenario 2) compared to the case of mobile weirs (Scenario 1). Indeed, in Scenario 1, the lowering of the weirs as the discharge rises minimizes delays of the flood wave due to storage. Nonetheless, the delays and changes in peak magnitude are not substantial due to the limited storage capacity of the Meuse River itself. The implementation of floodplains in the model would lead to more water storage; but it would still remain limited to a few percents (Kitsikoudis et al. (2020)).

2.6 Conclusion

This paper presents the implementation of empirical relationships for reproducing the effects of hydraulic structures in a discontinuous Galerkin finite element model of open-channel flow. The model was applied to the Belgian part of the Meuse River (approx. 143 km in length) with a complex network of canals (Campine Canal) connected to it. The simulations were run for a period characterized by discharges spanning a broad range of values. The model accuracy was assessed by comparison against literature data and field measurements. The results shows that model was able to keep stability even under fast transition conditions.

The simulations results are in good agreement with the measurements of the water level and discharge. For the Meuse River, the obtained NSE coefficients range between 0.65 and 0.78 for water levels, and between 0.9 and 0.95 for discharges and more than 92% model results within the 95% confidence interval. In the vicinity of the bifurcation between the Meuse River and one of the main branches of the canal network (Albert Canal), the implementation of the operation rules of a weir proved able to accurately represent measured series of water levels (at Marxhe). The discharge fed into the canal was found consistent with literature data, and two distinctive peaks simulated for two high flow events match the measurements. Within the canal system, the simulated water levels were compared to measurement data, and a good agreement was reached with error magnitudes on the mean value of the water level ranging from 1 to 7 cm. Discharge magnitudes are also in line with measurements and data reported in literature.

Some fluctuations visible in the measurements are not represented by the model, suggesting that other physical processes intervene, such as wind friction, waves caused by the operation of hydraulic structures and locks. This aspect is not considered since no data on shipping were used. The effect of lock operations on discharge was simply averaged in time. The model also tends to underestimate (cumulative deficit below 6.8 %) the peaks during high flows. This is due to the limited number of discharge measurements, which makes it difficult to accurately determine inflows to the system, such as runoff as well as contributions from small tributaries.

The DG method was thus validated for its capability to handle different hydraulic structures, such as weirs and underflow gates. The developed model proved to be an effective tool for understanding the intricate effects of the hydraulic structures on discharges and water levels in complex channel networks. Consequently, this model can help develop control algorithms that can integrate the operation of multiple structures effectively. Additionally, the flow simulation can be valuable in calculating sediment erosion/deposition and for pollution transport in such large systems spanning over 200 km.

To better represent the peaks, a hydrological model should be coupled to the developed hydrodynamic model, so that uncertainties related to inflows along the channels can be reduced. Additional discharge measurements would also open more opportunities for detailed model validation. If waves induced by individual operations of structures such as locks need to be predicted, data on boat traffic should be incorporated in the model.

CHAPTER 3

Numerical Modeling for the releases of ^{137}Cs and ^{131}I in the Meuse-Campine canal from NPPs.

This chapter is based on the following paper:
Patil, A., Perez, F., Lambrechts, J., Deleersnijder, E. (Submission intended for Journal of Radiological protection) *Numerical Modelling of the Transport and Impact of ^{137}Cs and ^{131}I on the Meuse-Campine Canals after a Potential Nuclear Accident*, Journal of Radiological Protection, vol. 45, no. 1, Mar. 2025, p. 011512, https://doi.org/10.1088/1361-6498/adc1db.

Abstract

The Meuse River in Belgium can be impacted by the two nuclear power plants (Tihange and Chooz) located on its banks. Nuclear disaster such as the Fukushima and Chernobyl accidents have illustrated the risks associated with the civilian nuclear industry. In such situations, predictive models become crucial for developing environmental strategies to minimize the potential impact. In this study, we use the discontinuous Galerkin method to simulate the transport of ^{137}Cs and ^{131}I in the Meuse River system in Belgium. Several hypothetical accidental scenarios are considered for the radionuclide releases based on past nuclear accidents. The simulated radioactivity distributions are then used to estimate the individual dose for drinking water. The radionuclide transport in the Meuse River is fast; however, higher peak concentration in the Meuse River result in higher individual dose. The Albert canal being the largest channel among the Campine canals; therefore, the radioactive plume stays longer. The estimated individual doses for releases from Chooz Nuclear power plant near Tailfer reached 0.2 mSv within three days. Although it takes days, the doses in the Albert Canal reach values up to 0.46 mSv at Haccourt (hypothetical locations). The water extraction points in Herentals, located downstream of the canal, has a negligible individual dose estimation. Higher doses are the consequence of ^{131}I than ^{137}Cs due to the larger release scenario.

3.1 Introduction

Environmental emergencies, such as the contamination of a freshwater ecosystem following the release of radionuclides into the environment, will require strategies to minimize the negative impact of radioactivity (Hofman et al. (2011b)). In this regard, numerical models are critical for predicting the behaviour of radionuclides in rivers and developing suitable plans for the management and remediation of contaminated areas (Monte et al. (2005)). After the Fukushima accident, the SPEEDI (System for Prediction of Environmental Emergency Dose Information) model results were not available for approximately two weeks; consequently, people were evacuated to areas with even higher concentrations due lack of precise information (Park et al. (2017)). Furthermore, high radioactivity concentrations were identified in tap water not just in Fukushima but also as far as Tokyo. Therefore, the International Atomic Energy Agency, in the wake of such nuclear accidents, have emphasized the need for numerical models (IAEA (2019)) in order to make rapid decisions. Numerical models have proven to be useful not only in predicting the transport and fate of radionuclides but also as the basis for remediation (Monte et al. (2009),Siclet et al. (2002),Zheleznyak (1998),Zheleznyak et al. (1992)). Furthermore, such models can provide necessary information for dose assessment in the acute phase after a severe nuclear accident before any intervention is possible (Simonsen et al. (2019)). This helps emergency responders take appropriate action while being informed about potential health risks.

During last two decades, numerical models have been developed to simulate radionuclide dispersion in rivers (Monte et al. (2006),Monte et al. (2005)). However, the conceptualization of these models considered elements with low affinity for sediments, such as tritium, technetium, iodine, and cesium, and thus, the predictions of these models have often ignored the interactions between radionuclides and solid matter (e.g., Behrens et al. (2012),Estournel et al. (2012),Tsumune et al. (2012)). This might be a reasonable simplification in short-term assessments, and for saving computational resources in accident cases when fast response is required (Duffa et al. (2016)).

In general, human activities rely significantly on waterways and has necessitated the construction of hydraulic structures to assure a continuous supply of drinking water and navigation. This in terms of water quality modeling requires additional considerations to accurately represent the radionuclide transport. Belgian Meuse River is one such unique navigation system, which is connected to a man-made canal system and features not one but two nuclear power stations (NPPs) on its banks. (Figure 3.1). Indeed, these rivers are complex ecosystems with significant economic, social, and environmental value. Therefore, models that could be applied to simulate the dispersion of radionuclides released due to a potential accident occurring in any of the NPPs are rare in the literature.

As initial environmental risk assessments (ERA) have predictive characteristics, uncertainty in radiological doses is at their highest. Initial ERAs use upper-bound predictions to account for the uncertainty. However, overly conservative predictions may raise unnecessary public concern. It is therefore important to obtain realistic worst-case (i.e., conservative) predictions that rely on process based models for radionuclide transport (Goulet et al. (2022)). For Meuse River – Campine canal systems, due to lack of knowledge regarding the radioactivity dispersion, such radiological dose impact studies are also lacking. Here the estimated dose, which may be external or internal to the body can be used to identify potential risk associated to public health and thus safety guidelines can be developed (IAEA (2016)) in the case of a nuclear emergency.

The purpose of the present paper is to fill the knowledge gap when describing the fate and transport of radionuclides in the Meuse River and its connected canal network (Campine canal). The two NPPs located on the banks are: the first is the Chooz NPP, which is in France near the border with Belgium, and the second is Tihange, that is located near Amay in Belgium. The scenarios used in the present study for these NPPs were chosen to analyze the impact of a worst-case scenario. Here, the downstream flow of the river across these NPPs passes through many important cities, such as Namur, Liege, and Maastricht. Moreover, the connected canal networks can transport contaminants all the way to Antwerp. Since the Meuse River and the Albert Canal (the largest among the Campine Canal) are the primary sources of drinking water, the consequences of an accidental release into the river should be assessed. Therefore, in this study we also present the dose ingestion calculation for drinking water supply. With this knowledge, suitable actions in terms of public health monitoring can be implemented.

3.2 Model Description

The Meuse River follows a transboundary course in Europe for up to 905 km in length (Beckers et al. (2013)). It originates in France and flows through Belgium to reach the North Sea through the Netherlands. The study area comprises the Meuse River in Belgium and the canal networks to which it is connected. The 143 km long stretch of the Meuse River considered here runs from the Belgian-French border to Maastricht in the Netherlands and is connected to the Albert Canal and the Zuid-Willemsvaart Canal. While the latter stretch over more than 46 km from Maastricht to Lozen, the former stretches more than 130 km from the Meuse River to the port of Antwerp. These two river-fed canals further distribute water into the smaller canals that are connected to one another. The study area thus includes a number of smaller canals, such as Bocholt-Herentals, Schoten-Dessel, Kwaadmechelen-Dessel, and Briegden-Neerharen. These smaller canals and the two river-fed canals together constitute the Campine canal. The domain of the study is shown in Figure 3.1.

The Tihange and Chooz nuclear power plants are located in the upstream part of the Meuse River. The Tihange NPP is located in Huy on the right bank of the Meuse River and includes two active pressurized water reactors with a combined capacity of 1992 MW. The Chooz NPP, located on the left bank at Belgian-French border, has two pressurized water reactors (PWR) with a combined net capacity of about 3 GW. In both NPPs, the river waters are used for cooling the reactors, among which 97% of the water used is returned to the river. Although, water discharges from nuclear power plants into the river contain some low-level radioactivity, the concentrations in the river water near the NPP are below the detection limits (FANC (2023)).

3.2.1 Meuse River systems

The Belgian part of the Meuse River is highly regulated by a combination of weir systems and lock chambers, which play a major role in river flow dynamics. Along the Meuse River in Belgium, there are 15 weirs between Chooz NPP and Maastricht. These weirs raise the water level to obtain a sufficient hull for navigation, even during dry periods. For high flows, as the weirs are movable, they are operated to maintain the targeted water level in the river, thus preventing flooding. The regulation of these weirs is based on feedback from measuring stations. Furthermore, if the discharge in the river reaches a certain threshold, the target water level that needs to be maintained is lowered. This is done in order to prevent the weir directly upstream of the weir under consideration from becoming submerged. In specific locations, such as the weir at Liège (referred to as the Monsin Weir) located in the Meuse River just downstream the diversion with the Albert Canal (Figure 3.1) controls the flow into the Albert Canal. A similar weir is also present in the river at the

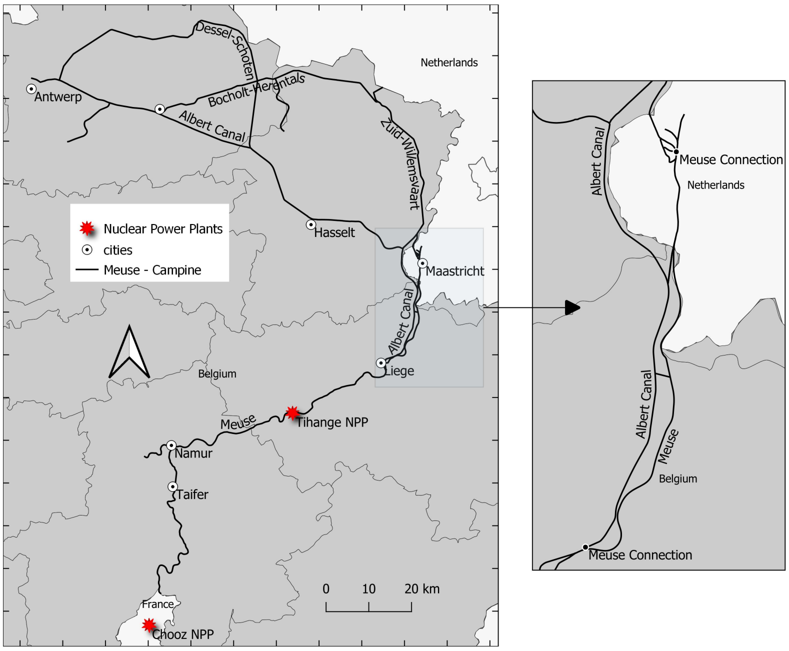

Fig. 3.1: Course of the flow for the Meuse River and its connection with the Campine Canals in Belgium: Location of the two NPPs located on the Bank of the Meuse River.

bifurcation of the Meuse at Maastricht. Upstream of this bifurcation on the left bank of the Meuse River, an underflow gate and lock chamber are used to feed water into the Zuid-Willemsvaart canal (Figure 3.1) and to allow navigation through it.

The Albert and the Campine Canals comprise a total of 28 locks. Among them, the Albert Canal has six locks, each bounded at both ends by a set of three lock chambers. Navigation in this canal allows larger vessels than in the other canals of the country. The smaller Campine canals, fed by the Zuid-Willemsvaart canal, are connected to the Albert Canal at four different places, as seen in Figure 3.1. These canals are smaller in size, and navigation is made possible by a single lock chamber. Like the Meuse River, maintaining the water level in these canals is also of vital importance. For this purpose, there are bypass channels constructed across the lock chamber that allow the water to flow continuously once the target water level is reached. For the lock chamber placed in the other Campine Canals, the flow continuity is regulated by the culvert used for filling and emptying the lock chamber.

3.2.2 Radionuclide Transport Model

The radionuclides are simulated according to a Eulerian approach including advection, diffusion and decay at a constant rate. The corresponding equations are presented in Eq. 3.1:

$$\frac{\partial Ac}{\partial t} + \frac{\partial}{\partial x}(Qc) = \frac{\partial}{\partial x}(DA\frac{\partial c}{\partial x}) + S - \lambda Ac \tag{3.1}$$

Where, t is the time, D is the diffusion coefficient, c is the radionuclide concentration, S is the source for the radionuclide under consideration, λ is the decay constant, which is calculated in terms of the half-life ($T_{1/2}$) of the radionuclide. The source term S here is used to define radioactive fallout into the rivers or direct liquid releases. In the model, it is assumed that the radionuclides that enter the simulation domain are well mixed in the element where the release point is located. The composition of radionuclides considered in the release scenario is based on previous nuclear accidents (such as Fukushima), which have shown that ^{137}Cs and ^{131}I were among the primary radioactive substances that caused initial exposure to humans. Other processes, such as radionuclide adsorption to biological matter and suspended sediment, are excluded. This assumption is valid for accidental releases where the duration of the simulation period is short, or in the case of elements such as ^{131}I that do not tend to readily adsorb themselves to the sediments (Periáñez et al. (2019)).

3.2.2.1 Tracer Verification: Analytical vs Model

Although regional authorities measure the radionuclide concentration in the river, the values are often below the detection limit. Moreover, the background radionuclides (from weapon testing and Chernobyl accidents) make it difficult to estimate the amount of concentration coming from the NPP directly. Due to the low activity levels the available information is not sufficient for the sake of validation. To the best of the author's knowledge, no other applicable measurement data exists for other types of pollutants. Therefore, the advection-diffusion-decay transport equations here are validated with a classical approach by comparing them with analytical solutions. For this purpose, we consider point sources and Gaussian distributed sources with pure advection, diffusion, and a combination of advection-diffusion and decay processes. Table 3.1 shows the distribution equations and respective boundary conditions used for the verification.

The pulse travels with a constant flow velocity $U = 0.5\frac{m}{s}$, $l = 30km$ and the diffusion coefficient $D = 10\frac{m^2}{s}$. While, advection diffusion with decay is considered using a decay term (λ) of 1e-4 s^{-1}. The exact solution used for the comparison has an infinite domain; however, here only a portion of the total domain is used. The fraction of the total concentration outside the

Test cases	**Initial Distribution**	**Boundary Conditions**
Pure Advection Pure Diffusion	$C(x,t=0) = \frac{1}{\sqrt{2\pi}} exp(-\frac{(x-\mu)^2}{2\sigma^2}) for 0 < x < l$	$C(x=0,t)=0$
Advection Diffusion Advection Diffusion and decay	$C(x,t=0) = \frac{M}{\sqrt{4D\pi t_c}} exp(-\frac{(x-Ut_c)^2}{4Dt_c}) for 0 < x < l$	$C(x=0,t)=0$
Continuous Source	$C(x=0,t)=0$	$C(x=0,t)=C_0=2$

Table 3.1: The initial distribution and boundary conditions to compute the analytical solution for model validation.

bounded domain is considered negligible. For detailed information regarding the analytical solution used here, refer to Szymkiewicz (2010) and Kärnä et al. (2010). The agreement between both the numerical and the exact solution is presented in Figure 3.2. The DG method solution shows a good comparison with the exact solution to the problem.

3.2.2.2 Discussion on Diffusion coefficient

The Advection-Diffusion-Decay equation (ADD) is implemented in tandem with the hydrodynamic model. The ADD equation requires defining the diffusion coefficient in order to represent the spreading of the pollutant. However, this coefficient needs to be defined either by using tracer experiments or by model calibration. Unfortunately, in this study, neither site specific nor activity concentration measurements were available for the selected rivers. Instead, we decided to base the values on empirical relationships that have been developed as a function of geometric and hydraulic parameters. These diffusion-induced dispersion equations will thus be based in the river's geometric features, such as the regularity of the river cross section and the width-to-depth ratio. Since the majority of the domain, in the Meuse River and traditionally the canal system are channelized, empirical relations suitable for this are chosen. Furthermore, a good precision is proven for rivers with a width-to-water depth (W/H) ratio of less than 100, this is the case for the aquatic systems considered in this study (Zeng and Huai (2013)). The empirical relationships used for the diffusion coefficients are represented in Eq. 3.2 (Iwasa and Aya (1991)).

$$D_x = 2.0(\frac{W}{H})^2 H u_* \tag{3.2}$$

Where, D_x is the diffusion coefficient in longitudinal direction and u_* is the shear velocity.

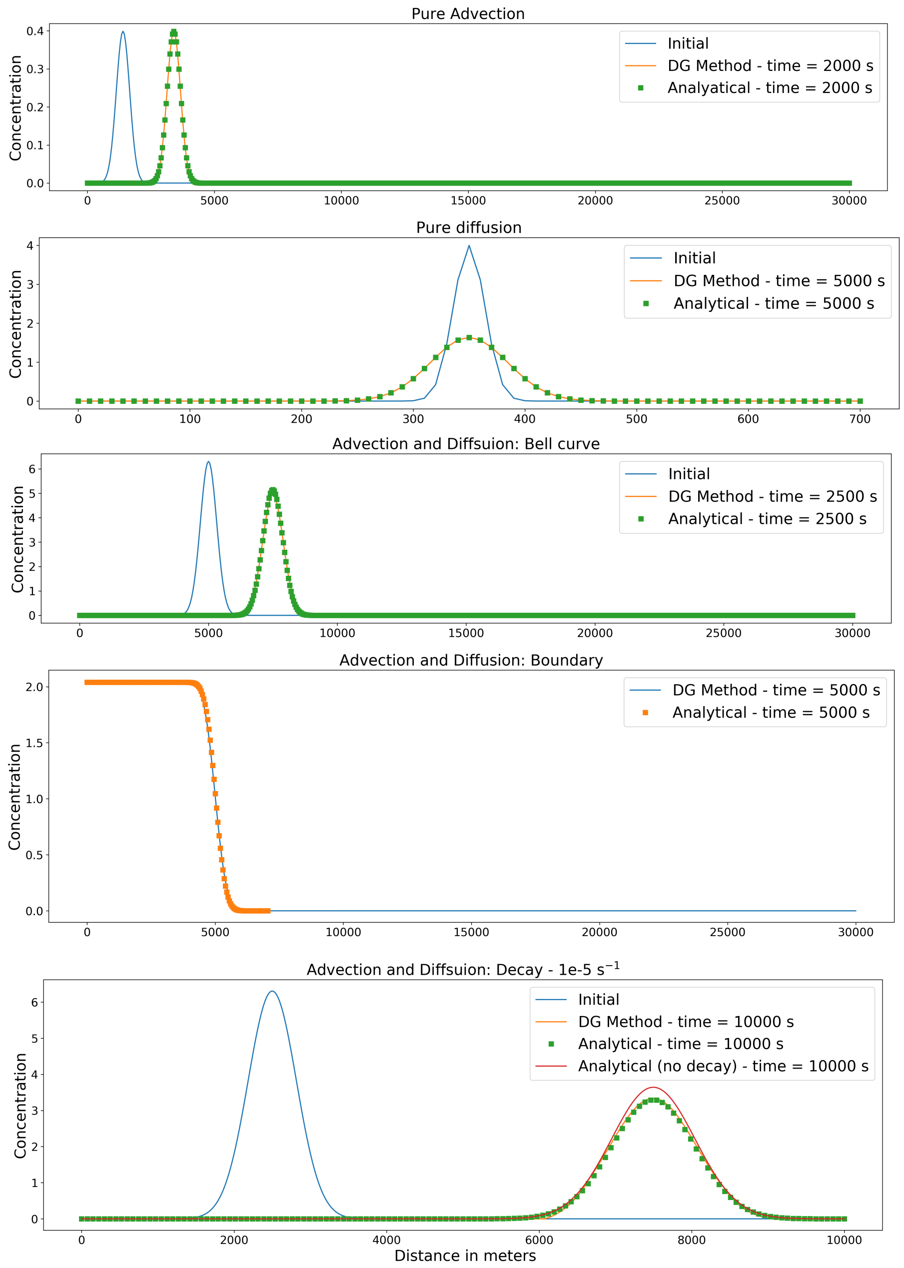

Fig. 3.2: Comparison of exact solution and modeled results for (a) Pure advection (b) Pure diffusion (c) Advection and Diffusion (d) Advection and diffusion Boundary and (e) Advection and diffusion with decay

3.3 Hypothetical Scenario Definition

3.3.1 Releases and source term definition

Here, we are interested in using this model to evaluate the impact of accidental releases coming from the Chooz and Tihange NPPs into the Meuse River. Several hypothetical accidents occurring in these two NPPs were considered and selected. These scenarios are selected in order to have worse-case conditions after atmospheric releases in the Meuse River systems. In previous nuclear accidents, such as the Fukushima disasters, this release pathway accounted for around 80% of the total contamination. The amount of radionuclide that is hypothetically released from both NPPs is based on the figures established in the Fukushima disaster by the UNSCEAR (United Nations Scientific Committee on the Effects of Atomic Radiation) working committees (UNSCEAR (2021)). Table 3.2 gives a description of the releases that were reported to occur during the Fukushima accident:

Radionuclides	Atmospheric releases (PBq)
^{131}I	100-500
^{137}Cs	5-20

Table 3.2: Total radionuclide releases as reported by UNSCEAR from the Fukushima nuclear accident to the atmosphere and as a direct release pathway into the aquatic environment.

For the atmospheric deposition source, the JRODOS atmospheric model (Raskob et al. (2016)) was used to determine the distribution of both the radionuclides and their activities on the surface of the Meuse River. The JRODOS has been previously utilized for assessments following the Fukushima Daiichi accident (Ievdin et al. (2012),Kovalets et al. (2014),Selivanova et al. (2023)). For this study, the radioactivity deposition results were obtained with an atmospheric release of 100 PBq in the case of ^{131}I and 10 PBq for the ^{137}Cs, assuming a release period of 6 hours. The release period is assumed based on observations, which show that most of the peak release is achieved within this period of time. In the case of the Fukushima disaster, the hydrogen explosions that occurred on March 12, 2011, led to peak activity concentrations in the atmosphere being detected within hours (Tsuruta et al. (2014)).

3.3.2 Meteorological Conditions of the Study Area

The river discharge has significant temporal variability in its flow that can influence the time scale and the distribution of radionuclide in these systems. During a year, the summer periods bring less precipitation, resulting in low discharges of around 50 m^3/s and in wet winter periods, higher discharges up to 3000 m^3/s can be observed (Ward et al. (2008)). Low discharges in the

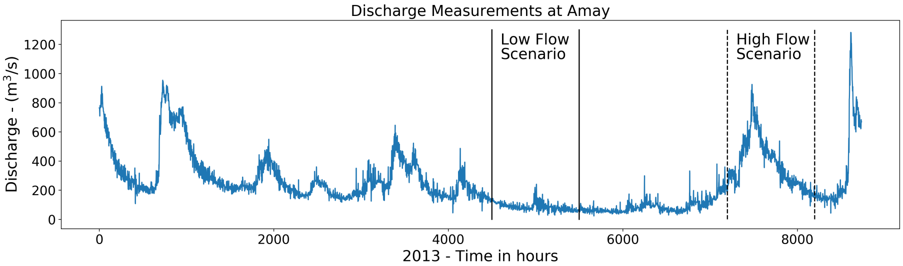

Fig. 3.3: Hydrograph in Meuse River at Tihange NPP (2013): period of flow in the Meuse River considered for the hypothetical scenarios in this study.

summer period can persist for a longer time, whereas high discharges usually reach a peak and subside as the precipitation reduces (Figure 3.3). For our purposes, we take into account two scenarios with realistic flow conditions: First, is the low flow scenario (with constant flow) and the other is high flow scenario (peak flows). Figure 3.3 shows a hydrograph of the Meuse River for the year 2013 and the flow scenario selected in this study. The high flow scenario peaks at 1025 m^3/s, while the low flow scenario reaches a minimum of 40 m^3/s with an average flow of 54 m^3/s over 42 days. Although the peak and the low flow periods in the Meuse River could vary between years, the aim here is to distinguish between the impact of low and high flow conditions on radionuclide distribution. In this perspective, the selected scenarios could be considered as average scenarios for the Meuse River. The recurrence of peak flow (near Maastricht: Figure 3.1) is usually higher than 800 m^3/s and lasts roughly 25 days, for discharge above 1300 m^3/s the duration of the event is around 165 days (Ward et al. (2008)).

In order to obtain a contamination event with maximum affected area and highest deposited activity, a constant wind speed of 1 m/s is chosen for both the NPPs, and a uniform and fixed direction of wind is chosen to be such that the released plume into the atmosphere is deposited towards the Meuse River basin. Figure 3.4 shows the area deposition of radionuclides, and Table 3.3 presents the parameters used for the scenarios. It should be noted that in Figure 3.4, the colourmap is limited to 7 MBq/m^2 for both radionuclides.

The liquid radioactivity released directly into the Meuse river during the scenarios presented in Table 3.3 is based on the releases that occurred during the Fukushima disaster (spanning from March–April 2011). As reported, it was very difficult to estimate the duration of the accidental release of radionuclides that occurred by using backward extrapolation of inventories (UNSCEAR (2021)). Here, we keep the assumption of an accidental scenario of a six-hour release period in order to keep the combination of atmospheric and direct liquid

NPP	Source term	Wind direction	Wind Speed m/s
Tihange	^{131}I - 100 PBq + ^{137}Cs - 10 PBq	236^0 SW	1
			3
			5
		44^0 NE	1
Chooz	^{131}I - 100 PBq + ^{137}Cs - 10 PBq	191^0 S^0	1
Direct releases	I-131 - 127 GBq/min	-	-
Tihange and Chooz	Cs-137 - 52 GBq/min	-	-

Table 3.3: Scenario definitions for ^{137}Cs and ^{131} and their amount of radioactivity released from the NPPs (Tihange and Chooz) into the Meuse basin.

NPP	Scenario	Date	Time	Wind Speed m/s	Wind direction	Precipitation(cm)
Tihange	1	30-01-2021	10:00 AM	3	45^0 NE	0.1
	2	14-05-2021	2:00 PM	2.5	225^0 SW	0.28

Table 3.4: Start time for the scenario definitions of real conditions used for atmospheric deposition for radioactivity released from the Tihange NPPs into the Meuse basin

release. The rate of release is estimated from the total amount of radionuclide released between March and April 2011, with inventories of ^{137}Cs at 5 PBq and ^{131}I at 12 PBq (UNSCEAR (2021)).

3.4 Real Scenarios

The meteorological condition in a time scale of hours is highly variable in the regions. Therefore, there are several possible combinations of wind speed and direction that could occur. The scenario for the realistic meteorological conditions is further considered to estimate the largest deposition area on the Meuse River basin (direct deposition on the river). The distribution of radioactive fallout is simulated for the selected values of wind direction, speed, and precipitation. Table 3.4 shows the date and time for the start of release and the corresponding conditions observed during this hour. A fallout period of 24 hours is considered, with a 6-hour release period from the nuclear power plant. The inventory of radioactive release is the same to that of hypothetical scenarios.

Figure 3.6 shows the radionuclide fallout due to atmospheric releases under real meteorological conditions. The realistic scenarios considered here clearly have larger area of extent due to spatial variation in the wind direction and increased wind speed, which can spread up to the Campine Canal. In the instance of hypothetical scenario (Figure 3.6a), a smaller coverage area than the second can be observed (Figure 3.6b). Therefore, the combination in these factors can result in a wide range of outcomes. The aim here is not only to compare the hypothetical scenarios chosen, but to evaluate the radioactivity

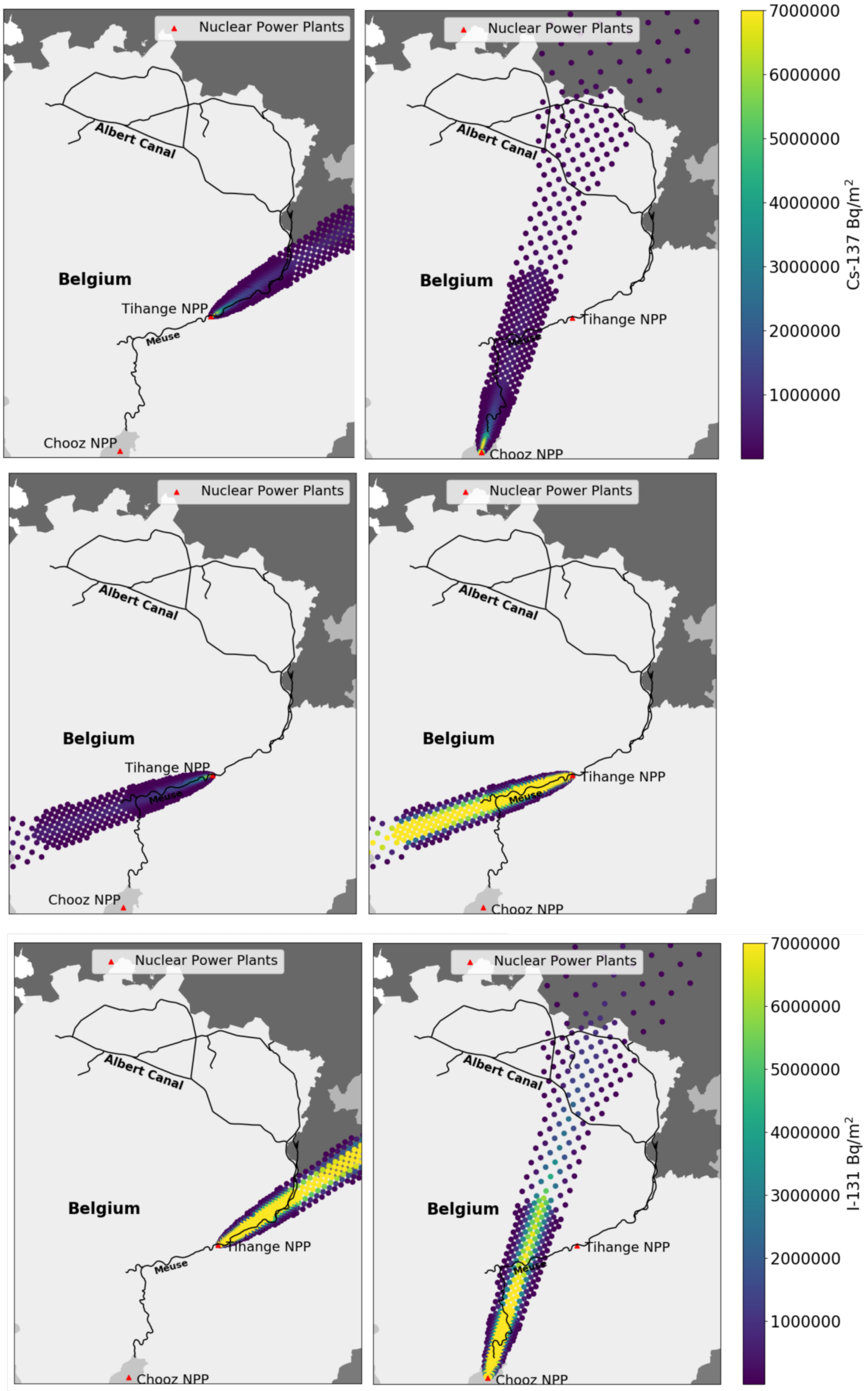

Fig. 3.4: Total amount of radionuclide deposited on the Meuse River basin after 24 hours of initial release as computed by the JRODOS model for ^{137}Cs and ^{131}I from Tihange NPP (wind direction: 236^0 and 44^0) and Chooz NPP (wind direction: 191^0)

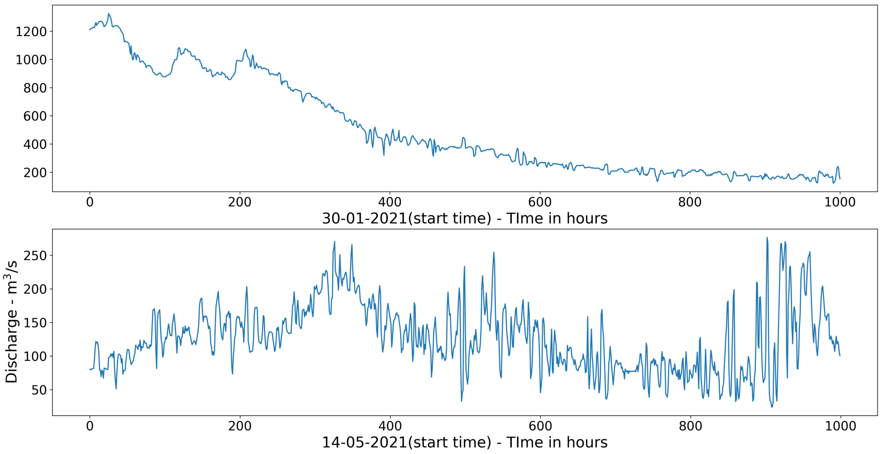

Fig. 3.5: River discharge at Amay for the selected period of real scenarios in Table 3.4 (a) scenario 1 (top) (b) scenario 2 (bottom)

distribution for such varied conditions.

The flow characteristics applied as boundary conditions were obtained from field measurements. Figure 3.5 shows the discharges in the Amay measurement location in the Meuse River for the selected periods. The first scenario can be considered as a high-flow event, whereas the second is a comparatively low flow event.

3.5 Routine Releases

As mentioned earlier the data regarding the radioactivity measurements in the river are scarce. However, data on the amount of liquid waste generated at the nuclear power station are available. But these will be further subjected to dilution and decay. Since, small concentrations of ^{131}I can decay quickly, there is no data available for this, hence only ^{137}Cs will be dealt with here. Nonetheless, under the worst-case scenario, we assume that all liquid waste generated is released into the river without any further treatment. Additionally, as observed in earlier scenarios, the low flow condition will have an increased concentration in the river. For this, we chose the year 2018, which was one of the driest in the recent decade, especially in the summer. Furthermore, low flow conditions generate lesser suspended sediments, resulting in minimal deposition or re-suspension. In this year, the reported figure for radioactive liquid waste was 2100 MBq (FANC (2023)). It is also assumed that the liquid is released as a continuous source that amounts to 3.7 mBq/(min.m^3) over a four-month simulation period starting on July 15th. Figure 3.7 depicts the discharge in the

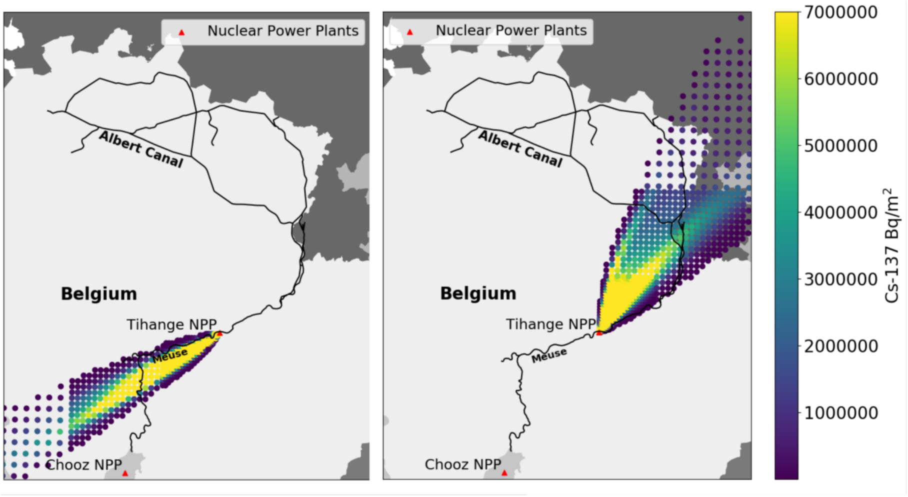

Fig. 3.6: Total amount of radionuclide deposited on the Meuse River basin after 24 hours of initial release as computed by the JRODOS model for ^{137}Cs from Tihange NPP for real meteorological conditions presented in Table 3.4

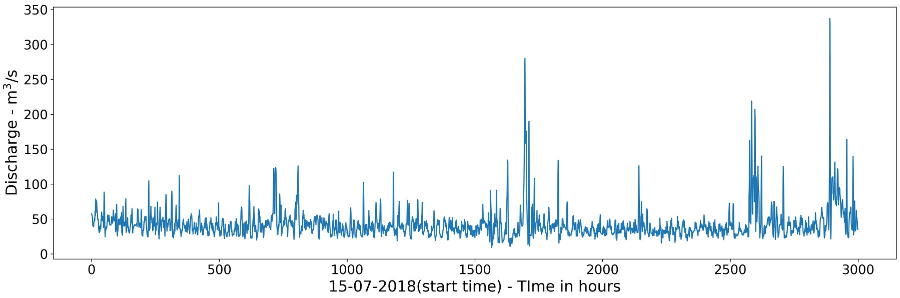

Fig. 3.7: River discharge at Chooz for the period selected of routine releases

river at Chooz during the period utilized as a boundary condition.

3.6 Dose Calculation for Drinking water

In order to obtain the individual dose arising from drinking the river water, the radionuclide concentration is multiplied by the dose coefficient for internal exposure via ingestion (internal dose rate).

$$Dose_k(mSv) = A_k \times B \times \sum_t c_k \qquad (3.3)$$

Where k is the radionuclide, A_k is the dose coefficient for radionuclide $k(mSv/Bq)$, B is the daily consumption of drinking water per person (lit/d), t is the number of days after the accident (consumption date), and c_k is the concentration of radionuclide k in drinking water at t hours after the accident. In this study, B was set at 2 lit/day, which is the IAEA's recommended value for dose estimation (IAEA (2016)). The dose coefficients of 1.3×10^{-8} for ^{137}Cs and $2.2 \times 10^{-8} Sv/Bq$ for ^{137}I are used (ICRP (2018)). The assessment is based on the two water extractions carried out in the study area: (1) the Meuse River (extracted at Tailfer), which supplies drinking water to the Brussels region with a population of approximately 2 million people, and (2) the Albert Canal (extracted at Herentals), which provides 40% of total drinking water to a population of 7 million people in Flanders. Figure 3.8 shows the location of these water extraction points. Additionally, the total population dose is calculated by multiplying the dose and the total population that consumes the contaminated water. This is done to determine the carcinogenic likelihood for the population, which is based on the observations made on the so-called bomb survivors of Hiroshima and Nagasaki (Picano and Vano (2011)).

3.7 Results and Discussion

3.7.1 Hypothetical Scenario Simulation: Activity concentrations in water

This section presents the radioactivity concentrations for the scenarios that were previously discussed in section 3.3.The results obtained have a range of concentrations up to a maximum of 22 MBq/m^3 for ^{131}I and up to 0.5 MBq/m^3 for ^{137}Cs, with high concentrations in the Meuse River near Amay (for location see Figure 3.8). It is perhaps worth mentioning that the maximum concentrations in Meuse river are the result of concentrated atmospheric deposition of the radionuclides. The recommended limit for radioactivity concentration is 10 kBq/m^3, according to the safety regulations under normal operating conditions (IAEA (2016)). However, it should be noted that these limits can be extended based on the level of accident as mentioned in section 1.5.2. The simulated affected areas by radioactivity are shown in the figure, together with their respective maximum activity concentrations. Figure 3.8 shows some of the important locations used in this section to show the temporal variation of the radionuclide activity. Sections 3.7.1.1 to 3.7.1.4 compare the results of Tihange NPP releases, whereas section 3.7.1.5 shows the results of Chooz NPP.

3.7.1.1 High vs Low Flow

The radionuclide takes about 8 hours to deposit on the river, following which it gets transported to the downstream region of the river and the Campine canal.

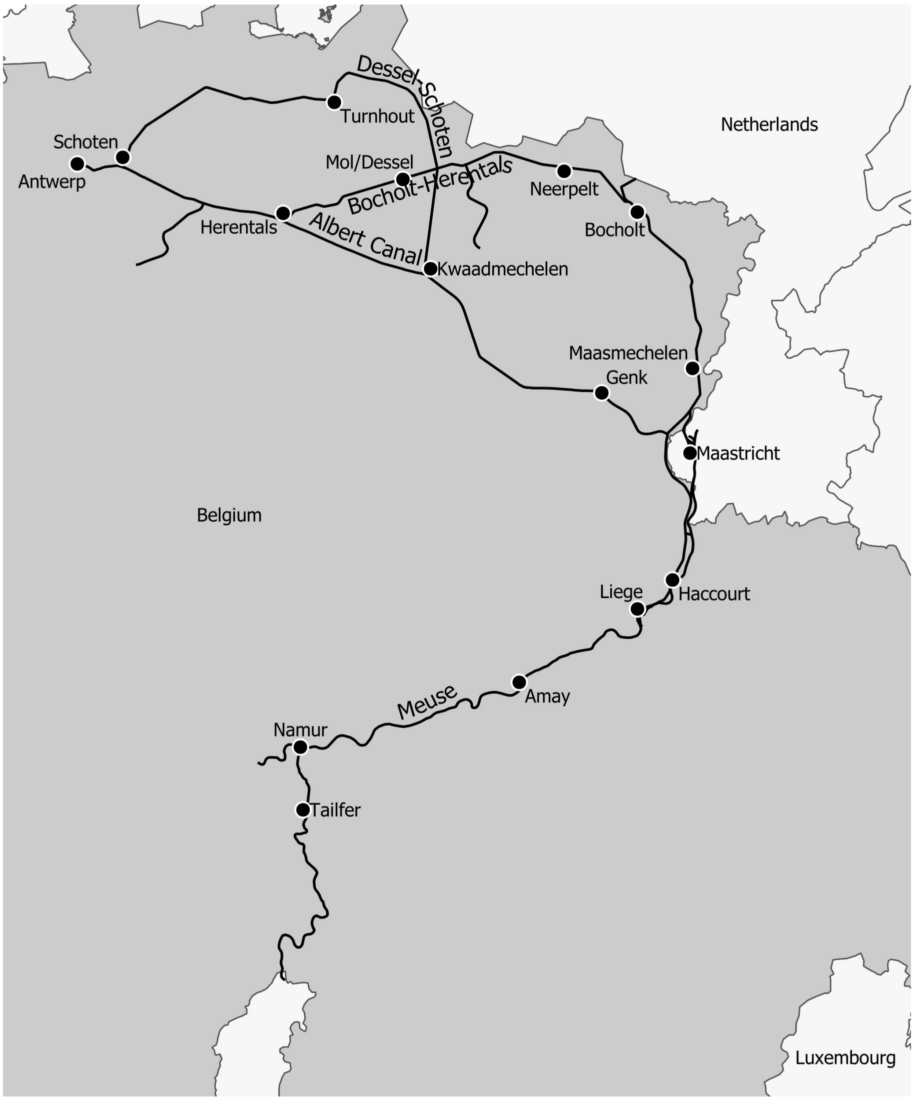

Fig. 3.8: Location of important places used for estimating the residence time and dose calculation presented in this section.

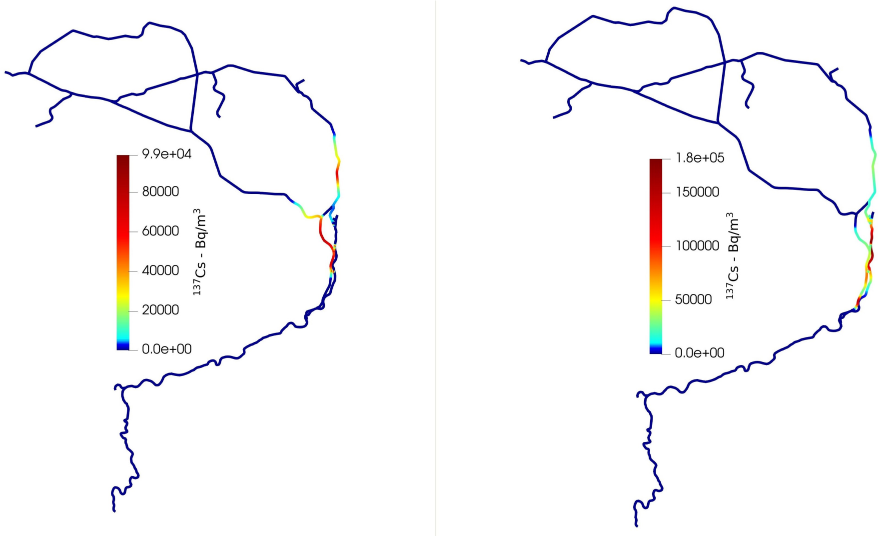

Fig. 3.9: ^{137}Cs distribution in the Meuse – Campine Canal after 100 hours of initial release for high flow scenario (left) and low flow scenario (right)

The distribution of radioactivity in these aquatic systems depends on the flow conditions of the river. Figure 3.9 shows the concentration of ^{137}Cs for both high and low flow scenarios (as described in Section 3.3.2) after approximately 4 days of initial release (i.e., 100 hours). As shown in Figure 3.9, in the initial days after the release, the affected areas of the radionuclide in the Campine canal are approximately similar for both low and high flow scenario. The maximum concentration at this hour for the case of high flow is 99 kBq/m^3 located in the Meuse River, while that for low flow is 108 kBq/m^3 located in the Albert Canal, closer to the river-canal confluence. Furthermore, Figure 3.9 shows near to zero radioactive contamination in the Meuse River in the high-flow scenario. This is because the high flow scenario in the Meuse River reduces the flushing time from five to two days (see Table 3.5). While notably, the longer flushing times in the Albert Canal is due to the operation of hydraulic structures at the confluence (river – canal). This also applies to the other connection from the river to the Zuid-Willemsvaart canal, where the water discharge is controlled by an underflow gate.

However, the radioactivity distribution in the canal system for low and high flow scenarios varies with time. Figure 3.10 shows the radionuclide distribution after approximately 28 days of simulation. Figure 3.10 shows that in the high flow scenario, the radioactive plume has reached Antwerp, whereas in the low flow scenario, it has only been transported until Genk (for location, see Figure

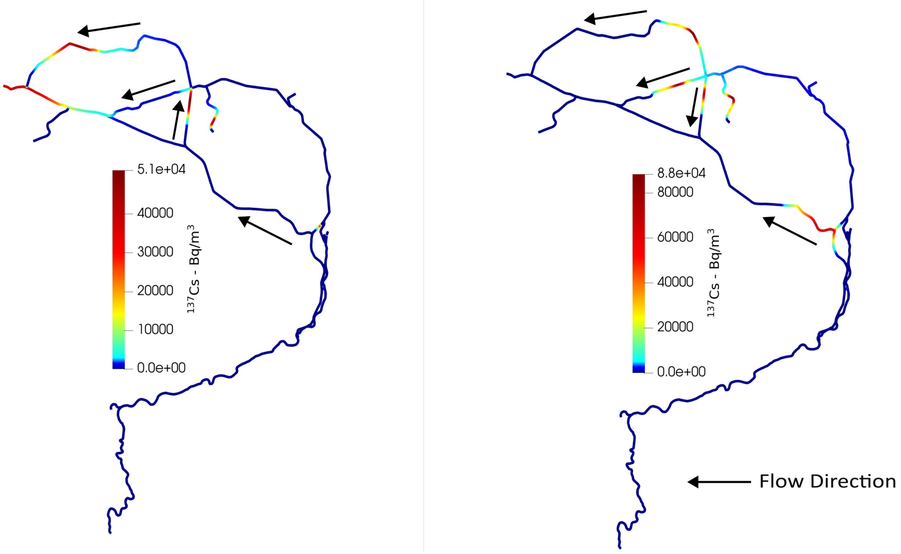

Fig. 3.10: ^{137}Cs distribution in the Meuse – Campine Canal after 700 hours of initial release (a) for high flow scenario (left) and (b) low flow scenario (right).

3.8). Furthermore, unlike the high flow scenario, the radioactive plume that is transported along the Zuid-Willemsvaart canal reaches the downstream section of the Albert Canal earlier than the radioactivity plume that travels along the Albert Canal itself. This is illustrated in Figure 3.11, which shows the concentration profile along the Albert Canal at the time the plume arrives from the connecting canals. In the low flow scenario (Figure 3.11a), the radioactivity spike near Kwaadmechelen and Herentals, is visible while the plume in the Albert Canal continue to move towards it. While in the high flow scenarios, the plume from the Zuid-Willemsvaart and its connecting canals coincides with the arrival of plume from the Albert canal (as illustrated by spikes in Figure 3.11b). The slower transport of the plume in the Albert Canal (175 m wide in Genk) can be partially explained by its larger size compared to the other canals (42 m wide in Neerpelt). In addition to that, during low flows in the Meuse River, discharge diversion into the Albert Canal is lower than during the high flows. Figure 3.10a further shows that the plume is still present in the Dessel-Kwaadmechelen Canal. This is due to the fact that during high flow in the Albert canal there is a shift in flow direction in into the Dessel-Kwaadmechelen Canal. Moreover, during low flows the velocities in this segment are rather low. The Dessel-Kwaadmechelen Canal connects the Albert- Canal and the Bocholt-Herentals canal without any regulation in between. Therefore, the direction highly depends on difference in water level between its both ends.

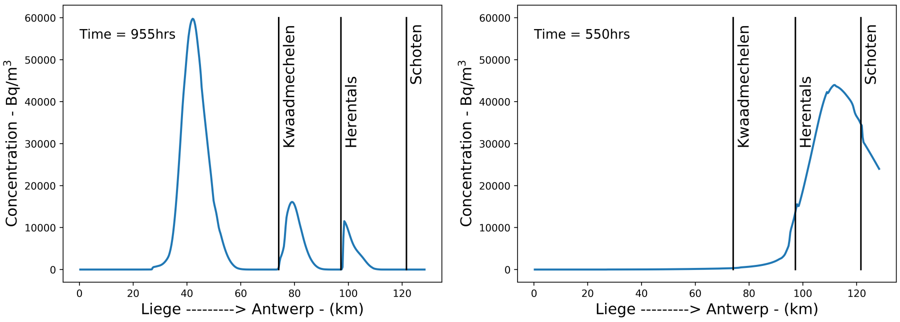

Fig. 3.11: ^{137}Cs longitudinal profile along the Albert Canal from Liege to Antwerp for (a) Low flow scenario at 955 hours (left) and (b) High flow scenario at 550 hours after initial release (right).

Scenario	**Canal Name**	**City Name**	**Arrival Time (h)**	**End Time (h)**	**Maximum Conc (Bq/m^3)**	**Time for Max Conc.**
Low Flow	Meuse River	Maastricht	20	148	166302.9	115
	Albert Canal	Genk	497	-	60835.5	842
	Albert Canal	Antwerp	0	0	-	-
	Dessel -Schoten	Turnhout	683	859	82983.9	794
	Dessel-Herentals	Mol	452	630	79857.3	558
	Zuid-Willemsvaart	Maasmechelen	61	204	120056.7	160
High Flow	Meuse River	Maastricht	14	61	142121.57	48
	Albert Canal	Genk	128	277	64108.54	220
	Albert Canal	Antwerp	525	668	39526.58	595
	Dessel -Schoten	Turnhout	460	545	47251.71	504
	Dessel-Herentals	Mol	664	944	22082.52	774
	Zuid-Willemsvaart	Maasmechelen	53	110	73778.51	89

Table 3.5: Arrival and end time of the potential plume in Meuse River and the network of Campine canal at specific location with maximum concentration and time of occurrence at that location

During high flow events in the Albert Canal the plume in this canal segment will be flushed to the north, while during low flows it will slowly travel to the Albert Canal.

Table 3.5 shows the arrival, the end time from the initial release and the maximum concentration of the radionuclides at locations inside each of the canals (for location, see Figure 3.8). It should be noted that the arrival and end times are estimated in terms of when the concentration reaches either below or above the recommended limit of 10000 Bq/m^3. From the arrival/end times in Table 3.5, it can be seen that the radionuclide contamination stays longer at a specific location during low flows than in the high flow scenario. For example, in Turnhout, the duration of the high contamination period for the release during the low flow scenario is 91 hours (4 days) longer than if released during the high flow scenario. Similarly in the Meuse River, the

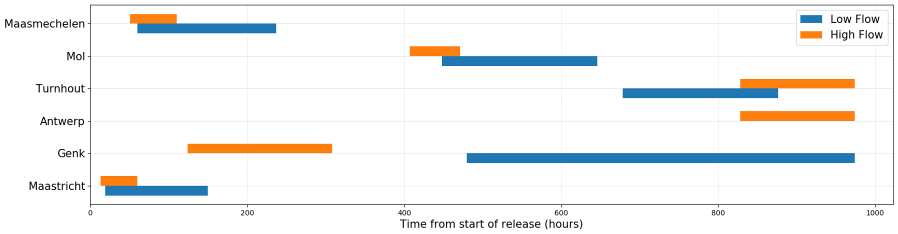

Fig. 3.12: Residence time of the potential plume in Meuse River and the network of Campine canal at specific location.

plume stays for 81 hours (3 days) longer in the case of a low flow scenario. This relatively lower period of contamination in the river than the canal can be related to the fact that the river's water velocities are high. Additionally, due to lower velocities in the canal the effect of diffusion increases. In most of the locations, the magnitude and time for peak concentration also decrease from low flow scenario to high flow scenario except at Mol. The change in time of peak concentration at Mol is a result of the shift in flow direction in high flow from the low flow scenario in the Dessel-Kwaadmechelen canal. Additionally, the water flow in the Dessel-Kwaadmechelen canal dilutes the radioactivity coming from the Zuid-Willemsvaart canal, but also introduces radioactive contaminants from the Albert Canal at a later time.

For the Zuid-Willemsvaart canal, the peak concentrations at Maasmechelen in the low flow scenario are higher than those obtained during high flow scenario (Table 3.5). Since the water in Brigeden–Nerhaaran canal is nearly stagnant, the radioactive plume in Zuid-Willemsvaart canal is mostly derived from the Meuse River. Figure 3.13 shows the distribution of radioactivity at the connection between the Zuid-Willemsvaart canal and the Meuse River in Maastricht after about 4 days of release. The period of maximum activity concentration at Maasmechelen (12 km from Maastricht) is 57 hours in high flow, i.e., 10 hours longer than at Maastricht (in Meuse River) and 143 hours in low flow, i.e., 15 hours longer. The longer times in the canal can be attributed to its slower velocities.

3.7.1.2 ^{131}I distribution

As described earlier for ^{137}Cs, the low flow scenario is typically the scenario for maximum impact in the Meuse River and the Campine canal. Therefore, the results for ^{131}I presented here are only for the low flow scenario. It is worth mentioning that the half life of ^{137}Cs (30 years) is significantly longer than ^{131}I (8 days). However, the amount of ^{131}I that is released in the scenarios is

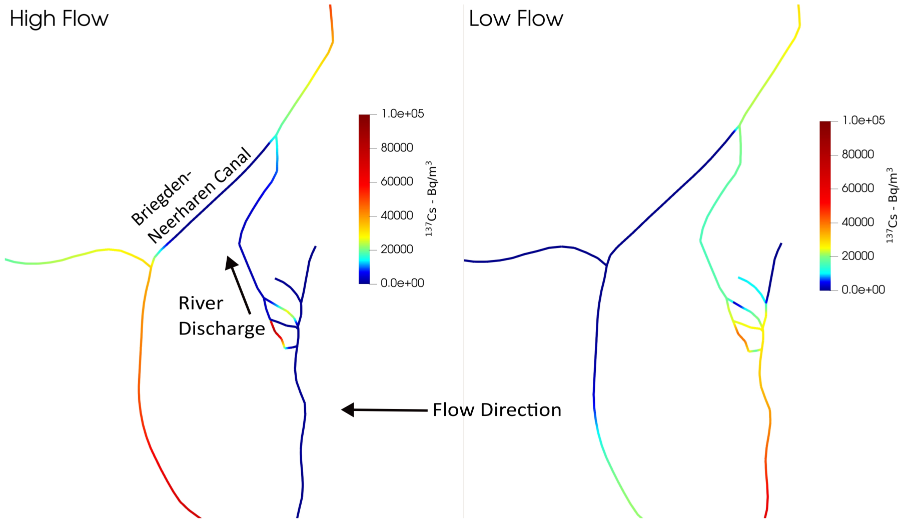

Fig. 3.13: ^{137}Cs distribution at the connection of the Meuse River and the Zuid Willemsvaart canal (a) for high flow scenario at 100 hours after initial release (left) (b) for low flow scenario at 132 hours after initial release (right).

10 times larger than the release of ^{137}Cs. Figure 3.14 shows the radionuclide distribution for ^{131}I after approximately 4 and 28 days of initial release.

Because of the high amount of ^{131}I released, the radioactive contamination is greater than ^{137}Cs after 4 days of release. Furthermore, Figure 3.14a shows that the peak concentration (7.9 MBq/m^3) is one order of magnitude higher than the ^{137}Cs. However, since ^{131}I has a faster decay rate, the concentration in the system reduces significantly. Moreover, in the case of the Campine canal, since the concentrations are smaller than in the Albert Canal the radioactivity concentration vanishes (approximately 10 times smaller than the initial value) after about 20-27 days (Figure 3.14b). However, for the high flow scenario, it is seen that the plume reaches Antwerp faster than plume of ^{137}Cs. This is due to the considerably larger magnitude of the release of ^{131}I. Figure 3.15 shows the radionuclide concentration for both radionuclides along the Albert Canal at different times and flow scenarios.

Figure 3.15a shows the radionuclide distribution of ^{131}I and ^{137}Cs, where it can be seen that both plumes arrive at same time. However, after nearly 28 days of the initial release, the activity concentration of ^{131}I is still higher than the activity concentration of ^{137}Cs. While the contribution to the activity of ^{131}I in the Albert Canal coming from the connecting canals is minimal. Similar results can also be observed in the high flow scenario (Figure 3.15b) but with a noticeable influence of the connecting canals (where the spike in activity

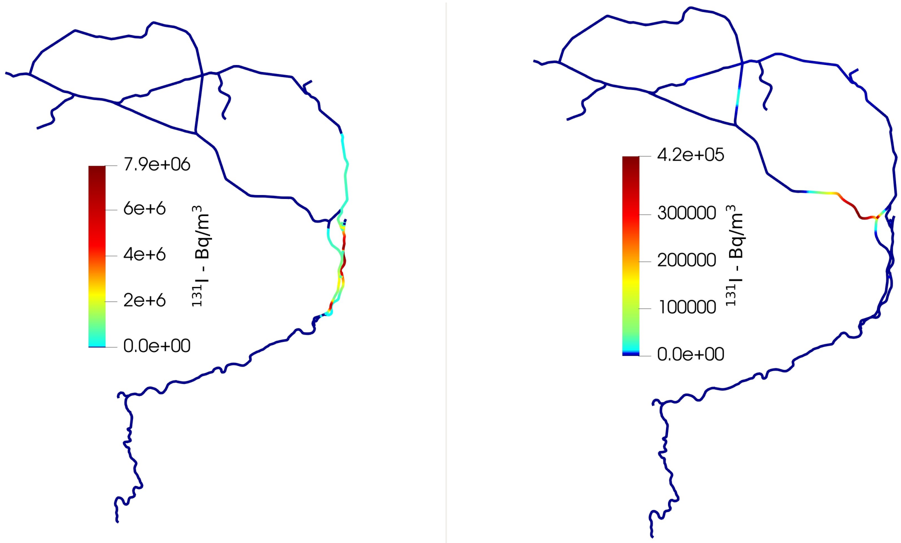

Fig. 3.14: ^{131}I distribution in the Meuse – Campine Canal for low flow scenario after (a) 100 hours of initial release (left) and 700 hours of initial release (right).

concentration are visible in Figure 3.15b; approximately 90 km). This is due to the faster transport of radionuclides and the slower decay. Although ^{131}I has a considerable impact on the Albert Canal at 7 days, as seen in Figure 3.11c, the concentration can drop fourfold within a couple of weeks. After 550 hours after the release, the peak concentration is higher for low flows than for the high flow scenario (Figure 3.15d). That can be justified by the fact that canals have higher discharge during the high flow scenario (more dilution).

In the case of the Meuse River, the peak ^{131}I concentration at Maastricht is 6.9 and 7 MBq/m^3 for high and low flows, respectively. Although the arrival time of the plume for high and low flows is similar, there is a significant difference in the passing time of the plume. In the event of high flow, the concentrations remain above the recommended limit for around 4 days, whereas in the case of low flow, they remain for about 22 days (Figure 3.16). Even though the ^{131}I decays fast, for low flows the other canal segments (vise and Lanaye) coming from the Albert Canal into the Meuse river bring additional contamination (Figure 3.16: enlarged area). This is because, in low flow circumstances, radioactive movement in the Albert Canal is exceedingly slow and radioactive plume stays around the bifurcation point for prolonged periods of time. Similarly, we observe the same effects for ^{137}Cs, but they remain below the activity concentration recommended limit.

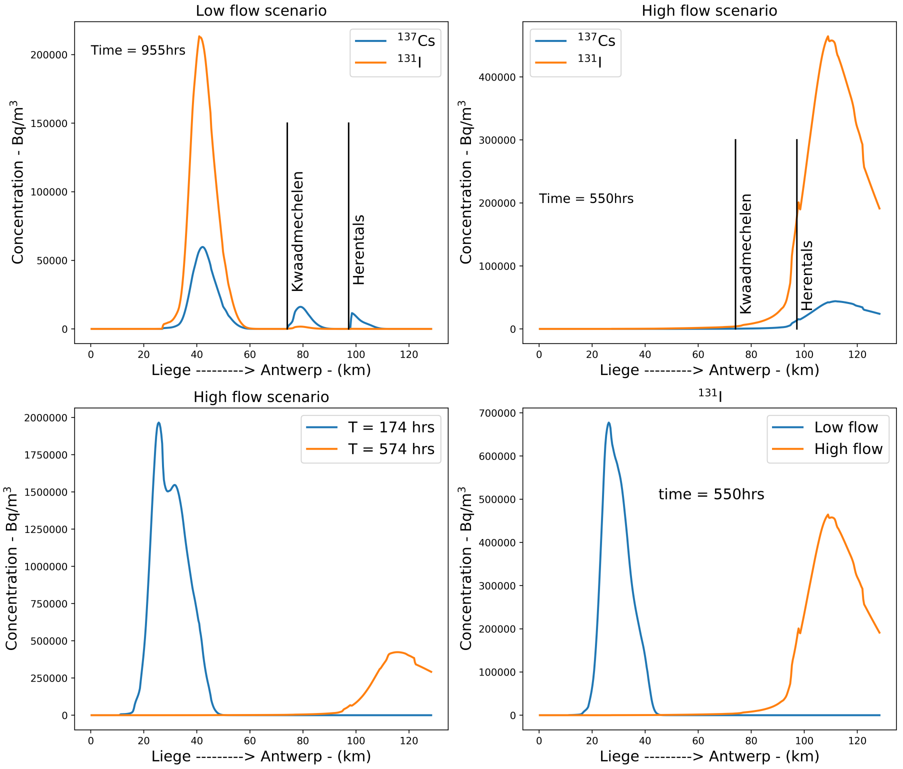

Fig. 3.15: Distribution along the longitudinal profile of the Albert Canal from Liege to Antwerp for (a) comparison of ^{131}I and ^{137}Cs for low flow (top left) (b) comparison of ^{131}I and ^{137}Cs for high flow (top right) (c) ^{131}I distribution after 174 hours and 574 hours for high flow scenario (bottom left) and (d) ^{131}I distribution for low and high flow after 550 hours (bottom right)

3.7.1.3 45^0 wind direction

Figure 3.17a shows the radioactivity distribution for ^{137}Cs due to atmospheric fallout for 45^0 wind direction and Figure 3.17b shows that for 236^0 wind direction from Tihange NPP under low flow conditions. Since the depositions for these releases are towards the upstream part of the river, the arrival times will be delayed compared to those deposited downstream. Table 3.6 shows the arrival times and end times for both the wind direction.

In the Meuse River (for ^{137}Cs) at Maastricht, the plume arrives approximately 5 days after the initial release for the low flow scenario, which is 4 days later than the 236^0 wind direction from Tihange. The delay in arrival times can

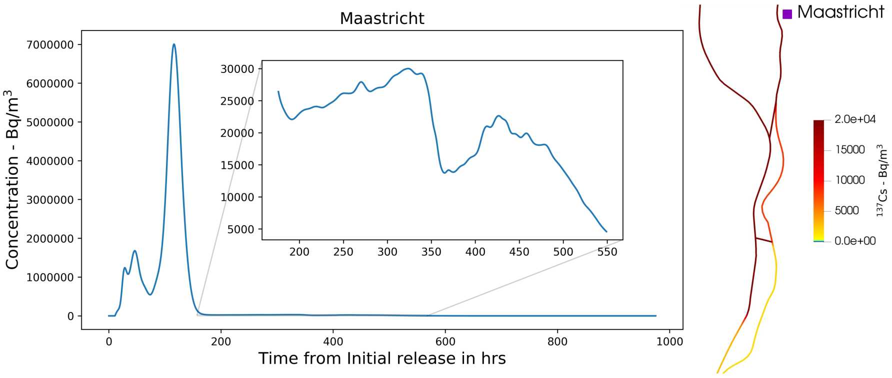

Fig. 3.16: Temporal variation of ^{131}I radioactivity concentration at Maastricht in the Meuse River and the distribution of ^{131}I at the connection with Albert canal and Meuse River.

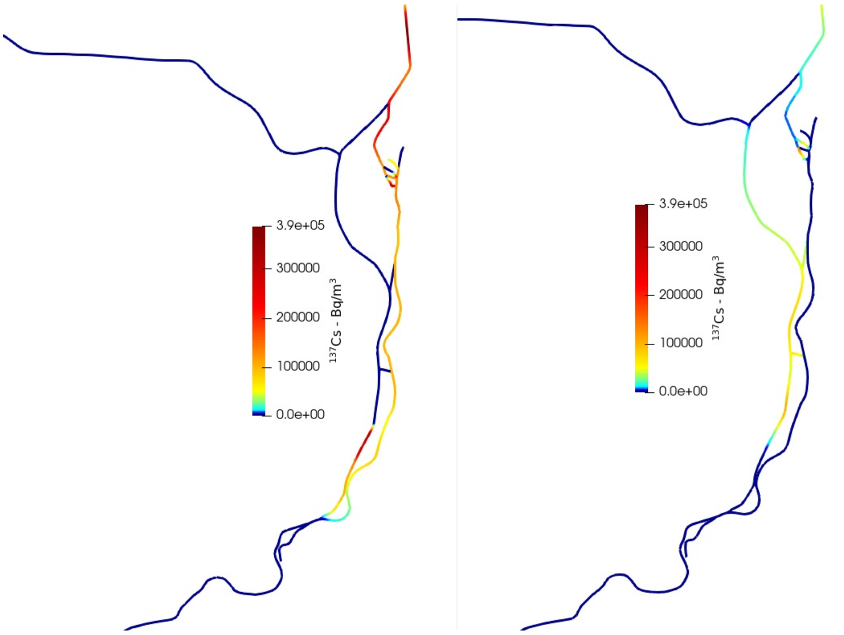

Fig. 3.17: Radioactivity distribution in the Meuse river – Campine canal for the deposition of ^{137}Cs from Tihange NPP at 176 hours for (a) 45^0 wind direction and (b) 236^0 wind direction

Wind Direction (low flows)	**City**	**Arrival time (hrs)**	**End time (hrs)**	**residence time (hrs)**
45^0	Maastricht	128	244	116
	Genk	961	-	-
236^0	Maastricht	19	150	131
	Genk	482	-	-

Table 3.6: Arrival and end times in the Meuse River at Maastricht (Meuse river) and at Genk (Albert Canal) under low flow for different wind direction

be attributed to slower velocities in the river due to low flow scenario, whereas the difference in arrival time for a high flow scenario is reduced to 2 days. The plume arrives at the Albert Canal in Genk after 40 days, while the other scenario (236^0 wind direction) from Tihange takes roughly 20 days. Furthermore in the Albert Canal, as illustrated in Figure 3.17, the extent for this scenario is less than that for plume directed towards 236^0 winds. This increase in arrival time and reduction in the radioactive extent is because the Albert Canal does not have any direct fallout. Although not significant in the low flow scenario, the lower residence time (Table 3.6) in the Meuse River is due to the lower extent of fallout (Figure 3.4).

3.7.1.4 Direct releases

In direct liquid releases the transport of radionuclide are similar to that discussed for atmospheric fallout. The concentration in the Meuse River can reach 120 MBq/m^3 for ^{131}I and 20 MBq/m^3 for ^{137}Cs and can last for up to 5 days in a low-flow condition. The concentration decreases in the Albert Canal, reaching up to 0.3 MBq/m^3 for ^{131}I and 0.1 MBq/m^3 for ^{137}Cs. The relatively higher concentration than atmospheric fallout even with lower inventory, is due to the fact that only a portion of what is released is deposited on the Meuse River. However, the extent of the radioactive plume in the canal and river is reduced (than atmospheric releases) because direct liquid release is a point source of 6 hours. Hence, it is evident that the extent of the radionuclide increases if the release period is increased.

3.7.1.5 Releases from Chooz NPP

The Chooz NPP is located further upstream the Meuse River from the Tihange NPP. Therefore, the deposition of atmospheric releases from Chooz NPP affects wider area. So much so that the release deposition, although less significant, can reach the Zuid Willemsvaart canal (Figure 3.4). Figure 3.18 shows the ^{131}I and ^{137}Cs distribution on the Meuse River–Canal System after approximately 5 days of release. After 6 hours continuous atmospheric release from Chooz NPP, the affected area in the Meuse River here is clearly larger than

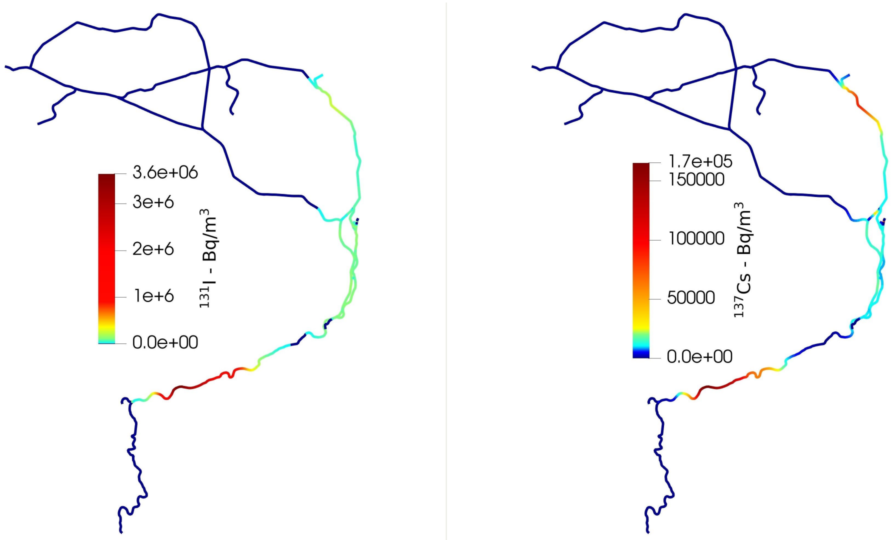

Fig. 3.18: Radioactivity distribution after 700 hrs in the Meuse – Campine Canal for low flow scenario from Chooz NPP for (a) ^{131}I (left) and (b) ^{137}Cs (right).

the releases from Tihange NPP (Figure 3.18). Furthermore, the arrival time (moment when activity is above recommended limit in the water) of the radioactive plume released in the Meuse River at Chooz arrives to Maastricht after 13 hours (which is only 2 hours later than that observed with Tihange releases). However, the time shift in peak concentration is significant, where it occurs after about 4 days in the case of Tihange and after 10 days in the case of Chooz releases. As a result, due to subsequent ^{131}I decay, the peak concentration in Maastricht is five times lower than that from Tihange releases. In addition, the impact of connecting canals (Vise and Lanaye) from Albert Canal is negligible due to the effect of decay, and thereby, the concentrations in the river remain below the recommended level of 10 kBq/m^3. Therefore, even if Tihange NPP is located further downstream than Chooz NPP, a longer period of time with activities (^{131}I) above the recommended level in Maastricht is observed due to the larger influence of connecting canal as explained in Section 3.7.1.2. Table 3.7 show the comparison of the arrival, end time and peak concentration (^{131}I) at Maastricht and Liege for both NPPs. This can be further justified by comparing the results in the Meuse River at Liege, which is located before the connection with the Albert Canal. Here, the residence time is much larger than the Tihange Npp because the length of the plume extents from the discharge point in the Chooz downstream the river. Therefore, once the release stops the contaminated water coming from Chooz is still

	City Name	Arrival Time (h)	End time (h)	Maximum Conc (Bq/m^3)	Time for max conc (h)
Chooz	Liege	12	308	2171397	251
	Maastricht	13	367	1317355	327
Tihange	Liege	2	85	13333026	48
	Maastricht	11	518	7009301	115

Table 3.7: Arrival and end time of the potential plume (^{131}I) in Meuse River and the network of Campine canal at specific location with maximum concentration and time of occurrence at that location.

travelling downstream. However, the peak of the release gradually decreases as it moves downstream (Table 3.7). In the case of the Campine Canal, as previously observed, the ^{131}I concentrations greatly decline over time, especially in the downstream canals. For example, in the Dessel-Herentals canal at Mol, the peak is about 9 kBq/m^3 and arrives about a month after the release that persists for about two days. However, the vulnerability of Albert Canal still remains with a high concentration of approximately 0.19 MBq/m^3, even after a month.

3.7.2 Real Scenarios

Figure 3.19 show the radioactivity distribution (^{137}Cs) for the real scenarios. For scenario 1, the radionuclide plume in the Albert canal reaches Antwerp in about 16 days. This is faster than that for the hypothetical scenarios. This happens because at the start of the release, the discharge in Meuse River is already at its peak value of about 1200 m^3/s, refer Figure 3.5 (More about the effect of peak discharge in section 3.7.4.3). As a result, the radioactive fallout in the Meuse River flushes within a day. The maximum concentration estimated for Liege is around 1.8 MBq/m^3, whereas Maastricht had 1.2 MBq/m^3. In contrast with the hypothetical situation, the activity concentration in the Meuse River reaches 3.8 MBq/m^3. The difference in peak concentration is caused by increasing wind speed, which increases the extent of the fallout while decreasing radioactive deposition per area. Additionally, due to high flow scenario it can be seen in Figure 3.19 that the flow in Dessel − Kwaadmechelen canal is reversed.

Scenario 2, unlike other hypothetical scenarios, the maximum deposition of radioactivity is seen to be near the connection of the Meuse River and Zuid-Willemsvaart canal (3.19). Hence, the radioactivity concentration near the connection in Zuid-Willemsvaart canal at Maasmechelen (for location see figure 3.8) increases to 10 MBq/m^3 within a day. The plume is transported to Bocholt in hours, although it does not reach peak concentration until 5 days later. In comparison, the activity concentration in the Albert Canal reaches only up to 1.9 MBq/m^3. Moreover, as seen in Figure 3.19 the radioactivity concentration

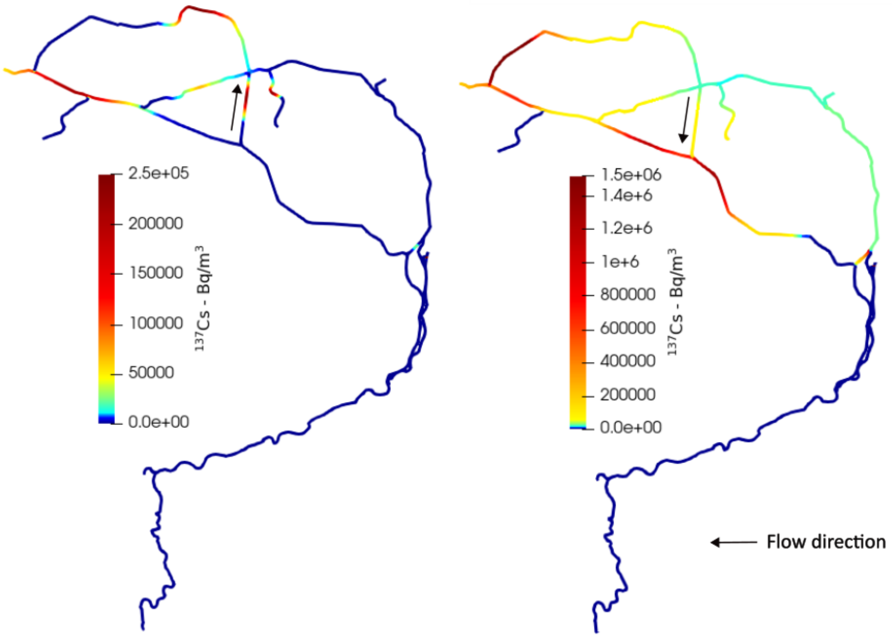

Fig. 3.19: Distribution of ^{137}Cs in the Meuse River – Campine Canal for real meteorological conditions after (a) 17 days of release for Scenario 1 and (b) after 41 days for Scenario 2.

in the entire Campine Canal does not reach below the recommended limit after the end of the simulation periods. This can be attributed to two things: first, is the impact of low flows; and second, the effect of diffusion of radioactivity within the canal network. This scenario highlights the vulnerability of the Campine Canal to direct radioactive fallout.

3.7.3 Routine Releases

Figure 3.20 shows the radioactivity concentration in the Meuse River for routine release scenario after 54 days and 91 days of continuous releases. As expected, under the low flow scenario, Figure 3.20a shows two plumes in the Albert Canal. This is because the plume from the connecting canals arrives faster than the plume from the Albert Canal. However, the distribution at 100 days indicates that the entire region after the Tihange NPP has been contaminated (Figure 3.20b). The maximum concentration in Liege is 0.177 Bq/m^3, which occurs around 1490 hours after the start of release. The highest concentrations in the Campine Canal are 0.12 Bq/m^3, which occurs after 1450 hours. High

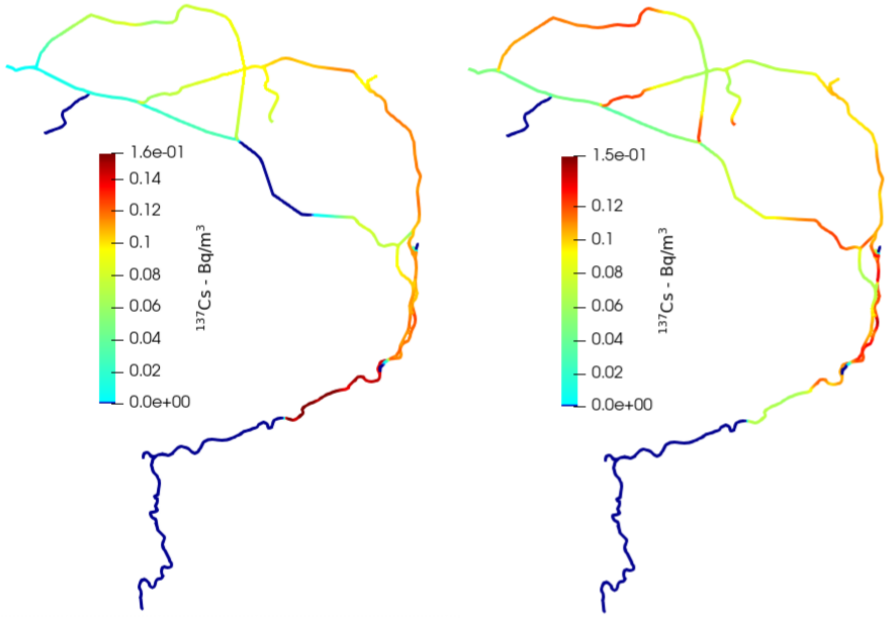

Fig. 3.20: Radioactivity concentration distribution in the Meuse river -Campine canal for routine releases (^{137}Cs) after (a) 54 days and (b) 91 days.

concentration around this time is because the river's discharge reaches its lowest value during this time period. These radioactivity concentrations are extremely small; to give you some perspective, the translated doses for this concentration are 11 orders of magnitude lower than the permissible limit of 1 mSv.

3.7.4 Sensitivity study

In this section we investigate the effects of different parameters and condition that influence the distribution and peak activity concentration in the Meuse River – Campine canal. First parameter is the dispersion coefficient, the second is the effect of wind speed for atmospheric deposition and the last is the effect of time of release before or after the peak is reached for a high flow scenario. The first two scenarios use a low flow condition, and all the scenarios are simulated for ^{137}Cs. Here, the temporal variation of the radioactivity is presented at specific location in the river and the canal.

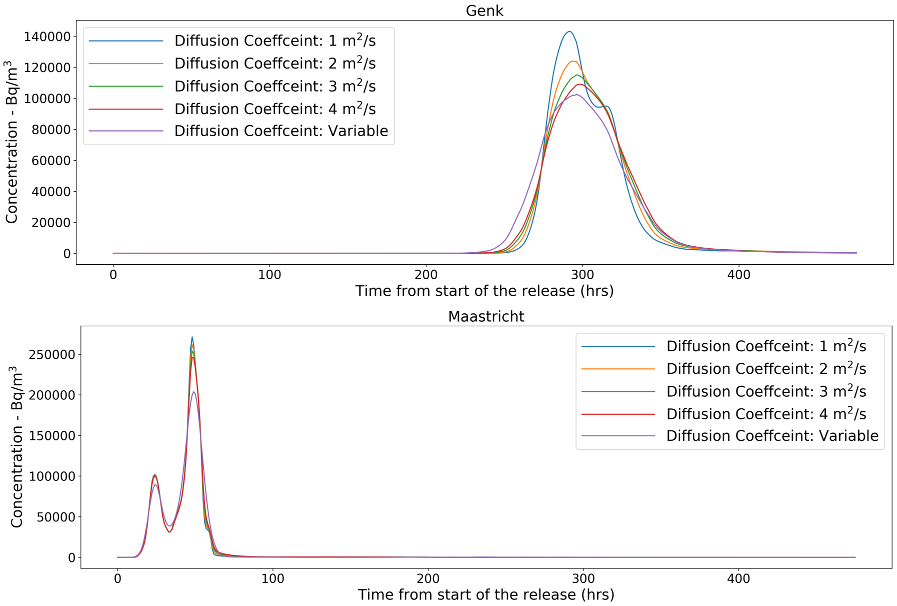

Fig. 3.21: Temporal variation of ^{137}Cs for different diffusion coefficients in (a) Albert Canal (Genk) and (b) Meuse river (Maastricht)

3.7.4.1 Diffusion Coefficient

The distribution of radioactivity is a combination of advection and diffusion processes that is difficult distinguish. Therefore, in order to understand the effect of only diffusion in the canal and river, the hypothetical scenario (wind direction: 45^0 from Tihange NPP) is simulated for different diffusion coefficients. A constant value on the entire domain is applied with diffusion coefficients of 1, 2, 3, 4, 10 and 50 m^2/s. The lower values are to compare the results with variable diffusion coefficient in the canal and higher values are that for the river.

Figure 3.21a shows the temporal variation of radioactivity in Maastricht, while Figure 3.21b shows the same in the Albert Canal at Genk. It is evident the diffusion in the Albert Canal has a greater influence than that in the Meuse River. For a lower diffusion coefficient of 1 m^2/s, the deposited plume is transported with a higher influence of advection, while higher values disperse the radioactive deposition with time. This effect is not seen in the Meuse River because of its higher advective characteristic. However, when the diffusion coefficient is increased to 10 and 50 m^2/s, the effect of diffusion becomes somewhat evident in the Meuse River. Figure 3.22a shows the temporal

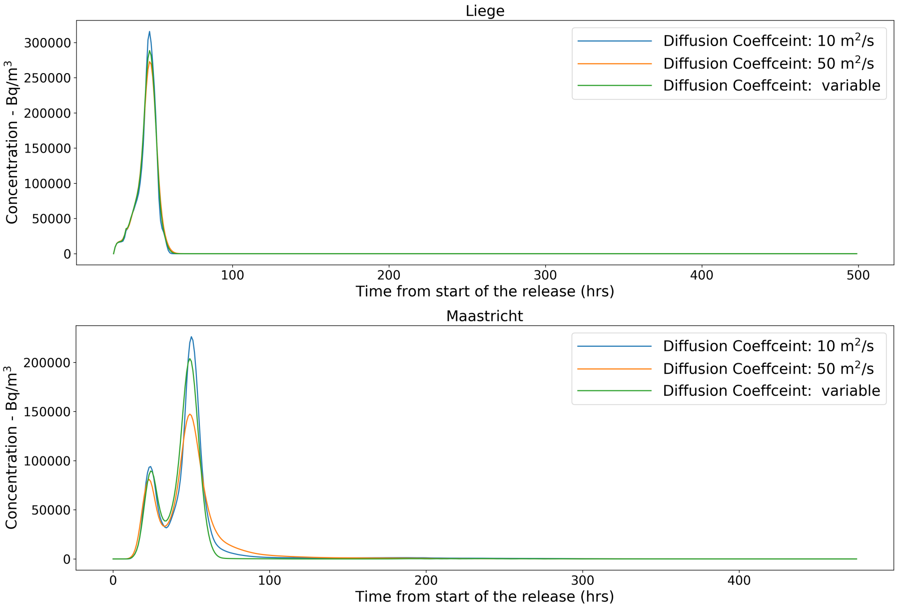

Fig. 3.22: Temporal variation of ^{137}Cs for different diffusion coefficients in Meuse river (a) Liege and (b) Maastricht

radioactive concentration at Maastricht and Liege for these two diffusion coefficients and variable diffusion. Although the peak values in Maastricht decrease with an increase in diffusion, the arrival/end stay essentially similar. Along with the diffusion in the Meuse River, the higher diffusion coefficients in the Albert Canal increases the radioactivity flux from the river. This can be seen in Figure 3.22b, where the temporal variation in Liege (prior to connection with the Albert Canal) shows a less significant fall in peak value.

3.7.4.2 Effect of Wind Speed

The wind speed plays a role in the distribution of the radionuclide deposition due to atmospheric releases. As discussed earlier, a higher wind speed will result in a widespread deposition of the radionuclides and thus decreasing the value of point depositions. In order to study the effect of different radionuclide distribution on its transport we consider three wind speeds of 1,3 and 5 m/s for the meteorological conditions. Figure 3.23 shows the temporal variation of radioactivity in the Albert Canal and Meuse River. It is expected that the peak values have decreased in both the Albert Canal and the Meuse River as the wind speed increases. However, the difference in the arrival/end times

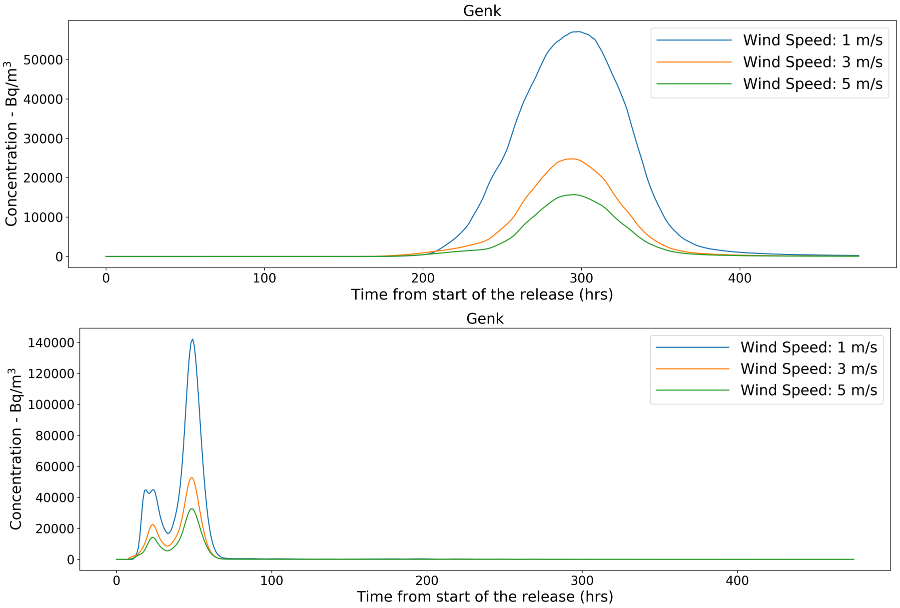

Fig. 3.23: Temporal variation of ^{137}Cs for different wind speeds in (a) Meuse river at Maastricht and (b) in Albert Canal at Genk

for higher wind speed in case of Albert Canal is significant in comparison to Meuse River. The radioactive plume arrives at Genk (Albert Canal) for 1 m/s wind speed almost 3 days earlier than that of higher wind speeds, whereas it reaches only couple of hours before at Maastricht (Meuse River). This can be attributed to the higher diffusion in the canal due to higher spatial variation in concentration.

3.7.4.3 High Flow study – Effect of time of deposition

In the high flow scenario (i.e., Peak Flow), the discharge in the river at the time of release becomes important. This can be seen in the case of real scenario (section 3.7.2), where the arrival of plume is faster. To evaluate the effect, we vary the start time of the release in the nuclear power plant, such that they are deposited at different discharge values in the river during the rise and fall of the hydrograph. This is illustrated in Figure 3.24, that shows the discharge in the Meuse River considered for high flow scenario. Here, as the first simulation, start of deposition begins (i.e., the beginning of the rising limb) at the 210^{th} hour in the hydrograph (Figure 3.24). The simulations are then carried out for the start of release every 48 hours (beginning with the 210^{th} hour) in the

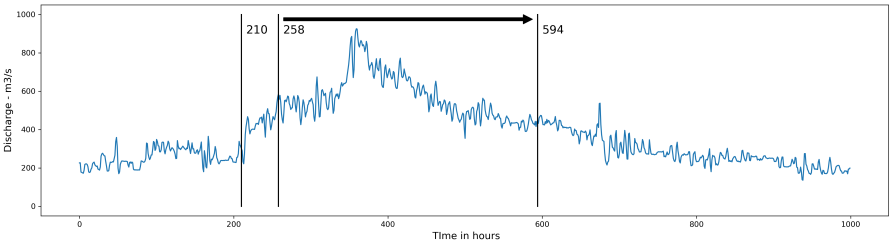

Fig. 3.24: The hydrograph of Meuse river at Amay chosen to study the effect of time of deposition starting from 210^th hour till 594^th hour for every 48 hours

hydrograph until the 594^{th} hour (fall of discharge).

Figure 3.25 shows the temporal variations (since the start of release) for atmospheric release at various times in the peak flow hydrograph at different locations in the Meuse River and the Campine Canal. As seen in Figure 3.25a, the time for the peak concentration in the Albert Canal increases as the radionuclides are released during the fall of the discharge limb (i.e., from 402 to 594) in the Meuse River and decreases for the rise in the discharge limb (i.e., from 210 to 306). However, the difference during the rise in the discharge limb is less pronounced than during the fall. The period with higher concentrations (referred to as residence time from hereon) at Genk increases from 104 hours (i.e., released at the 210th hour) to 154 hours (i.e., released at the 594th hour) (Figure 3.26b). While in the Meuse River, the period of high concentration decreases as it reaches peak discharge and then increases again (Figure 3.26a). For the arrival times of the peak concentration, the first simulation (i.e., at the 210th hour) is the one that arrives later than the others. Moreover, the peak value released at the 258th hour arrives before the 546th and 594th hour. Such variation in the Meuse River is due to the residence time of the plume (i.e., typically within a couple of days), whereas the hydrograph extends up to 16 days. The plume deposited at the 210th hour has flushed out of the Meuse River even before the peak discharge is reached. Therefore, the residence time in the Meuse River decreases as it reaches peak discharge and then increases again. At Neerpelt (Bocholt-Herentals Canal) the peak value appears earlier during an increase in discharge and later during a decrease in discharge. This is primarily due to the controlled discharge into the Zuid-Willemsvaart canal.

As seen in Figure 3.26, although the periods of high concentration in the Meuse River decrease during the rising limb of the discharge, similar trend does not happen at Genk for the Albert Canal. This might be explained by the fact that the Albert Canal, as mentioned in Section 3.7.4.1, is relatively sensitive to diffusion and that the diffusion is proportionate to shear velocity. For instance, the decrease in residence time in the Meuse River from release at 210th to 258th

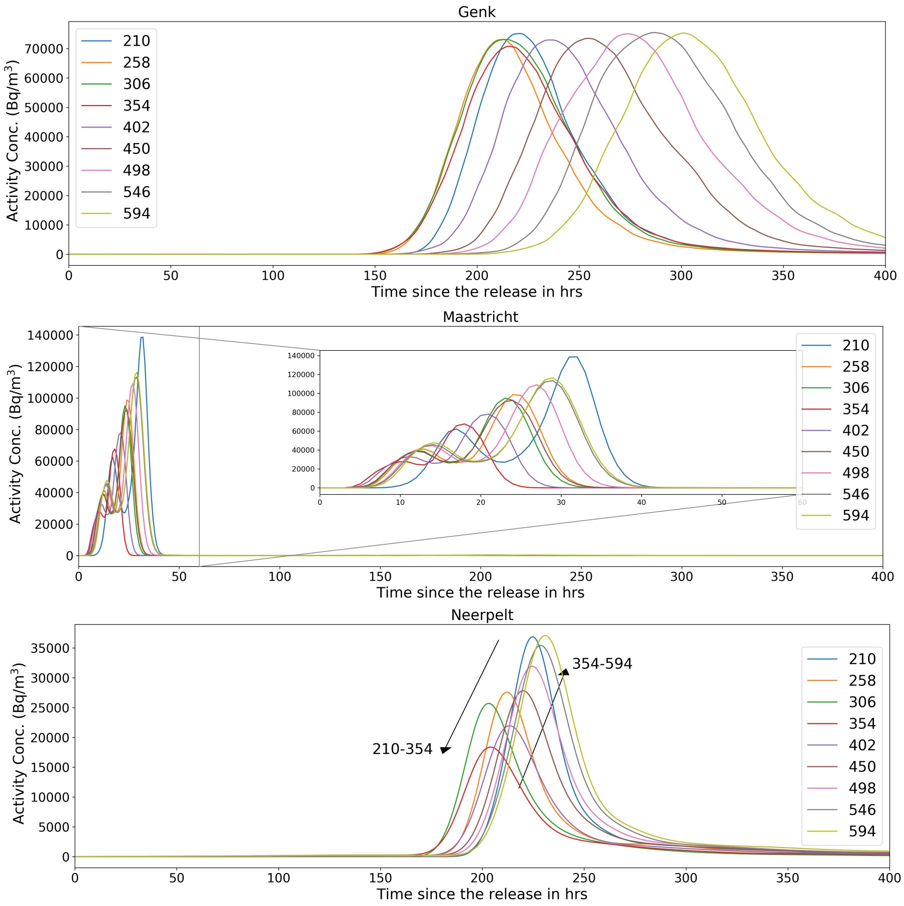

Fig. 3.25: Temporal variation of ^{137}Cs for different release time in the river in (a) Albert Canal at Genk (b) Meuse river at Maastricht and (c) Bocholt-herentals canal at Neerpelt

hour is 3 hours, which corresponds to the increased residence time (Figure 3.21a) due to higher diffusion. Additionally, it should be noted that the peak discharge hydrograph is a field measurement and therefore exhibits non-linear behavior during the rise/fall of discharge. Therefore, the variation in residence time will also depend on this. For instance, the rise in discharge between 258 to 306 (Figure 3.24) is small, thus resulting in a small drop in residence time than that between 306 and 354 (Figure 3.26).

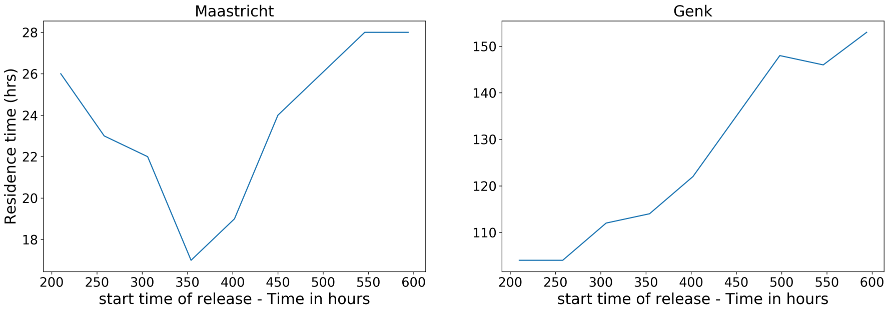

Fig. 3.26: Residence time for different release start time in (a) Meuse river at Maastricht and (b) Albert Canal at Genk

3.7.5 Dose assessment for population

To determine the impact of the releases of nuclear power plants in rivers, the dose due to ingestion can be used to provide some context to the simulations of activity concentrations. For that, the standard procedure suggested by the ICRP (2009) and ICRP (2018) is followed. Dose limits allowed in Belgium are based on European directives and on the recommendations of international organizations, that stipulates that the total annual dose resulting from the ingestion of drinking water must not exceed 0.1 mSv per year (FANC (2023)). This value excludes natural radiation or radiation used for medical purposes. As described in Section 3.6, the current water extraction points considered are located at Tailfer in the Meuse River and Herentals in the Albert Canal. It is worth emphasizing that because Tailfer is located upstream from Tihange NPP, the influence of Tihange nuclear power plant is not feasible.

3.7.5.1 Individual doses

As described earlier, since low flow scenarios have the maximum impact in terms of peak concentration and residence time, they are used to calculate the dose. However, the model allows to assess the impact at any point located on and at the sides of the river. In order to quantify the impact of the radioactive release during low flow scenarios, an additional location placed at Haccourt (in the Albert Canal) and Maastricht (in the Meuse River) are also selected to calculate the dose (For location, refer to Figure 3.8). Figure 3.27 shows the temporal evolution of the cumulative dose and the final dose for releases from Chooz.

Figure 3.27 shows that the cumulative dose of ^{137}Cs in the Meuse River basin and Campine canals is far lower than the regulatory limit of 0.1 mSv. Since the low flow scenario in either case does not reach Herentals, the dose

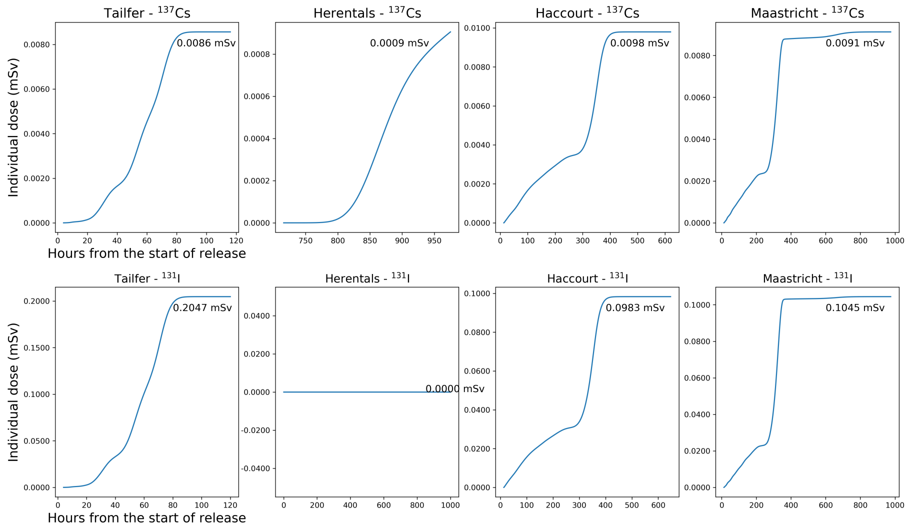

Fig. 3.27: Temporal variation of cumulative Individual dose at drinking water extraction points (Tailfer and Herentals) and hypothetical extraction points (Haccourt and Maastricht) for (a) ^{137}Cs (top) and (b) ^{131}I (bottom): Releases from Chooz Npp

here is extremely low, even for ^{131}I. However, other locations (Tailfer, Haccourt, and Maastricht) have relatively higher individual dose for ^{131}I. The doses in the hypothetical locations of Haccourt and Maastricht is close to 0.1 mSv, but the dose in Tailfer (which provides drinking water to Brussels) is double the valu 0f 0.1 mSv. This is not the case with ^{137}Cs, as the dose here are comparable (0.0086 – 0.0098 mSv). This phenomenon, as previously mentioned, is the result of ^{131}I decay. Nonetheless, the results show that for the Chooz releases, will have significant consequences on the water extraction in Tailfer. Furthermore, the cumulative dose here reaches such level within 3 days, whereas in other locations, the cumulative dose (even if around the limit) is reached after about two weeks.

Figure 3.28 shows temporal evolution of the cumulative dose, and the final dose for releases from Tihange. Herentals (about 100 km from the confluence) show little dose effects, as expected, thus it is safe to conclude that the true impact on drinking water is minimal for releases from Thiange. Again, ^{137}Cs does not exceed the limit. However, for ^{131}I, at Haccourt and Maastricht have a considerable influence, with levels three to four times higher than the permissible limits after about 5-7 days. Although, no water extraction occurs at these points, the values can be indicative of heightened vulnerability for individuals from other exposure pathways (such as fish consumption, recreational

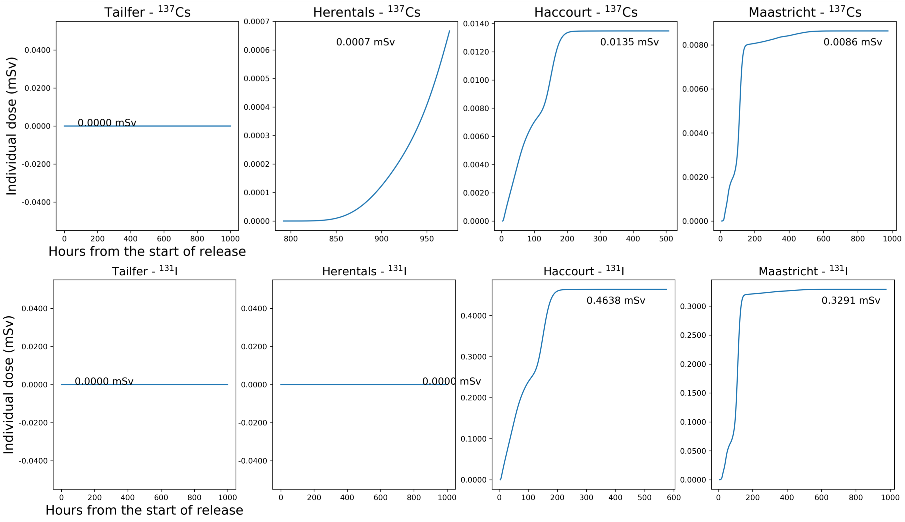

Fig. 3.28: Temporal variation of cumulative Individual dose at drinking water extraction points (Tailfer and Herentals) and hypothetical extraction points (Haccourt and Maastricht) for (a) ^{137}Cs (top) and (b) ^{131}I (bottom): Releases from Tihange NPP

activities, etc.).

3.7.5.2 Dose comparison to Fukushima disaster

Studies regarding the dose estimation regarding the contamination of drinking water occurring due to Fukushima releases has been calculated. Since, we derive our hypothetical scenarios from Fukushima disaster, the dose calculated here are compared with those calculated in this study. Miyatake et al. (2019) estimated the thyroid equivalent dose due to drinking water for ^{131}I consumption for adults to be from 0.1 mSv to 3.9 mSv (corresponds to 0.16 effective dose) and Murakami and Oki (2014) reported effective doses of ^{134}Cs and ^{137}Cs to be 0.12, 0.006, and 0.001 mSv for citizens of Fukushima City, Tokyo, and Osaka. In this study the calculated dose at Tailfer (for releases from Chooz) is approximately 0.2 mSv for ^{131}I and 0.008 mSv for ^{137}Cs. The maximum dose estimated was at Maastricht with 0.46 mSv for ^{131}I and 0.0135 mSv for ^{137}Cs. The maximum dose estimated was at Maastricht with 0.46 mSv for ^{131}I and 0.0135 mSv for ^{137}Cs. The values obtained here are in accordance with the maximum doses of 0.16 mSv indicated in the Fukishima releases. This implies that the radioactive exposure risk from drinking water (at Tailfer) are comparable to the levels seen in the Fukushima disaster scenario.

3.7.5.3 Population dose

The population doses are calculated from the individual doses estimated for releases from Chooz NPP at Tailfer, which supplies water to the Brussels region. Since individual doses at Herentals (supplies water to Flanders) for releases from both NPPs are exceedingly low, they are not included here. The determination of carcinogenic effects is based on dose-effect relationships derived from epidemiological evidence (Picano and Vano (2011)). The population dose calculated for the consumption of drinking water from Tailfer is 220 manSv in the Brussels region. This corresponds to a 5-10 % increased chance of cancer for 220 people in a 1.2 million population. This indicates that 1 in 6,500 people in the Brussels region has an increased chance of risk due to the radiation exposure from drinking water at Tailfer. The radiation exposure to low individual doses (<100 mSV) is still not fully understood, especially for long term effects. Therefore, the doses and cancer risks calculated in this study will be essential information for countermeasures and to monitor the population for long term health effects.

3.8 Conclusions

The study evaluates the potential impact of radioactive releases at the Chooz and Tihange nuclear power plants on the aquatic systems in the Meuse River basin. An advection-diffusion-decay model is developed in order to simulate the transport and dispersion of ^{131}I and ^{137}Cs radioactivity. For this, hypothetical accidents at nuclear power plants are considered for worst-case contamination scenarios based on past incidents such as Fukushima. The JRODOS atmospheric model is used to obtain the radionuclide fallout in the Meuse River basin. In regard to hydrodynamic conditions, two flow scenarios (low and high flow scenarios) are considered. The results show varying contamination levels in different canals and rivers, with implications for population exposure through drinking water.

In comparison to the canal system the radioactivity concentration in the Meuse River declines within days. Notably, radioactive transport in the Albert Canal is slower, particularly in low flow scenarios. Furthermore, in the low flow scenario, it is observed that the radioactive plume from connected canals reached the downstream region of the Albert Canal faster. In general, the low flow scenario had a higher peak concentration and longer residence times for both radionuclides. However, high flows in the Albert Canal cause a shift in flow direction in the Dessel-Kwaadmechelen Canal, resulting in recontamination of the Campine Canal after the initial plume has passed. The complex network in and out of Albert Canal has the potential to recontaminate not just the canals but also the Meuse River, as shown in the case of ^{131}I during low flows.

The distribution of ^{131}I in the Meuse River and Campine Canal varies from that of ^{137}Cs, due to its larger release amount and shorter half-life. Despite the tenfold increase in the initial release of ^{131}I compared to ^{137}Cs, its rapid decay results in substantial reductions in concentration over time. Initial contamination levels for ^{131}I are higher, with peak concentrations around 7.9 MBq/m^3 after four days, an order of magnitude greater than ^{137}Cs. The faster decay rate of ^{131}I leads to a concentration lower than the recommended limit in the Campine Canal within 20-27 days, except for the Albert Canal. The ^{131}I concentrations here remain reasonably high, but no plume from connecting canals can be observed for the low flow scenario due to longer transport time. Furthermore, the radioactivity concentration in Albert reduces fourfold within a couple of weeks. The release scenario at Chooz, which is located in the upstream stretch of the river, results in more affected areas in the Meuse River than the Tihange. The initial arrival of radionuclides from Chooz to Maastricht in the Meuse River is delayed compared to Tihange, resulting in lower peak concentrations. However, areas close to Chooz NPP (i.e., upstream reach of the river) show significant radioactivity concentrations.

Individual dose are calculated to assess the impact of low flow scenarios on peak concentration and residence time. The study highlights the significant consequences of releases from the Chooz NPP, particularly at Tailfer (which supplies water to the Brussels region), where the dose exceeds the permissible limit, necessitating immediate action. The results show that while the cumulative dose of ^{137}Cs in the Meuse River basin and Campine canals remains below the 0.1 mSv limit, the doses for ^{131}I at hypothetical locations like Haccourt and Maastricht approach the 0.1 mSv limit . Comparatively, releases from the Tihange NPP show minimal impact on drinking water, with ^{137}Cs levels below the limit, but an impact of ^{131}I at hypothetical sites can be seen. The calculated population dose of 220 Sv corresponds to a 5-10% increased cancer risk for 220 individuals in a population of 1.2 million.

A future improvement for the model is to use detailed field measurements for radionuclide concentration in order to validate the model and estimate the diffusion coefficients. This validation process would help to ensure that the model is accurately representing the real-world behavior of radionuclides and would also provide a more precise estimate of diffusion in the canal systems. Additionally, coupled sediment transport and bed evolution models can be beneficial in investigating the deposition and resuspension of sediments, which can also improve the model's accuracy. In this regard, sediment characteristics and concentration measurements will be necessary in order to set up the model. Which can then be used for long-term studies of the Meuse River basin.

Chapter 4

A multiscale 1D-2D coupled model of the Scheldt Estuary, Rivers, and the European continental shelf

This chapter is based on the following paper:
Patil, A., Perez, F., Lambrechts, J., Draoui, I., Deleersnijder, E., 2024. *A Multiscale 1D-2D Coupled Model Of The Scheldt Estuary Rivers And The European Continental Shelf*, https://doi.org/10.59490/coastlab.2024.692.

Abstract

This section presents a model for simulating the interaction of river influxes with tidal propagation in region of varying complexity for the Scheldt basin (river, tributaries and estuary) and the European continental shelf. While the domain for inland rivers is one-dimensional and extends until the limit of tidal influence, the estuary and shelf region are dealt by means of two-dimensional equations. Within this region, there exists a hydraulic structure in one of the Scheldt tributaries (Dyle River), that is implemented to simulate the bidirectional flow of the tide. In this model a tidal forcing at the shelf break, meteorological forcing at the free water surface and hourly discharges for the rivers and tributaries at the upstream boundaries are applied. Using this, the coupled model was firstly calibrated for the Manning coefficient for a relatively quiet period. Then it is extensively validated using available measurements for simulations in the month of January (2021), which is generally marked by strong tides. Moreover, the shelf region of the model was evaluated with the existing literature for the harmonic analysis of the dominant M_2 tide. The simulated results show good agreement with a RMSE under 0.3 meters for the measured water levels.

4.1 Introduction

The Scheldt basin is a complex system with the tide propagation from the North Sea and the influx from the rivers and tributaries that merge in the estuary to form a transition region. Such systems, in part or in combination are primarily impacted by tides, wind and hydrological processes, including fresh water flow. Therefore, in terms of modeling, it is essential to simultaneously represent the coastal region and the river flow, especially if the aim is to simulate the influence of strong tides (Fringer et al. (2019)). Moreover, the Scheldt system represents a domain of multiscale nature that deals with everything from the sea to the more shallow environment of rivers. The interaction of the physical forcings within such a domain can result in a highly variable distribution of energy (Arndt et al. (2007)).

Among the regions in the Scheldt ecosystems that can be characterized based on flow energy distribution, the freshwater riverine section, the estuary, and the European Continental Shelf are the most important ones. In contrast to the deep ocean, the currents over the European continental shelf (henceforth referred to as the shelf region) are stronger and can amplify the oceanic tide that can form several amphidromic systems (Reynaud and Dalrymple (2012)). Additionally, since the shelf region has exceptionally rich data, there has been a particular interest in modeling these amphidromic systems (Coughlan and Stips (2015)). On one hand, taking into account all the small-scale systems surrounding the shelf region, like the Scheldt, can make it very complex, without affecting the accuracy in the shelf region. The shelf hydrodynamics, on the other hand, has a large influence on the coastal ecosystems, where the environment is quite shallow. Therefore studies concentrating on shelf hydrodynamics, that can adequately represent the amphidromic system, do not require to consider such small-scale systems. But in terms of water quality, the fresh water systems tend to have an influence on coastal water, as can be seen in the case of salinity (Lacroix et al. (2004)).

The interaction of the tidal motion from the shelf region with the fresh water flow in the Scheldt estuarine part produces a unique ecosystem. Therefore, the few studies that have been conducted to capture the multiscale nature of the Scheldt basin are employed to examine water quality mainly in the estuarine region (Arndt et al. (2007),de Brye et al. (2010)). But the strong tidal influence of the shelf region can extend up to around 180 km from the mouth into the

Scheldt river and its tributaries before subsiding (van Rijn (2013)). Due to dissipative processes, the tidal amplitude gradually decreases upstream of the river and fresh water dynamics begins to become predominant. Also, particular consideration needs to be given to the hydraulic structure in order to accurately represent the flow dynamics in one of the tributaries, the Dyle River.

In this study, we develop a model that aims to simultaneously reproduce not only the flow in estuaries but also the flow in rivers and the European continental shelf. Therefore, in order to represent the river, the hydraulic structure module is implemented in the discontinuous Galerkin finite element method for the tidal motion. Later, the model simulation is compared for the estuary and rivers, including tributaries, using measurement data that includes a period of strong tides in 2021 (January). The amphidromic system derived based on measurements are used to assess the model's performance in the shelf region.

4.2 Multi-scale Model

The upstream limits of the domain were defined based on the location of hydrometric stations in order to use discharge information for the definition of boundary conditions in the model. Most of these stations are located upstream, at the end of the tidal zone for the Scheldt basin. The downstream boundary of the model coincides with the shelf break in the North Atlantic Ocean. While the upstream boundary conditions were chosen according to the availability of high-quality measurements. The boundary in the sea was placed far away from the area of study in order to minimize its influence on simulations. The hydrodynamic conditions along the sea boundary were obtained from the global tidal models. However, these models can become inaccurate as they approach the shallow regions (de Brye et al. (2010)).

The entire system of the Scheldt in Belgium includes rivers, estuary, and the European continental shelf (herein referred to as the shelf region). The representation of such a system in a model involves a multiscale approach (Figure 4.1). In this regard, the domain can be divided into two sections: the first section is the tidal Scheldt rivers and their tributaries, and the second is the Scheldt estuary and the shelf region.

The first region comprises (1) the tidal part of the Scheldt River, which extends from Ghent to the Hemiksem, with a width increasing from 50 m at Ghent up to around 500 m at the Hemiksem and (2) the tributaries of the Scheldt: The Durme, Rupel, Dyle, Kleine Nete, Grote Nete, and Zenne (widths ranging from 10 m), whose starting points are placed upstream the tidal zone. Since the variation of the hydrodynamic variables across the river section can be neglected for the rivers inside the first region, we use the one-dimensional section averaged equations for the representation of flow and transport. The

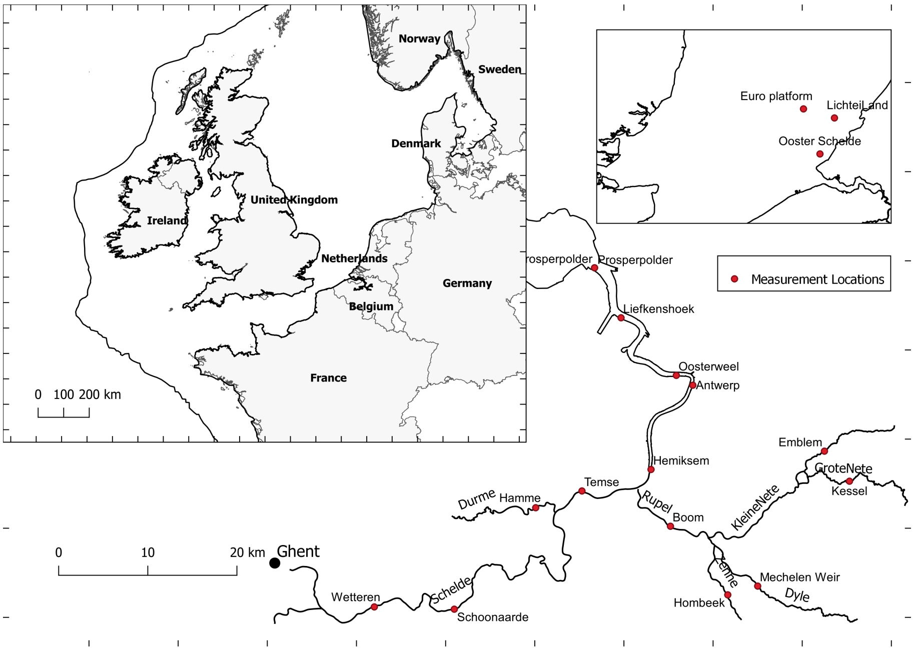

Fig. 4.1: Model domain for the one-dimensional component that includes the Scheldt River and its tributaries and the two-dimensional part that includes the Scheldt Estuary and the Shelf Region, with the measurement locations used for comparing numerical results with field data

second region extends from Hemiksem (just after the confluence with Rupel) up until the shelf break. The mouth of the estuary is roughly 8 kilometers wide at Vlissingen. In this region, the flow circulation is predominantly two-dimensional. The measurements inside the estuary show that during flood and ebb tides, the water flows through different pathways. Therefore, in this region, the simulation of flow and transport is done by using two-dimensional depth-averaged equations. In order to represent a continuous transition between the rivers and the estuary-sea, both regions are connected.

4.2.1 Coupled Hydrodynamics Module

In the first region, the Saint-Venant equations are formulated in terms of discharge (Q) and cross-sectional area (A) in Eq. 4.1-4.2 (derived from (2.1) - (2.2)):

$$\frac{\partial A}{\partial x} + \frac{\partial Q}{\partial x} = s \tag{4.1}$$

$$\frac{\partial Q}{\partial t} + \frac{\partial}{\partial x}(\frac{Q^2}{A} + \frac{P}{\rho}) = -gA\frac{\partial h}{\partial x} - gAS + \frac{F}{\rho} \tag{4.2}$$

Where, t is the time, x is the spatial coordinate along the river, g is the acceleration due to gravity,s is the source term, h represents the water depth to the deepest point in cross section, $P = \rho g \int_0^H (H - z) b dz$ is the hydrostatic pressure force, $F = \rho g \int_0^H (H - z)\frac{\partial b}{\partial x} dz$ is the along-flow component of the pressure force resulting from the width variation, and S is a frictional term estimated according to the Manning formula, i.e.,

$$S = n^2 \frac{Q|Q|}{A^2 H^{*4/3}} \tag{4.3}$$

In the above relation, n is the Manning coefficient,$H^* = \frac{A}{b^*}$ is the effective depth and $b*$ is the free surface width. The cross-section A depends on the riverbed elevation profile and the free water surface level (η) at position x. The domain is divided into line segments, and the solution is then discretized at each elemental node. On each node of the discretized elements, the cross-section profile for the rivers is extracted from the bathymetric data collected by ‘Flanders Hydraulic Research’. Hourly discharge measurements are applied to the upstream node boundary of each river. At the confluence points of the rivers, a bifurcation solver is used. The existing hydraulic works are also included in the discretization, and they consider the changes in direction and different submersion conditions.

The second component of the domain is simulated using two-dimensional depth-averaged equations. The shallow water equations here are formulated in terms of the velocity (u) and the actual water depth (H) at a position of x and y in Eq. 4.4-4.7:

$$\frac{\partial U}{\partial t} + \nabla . F(U) = G(U) \tag{4.4}$$

Where,

$$U = \begin{bmatrix} \eta \\ Hu \\ Hv \end{bmatrix} \tag{4.5}$$

$$F(U) = \begin{bmatrix} Hu & Hv \\ Hu^2 + g\frac{H^2}{2} - H\nu\frac{\partial u}{\partial x} & Huv - H\nu\frac{\partial u}{\partial y} \\ Huv - H\nu\frac{\partial v}{\partial x} & Hv^2 + g\frac{H^2}{2} - H\nu\frac{\partial v}{\partial y} \end{bmatrix} \tag{4.6}$$

$$G(U) = \begin{bmatrix} 0 \\ -g\tau_x + gH\frac{\partial h}{\partial x} + fv \\ -g\tau_y + gH\frac{\partial h}{\partial y} - fu \end{bmatrix} \tag{4.7}$$

$U = (u, v)$ is the depth averaged horizontal velocity, ν is the horizontal eddy viscosity, f is the Coriolis factor, and τ is the bed shear stress as represented in Eq. 4.7.

$$\tau = n^2 \frac{Hu|Hu|}{H^{7/3}} \tag{4.8}$$

where n is the Manning coefficient. The domain here is represented by an unstructured mesh consisting of triangular elements (28,000 triangular elements), as presented in Figure 4.2a. Since the domain of interest is the Scheldt estuary, a finer mesh is used in the upper estuary and the southern bight of the shelf area (Belgian Coastal Region) (Figure 4.2b). Here, elements with a maximum width of 750 m are used. For shallower regions, such as the lower estuary, the maximum width size of the elements is around 100 m (Figure 4.2c). Since computational time is of importance, the mesh size is optimized. The bathymetry of the region was obtained from EMODnet. The boundary conditions imposed at the shelf break were obtained from the simulations of elevation and velocity harmonics done by the global ocean tidal model (TPXO9.1) (Egbert and Erofeeva (2002)). For the meteorological forcing, wind velocities (10 m above sea level) were obtained from the Copernicus climate database (Hersbach et al. (2020)).

For the connection between regions, a boundary-connected coupling based on flux continuity is adopted. The hydraulic structures are implemented by using a flux term that allows to represent the stage-discharge relationship in the discontinuous Galerkin (DG) method. The whole system of equations is then solved using the DG method of the SLIM (Second Generation Louvain-la-Neuve Ice Ocean Model, www.slim-ocean.be) modeling framework (Bladé et al. (2012),Draoui et al. (2020),Draoui et al. (2022)).

4.2.1.1 Hydraulic Structures: Influence of tides

The weir present within the zone of tidal influence of one of the Scheldt tributaries (i.e., the Dyle River) exhibits a bidirectional flow. For this, the one-dimensional DG method used to solve the shallow water equations is developed in order to incorporate additional modules for hydraulic structures. The DG method computes the state variables of one-dimensional governing equations ($U = [Area, Discharge]^T$) between the nodes of its non-overlapping elements using the Riemann problem solver (left and right nodes in Figure 4.3). For the implementation of the structure, at the node of this location, the Riemann problem solver is replaced by the stage-discharge equation for the weirs in order to compute the variables (center node in Figure 4.3).

The stage–discharge relationship calculates the discharge over the weirs as a function of the water levels upstream (H_{us}) and downstream (H_{ds}) of the structure (Figure 4.3) using Equation (1). Two conditions relating H_{ds}, H_{us},

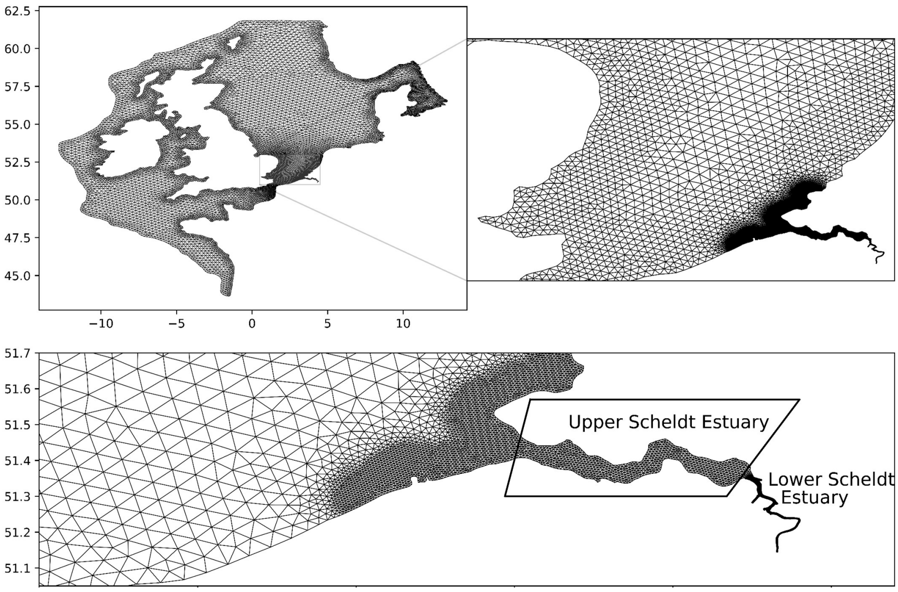

Fig. 4.2: (a) Unstructured triangular mesh generated for the discretization of a two-dimensional section of the model domain (Top left), (b) with higher mesh resolution in the upper (top right) and (c) lower estuary (Bottom).

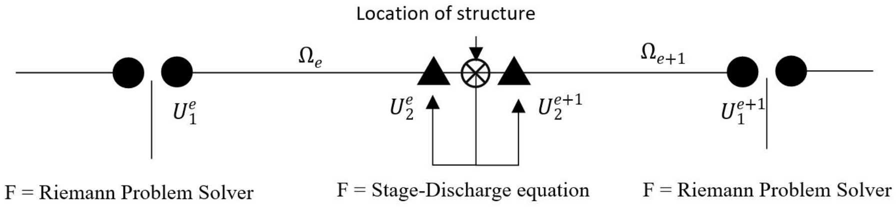

Fig. 4.3: Representation of the nodes in DG method and the treatment of flux by stage-discharge relationships for the imposed discontinuity at the location of a hydraulic structure.

and H_w are applied in order to determine whether the downstream water level influences the upstream flow

$$Q_{stage} = \begin{cases} C_1 W(H_{us} - H_W)\sqrt{(H_{us} - H_W)} : \frac{H_{ds}-H_W}{H_{us}} < \frac{2}{3} \quad Free \quad flow \\ C_2 W(H_{ds} - H_W)\sqrt{(H_{us} - H_{ds})} : \frac{H_{ds}-H_W}{H_{us}} \geq \frac{2}{3} \quad Sub \quad flow \end{cases} \tag{4.9}$$

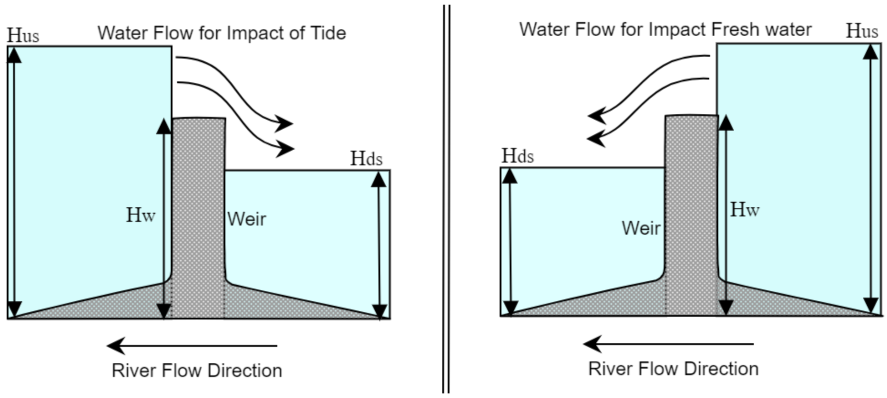

Fig. 4.4: Schematic of the weir and the terms corresponding to the computation of the discharge in the weir equations.

Since the DG method transfers information in both directions, the flow characteristics are inherently bidirectional. In the stage discharge relationship, the water level variables are employed according to the direction of dominant flow, i.e., the side with the highest water level becomes H_{us} and the lower level is H_{ds}, as illustrated in Figure 4.4. Consequently, the flow of water will always be from a higher water level to a lower one, making it possible to calculate the flow across the structure in both directions. Since the DG method is less sensitive to flux treatments, the model handles the transition from one direction to another quite efficiently.

4.2.2 Model Calibration

The model is calibrated for the Manning coefficient with observed water level data during a relatively calm summer period (July 2021). During the calibration, it was found that using two different Manning coefficients for the two-dimensional and one-dimensional parts yielded better results. In the case of hydraulics structures, since the dimensions of the structure are not available to the author, the model is calibrated for the weir height for the measurements done upstream (to river flow) the structure.

The simulation results for the two locations of the measurements used to calibrate the model—Euro-platform (2D part), which is located close to the shore, and Schoonarde (1D part), which is located upstream of the Scheldt River—are presented in Figures 4.5a and 4.5b. The figures in this study show the water levels in their original reference system of measurement, where TAW (Tweede Algemene Waterpassing) refers to the Belgian reference system and NAP (Normaal Amsterdams Peil) refers to the Dutch reference system. The

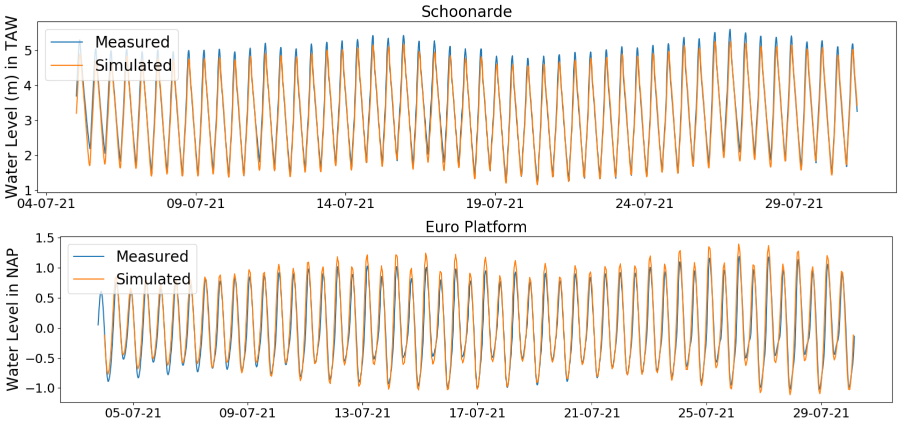

Fig. 4.5: (a) Euro-Platform : comparison of simulated and measured water levels and (b) Schoonarde: comparison of simulated and measured water levels located at the upstream reach of the river (Bottom): location used for model calibration.

root–mean–square error (RMSE) was used to assess the accuracy of the model. These criteria are defined in Eq. 4.10.

$$RMSE = \sqrt{\frac{\sum(M - D)^2}{n}} \tag{4.10}$$

where D is the measurement data, M is the corresponding modeled data and n is the total number of pairs. The RMSE value obtained for Euro-platform is 0.17m and that of Schoonarde is 0.21 m, and the calibrated Manning coefficient was 0.03 and 0.028 $\mathrm{m}^{1/3}\mathrm{s}$ for two-dimensional and one-dimensional parts respectively. These small differences in the RMSE indicate that the model achieved good performance.

4.3 Results and Discussion

The model was assessed by comparing the model simulations with measurements located along the rivers, the estuary and the Belgian coast for the month of January 2021. All the measurement locations used for validation are presented in Figure 4.1. In the estuary and the river, the majority of the measurements used for validation are water level, except at Oosterweel, where both the direction and velocity of water flow are used for comparison. On the other hand, the harmonic data comparisons for the dominant M_2 tide were used to access the model performance on the European continental shelf.

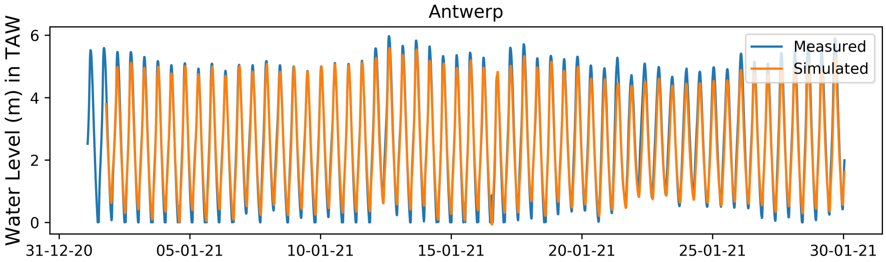

Fig. 4.6: Comparison of simulated and measured water levels at Antwerp for model validation

4.3.1 Scheldt Estuary

During the model validation, the simulation of the water levels, velocity and directions was evaluated by comparing their magnitudes against measurements. The evaluation period corresponds to January 2021. All the locations where measurements are available are presented in Figure 4.1.

Figure 4.6 shows the water level comparison at Antwerp and Figure 4.7 shows the flow velocity and 4.8 the direction at Oosterweel which is located close to Antwerp in the Scheldt Estuary. Note that due to lack of measurement value, the comparison of velocity magnitude and direction is not shown between January 7th and January 14th. Figure 4.6 illustrates the good agreement for the water level in Antwerp with an RMSE value of 0.28 meters. The differences in water level seen in Figure 4.6, however, might be the result of less-than-accurate boundary conditions or the need for a better wind parametrization in the shelf break (Gourgue et al. (2015)), that can be attenuated in such relatively shallow regions. Nonetheless, It can be seen in Figure 4.6 that the model reproduces the shifts caused by the storm surge that occurred on January 12 and 13th. For the Oosterweel measurements that are carried out at a position closer to Antwerp, the model prediction for both measurements are accurately represented, with the model is capable of representing the change in the water flow's direction (Figure 4.7 4.8). This shows that such variations in water level have no appreciable impact on the water flow characteristics, which are crucial for studies related to transport of pollutants (e.g., radionuclide transport).

4.3.2 Scheldt River

The Scheldt River simulation was validated using two measurement locations: Temse, which is closer to the estuary (downstream of the river), and Schoonarde, which is in the river's upstream reach(Figure 4.1). The results are shown in Figures 4.11b and 4.11a, respectively. The RMSE of the hourly water level com-

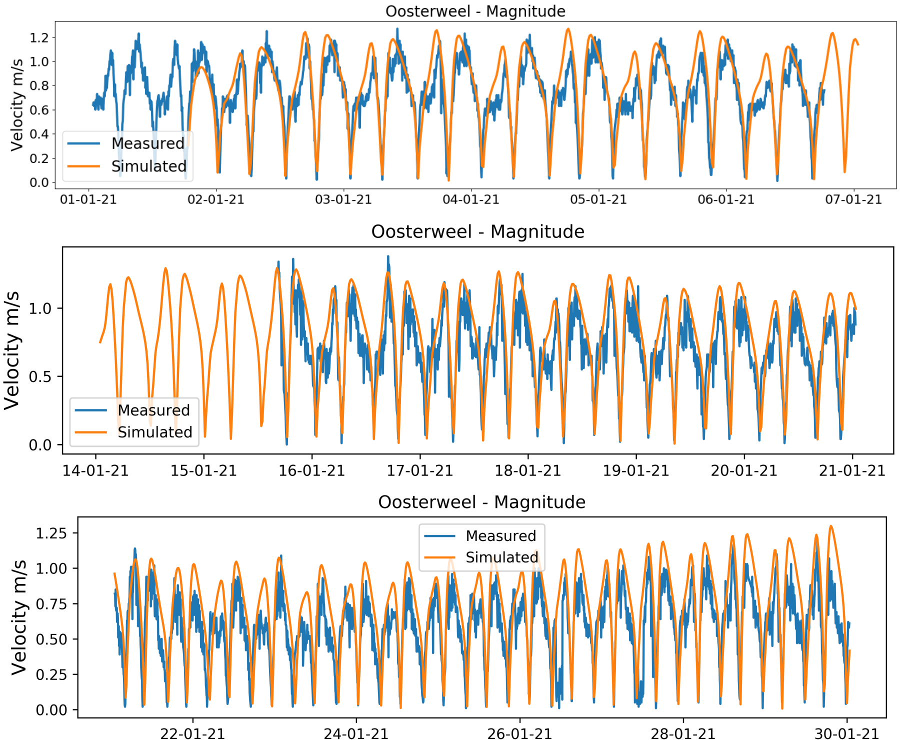

Fig. 4.7: Oosterweel: comparison of simulated and measured magnitude of velocity for model validation

Location	RMSE Value (m)	Scheldt Basin
Prosperpolder	0.26	Estuary
Liefkenshoek	0.25	Estuary
Ooster Schelde	0.12	Coast
Liechtland	0.14	Coast
Euro-platform	0.15	Coast

Table 4.1: RMSE values obtained for the model comparison in regard to water levels at other locations in the coast and estuary

parison between the measured and model values is 0.3 meters for Schoonarde and 0.24 meters for Temse. Among all the measurement stations in the Scheldt basin that were taken into consideration for comparison, Schoonarde had the highest RMSE value. The high value obtained at this place can be explained by the occurrence of a series of storms that happened after January 12th. Since the model predictions during calm periods are accurate, the results obtained

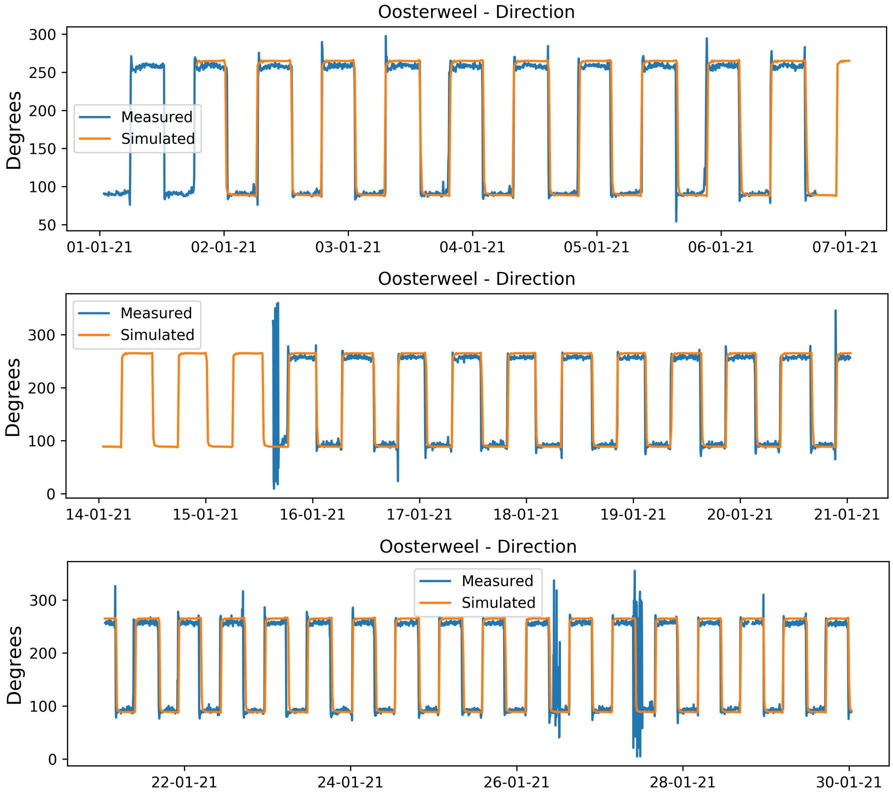

Fig. 4.8: Oosterweel: comparison of simulated and measured direction of flow for model validation

for this period could suggest that additional forcing, such as wind, needs to be included in one-dimensional simulations. On further observation of meteorological data, the wind speed over Schoornarde on January 12th reached up to 32 km/h in comparison to a maximum of 13 km/h during calm periods (NOAA Global Forecast System).

Overall, the model does represent the tides in the river and can simulate the shifts in water level due to the impact of strong tides in the Scheldt River. In fact, the model prediction for the peak values of both low and high tides is represented well in the case of calmer periods, with a maximum of 16 cm. For the period of strong tides the deviation is up to 50 cm, as shown in Table 4.2. A similar impact can be seen in regard to Temse, but with lower deviations compared to Schoonarde.

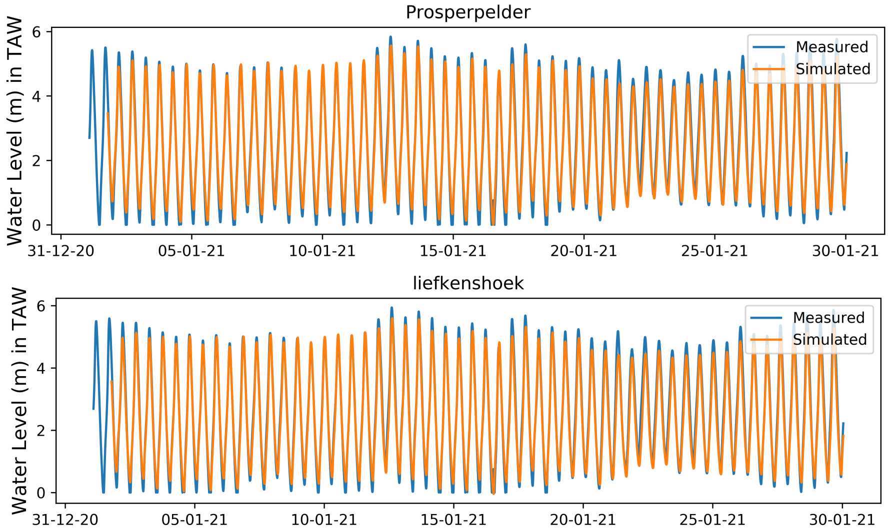

Fig. 4.9: Comparison of simulated and measured water level for model validation in estuary at (a) Prosperpolder and (b) Liefkenshoek

		Low Tide Peak			High Tide Peak		
	Date	Measured (m)	Simulated (m)	Error (m)	Measured (m)	Simulated (m)	Error (m)
Calm Period	05/01	1.73	1.73	0.00	4.83	4.70	0.13
	07/01	1.68	1.62	0.05	4.99	4.82	0.16
	09/01	1.52	1.51	0.01	4.77	4.80	-0.03
Strong Tide Period	12/01	2.53	1.99	0.54	6.12	5.73	0.39
	13/01	2.98	2.54	0.43	5.79	5.61	0.18

Table 4.2: Peak values of the measured and simulated water level for both the low and high tide shown in Figure 4.11a during the periods for calm and strong tides.

4.3.3 Scheldt Tributaries

There are several available measurements of the water level in Scheldt's tributaries, which were compared for accuracy. However, in this section, the measurements done at locations for farther-reaching tributaries, such as the Kleine Nete and the Grote Nete are shown. Additionally, water level measurements upstream and downstream of the structures in the Dyle River at Mechelen are presented for the hydraulic structure implementation in the model.

Figure 4.12a shows the water level comparison of simulated results and measurements at Emblem in the Kleine Nete River and Figure 4.12b shows the comparison of water level at Kessel in the Grote Nete (for location see Figure 4.1). Since these two locations are situated so far away from the sea, the influence of the tide is considerably reduced. This becomes even more apparent

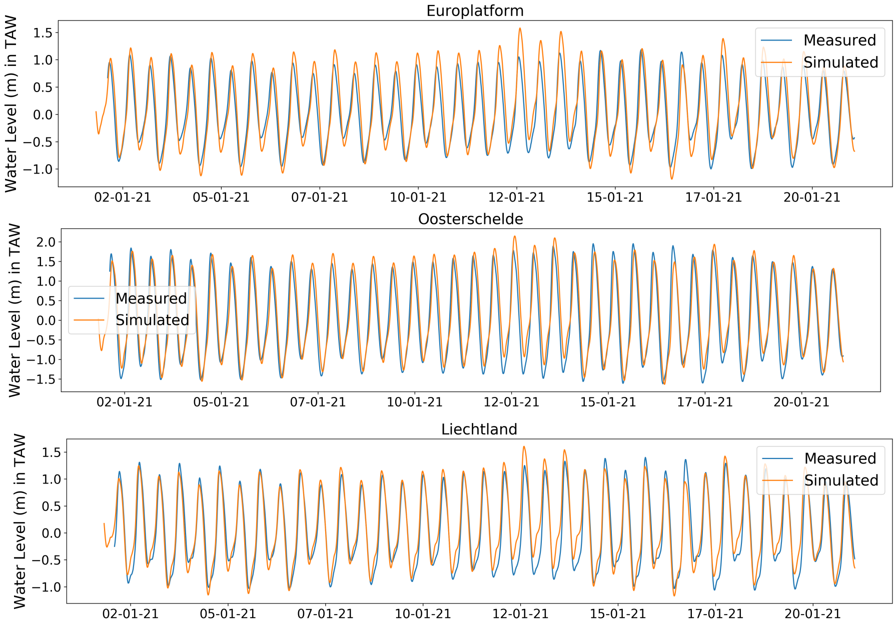

Fig. 4.10: Comparison of simulated and measured water level for model validation at the coast as (a) Europlatform, (b) Ooster schelde and (c) Liechtland

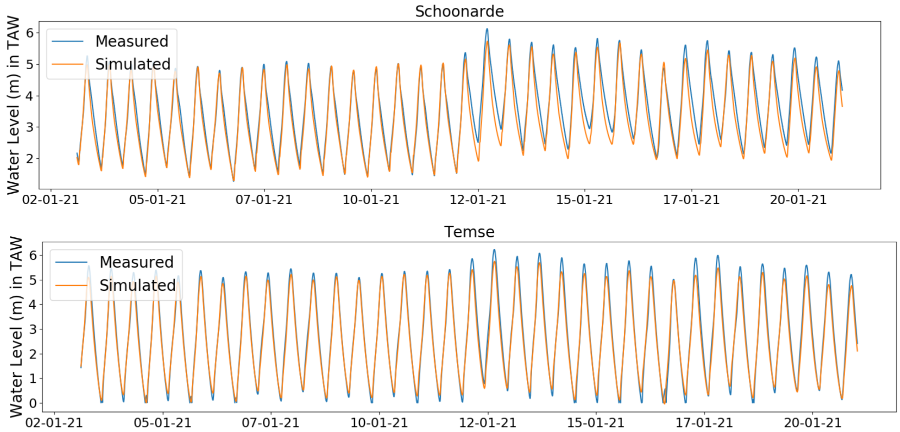

Fig. 4.11: Model comparison for the simulated and measured water levels in the Scheldt River at (a) Schoonarde located upstream (Top) (b) (Bottom) Temse located downstream

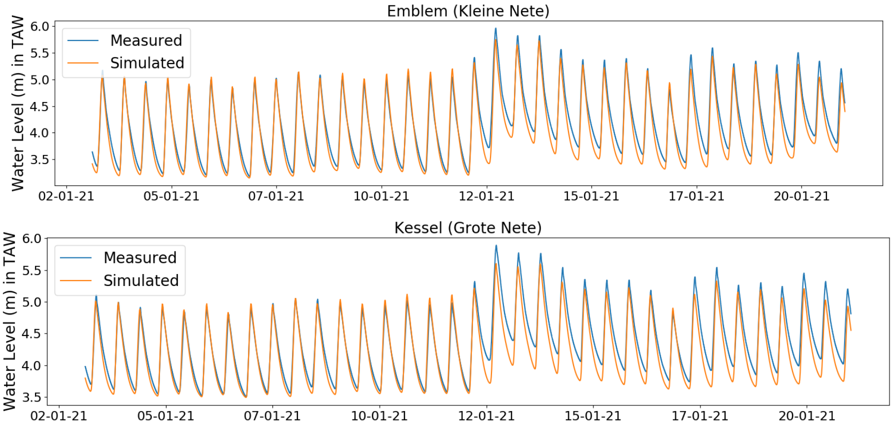

Fig. 4.12: Model comparison for the simulated and measured water levels in Scheldt tributaries at (a) Emblem in the Kleine Nete River (Top) (b) Kessel in the Grote Nete River (Bottom)

when looking at tidal range, where it is just around 1.8 meters here and about 5 meters near the confluence with the Scheldt River. At both locations, the root mean square error (RMSE) is approximately 0.15 meters, indicating a good agreement with the observed value. However, as we examine Figures 4.12a and 4.12b, we can see that the model has a slightly lower performance in the later phase (that is, following the January 12th tides) of the water levels. Since the effects of tidal influence have receded and the impact of river discharge increases, it is likely that lateral water sources not represented in the model—such as river runoff, point discharge flash floods originating from urban areas etc.—are the cause of the deviations. Nevertheless, with its low RMSE value, even for the distant measurement location, the model shows a good performance in representing the flow.

Figure 4.13a shows the comparison of water levels for the measurement located upstream of the river flow for the hydraulic structure and Figure 4.13b shows the comparison of water levels for that located downstream of the structure. Both measurements are located in close proximity to the structure. In contrast to the downstream measurements, the upstream water level (Figure 4.13a) show a relatively flat gradient at low tide, which shows the influence of structure that does not allow the water level to fall below a threshold value. With the calibrated model for the hydraulic structure, it can be seen that the model does predict the water levels rather well, with an RMSE value of 0.25 meters. The reason for deviation from measurements in the later phase (after the January 12th tides) is that the structures can be operated to change the

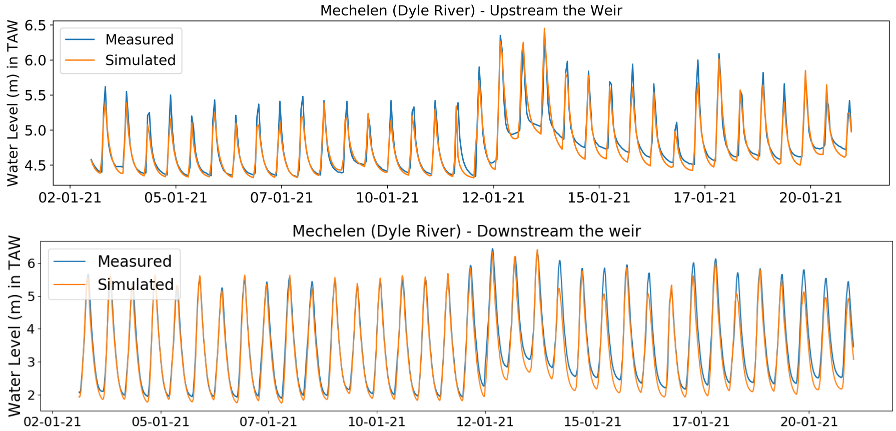

Fig. 4.13: Model comparison for the simulated and measured water levels in Dyle river at Mechelen (a) upstream the weir (Top) (b) downstream the weir (Bottom)

height, as evidenced by measurements where the water level can drop to up to 2.8 meters. Since the authors lack information on the operating rules, they are not applied in the model. But in the case of the water level comparison downstream of the weir, as shown in Figure 4.13b, a lower RMSE value of 0.21 is achieved than that of upstream measurements. A good performance both downstream and upstream suggests that the discharge calculation and implementation of the stage-discharge relationship in the DG method are quite accurate. Furthermore, a lower RMSE value downstream indicates that the operation of the structures has an effect on the water level upstream. Similar to the model results in the Kleine Nete and Grote Nete, the water level is underestimated at this location as well, which can also be attributed to the deficiencies of lateral discharge in the model.

4.3.4 European continental shelf

For the validation of the two-dimensional component of the model in the European continental shelf, analysis of the harmonic components for the M_2 tide was done. The predominant semi-diurnal lunar tide (M_2) gives a good first approximation of the tidal motion in the North Sea (Otto et al. (1990)). Consequently, the computed amphidromic points in these charts are compared to existing charts based on measurements reported in the literature (Figure 4.14).

The amphidromic system generated is generally well predicted, especially in the southern bight region (i.e., on the Belgian-Dutch coast). But the point at the southern tip of Norway shifts towards the western direction in comparison to

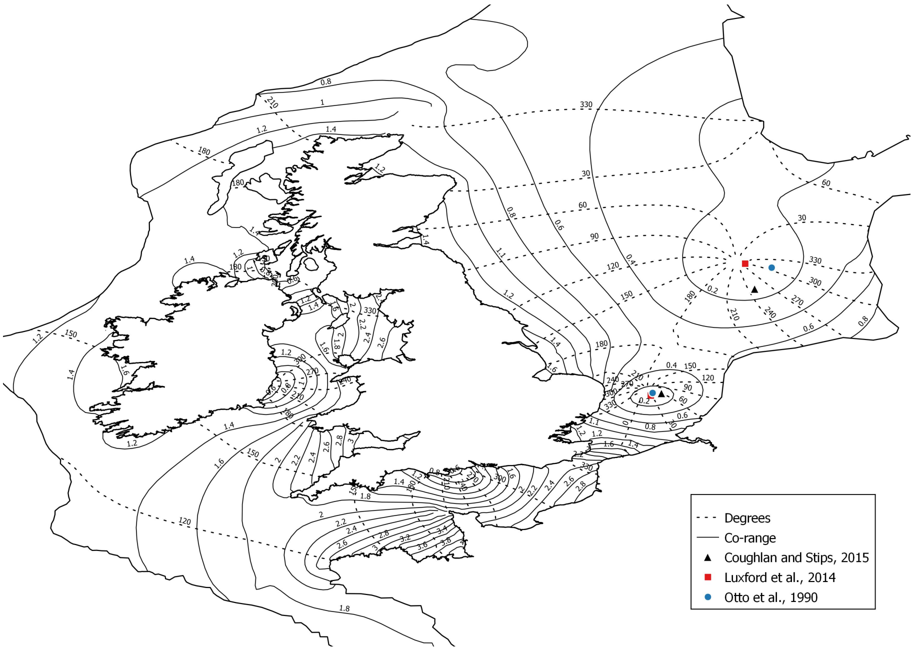

Fig. 4.14: Model comparison for the amphidromic points and model representation for the isometric lines of the co-phase (degrees) and co-range lines (amplitudes in m) for the dominate M_2 tide.

measurements reported in other studies (Coughlan and Stips (2015),Otto et al. (1990)), while it matches well with the chart reported by Luxford et al. (2014). Furthermore, the co-range (amplitudes) and phase lines were also compared with these charts, and good approximations were obtained, with approximated errors of less than 0.1 m in the southern bight and around 0.2 m in the other regions. The model tendency to shift the amphidromic point near the coast of Norway is possibly due to coarser mesh, which could lead to imperfect bathymetry representation. Since the Southern Bight region, which is close to the mouth of the Scheldt Estuary, is the focus of the transport model, it performs well in this regard thanks to the high-resolution mesh used for the simulation in this area.

4.4 Conclusions

A hydrodynamic radionuclide transport model was developed to simulate the fate of radionuclides in the Scheldt basin as a decision-support tool for emergency. Therefore, to avoid large computation costs, the rivers and their tributaries in the Scheldt Basin are modeled as a one-dimensional domain, and the estuary and European continental shelf are modeled as a two-dimensional domain. It was shown that the hydrodynamic model successfully simulated the water levels, velocity, and flow direction when compared with measurements in the estuary, coast, river, and tributaries, with a maximum RMSE value of 0.28 m. The hydrodynamic model was successfully validated on the European continental shelf using harmonic data for the dominant M_2 tide. Good agreement was observed for amphidromic points, especially at the coast near the Scheldt Estuary.

The simulation results were compared to the hourly measurements available in these locations, and it was shown that the model performs well and predicts the shifts in water level caused by storm surges. Though there are deviations from measurements that rise as the tide propagates upstream the Scheldt river, this does not imply that the model's accuracy is limited. But other physical phenomena, such as the effect of wind friction in one-dimensional domain, the lack of lateral inflows in these region and the operation regulation of structures, can also influence the flow dynamics. Nonetheless, it was demonstrated in the case of estuary dynamics that, despite variations in water level, the model performed well in computing the velocity components that represent the complex estuarine environment. In terms of hydraulic structure implementation, it is shown that the model accurately represents the impact of such a structure that is subjected to tidal motion. However, due to lack of data regarding the operational rules for the structures, variations from measurements, especially during low tides are observed. Furthermore, the model performs well in the southern Bight region but suffers slightly in the shelf region due to the larger mesh size.

Based on the model results obtained after calibration and validation, it is reasonable to state that the model results are in good agreement with measurements and perform quite well during calm meteorological conditions. As a result, SLIM can be coupled to a water quality module to simulate pollutant fate in such a vast system even for longer time periods that considers seasonal variations.

CHAPTER 5

Numerical Modeling for the releases of ^{137}Cs and ^{131}I in the Scheldt Basin from NPPs

This chapter is based on the following paper:
Patil, A., Perez, F., Lambrechts, J., Draoui, I., Deleersnijder, E. *Numerical Modelling for the Distribution of ^{137}Cs and ^{131}I in the Scheldt Basin after a Potential Nuclear Accident*, Journal of Environmental Radioactivity, vol. 280, Dec. 2024, p. 107568, https://doi.org/10.1016/j.jenvrad.2024.107568.

Abstract

Using the discontinuous Galerkin method in the SLIM modeling framework, we study the transport in the Scheldt basin and adjacent coastal area of radionuclides possibly emitted by Doel nuclear power plant in the aftermath of an accident. The contamination pathways taken into consideration are direct liquid releases into the water and deposition via the atmosphere. In past nuclear accidents, several radionuclides were released, among which, ^{131}I and ^{137}Cs were considered herein. The hydrodynamics and atmospheric conditions are selected to simulate the worst-case scenario in the domain of interest. The radionuclide deposition towards the North Sea results in ^{131}I and ^{137}Cs being transported to the Belgian coastal region. In case of deposition towards the river, radioactivity from upstream tributaries can reach the estuary within days.

Direct liquid releases spread downstream until the mouth of the estuary after about few weeks and extend upstream into the Scheldt River. In all cases, due to tidal influence, the estuary becomes most vulnerable, with radioactivity potentially circulating for over a month. Additionally, higher river discharge resulted in decreased radioactivity levels in the estuary.

5.1 Introduction

Predictive models to develop environmental strategies for intervention are critical in making rapid decisions to minimize the potential impact of a nuclear disaster. The contamination of water bodies, such as estuaries and rivers, after liquid radioactive releases coming from nuclear installations does not represent a threat to the environment and human health due to relatively low levels of activity. However, accidental releases such as those that happened during the Chernobyl disaster can become a concern. In Chernobyl, the radioactive contamination transported by the Pripyat river affected roughly 30 million people and eventually contaminated the Black Sea (IAEA (2006c)). The International Atomic Energy Agency (IAEA) has thus highlighted the need to have process-based models for radionuclide transport in regions that could be potentially affected by a nuclear accident (IAEA (2019)). The model simulations then provide useful information that allows efficient planning of human protection and environmental remediation measurements.

Early experiences with the use of transport models for radionuclides can be found in the work of (Prandle and Charnock (1997)), who simulated the transport of dissolved ^{137}Cs from the Sellafield (UK) nuclear fuel reprocessing plant into the European Shelf Sea (Irish Sea) and similar work has been done for La Hague nuclear fuel reprocessing plant (Breton and Salomon (1995)). In the case of other facilities in Europe, such as the two nuclear power reactors (Doel and Borssele; Figure 5.1) in the Belgian-Dutch Scheldt Estuary, the use of models as assessment tools is a priority for the nuclear operators and national regulators. The tidal currents here are often strong, with a tidal range that can reach up to 5 m. Because of this, the contaminants spread quickly upstream and downstream of the release point from the nuclear power plant.

Estuaries are subjected to marine influences such as tides, waves, and the influx of saline water and to fluvial influences such as flow of fresh water and sediments. Depending on the extent of these influences, the estuaries can be classified as high or low energy estuaries. High-energy or tide dominated estuaries are dynamic ecosystems shaped by strong tidal energy at the mouth compared to wave energy (Reynaud et al. (2018)). The tidal impact in these estuaries can reach hundreds of kilometers. Some examples of high-energy estuaries are Scheldt estuary in the European coast (Arndt et al. (2007)), Columbia River estuary in the USA (Kärnä et al. (2015)) and Humber estuary in the UK (Eke et al. (2021)). Radionuclide pollution transport in such high-energy estuaries is a challenging task because of the strong tidal currents with varying length and time scales (Periáñez et al. (2019)). Although efforts have been made to develop marine radionuclide transport models (Brovchenko et al. (2022),Park et al. (2017),Periáñez et al. (2021),Periáñez and Cortés (2023),Tsabaris et al. (2022)), specific consideration must be given to tide-dominated estuaries. This is because it is important to deal with all the subdomains (rivers, sea, and estuary) simultaneously. This study focuses on the Scheldt estuary, which is representative of tide-dominated estuaries.

The Scheldt Estuary is a transitional zone with a unique ecosystem that is influenced by the Scheldt basin rivers and the currents of the North Sea. While the influence of the tides extends up to around 180 km upstream from the mouth of the estuary (van Rijn (2013)), the rivers still affect the near-shore dynamics of the Scheldt Estuary (Lacroix et al. (2004)). Therefore, in order to simulate the fate of radionuclides in the Scheldt estuary, it is necessary to represent the circulation patterns in the European shelf region and the river hydrodynamics. However, the simulation of such a system is complex due to its multiscale nature (e.g., river, estuary, coast, and sea).

The contamination of water systems during an accident is not restricted to direct radioactive liquid releases from nuclear installations but also due to atmospheric releases in the form of radioactive wet and dry deposition. In past nuclear accidents, in addition to direct leaks into the ocean, wet and dry depositions resulted in a significant amount of radioactive contaminants in aquatic systems (Kawamura et al. (2011),Kobayashi et al. (2013)UNSCEAR (2021)). Besides, the circulation patterns and the release pathways, the characteristics of the source term (radioactive composition of the release) are equally important. It was found that ^{137}Cs and ^{131}I were the large contributor for short-term radiation exposure to humans (UNSCEAR (2021)). ^{137}Cs is a non-conservative radionuclide due to its adsorption property on sediment particles, and given its long half-life of 30 years, it usually lingers in the ocean for years (Behrens et al. (2012),Estournel et al. (2012),Prandle and Charnock (1997),Tsumune et al. (2012)).

This study introduces a computational model for simulating the ^{137}Cs and ^{131}I transport in the Scheldt basin (estuary, river, and European Shelf region). In this framework, two-dimensional shallow water equations are coupled with section-averaged river models. The model includes the advection by the currents and river flow, turbulent mixing in the estuary, and the radioactive decay of the radionuclides. The model is then employed for the simulation of radionuclide transport under hypothetical scenarios for radioactive releases from the Doel NPP located on the bank of the estuary. The scenarios in this study are chosen in such a way that they lead to a worst-case release condition in the Scheldt environment. As a result, the meteorological variables are all selected to meet this criterion. In order to demonstrate the model's capability to simulate the fate and transport of radionuclides, the salinity are compared with the field measurements.

5.2 Model setup

5.2.1 Model domain

The entire multi-scale system of the Scheldt in Belgium, including its rivers, estuaries, and shelf regions, as represented by the model's domain, is shown in Figure 5.1. The tidal part of the Scheldt river extends from Ghent to the mouth of the estuary at Vlissingen, with a width ranging from 50 m at Ghent to 8 km in Vlissingen. Due to the presence of the sluice upstream, the influence of the tide in the Scheldt river does not extend beyond Ghent. Therefore, the model domain for the Scheldt river is extended until Ghent, whereas all of its major tributaries, such as Durme, Rupel, Dyle, Kleine Nete, Grote Nete and Zenne are considered up to the limit of tidal influence.

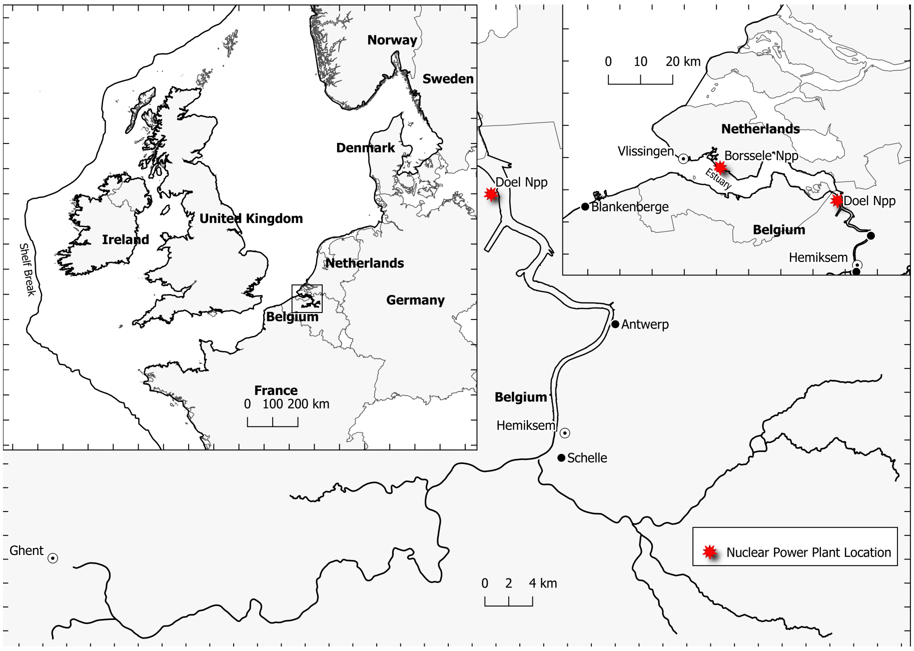

Fig. 5.1: Model domain for the one-dimensional region that includes the Scheldt River (from Ghent to Hemiksem) and its tributaries, along with the two-dimensional region that includes the Scheldt Estuary (from Hemiksem to Vlissingen) and the Shelf Region, with the location of NPPs.

5.2.2 Transport Module: Radionuclide Model

The radionuclides transport is simulated according to a Eulerian approach including advection, diffusion and decay at a constant rate. ^{137}Cs has a half-life of 30 years, while that of ^{131}I is just 8 days. The corresponding equations are:

For 1d domain:

$$\frac{\partial Ac}{\partial t} + \frac{\partial}{\partial x}(Qc) = \frac{\partial}{\partial x}(DA\frac{\partial c}{\partial x}) + S - \lambda Ac \tag{5.1}$$

For 2d domain:

$$\frac{\partial Hc}{\partial t} + \nabla.(Huc) = \nabla.(HD\nabla.c) + S - \lambda Hc \tag{5.2}$$

$$\lambda = \frac{ln2}{T_{1/2}} \tag{5.3}$$

where S is the source for the radionuclide under consideration, λ is the decay constant, and is calculated in terms of the half-life ($T_{1/2}$) of the radionuclide. The source term S here is used to define radioactive fallout or direct liquid releases. In the model, it is assumed that the radionuclides that enter the simulation domain are well mixed in the element where the release point is located. Other processes, such as biological and suspended sediment adsorption, are excluded. This assumption is valid for accidental releases where the duration of the simulation period is short, or in the case of radionuclides such as ^{137}I that do not tend to readily adsorb themselves to the sediments (Periáñez et al. (2019)). Studies have shown good agreement when ignoring such effects (i.e., adsorption on sediments) under these circumstances (Tsumune et al. (2012)). However, this assumption does not hold for long-term simulation where accumulation, settling, and resuspension plays a significant role for radionuclides such as ^{137}Cs. It is also worth noting that the adsorption property of ^{137}Cs to the sediment decreases significantly if the salinity increases (Wang et al. (2022)).

5.2.3 Salinity Model

The salinity model is simulated using the same set of equations as the radionuclide transport model, with the exception that the decay term is dropped and the source term is restricted to just saline liquid releases. The simulation units are expressed as practical salinity units (PSU). The changes in salinity caused by biological or chemical interactions can be neglected. Salinity is, thus, referred to as a conservative quantity that is merely transported by advection and diffusion processes and hence provides a good tracer of water masses. Furthermore, due to the available measurements of this variable, salinity becomes an ideal choice for the verification of the transport model.

In the model, the entering salinity of the river and its tributaries is set to zero. For inflow periods, the salinity at the shelf break boundary is prescribed to be 35, which corresponds to an average of climatology data and measurements (Lacroix et al. (2004)). The initial condition in the model is considered to be a linear salinity profile in the estuary that extends from the point of zero observed salinity in the Scheldt River near Hemiksem to the Belgian shore at a salinity level of 35. In the rest of the shelf region, a uniform salinity level of 35 is used as the initial condition, with zero salinity in the rivers and tributaries.

5.3 Hypothetical Scenario Definition

5.3.1 Releases and source term definition

Here, we are interested in using this model to evaluate the impact of accidental releases coming from the Doel nuclear power plant into the Scheldt estuary. The Doel NPP is located on the banks of the Scheldt estuary near Antwerp (Belgium), coordinated at $51^0 19'$ N $4^0 15'$ E (Figure 5.1). The source term (radionuclide composition) is restricted to ^{137}Cs and ^{131}I. These two radionuclides were selected based on the values established in the Fukushima disaster. Several hypothetical accidents occurring at the Doel nuclear power plant were considered and simulated. These scenarios are selected in order to have worst case conditions after atmospheric and direct releases in the Scheldt basin. The amount of radionuclides that are hypothetically released from the Doel NPP in this study is based on the Fukushima accident as reported by UNSCEAR (United Nations Scientific Committee on the Effects of Atomic Radiation) working committees (UNSCEAR (2021)). Table 5.1 gives a description of the releases that were reported to occur during the Fukushima accident:

Pathways	**Total Release (PBq)**	
	^{131}I	^{137}Cs
Atmospheric deposition	100-500	6-20
Direct release (March – April 2011)	9-13	3.5-5.6

Table 5.1: Total radionuclide releases as reported by UNSCEAR from the Fukushima nuclear accident to the atmosphere and as a direct release pathway into the aquatic environment.

For the atmospheric deposition source, the JRODOS atmospheric model (Raskob et al. (2016)) was used to determine the distribution of both the radionuclides and their activities on the surface of the Scheldt basin. The JRODOS has been previously utilized for assessments following the Fukushima Daiichi accident (Ievdin et al. (2012),Kovalets et al. (2014),Selivanova et al. (2023)). For this study, the radioactivity deposition results were obtained after an atmospheric release of 100 PBq in the case of ^{131}I and 10 PBq for ^{137}Cs during a release period of 6 hours. The release period is assumed based on observations and shows that most of the peak release is achieved within this period of time. In the case of the Fukushima disaster, the hydrogen explosions that occurred on March 12, 2011, led to peak activity concentrations in the atmosphere being detected within hours (Tsuruta et al. (2014)).

5.3.2 Meteorological conditions of the study area

The water currents and meteorological conditions of the Scheldt Estuary are quite variable. For our purpose, we consider a realistic combination of conditions that could deliver the maximum impact. Therefore, the simulation period starts on the first day of July (the summer period), when, in average the freshwater flows are low (the dry period). Moreover, the winds (Northwest winds) in the shelf region and water currents are generally more regular than in other seasons (Hossen and Akhter (2015)). During this period, the wind speed over the estuary can range from 0 and up to 3-4 m/s (Hossen and Akhter (2015)). In the Scheldt estuary, the maximum frequency in a year for wind direction occurs between $180^0 - 300^0$ (180^0 is in the south direction) (Hossen and Akhter (2015)). That indicates that in a possible scenario of accidental release, there is a higher probability that the atmospheric release plume will move towards the Scheldt River; moreover, the lower wind velocities would result in a highly concentrated deposition of radionuclides.

There are several possible combinations of wind speed and direction that could occur at the moment of an accident. We considered two specific meteorological conditions: (1) atmospheric releases are directed towards the lower estuary, rivers, and tributaries; and (2) the release is towards the sea. Figure 5.2 shows the area of deposition for radionuclides considered in the scenarios, and Table 5.2 presents the parameters used for them.

Scenario	Radionuclide	Pathways	Amount released	Wind speed	Wind Direction
1	^{137}Cs	Atmospheric depositions	10 PBq	1 m/s	110^0
2					315^0
3		Direct Release	52 GBq/min		
4	^{131}I	Atmospheric depositions	100 PBq	1 m/s	110^0
5					315^0
6		Direct Release	127 GBq/min		

Table 5.2: Scenario definitions for ^{137}Cs and ^{131}I and their amount of radioactivity released in the Scheldt basin for the model.

The liquid radioactivity released directly into the estuary during the scenarios presented in Table 5.2 is based on the releases that occurred during the Fukushima disaster (spanning from March–April 2011). As reported, it was very difficult to estimate the duration of the accidental release of radionuclides that occurred by using backward extrapolation of inventories (UNSCEAR (2021)). Here, we keep the assumption of an accidental scenario of a six-hour

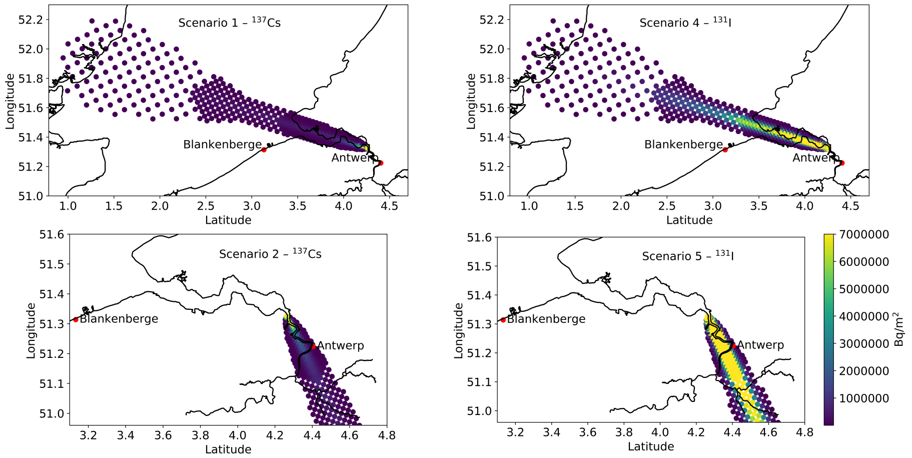

Fig. 5.2: Total amount of radionuclide deposited on the Scheldt basin after 24 hours of initial release as computed by the JRODOS model for ^{137}Cs and ^{131}I and two wind direction for scenario 1,2,4 and 5

release period in order to keep the combination of atmospheric and direct liquid release. The rate of release is estimated from the total amount of radionuclide released between March and May 2011, with inventories of ^{137}Cs at 5 PBq and ^{131}I at 12 PBq (UNSCEAR (2021)). The simulation period considered here is about a month after the initial release since the model is developed with the aim to catch the peak activity concentration and to guide the actions to be taken during and immediately after the accident. In case of longer periods, monitoring measurements of activity are feasible and more reliable (Cao et al. (2022)).

5.3.3 Hydrodynamic conditions

The scenarios considered earlier (Table 5.2) primarily involved radioactive release from different pathways and meteorological conditions. Here, we consider the effects of the hydrodynamics in the Scheldt basin on the distribution of radioactivity. For this, we consider two cases: firstly, the influence of releases starting at high and low tide (at the point of release), and secondly, the difference between the periods of January and July. The Scheldt estuary, where the NPP is located, is greatly influenced by tides; thus, the tide conditions at the start of release can play a role in the distribution of the radioactivity. For instance, if the plume is released during low tide, it is likely to move towards inland region in the first six hours. Therefore, the impact of tide on the distribution of radioactivity levels is of relevance. During the wet season additional fresh water is delivered in the Scheldt basin and this could potentially alter the activity levels as well as the spatial distribution. Therefore, the model is simulated for January, which has more rainfall and storm surges than July. For all the scenarios discussed here, we use the conditions indicated in scenario 1, which involves ^{137}Cs.

5.4 Results

In this section, we present the salinity simulation results that were used for the calibration and validation of the transport model (diffusion coefficient). Salinity measurements in the estuary are available as time series at different stations placed across and along the estuary (Flemish environment agency, 2023). The salinity was selected as a proxy for the evaluation of radionuclide transport model due to lack of direct radionuclide specific measurements that are more expensive and complex than salinity. Finally, the simulation results for the fate of radionuclides obtained for the different scenarios are presented.

5.4.1 Salinity Model

Time series values of salinity are available at different locations in the estuary. Since a good simulation performance in salinity also suggests good capabilities for the simulation of other pollutants in solution, salinity can be used as a proxy. For the validation of the transport model, the model results at three different locations were compared against salinity measurements (Prosperpelder, Liefkenshoek, and Hemiksem) that are shown in Figure 5.3.

Figure 5.4 shows a good agreement between the model and the observations, especially for the downstream stations (Prosperpelder). However, the discrepancy is larger for the upstream stations (Liefkenshoek and Hemiksem), where the amplitude of the salinity variations is small compared to the measurements. Firstly, it should be emphasized that the initial conditions at the coastline region are unknown and achieving a good initial condition would require a long warming up simulation. Secondly, the salinity simulation was carried out in the month of January that involves a higher impact of freshwater and tidal interaction in the estuary. Nonetheless, the main aim here was to validate the transport model with a simple setup for salinity and to estimate the impact of the diffusion coefficient. During the model calibration for diffusion, the simulation is carried out during the month of June, which has calmer periods. The salinity was simulated for three different diffusion coefficients (100, 10, and 0 m^2/s), and the results are shown in figure 5.5. It can be seen here that, in comparison to measured values, the model simulation has a lower RMSE value for zero diffusion coefficient. This does not mean that there is no physical diffusion; however, numerical diffusion compensates for it.

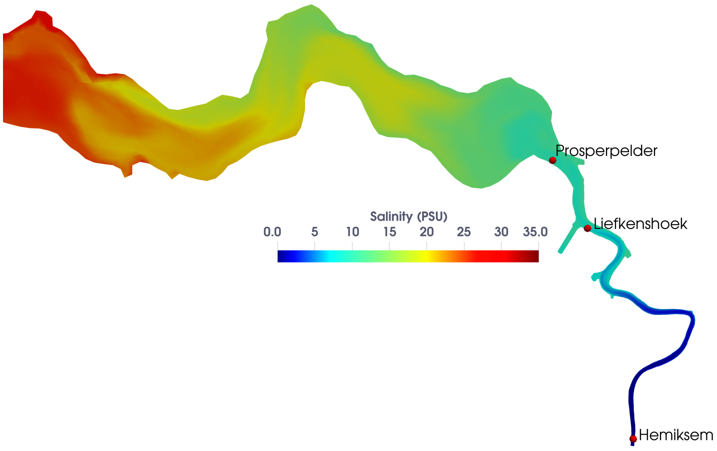

Fig. 5.3: Snapshot of the modeled salinity field with measurement location used to compare the simulated results.

5.4.2 Scenario Simulations: Results

The activity concentration of radionuclides under the scenarios previously discussed in Section 5.3 is presented in this section. The recommended limit for radioactive concentration is 10 kBq/m^3, according to the safety regulations under normal operating conditions (IAEA (2016)). The simulation of affected areas are shown in the figures (Figure 5.7, 5.10, 5.13, 5.15, 5.17, 5.19, 5.20, 5.22), together with their respective maximum activity concentrations.The maximum concentration in the estuary reached up to 88 MBq/m^3 for ^{131}I immediately after the release. While ^{137}Cs had a maximum concentration of just 1.4 MBq/m^3. It is worth mentioning that the maximum concentration of these radionuclides is present at the mouth after the lower estuary (i.e., near Doel NPP). The figure (Figure 5.7, 5.10, 5.13) in the left shows the impact after an initial period of release, and those in the right shows the impact after a sufficiently long period of 25 days. The locations used to asses the impact of different scenarios are shown in Figure 5.6.

5.4.2.1 Atmospheric Releases: Scenario 1 and 4

Figure 5.7a and 5.7c show the activity concentration of radionuclides ^{137}Cs and ^{131}I respectively, after 72 hours (3 days) of release and Figure 5.7b and 5.7d show the concentration after 25 days of release.

The radioactivity concentration of ^{131}I is substantially higher than that of ^{137}Cs, particularly in the initial days following the release. This larger initial

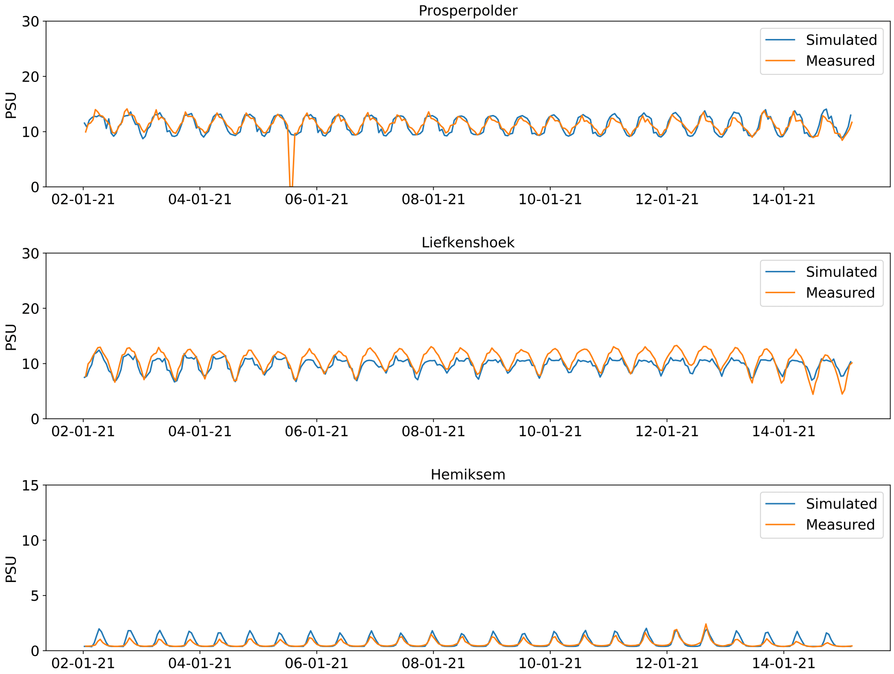

Fig. 5.4: Model comparison for the simulated and measured salinity in the Scheldt estuary (a) at Prosperpelder (Top) (b) at Liefkenshoek (Middle) and (c) at Hemiksem (Bottom) for location shown in Fig. 5.3

concentration occurs because the overall amount of ^{131}I emitted is ten times higher than the amount of ^{137}Cs. In this scenario, where the deposition is towards the coast, the plume in the estuary is already starting to move towards the Belgian coast. This is quite expected due to the tidal motion known for this estuary (Lacroix et al. (2004) for salinity). The concentration of ^{131}I at the coast is higher than the recommended water concentrations (>10 kBq/m^3). While for ^{137}Cs, the concentration never exceeds this limit. Figure 5.8 shows the concentration level of both radionuclides at the location of Blankenberge (for location, see Figure 5.6). It is evident that in the coastal region the release of ^{131}I has a more impact than the release of ^{137}Cs. But a higher concentration (>10 kBq/m^3) for ^{131}I is not expected to reach until seven days following the first release.

Since ^{131}I decays faster than ^{137}Cs, the concentration starts to decline after about nine days, after which the radioactivity concentration drops below the recommended levels (at about 16 days after the initial release). Moreover, as

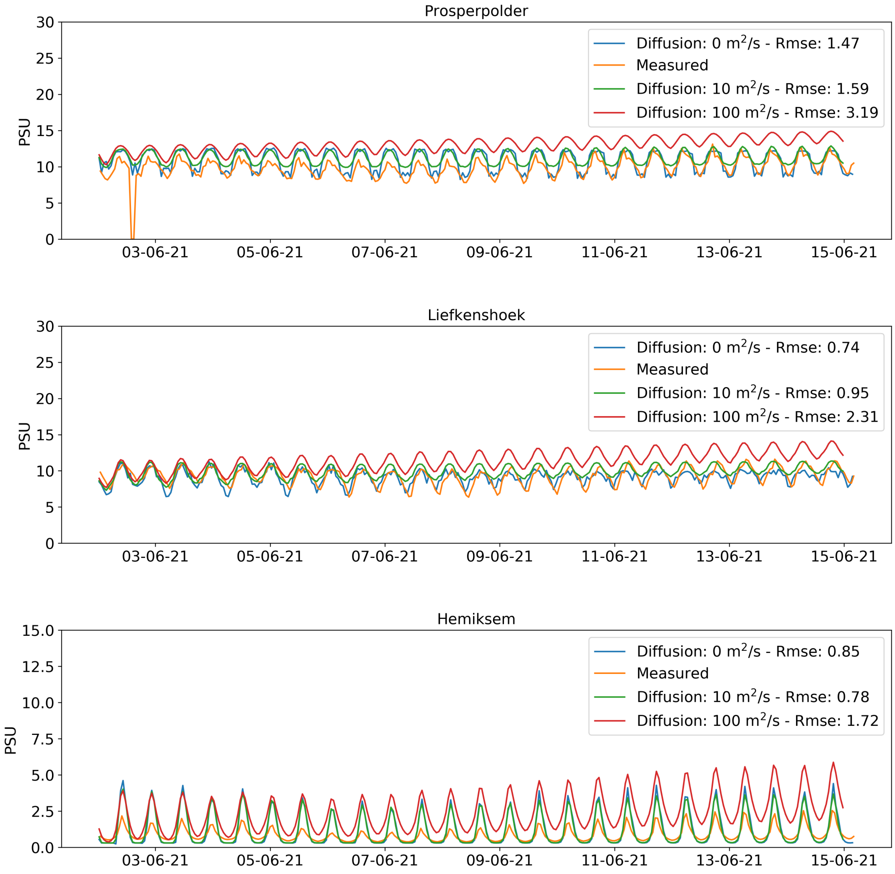

Fig. 5.5: Model comparison for the simulated salinity for different diffusion coefficients and measured salinity with RMSE value in the Scheldt estuary (a) at Prosperpelder (Top) (b) at Liefkenshoek (Middle) and (c) at Hemiksem (Bottom)

seen in Figure 5.8, the ^{131}I concentration is comparable to the ^{137}Cs concentration at around 25 days. For ^{137}Cs, the decrease in concentration is seen due to the water influxes from the English Channel from the south-east towards the Southern Bight region (i.e., the Belgian Coast). Therefore, in the case of ^{131}I too, the dilution could be an additional reason for the decrease in concentrations.

After a nuclear incident, the Scheldt Estuary would be most affected by atmospheric deposition because of its proximity to the NPP. It is worth mentioning that the maximum concentration of these radionuclides is present at the

[ht]

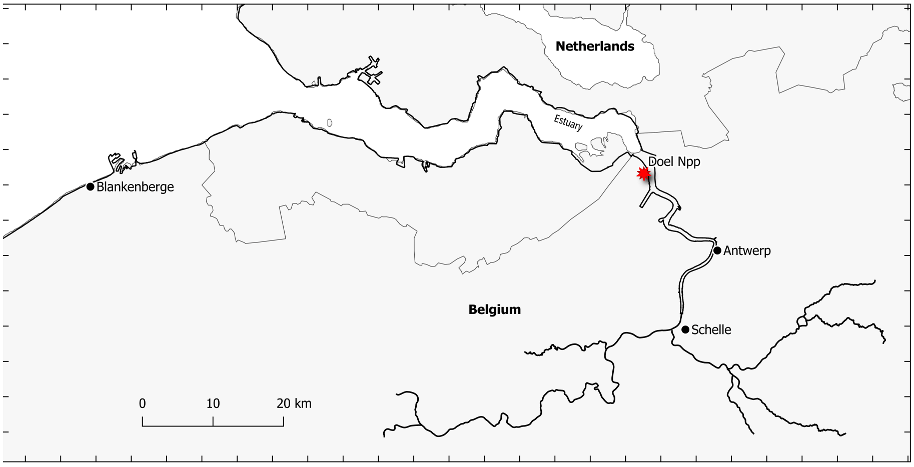

Fig. 5.6: Location of the Doel Nuclear power plant and important cities in the coast, estuary and the river that are used to assess the impact of different scenarios for ^{137}Cs and ^{131}I.

mouth of the lower estuary (i.e., after Prosperpelder; for location, see Figure 5.3). Even though the release is towards the coast, the tidal motion in the estuarine part transports the radionuclides towards the inland basin. Antwerp city (Figure 5.6), located upstream from the NPP, is one of the important urban and industrial settlements that is expected to be the most affected by these releases. Figure 5.9 shows the temporal variations of the concentration at the banks of the Antwerp:

It can be seen from Figure 5.9 that the tidal motion brings a significant amount of radioactivity back towards upstream parts of the estuary. Though both radionuclides exceed zero in arround two days, the ^{131}I exceeds the recommended limit only after three days and the ^{137}Cs after ten days of release from the NPP. The radioactivity reaches maximum at around the 12th and 18th day for ^{131}I and ^{137}Cs, respectively. However, the backward motion of the plume of radionuclide never goes beyond Hemiksem in the inland river basin. The concentration in the estuary is one order of magnitude higher than the concentration along the coast.

5.4.2.2 Atmospheric Releases: Scenario 2 and 5

Figure 5.10a and 5.10c show the concentration of radionuclides (^{137}Cs and ^{131}I) after 48 hours. This shows that the deposited plume on the far reach of tributaries moves faster downstream towards the confluence with the Rupel

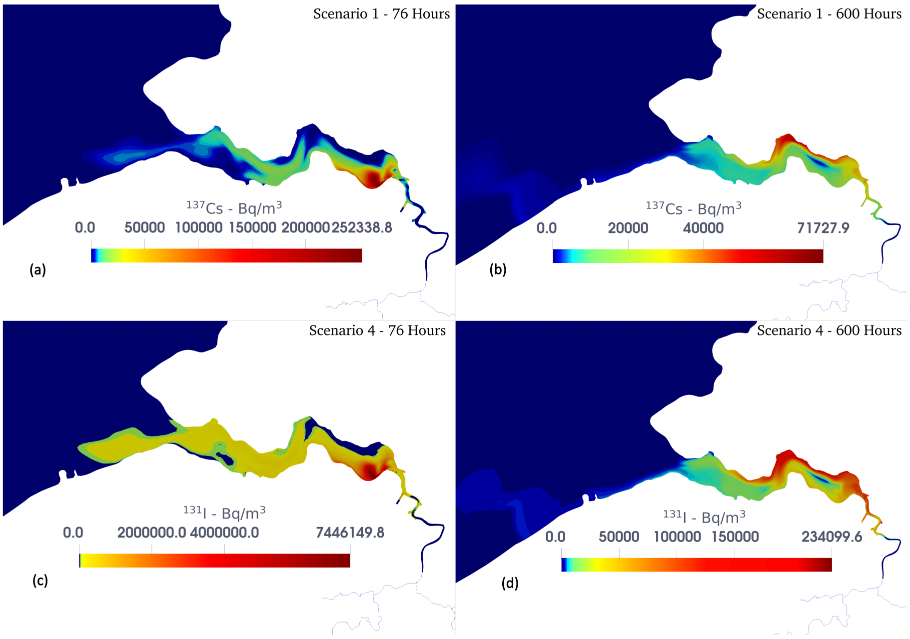

Fig. 5.7: Simulated radionuclide concentrations in surface waters (Bq/m^3) (a) after 3 days of initial release for ^{137}Cs (top left), (b) after 25 days of initial release for ^{137}Cs (top right) as defined in scenarios 1, (c) after 3 days of initial release for ^{131}I (bottom left), and (d) after 25 days of initial release for ^{131}I (bottom right) for scenarios 4.

River. This is primarily because freshwater dynamics can become dominant towards the upstream reach of the tributaries, thus decreasing the flushing time. Nonetheless, even if the plume moves downstream faster (within hours) towards the mouth of the Rupel River (Figure 5.10a and 5.10c), it takes a few days to reach activities below the recommended threshold levels in Rupel (roughly 6 days for ^{137}Cs and 19 days in the case of ^{131}I). Naturally, this is due to the fact that ^{131}I is released in greater quantities than ^{137}Cs. But it is essential to note that larger depositions in the tributaries would result in a longer period to reach the recommended limit in the Rupel River. Figure 5.10b and 5.10d show the radionuclide distribution for ^{137}Cs and ^{131}I after 25 days of release. In this case, it can be seen that the activity concentration is spread in the estuary and that no activity is present in the coast.

Figure 5.11 shows the concentration of radionuclides in tributaries right before its confluence with the main river. which are: the Dyle River connected to Rupel (Figure 5.11a), the Grote Nete connected to Rupel (Figure 5.11b), and then the Rupel connected to the Scheldt River (Figure 5.11c).

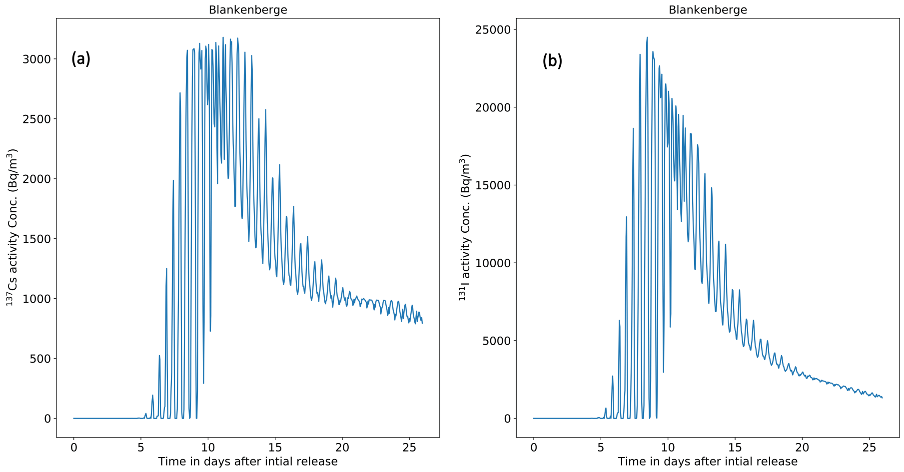

Fig. 5.8: Temporal variation of activity concentrations at Blankenberge located at the Belgian Coast: (a) ^{137}Cs for model parameters defined in scenario 1 (left) and (b) ^{131}I for model parameters defined in scenario 4 (right)

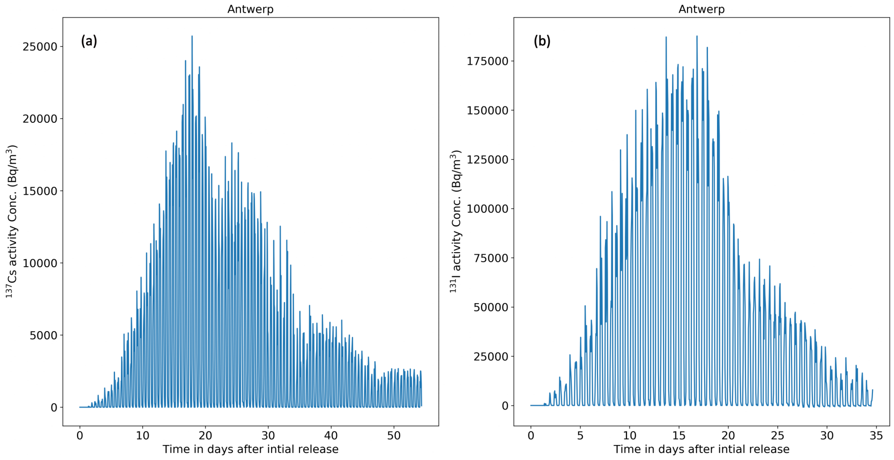

Fig. 5.9: Temporal variation of activity concentrations at Antwerp located at the Scheldt estuary: (a) ^{137}Cs for model parameters defined in scenario 1 (left) and (b) ^{131}I for model parameters defined in scenario 4 (right)

It is important to note that the confluence of the Rupel with the Scheldt River is approximately 12 km downstream the beginning of the Rupel River

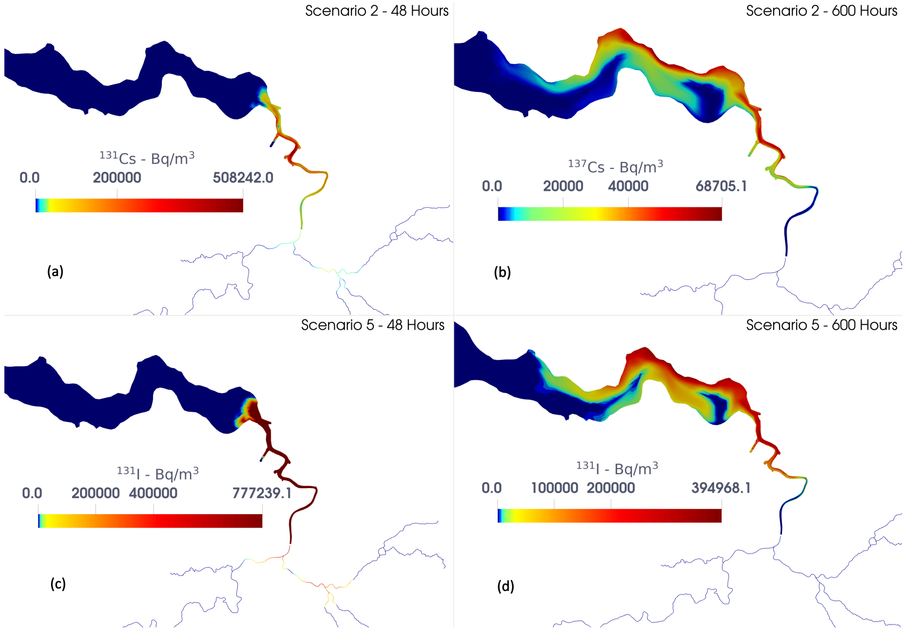

Fig. 5.10: Simulated radionuclide concentrations in surface waters (Bq/m^3) (a) after 1 day of initial release for ^{137}Cs (top left), (b) after 25 days of initial release for ^{137}Cs (top right) as defined in scenarios 2, (c) after 1 day of initial release for ^{131}I (bottom left), and (d) after 25 days of initial release for ^{131}I (bottom right) for scenarios 5

(the confluence point of the Nete, Dyle and Zenne rivers). In the tributaries of the Rupel, the radionuclide plume stays for approximately 4 days, but the concentrations reach significant quantities of up to 70 KBq/m^3 in the case of ^{137}Cs and 1 MBq/m^3 for ^{131}I. In the Rupel river, two activity hot spots are noticeable. One coming from upstream, transported by the water from its tributaries and another from downstream, transported by the tidal motion. This is clearly presented in Figure 5.10c, where the separated plumes coming from the estuary (downstream) and its tributaries (upstream) are visible. As seen by the spikes in Figure 5.11c between days 3 and 4, both the plumes join in the Rupel River and travel towards the estuary.

Figure 5.12 shows the activity concentrations of both radionuclides in Antwerp, showing that it is once again one of the most vulnerable locations in this scenario. Moreover, since the atmospheric releases deposit on the surroundings of Antwerp, the rise in concentration to its maximum value is almost immediate and is also higher compared to scenarios 1 and 4. Since inland depositions also reach these areas, as described in scenarios 2 and 5, they have the greatest

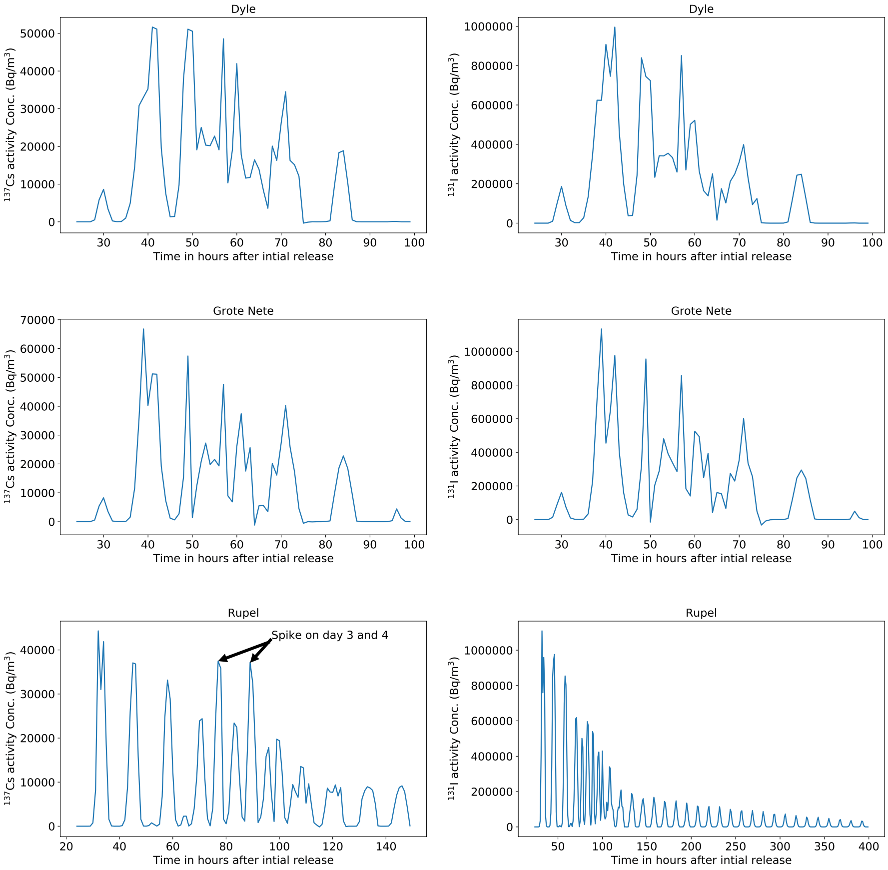

Fig. 5.11: Temporal variation of concentrations in the tributaries of the Scheldt River: (a) ^{137}Cs and ^{131}I in the Dyle River for scenarios 2 and 5 respectively (top), (b) ^{137}Cs and ^{131}I in the Grote Nete River for scenarios 2 and 5 respectively (middle) and (c) ^{137}Cs and ^{131}I in the Rupel River for scenarios 2 and 5 respectively (bottom). The extracted concentration is located immediately before the confluence with the main river.

effect in this location. The concentration of ^{131}I after the end of the simulation period is 124 kBq/m^3, and that of ^{137}Cs is 30 kBq/m^3, which is still above the recommended limit.

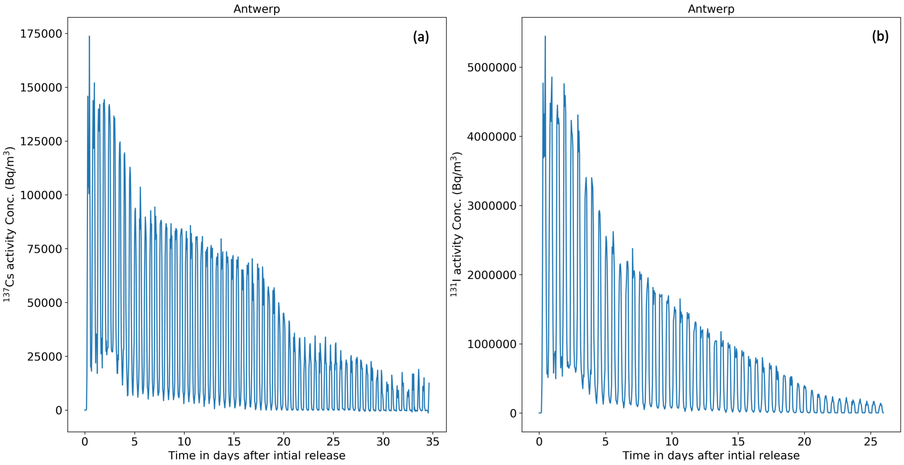

Fig. 5.12: Temporal variation of concentrations at Antwerp located at the Scheldt estuary: (a) ^{137}Cs for model parameters defined in scenario 2 (left) and (b) ^{131}I for model parameters defined in scenario 5 (right)

5.4.2.3 Direct liquid releases: Scenario 3 and 6

The distribution of radionuclides (^{137}Cs and ^{131}I) in surface water for direct release scenarios 3 and 6 is shown in Figure 5.13. Figure 5.13a and 5.13c show the activity concentrations of radionuclides ^{137}Cs and ^{131}I, respectively, after 72 hours (3 days) of release, and Figure 5.13b and 5.13d show the concentrations after 25 days of release.

Direct release scenarios are generally treated as point source releases into the Scheldt estuary that are subjected to advection and dispersion. Due to the high release concentration for both radionuclides and the fact that transport in the estuary is dominated by advection, the extent of the affected areas (>10 kBq/m^3) after two days of release for both radionuclides is comparable. Even if ^{131}I has a one-order-of-magnitude higher release rate, the concentrations of both radionuclides after about a week become equivalent in magnitude. This can be observed at the location of Antwerp, where the concentration becomes similar after about 8 days of release. Later, the concentration of ^{131}I starts decreasing considerably (Figure 5.14).

In fact, around a month after the release, the extent of affected areas for both radionuclides is comparable (Figure 5.13c and 5.13d). The total inventory released in these scenarios is 45.72 TBq of ^{131}I and 1.8 TBq of ^{137}Cs. Even though these are considerably smaller than the atmospheric releases (5.2), it must be kept in mind that only a portion of what is released is deposited on the Scheldt. While in the event of a direct release, the total inventory is released.

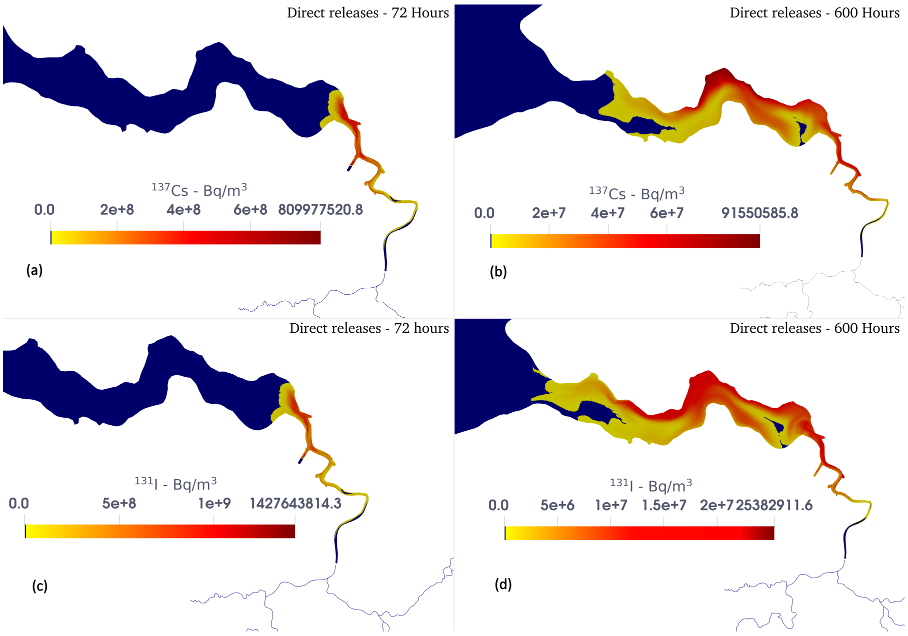

Fig. 5.13: Simulated radionuclide concentrations in surface waters (Bq/m^3) (a) after 3 days of initial release for ^{137}Cs (top left), (b) after 25 days of initial release for ^{137}Cs (top right) as defined in scenarios 3, (c) after 3 days of initial release for ^{131}I (bottom left), and (d) after 25 days of initial release for ^{131}I (bottom right) for scenarios 6

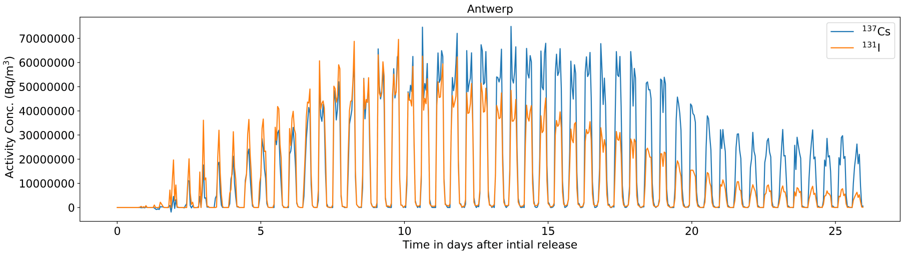

Fig. 5.14: Temporal variation of concentrations at Antwerp located at the Scheldt estuary for ^{137}Cs (model parameters defined in scenario 3) and ^{131}I for (model parameters defined in scenario 6)

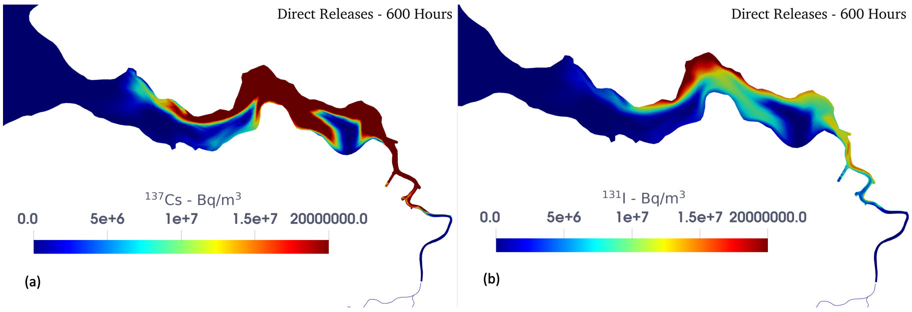

Fig. 5.15: Simulated radionuclide concentrations in surface waters (Bq/m^3) (a) after 25 days of initial release for ^{137}Cs (left), (b) after 25 days of initial release for ^{131}I (top right) as defined in scenarios 3 and 6 respectively that is scaled up to 20 MBq/m^3 to show that impact of degradation in the case of ^{131}I.

That leads to concentrations that are considerably above the limit. It is important to emphasize that following the initial release, the entire lower estuary becomes contaminated within a few days and begins to spread in the upper estuary. As seen in Figure 5.13a and 5.13b, both radionuclides reach the mouth of the estuary approximately 25 days after discharge. However, compared to ^{137}Cs, the concentration of ^{131}I has now decreased. This is visible when the scale of the figures is kept the same for both radionuclides, as shown in Figure 5.15a and 5.15b. Under these scenarios, the radioactive plume in the Scheldt River propagates upstream until about the mouth of the Durme River and until Boom (Figure 4.1), located upstream the Rupel River. Furthermore, the extent of affected areas toward inland rivers appears to be greater in scenarios 3 and 6 than in the others (liquid releases vs atmospheric releases). Figure 5.16 show the concentration of the radionuclides for ^{137}Cs and ^{131}I at the location of Schelle (see Figure 5.6 for location) for the different scenarios. For scenarios 1 and 4, which involve radioactive deposition towards the coast, there is no significant impact at Schelle and is thus excluded from Figure 5.16. Moreover, as shown in Figure 5.16a, the impact of ^{137}Cs in the case of atmospheric releases is negligible compared to direct releases. Not only does the direct release scenario affect a larger area towards the rivers than the other scenarios, but it also has a higher concentration. However, scenario 5 and, even to a smaller extent, scenario 2 have an impact at this location that occurs earlier, whereas the concentration in the direct release scenario stays below the recommended level for up to 4-5 days. The peak of ^{131}I occurs on the 11th day after release, followed by the peak of ^{137}Cs two days later. Figure 5.16 shows that at this location, the peak concentration for ^{131}I (1.9 MBq/m^3) is now lower than that

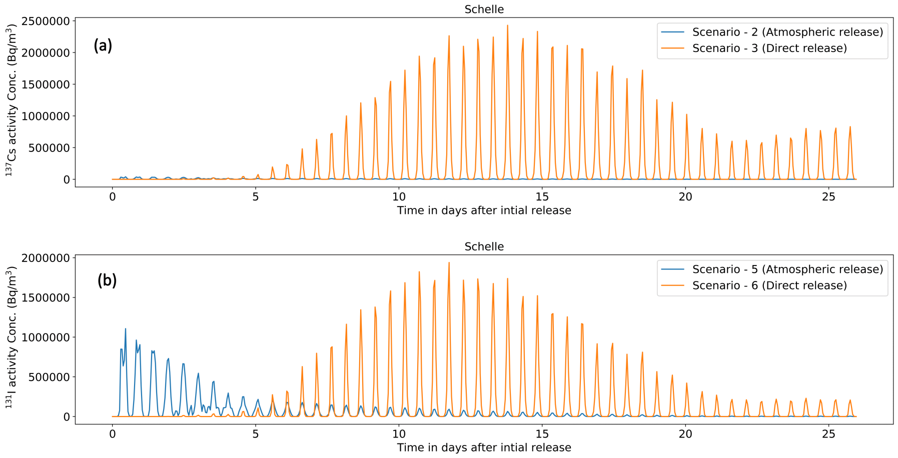

Fig. 5.16: Temporal variation of concentrations at Schelle located in the Scheldt River: (a) ^{137}Cs for model parameters defined in scenario 2 and 3 (Top) and (b) ^{131}I for model parameters defined in scenario 5 and 6 (bottom)

for ^{137}Cs (2.56 MBq/m^3).

5.4.2.4 Low and High Tide

Figure 5.17 shows that radioactivity distribution for ^{137}Cs in the Scheldt estuary after about 18 days of simulation for start of release at lowest peak of tide (low tide: Figure 5.17a) and at the highest peak of the tide (high tide: Figure 5.17b).

The distribution of radioactivity in the Scheldt estuary remains consistent regardless of whether the release occurs at high or low tide (Figure 5.17). Furthermore, the extent of the plume towards inland and, to some extent, maximum concentrations are comparable. This can be seen in Antwerp (Figure 5.18), where the temporal variation for concentration follows the same trend except for the peak values. The difference in peak values for the release at high tide are generally lower than that for releases at low tide. This is expected because Antwerp is located upstream the release (no direct deposition here: see Figure 5.2 for scenario 1) and the plume released at low tide is transported towards the rivers, increasing the concentration. The difference in peak values is more pronounced in the initial weeks, however, after approximately 21 days the peak values for both cases become similar.

The start of release at high tide has a greater impact on the coast than the release at low tide (Figure 5.19). However, the radioactivity concentration at the coast, released at high tide, does not exceed 7000 Bq/m^3, whereas no

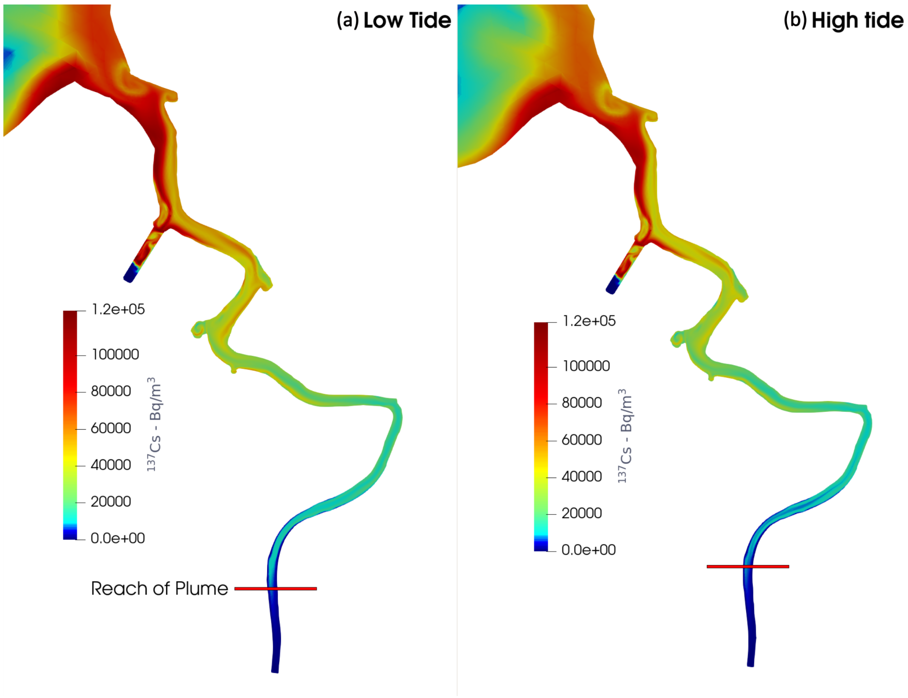

Fig. 5.17: Simulated radioactivity concentration in the Scheldt estuary for ^{137}Cs after approxiamtly 13 days of initial release, starting from (a) low tide (left) and (b) high tide (right).

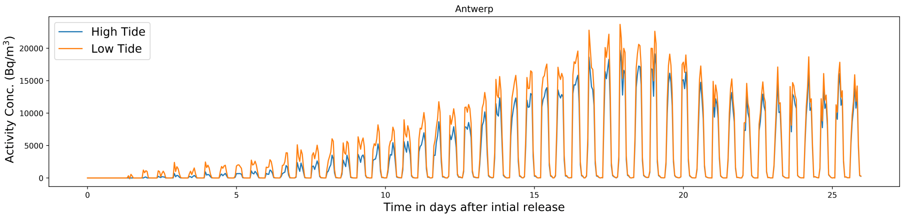

Fig. 5.18: Temporal variation of radioactivity concentration for ^{137}Cs at Antwerp for release starting from low tide and high tide.

radioactivity is observed here for the releases during low tide. Moreover, for scenario 1 (in Section 5.4.2.1), the radioactive contamination is lower than that seen here (for high tide) at the coast since the starting time of scenario 1 was selected as first hour of first day of July (2 hours after the start of high tide).

Nonetheless, it should be noted that the increase in concentrations is less than 5%.

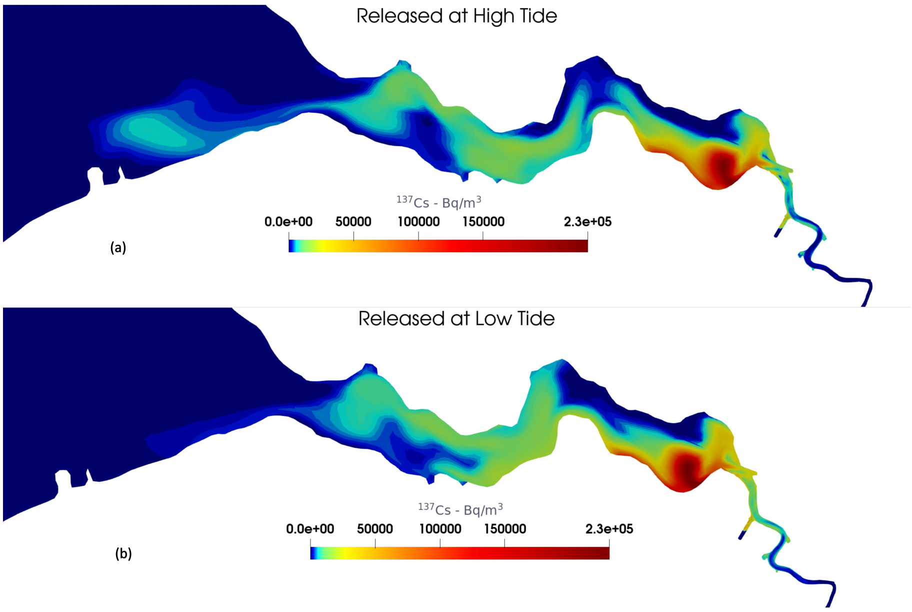

Fig. 5.19: Simulated radioactivity concentration in the coast and the estuary for ^{137}Cs after 5 days of initial release, starting from (a) high tide (top) and (b) low tide (bottom).

5.4.2.5 January and July

Figure 5.20 shows that radioactivity distribution for ^{137}Cs in the Scheldt estuary after 5 days of simulation during the month of July (Figure 5.20a) and 5 days of simulation during January (Figure 5.20b). In both cases the release period begins on the first day of their respective month.

After roughly 5 days, the concentrations obtained for July and January have a similar peak concentration of around 5000 Bq/m^3 at the coast. However, the distribution for each month shows a distinct spatial distribution. The biggest difference happens in the estuary where the concentrations are significantly lower for January than for July. Figure 5.21 shows the temporal variation of radioactivity in Antwerp for the month of July and January. It can be seen here that after the initial week the concentration in July increases, whereas that in January remains lower. This is because of higher discharge from the

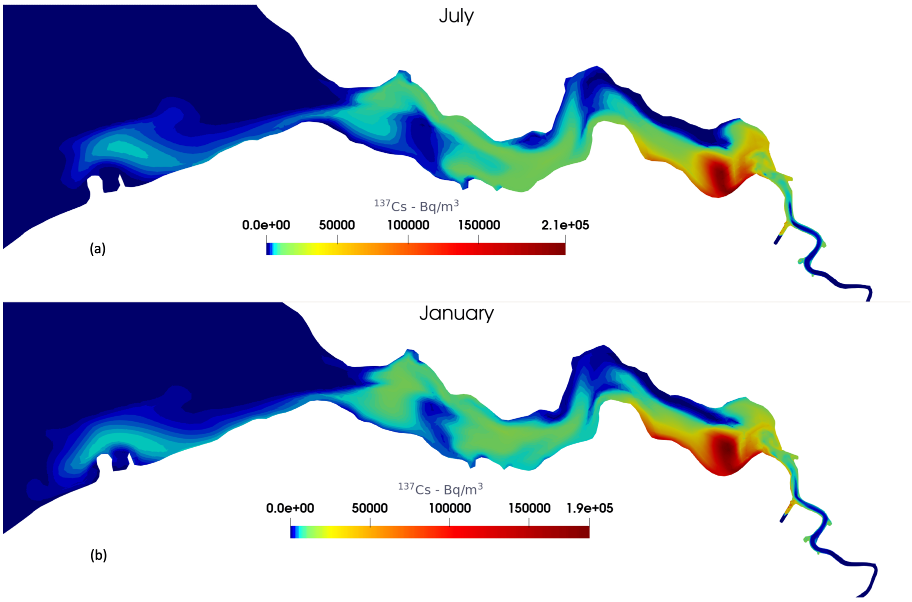

Fig. 5.20: Simulated radioactivity concentration in the coast and the estuary for ^{137}Cs after 5 days of initial release for the month of (a) July (Top) and (b) January (Bottom).

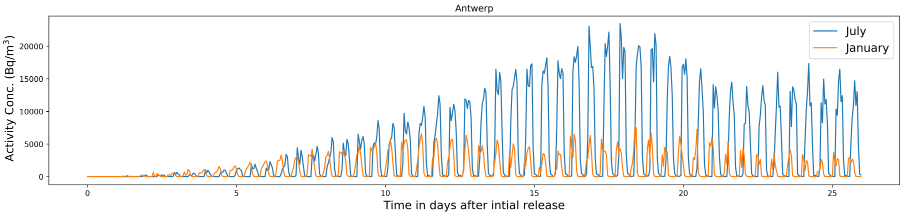

Fig. 5.21: Temporal variation of radioactivity concentration for ^{137}Cs at Antwerp for the period of July and January

river. Additionally, due to this, the extent of plume towards the river is lower in January than in July (figure 5.22).

5.4.2.6 Individual dose assessment

To the best of the author's knowledge, the saline water in Scheldt prevents the extraction of water for drinking and irrigation purposes. However, desalination plants are expected to be operational by 2025 in the coastal region of Belgium.

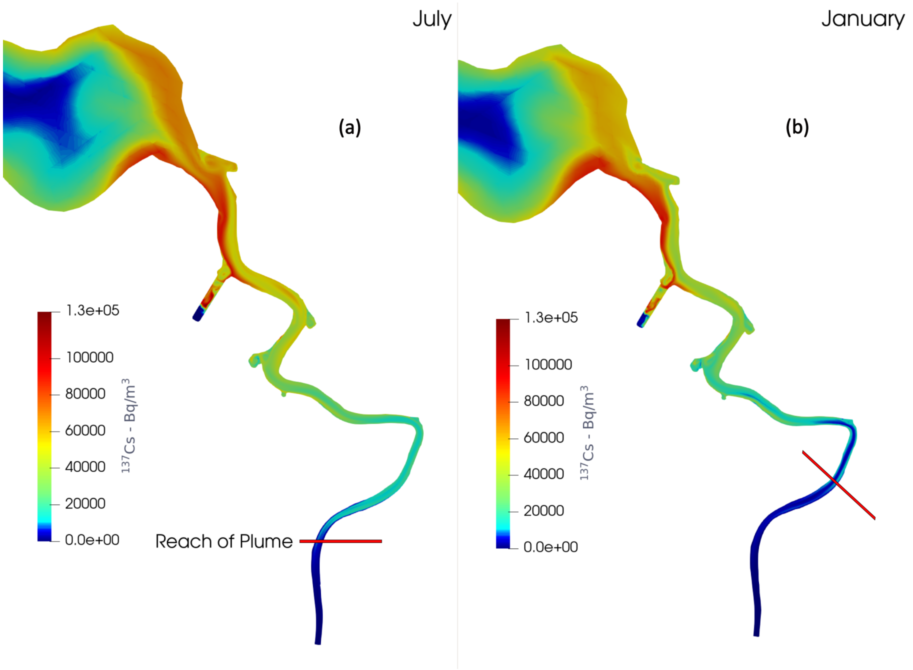

Fig. 5.22: Simulated radioactivity concentration for ^{137}Cs after approximately 13 days of initial release for the month of (a) July (left) and (b) January (right).

The individual doses were thus calculated for drinking water contamination along the coast using the equation and parameters presented in Section 3.6 of Chapter 3. The calculated individual doses were of the order 10^{-9} to 10^{-10} mSv at the coast. In the case of the estuary, since no water extraction is done for drinking purposes, the doses were calculated for swimming (body immersion in water). Even with the assumption that the swimming activity is carried out for the entire period of simulation, the individual doses are the order of magnitude between 10^{-10} to 10^{-6} mSv at Antwerp. These individual doses are far below the recommended levels of 0.1mSv. This is because of the significantly lower dose coefficients ($3.88 \times 10^{-16} Sv.m^3/hBq$ for ^{137}Cs and $1.23 \times 10^{-13} Sv.m^3/hBq$ for ^{131}I) for external exposure such as swimming. Therefore, the direct impact on humans due to radioactivity contamination for the scenarios considered here are low. However, the impact on the estuarine ecology (roughly 80 km long) can be severe. Furthermore, due to radioactivity accumulation in fish, their consumption may pose a potential risk for human health.

5.5 Conclusions

A hydrodynamic model was developed to simulate the fate of radionuclides in the Scheldt basin as a decision-support tool for emergency planning. The model has proved to be useful to simulate the spreading of radioactivity originated from both distributed (atmospheric releases) and point (direct releases) sources over any temporal scale. It provides valuable insight about the magnitude of activity concentration that could be found in this water system. The model includes the effect of wind drag and encloses a domain that covers the complete continental shelf region. This minimizes the impact of the boundary conditions on the calculations in the area of interest. The model has the capabilities to couple 1D and 2D domains with low computational cost. This characteristic is desirable in the case of emergency situations.

Several hypothetical accidents (atmospheric and direct liquid releases) were simulated from Doel NPP, considering the worst-case scenarios based on the Fukushima accident. The simulation results show that due to tidal motion, radionuclides released in the Scheldt Estuary can last for more than a month with activity concentrations above 10 kBq/m^3. For atmospheric releases, when the wind direction points towards the sea, the results show that the deposited radionuclides on the estuary are transported towards the sea. However, the radioactivity concentrations around the coast are significantly lower than those found in the estuary. This is explained by the dilution effect of the water currents along the coast and the tidal movement. The effect of the tides was evident because after atmospheric releases occurred during the high tide, a higher concentration of ^{137}Cs was predicted in the coastal region. On the other hand, the radioactivity deposited on the estuary is not transported into the upstream reach of the rivers beyond Hemiksem. The effect of the seasonality on the magnitude of the activity concentration was also observed. The increase in the river discharges during the month of January (wet period) led to the decrease of the concentrations in the lower estuary nearby Antwerp. Moreover, the river discharge has a significant influence on the tidal motion in the tributaries of the estuary (Grote Nete and Dyle). When the wind direction is directed towards inland, the radionuclides deposited on the upstream tributaries of the estuary are flushed to the estuary within days. However, as the tributaries are closer to the estuary, this flushing time increases due to an increase in the tidal effect on the river flow. In the case of direct liquid releases, the lower estuary is contaminated very fast, mostly within a couple of days. In contrast to atmospheric deposition, the direct liquid releases led to significantly higher concentrations in the upper part of the Scheldt River. This is because the activity released directly from a point source is higher than the same activity spread over a larger area, where only a portion of the total release settles on the water surface. Since the decay rate for ^{131}I is faster, the results show that radioactivity in the domain falls rapidly than ^{137}Cs. For instance, when the ^{131}I concentration is transported towards Antwerp (for atmospheric release where the wind direction points to the sea), the magnitude of the peak declines up to 1/5th within a couple of weeks. Therefore, around few weeks, even though ^{131}I is released in a larger amount than ^{137}Cs, the impact of ^{137}Cs can be higher.

Independently of the release source, the tides in the estuary are the primary driving force in the distribution of radioactivity. Thus, the Scheldt estuary is the most vulnerable region where high activity concentrations are found for long periods. That is due to the constant change in direction induced by low and high tides. In the inland rivers, the river discharge plays a significant role in the upstream propagation and flushing of the radioactive plume. The combination of the different flow regions is made possible to understand better the exchange of radioactivity between estuary-sea and river system by taking into account: (1) the seasonality (impact of variability of the river's discharge on the propagation of the plume in the upstream river system), (2) the impact of the tides and winds on radionuclide distribution in the complete system, and (3) to consider the recirculation of the radioactive plume mainly along the coast. In models restricted just to the area of interest, the radioactive mass that leaves the domain is not taken into account. Here, SLIM makes it possible to simulate a sufficiently large domain that keeps better track of the mass.

The model simulation for radioactivity distribution and its levels provides information for emergency responders to make informed decisions. For instance, even with such a large release amount, the results show that the impact on the Belgian coast is rather limited in space (within 35 km from the estuary mouth). For the deposition in rivers, the radioactivity level subsides within a few days. This can further aid in the effective planning of radioactivity measurements that need to be undertaken in the wake of an accidents. Since tidal motions vary concentrations, the model can assist in foreseeing the time to observe maximum concentration. For instance, measurements taken at low tide in Antwerp will provide extremely low radioactive levels. Subsequently, protective measures for the public can be implemented in areas with high radioactive concentrations. Additionally, with available projected data for discharge and tides, the model can support decisions by simulating the evolution of the radioactivity distribution in the event of a nuclear accident.

Chapter 6

Conclusions

6.1 Conclusions and perspectives

In this thesis, we have developed a hydrodynamic and radionuclide transport model to investigate the impact of radioactive releases on aquatic systems. Our model is able to accurately represent the flow dynamics not only in the rivers but also in the estuary and the sea in order to study the transport process of radionuclides. For this, the model had to first take into account the influence of hydraulic structures in the Meuse River and its canal systems on hydrodynamics. Secondly, the model had to represent the tidal – freshwater dynamics of the Scheldt system with consideration of its multiscale nature, without increasing the computational cost. This was performed by coupling the geometrically simpler one-dimensional model with the two-dimensional model of the SLIM. Later, both components were coupled with a radionuclide transport model to study the fate and transport of radioactivity. In all cases, the model simulations was in line with available measurement and literature data.

In order to account for hydraulic structures in rivers and canals, we incorporate them in the discontinuous Galerkin method of the SLIM modeling framework. In which, rather than using a conventional numerical flux, we use the stage-discharge relationships specific to the structures (weirs and sluice gate). Such implementation allows us to solve for the discontinuity in the solution brought by the structures. Furthermore, certain considerations have been given in order to account for submerged flow and the transition from free flow to submerged flow. Thus, the structure implementation is robust in terms of hydrodynamic representation. However, it was observed that the water level in the Meuse River and the canal are highly regulated by operating the hydraulic structures. To represent the water level and, consequently, the correct velocities, a methodology is applied to model the operation of the structures. This was not only important for regulation but also to account for water diversion into the Campine canal, which is then distributed in the canal network. In total, more than 20 hydraulic structures were implemented, each with a set of operating principles.

The Meuse River model with the hydraulic structure module was able to reproduce the observed water levels and discharge rather satisfactory. The NSE coefficients for the Meuse River show good model performance, ranging from 0.65 to 0.78 for water levels and 0.9 to 0.95 for discharges with 92 % of results falling into the confidence interval. This showed that the SLIM model is capable of representing the flow trends and the water levels. Though the fluctuations are not captured, it does not necessarily mean that the accuracy of the model is limited. But it points out that other physical phenomena such as wind friction and waves induced by operation of structure could also influence the flow dynamics. These phenomena could also explain the oscillations observed in the measured data. Moreover, the percentage of simulated data within the confidence interval shows that some water inflows are not considered. The lack of discharge measurement stations makes it difficult to correctly estimate the lateral inflow rate during rainfall events due to surface runoff, point discharge flash flood originated in urban areas and small streams. The uncertainties in the source term can be reduced if hydrological models are used for the simulation of rainfall-runoff. This would facilitate the estimation of the lateral inflow and the point sources along the rivers. Additionally, further studies are required to determine the contribution of the wind and navigation induced waves to oscillations registered by the water level stations.

In the case of the bifurcation with Albert Canal, with the implementation of the weir operation rules, the model is able to represents the water level at Marxhe station and discharges that feed the Albert canal. This is only possible because of the operation rules implemented in the model. Such implementation allowed us to account for the discharge variability in the Meuse River. Within the canal system, the simulated water levels were compared to the measurement data, and a good agreement was reached with a maximum variation in water level of 0.3 m. The variation in water level is due to the operation of lock chamber and the waves generated affects the flow in the canals. Nevertheless, the lack of accurate discharge measurements makes the validation difficult. It would be worthwhile studying the translation waves propagated due to the structural operation (Wan et al. (2022)) in the canal and their superimposition with the canal discharge. If these waves can be separated from the measurement data, the actual discharge in the canals can prove essential.

The Scheldt model included the Scheldt rivers and its tributaries, the estuary, and the shelf region. To ensure accurate representation of the flow conditions in the model, the domain has been extended till the shelf break. Although not in the scope of this thesis the model can be used to evaluate the risk of other nuclear power plants (See section 6.2.2 on future works)) located in the North Sea countries. The simulated water level comparison to measurement in the Scheldt estuary achieved satisfactory results with maximum RMSE value of 0.3 m. Only one of the few velocity observations in the Scheldt estuary provided sufficient historical data. The model results, compared to this velocity data (Oosterweel), showed good agreement. Furthermore, the shift in direction owing to tidal motion is accurately represented. Since it is located in the estuary where the tide-river discharge interaction is strongest and is nearest to the Doel nuclear power station, it becomes an important validation location. The simulated water levels to measurements in the estuary, Antwerp (near Oosterweel) had an RMSE value of 0.26, which was higher than the coastal values of 0.17 m. The good agreement of the velocity comparison indicates that these RMSE value for the water levels in the estuary is adequate. The increased RMSE values can be attributed to the influence of the tide. However, the impact of river discharge cannot be overlooked. Consequently, further parametric study done independently can aid in better understanding the influences that each of them has (Wang et al. (2021)).

The water level comparison in the Scheldt River also showed a good agreement with 0.26 m towards the sea and 0.3 towards upstream reach of the river. The RMSE value at upstream reach is the highest among all the measurement stations in the Scheldt basin. Since the discharge boundary conditions are closest at this location, it is apparent that tidal propagation into the upstream reach of the river is the cause of deviation in the RMSE. Although, wind drag could possibly be one reason for higher RMSE value. However, reduced tidal energy at the upstream reach could also be due to the energy dissipation induced by lateral discharges and base flows in upstream rivers. Furthermore, the fact that model predictions during calm periods in July had lower RMSE values than those during storm surges in January suggests that the variation is caused by greater tidal impact.

The RMSE values in the tributaries is 0.15 m, showing a good agreement with the measured value. However, the model has a slightly lower performance for the period following the storm surges. The cause of the differences can be linked to lateral water sources that are not included in the model, such as river runoff, base flow, etc. The comparison of water levels for the measurement located upstream of the tidal control weir had an RMSE value of 0.25 m. A reason for the difference between simulation and measurements could be due to the lack of information about the operational rules of the weir. Moreover, a lower RMSE value of 0.21 m obtained downstream further shows that the weir parameters play a role.

The model validation on the European continental shelf was done using the harmonic data comparisons for the dominant M_2 tide. The chart for isometric lines for the co-range and phases of the M_2 tide show a good prediction of the amphidromic points. However, the point at the southern tip of Norway shifts towards the western direction in comparison to measurements reported. Furthermore, in the validation step, the co-range and phase lines had a good comparison, especially in the Southern Bight region. The lower mesh resolution in other region resulted in less accuracy, which was done in order to save computing cost.

Specific scenarios (atmospheric and direct liquid releases) were drawn for accidental radioactive releases from the NPPs while considering the worst-case contamination based on past nuclear accidents. In the case of the Meuse River, the study explores the impact of hypothetical nuclear accidents at the Chooz and Tihange nuclear power plants. Results show significant contamination, particularly under low flow scenarios, which lead to prolonged contamination. The concentration of ^{137}Cs in the Meuse River after approximately 7 days is negligible. In fact, for high flow conditions, the concentration in Maastricht reaches low level of radioactivity in just two days. The radioactive levels of ^{131}I can stay high up to 20 days in the Meuse River due to contaminants arriving from Vise and Lanaye under a low flow scenario. In the case of the Albert Canal, the results show that the radioactivity can remain here for more than a month. This is due to the fact that radionuclide movement is slower in the Albert Canal. However, even if only for a short time, the maximum concentration that flows in the river across Maastricht towards the Netherlands is higher than that of the Albert Canal. In the case of a low flow scenario, the plume entering the Zuid-Willemsvaart canal at Maastricht from the Meuse River reaches Antwerp much sooner than the Albert Canal itself. But the concentration from the Zuid-Willemsvaart canal flowing towards Antwerp is seven times smaller than that present in the Albert Canal.

In certain scenarios, it is seen that the activity concentrations are moving from the Albert Canal towards the Dessel-Herentals Canal. This is specifically observed in the case of relatively higher flow in the Meuse River, where the flow on the Dessel–Kwaadmechlen Canal is reversed. Therefore, even though the activity of ^{131}I or even ^{137}Cs is reduced, there can be a spike in radioactivity in the network of canals during special flow conditions. Therefore, it is shown that the complex network of the canal had the potential to re-contaminate and in certain scenarios the flushing time in the river also increased to days. Similar results were seen for releases by the Chooz NPP plant; however, affected areas in Belgium along the Meuse River increased due to its location further upstream the river. Routine discharges have no substantial concentration and thus had negligible dose impact on humans.

Furthermore, sensitivity studies regarding effect of wind speed, diffusion were done. It was seen that these parameters had a varying effect on the distribution of the radioactivity. The Albert Canal has a comparably (to river) higher influence of diffusion. While higher wind speeds in the atmosphere would lead to lower peak concentration but wider spreading. It was also shown that the flow conditions in the river can also impact the radioactivity in the river and consequently the canal. Therefore, although worst-case scenarios are drawn, other specific occurrence of releases can lead to a different radioactivity concentration distribution. This was shown by simulating real meteorological conditions for ^{137}Cs that had a much larger contamination area. Hence, the developed model will serve as an important tool for evaluating potential hazards for future accidents, both for projections and real-time decision-making.

The study also calculates individual dose rates, highlighting that while ^{137}Cs levels generally remain below limits, ^{131}I concentrations at certain locations approach or exceed 0.1 mSv limits. Notably, the water extraction points at Tailfer had individual doses of 0.2 mSv, whereas the other location in the Albert canal were well below the 0.1 mSv limit, primarily because of long transport time that would decay ^{131}I substantially. Therefore, Chooz Npp releases had a greater impact on humans due to its proximity to drinking water extraction at Tailfer. This does not mean the Tihange is less impactful, but that the water extraction location is far away downstream from it. Nonetheless, several hypothetical locations were chosen as additional control and it was seen that the doses reached up to 0.4 mSv. In the Brussels region, the cumulative population dose indicates a 5-10% increased cancer risk for 220 individuals in a population of 1.2 million due to Chooz releases.

The study examines the activity concentration of radionuclides released under various scenarios (both atmospheric and Direct liquid releases) near the Doel Nuclear Power Plant (NPP), focusing on the distribution and impact of ^{137}Cs and ^{131}I in the surrounding environment of Scheldt estuary. The results show that radionuclide concentrations vary from 0 to 88 MBq/m^3, with higher levels detected near the NPP. The study highlights areas exceeding this limit and shows the distribution of radioactivity over time in Scheldt aquatic systems.

In scenarios involving deposition after atmospheric releases, the concentration of ^{131}I was significantly higher than ^{137}Cs, especially in the initial days following the release. This was due to the larger quantity of ^{131}I emitted. The plume moved towards the Belgian coast, influenced by tidal motions. In coastal regions like Blankenberge, ^{131}I concentrations exceeded 10000 Bq/m^3 within seven days of release but started declining after nine days, dropping below restricted levels around the 16th day. In contrast, ^{137}Cs concentrations remained below the recommended limit throughout the study period. The Scheldt Estuary was notably affected due to its proximity to the Doel NPP. Antwerp, located upstream, was identified as a major urban area likely to be impacted, with radionuclide levels peaking around 12 and 18 days for ^{131}I and ^{137}Cs, respectively. Tidal motions significantly influenced the dispersion of these radionuclides, moving them towards inland regions but never beyond Hemiksem in the river basin. In scenarios involving releases towards the tributary, radionuclides were observed to move rapidly downstream towards the confluence with the Rupel River. The study noted that ^{131}I, released in greater quantities than ^{137}Cs, took longer to reach low level of radioactivity in the Rupel River.

Direct liquid release scenarios presented a different distribution pattern, with radionuclides released directly into the Scheldt estuary. These scenarios resulted in higher concentrations due to the direct release of large inventories into the water. The radionuclides spread rapidly within the estuary, contaminating the lower and upper parts. Concentrations of ^{131}I decreased significantly over time, but ^{137}Cs levels remained consistently high. The estuary's tidal dynamics played a critical role in the distribution, with both radionuclides reaching the mouth of the estuary after 25 days. The study also compared the impact of radionuclide releases at low and high tides. It found that high tide releases (when the inversion from high tides to low tides begins) led to higher concentrations along the coast initially, while low tide releases increased concentrations in upstream regions like Antwerp. Over time, the differences in peak values diminished. Seasonal variations were also considered, showing distinct differences in radionuclide distribution between January and July due to varying river discharges.

The individual doses for drinking water due to coastal contamination is negligible (10^{-10} mSv). For other exposure pathways too, individual doses (10^{-6} to 10^{-9} mSv) from external exposure (such as swimming) are significantly lower than the recommended limit (<0.1 mSv). Furthermore, because of the larger water volume, routine releases are expected to have a far lower impact in the estuary than in the Meuse River, where the calculated individual dose in the Meuse River are 11 orders lower than the recommended value. As a result, the Doel NPP, which has an average routine release of 2.5 GBq/year that is equivalent to the Tihange NPP (2.1 GBq/year), is not evaluated for routine releases.

6.2 Perspectives for future works

6.2.1 Sediment transport model

The radionuclide transport model does not account for the effects of radionuclides sorption to sediments. During the transport, radionuclides can be either fixed onto solids suspended in water, which can settle afterwards, or they are sorbed directly onto sediments already deposited on the riverbed. These sediments can then resuspend later depending on the flow conditions. However, this process can take a long time to show any significant increase in radioactivity. For instance, in the aftermath of the 1987 Chernobyl accident, the January 1991 flood increased radioactivity in the Pripyat River by more than 10000 Bq/m^3. This was attributed to the continuing deposition of contaminated sediments in the flood plain, which was resuspended after a major flood (Zheleznyak et al. (1997)). Similar case was observed in the aftermath of Fukushima disaster, where the dissolved ^{137}Cs concentration reduced to pre accident level by dilution and dispersion, but long retained ^{137}Cs in sea bed have become the main source of remobilization of radioactivity to water (Kamidaira et al. (2021)).Therefore, sediment transport coupled model can be useful for assessing the impact in long term.

The affinity of radionuclides (defined as partition coefficients) towards the sediments will depend on their respective characteristics. For instance, the same radionuclides can have different partition coefficients for different sediments of similar type (like clay). This is due to sediment minerology and also the influence of structural characteristics such as frayed edge locations (Wauters et al. (1996)). Therefore, experimental studies for the interaction of radionuclides with site specific sediments will lead to more reliable results. Moreover, as mentioned before, the salinity of the water can reduce the partition coefficient of a radionuclide. Hence, modeling the radionuclide absorption and even desorption in sediments is a complex task.

6.2.2 Other Nuclear Power Plants

Since the model domain extends up until the shelf break, it can be used to evaluate the impact of several other nuclear power plants along the coast of France and the United Kingdom. Figure 6.1 shows the location of the NPPs in the domain.

There are four nuclear sites off the coast of France, and several more in the United Kingdom The nuclear plant in France will have a substantial impact on the Belgian coast because of the ocean currents that move towards the southern bight region (Belgian border). As a result, a major nuclear accident has the potential to impact the Belgian coast. Although, the mesh is intended to represent the Doel NPP and even the Borssele NPP, an adequate evaluation of the fate and transport of radioactivity can be a valuable source of information in terms of emergency planning.

6.2.3 Lateral radioactive contamination due to runoff

Radioactive pollution from atmospheric releases mostly affects the land, and in the event of precipitation, these deposits can be carried into the river. This could lead to an increase in radioactive concentration in the river due to lateral contamination. The simulations do not include lateral sources because the model does not address them. However, because we analyze scenarios with maximum deposition on the river, lateral radioactive influx from land is not taken into account. However, it does not mean that radioactive material deposited on impervious areas such as cities, parking lots, and roads could not

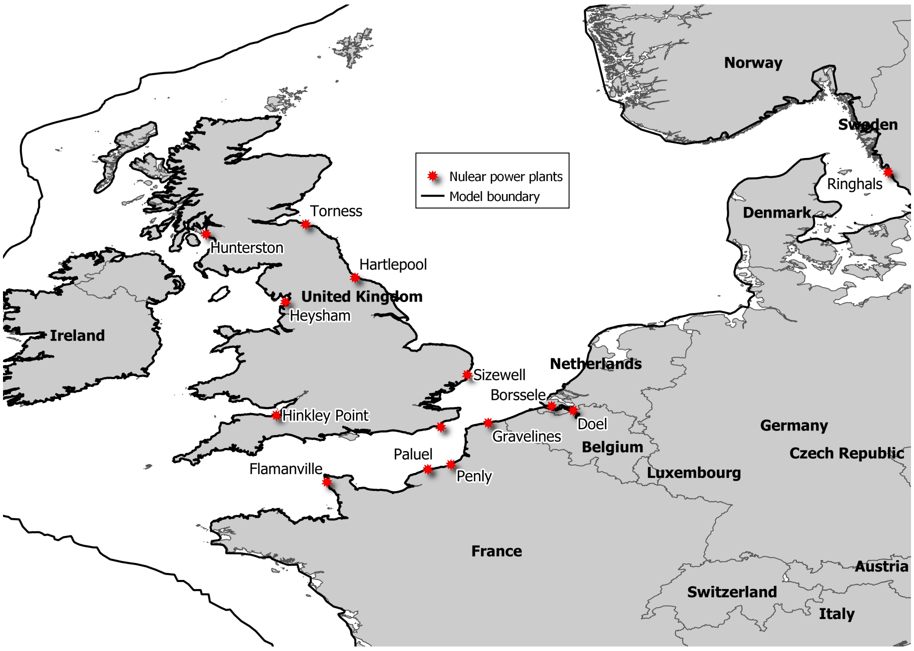

Fig. 6.1: Nuclear installations in the coast of the European shelf region that can be considered for the future impact studies

reach the estuary as released via the sewer system. The inclusion of these pathways will require a complex model that takes into account the topographic details of the huge river catchment as well as the land characteristics (such as soil properties, etc.) to determine the quantity of radioactivity that will be carried by the runoff into the river. Most likely, it will greatly increase the computational cost. Alternatively, a simpler box approach can reduce the calculation time in order to have a good estimate of the amount.

Bibliography

Anastasiou, K., Chan, C., 1997. Solution of the 2d shallow water equations using the finite volume method on unstructured triangular meshcs. International Journal for Numerical Methods in Fluids 24, 1225–1245.

Arcement, G.J., Schneider, V.R., 1989. Guide for selecting Manning's roughness coefficients for natural channels and flood plains. USGS Numbered Series 2339. U.S. Geological Survey,.

Arndt, S., Vanderborght, J.P., Regnier, P., 2007. Diatom growth response to physical forcing in a macrotidal estuary: Coupling hydrodynamics, sediment transport, and biogeochemistry. Journal of Geophysical Research: Oceans 112.

Ashagrie, A.G., de Laat, P.J., de Wit, M.J., Tu, M., Uhlenbrook, S., 2006. Detecting the influence of land use changes on discharges and floods in the Meuse River Basin - the predictive power of a ninety-year rainfall-runoff relation? Hydrology and Earth System Sciences 10, 691–701. Publisher: Copernicus GmbH.

Batlle-Aguilar, J., Orban, P., Dassargues, A., Brouyère, S., 2007. Identification of groundwater quality trends in a chalk aquifer threatened by intensive agriculture in Belgium. Hydrogeology Journal 15, 1615–1627.

Beckers, A., Dewals, B., Erpicum, S., Dujardin, S., Detrembleur, S., Teller, J., Pirotton, M., Archambeau, P., 2013. Contribution of land use changes to future flood damage along the river Meuse in the Walloon region. Natural Hazards and Earth System Sciences 13, 2301–2318. Publisher: Copernicus GmbH.

Behrens, E., Schwarzkopf, F.U., Lübbecke, J.F., Böning, C.W., 2012. Model simulations on the long-term dispersal of 137Cs released into the Pacific Ocean off Fukushima. Environmental Research Letters 7, 034004. Publisher: IOP Publishing.

Bertels, D., Willems, P., 2022. Climate change impact on salinization of drinking water inlets along the Campine Canals, Belgium. Journal of Hydrology: Regional Studies 42, 101129.

Bezhenar, R., Jung, K.T., Maderich, V., Willemsen, S., de With, G., Qiao, F., 2016. Transfer of radiocaesium from contaminated bottom sediments to marine organisms through benthic food chains in post-Fukushima and post-Chernobyl periods. Biogeosciences 13, 3021–3034. Publisher: Copernicus GmbH.

Bladé, E., Gómez-Valentín, M., Dolz, J., Aragón-Hernández, J.L., Corestein, G., Sánchez-Juny, M., 2012. Integration of 1D and 2D finite volume schemes for computations of water flow in natural channels. Advances in Water Resources 42, 17–29.

Bos, M.G., 1989. Discharge measurement structures .

Breton, M., Salomon, J.C., 1995. A 2D long term advection-dispersion model for the Channel and Southern North Sea Part A: Validation through comparison with artificial radionuclides. Journal of Marine Systems 6, 495–513.

Brovchenko, I., Kim, K.O., Maderich, V., Jung, K.T., Bezhenar, R., Ryu, J.H., Min, J.E., 2022. Sediment and Radioactivity Transport in the Bohai, Yellow, and East China Seas: A Modeling Study. Journal of Marine Science and Engineering 10, 596. Number: 5 Publisher: Multidisciplinary Digital Publishing Institute.

de Brye, B., de Brauwere, A., Gourgue, O., Kärnä, T., Lambrechts, J., Comblen, R., Deleersnijder, E., 2010. A finite-element, multi-scale model of the Scheldt tributaries, river, estuary and ROFI. Coastal Engineering 57, 850–863.

Cao, Y., Lin, J., Zhai, K., Jiang, W., Zou, H., Ren, H., Wang, P., Gao, X., Zhang, M., Yu, S., Zhao, Y., Xuan, Z., Zhang, D., Liu, Y., Lou, X., 2022. Long-term investigation of environmental radioactivity levels and public health around the Qinshan Nuclear Power Plant, China. Scientific Reports 12, 4945.

Caviedes-Voullième, D., Gerhard, N., Sikstel, A., Müller, S., 2020. Multiwavelet-based mesh adaptivity with discontinuous galerkin schemes: Exploring 2d shallow water problems. Advances in Water Resources 138, 103559.

Charriau, A., Bodineau, L., Ouddane, B., Fischer, J.C., 2009. Polycyclic aromatic hydrocarbons and n-alkanes in sediments of the Upper Scheldt River

Basin: contamination levels and source apportionment. Journal of Environmental Monitoring 11, 1086–1093. Publisher: The Royal Society of Chemistry.

Chung, T.Y., 2002. Computational fluid dynamics. Cambridge University Press, Cambridge.

Cockburn, B., Hou, S., Shu, C.W., 1990. The Runge-Kutta Local Projection Discontinuous Galerkin Finite Element Method for Conservation Laws. IV: The Multidimensional Case. Mathematics of Computation 54, 545–581. Publisher: American Mathematical Society.

Cockburn, B., Shu, C.W., 1989. TVB Runge-Kutta Local Projection Discontinuous Galerkin Finite Element Method for Conservation Laws II: General Framework. Mathematics of Computation 52, 411–435. Publisher: American Mathematical Society.

Costanza, R., Kemp, W.M., Baynton, W.R., 1993. Predictability, scale and biodiversity in coastal and estuarine ecosystems: implications for management. Ambio 22, 88–96.

Coughlan, C., Stips, A., 2015. Modelling the tides on the North West European Shelf. Technical Report JRC93441. Publications Office of the European Union. Luxembourg.

Day, J.W., Hall, A.S., Kemp, W.M., Yanez-Arancibia, A., 2022. Estuarine Ecology. Willey, New York.

Dazzi, S., Vacondio, R., Mignosa, P., 2020. Internal boundary conditions for a GPU-accelerated 2D shallow water model: Implementation and applications. Advances in Water Resources 137, 103525.

De smedt, F., Van der beken, A., 1982. Het transport van conservatieve stoffen in het Albertkanaal en de Kempische kanalen .

Draoui, I., Lambrechts, J., Legat, V., Deleersnijder, E., 2022. The discontinuous Galerkin method for coupling a 1D river model to a 2D shallow water one. Technical Report EGU22-1084. Copernicus Meetings. Conference Name: EGU22.

Draoui, I., Lambrechts, J., Legat, V., Soares-Frazão, S., Hoitink, A., Deleersnijder, E., 2020. Discontinuous Galerkin method for 1D river flows, pp. 1114–1121.

Duchesne, S., Boyer, P., Beaugelin-Seiller, K., 2003. Sensitivity and uncertainty analysis of a model computing radionuclides transfers in fluvial ecosystems (CASTEAUR): application to 137Cs accumulation in chubs. Ecological Modelling 166, 257–276.

Duffa, C., Bailly du Bois, P., Caillaud, M., Charmasson, S., Couvez, C., Didier, D., Dumas, F., Fievet, B., Morillon, M., Renaud, P., Thébault, H., 2016. Development of emergency response tools for accidental radiological contamination of French coastal areas. Journal of Environmental Radioactivity 151, 487–494.

Echeverribar, I., Morales-Hernández, M., Brufau, P., García-Navarro, P., 2019. Use of internal boundary conditions for levees representation: application to river flood management. Environmental Fluid Mechanics 19, 1253–1271.

Egbert, G.D., Erofeeva, S.Y., 2002. Efficient Inverse Modeling of Barotropic Ocean Tides. Journal of Atmospheric and Oceanic Technology 19, 183–204. Publisher: American Meteorological Society Section: Journal of Atmospheric and Oceanic Technology.

Eke, C.D., Anifowose, B., Van De Wiel, M.J., Lawler, D., Knaapen, M.A.F., 2021. Numerical Modelling of Oil Spill Transport in Tide-Dominated Estuaries: A Case Study of Humber Estuary, UK. Journal of Marine Science and Engineering 9, 1034. Number: 9 Publisher: Multidisciplinary Digital Publishing Institute.

Erpicum, S., Dewals, B., Archambeau, P., Detrembleur, S., Pirotton, M., 2010. Detailed Inundation Modelling Using High Resolution DEMs. Engineering Applications of Computational Fluid Mechanics 4, 196–208. Publisher: Taylor & Francis _eprint: https://doi.org/10.1080/19942060.2010.11015310.

Estournel, C., Bosc, E., Bocquet, M., Ulses, C., Marsaleix, P., Winiarek, V., Osvath, I., Nguyen, C., Duhaut, T., Lyard, F., Michaud, H., Auclair, F., 2012. Assessment of the amount of cesium-137 released into the Pacific Ocean after the Fukushima accident and analysis of its dispersion in Japanese coastal waters. Journal of Geophysical Research: Oceans 117. _eprint: https://onlinelibrary.wiley.com/doi/pdf/10.1029/2012JC007933.

FANC, 2022. Radiological surveillance of the territory and discharges of class 1 nuclear facilities 2022. Fedral Agency for Nuclear control, Belgium.

FANC, 2023. Radiological surveillance of the territory and discharges of class 1 nuclear facilities 2022.

FHR, 2005. Watersysteem van het albertkanaal en de kempense kanalen. Technical Report MOD 720/4. Flander Hydraulic Research.

Flood-Modeller, 2023. Flood Modeller Technical Reference. URL: `https://help.floodmodeller.com/docs/1d-modelling-theory-overview`.

Fringer, O.B., Dawson, C.N., He, R., Ralston, D.K., Zhang, Y.J., 2019. The future of coastal and estuarine modeling: Findings from a workshop. Ocean Modelling 143, 101458.

Gallagher, R., Zienkiewicz, O., Oden, J., Morandi Cecchi, M., Taylor, C., 1978. Finite elements in fluids. volume 3. New York: Wiley.

García, R., 2005. Analysis of Manning coefficient for small-depth flows on vegetated beds. Hydrological Processes 19, 3221–3233.

García-Alén, G., García-Fonte, O., Cea, L., Pena, L., Puertas, J., 2021. Modelling Weirs in Two-Dimensional Shallow Water Models. Water 13, 2152.

Gavrilin, Y., Khrouch, V., Shinkarev, S., Drozdovitch, V., Minenko, V., Shemiakina, E., Ulanovsky, A., Bouville, A., Anspaugh, L., Voillequé, P., Luckyanov, N., 2004. Individual thyroid dose estimation for a case-control study of Chernobyl-related thyroid cancer among children of Belarus-part I: 131I, short-lived radioiodines (132I, 133I, 135I), and short-lived radiotelluriums (131MTe and 132Te). Health Physics 86, 565–585.

Godunov, S.K., Bohachevsky, I., 1959. Finite difference method for numerical computation of discontinuous solutions of the equations of fluid dynamics. Matematičeskij sbornik 47, 271–306.

Goulet, R.R., Newsome, L., Vandenhove, H., Keum, D.K., Horyna, J., Kamboj, S., Brown, J., Johansen, M.P., Twining, J., Wood, M.D., Černe, M., Beaugelin-Seiller, K., Beresford, N.A., 2022. Best practices for predictions of radionuclide activity concentrations and total absorbed dose rates to freshwater organisms exposed to uranium mining/milling. Journal of Environmental Radioactivity 244-245, 106826.

Gourgue, O., Sishah, B.B., Vanlede, J., Chen, M., Komijani, H., 2015. Modelling tides and storm surges on the European continental shelf. In 22nd TELEMAC-MASCARET User Conference,Warrington, United Kingdom, October 15–16, 2015. , 1–6.

Hanert, E., Mohammed, A.V., Veerasingam, S., Dobbelaere, T., Vallaeys, V., Vethamony, P., 2023. A multiscale ocean modelling system for the central Arabian/Persian Gulf: From regional to structure scale circulation patterns. Estuarine, Coastal and Shelf Science 282, 108230.

HEC-RAS, 2017. HEC-RAS River Analysis System. URL: https://www.hec.usace.army.mil/software/hec-ras/documentation/HEC-RAS%205.0%20Reference%20Manual.pdf.

Hersbach, H., Bell, B., Berrisford, P., Hirahara, S., Horányi, A., Muñoz-Sabater, J., Nicolas, J., Peubey, C., Radu, R., Schepers, D., Simmons, A., Soci, C., Abdalla, S., Abellan, X., Balsamo, G., Bechtold, P., Biavati, G., Bidlot, J., Bonavita, M., Chiara, G., Dahlgren, P., Dee, D., Diamantakis, M., Dragani, R., Flemming, J., Forbes, R., Fuentes, M., Geer, A., Haimberger, L., Healy, S., Hogan, R.J., Hólm, E., Janisková, M., Keeley, S., Laloyaux, P., Lopez, P., Lupu, C., Radnoti, G., Rosnay, P., Rozum, I., Vamborg, F., Villaume, S., Thépaut, J., 2020. The ERA5 global reanalysis. Quarterly Journal of the Royal Meteorological Society 146, 1999–2049.

Hirose, K., 2016. Fukushima Daiichi Nuclear Plant accident: Atmospheric and oceanic impacts over the five years. Journal of Environmental Radioactivity 157, 113–130.

Hirsch, C., 1978. Numerical Computation of Internal and External flows: The Fundamentals of Computational Fluid Dynamics. Elsevier.

Hodges, B.R., 2013. Challenges in Continental River Dynamics. Environmental Modelling & Software 50, 16–20.

Hofman, D., Monte, L., Boyer, P., Boyer, P., Brittain, J., Donchyts, G., Gallego, E., Gheorghiu, D., Hakanson, L., Heling, R., Kerekes, A., Kocsy, G., Lepicard, S., Slavik, O., Slavnicu, D., Smith, J., Zheleznyak, M., 2011a. Computerised decision support systems for the management of freshwater radioecological emergencies: Assesment of the state-of-the-art with respect to the experiences and needs of end-users. Journal of Environmental Radioactivity 102, 119–127.

Hofman, D., Monte, L., Boyer, P., Brittain, J., Donchyts, G., Gallego, E., Gheorghiu, D., Håkanson, L., Heling, R., Kerekes, A., Kocsy, G., Lepicard, S., Slavik, O., Slavnicu, D., Smith, J., Zheleznyak, M., 2011b. Computerised Decision Support Systems for the management of freshwater radioecological emergencies: assessment of the state-of-the-art with respect to the experiences and needs of end-users. Journal of Environmental Radioactivity 102, 119–127.

Hossen, M.A., Akhter, F., 2015. Study Of the Wind Speed, Rainfall And Storm Surges For The Scheldt Estuary In Belgium 4.

IAEA, 1971. Disposal of Radioactive Wastes into Rivers, Lakes and Estuaries. International Atomic Energy Agency.

IAEA, 1998. Marine Environment Assessment of the Black Sea: Final Report, Technical Cooperation Project RER/2/00. International Atomic Energy Agency.

IAEA, 2006a. Environmental Consequences of the Chernobyl Accident and their Remediation: Twenty Years of Experience. Technical Report. International Atomic Energy Agency. Vienna.

IAEA, 2006b. Environmental Consequences of the Chernobyl Accident and their Remediation: Twenty Years of Experience. International Atomic Energy Agency.

IAEA, 2006c. Radiological Conditions in the Dnieper River Basin. Technical Report. International Atomic Energy Agency. Vienna. ISBN: 9789201049056.

IAEA, 2016. Criteria for Radionuclide Activity Concentrations for Food and Drinking Water. IAEA-TECDOC-1788. International Atomic Energy Agency. Vienna.

IAEA, 2019. Modelling of Marine Dispersion and Transfer of Radionuclides Accidentally Released from Land Based Facilities. Technical Report IAEA-TECDOC-1876. International Atomic Energy Agency.

ICRP, 2009. Application of the commission's recommendations for the protection of people in emergency exposure situations.

ICRP, 2012. Compendium of Dose Coefccients based on ICRP publication 60. Ann. ICRP 41(Suppl.). ICRP Publication 119.

ICRP, 2018. Dose Coefficients for External Exposures to Environmental Sources. Technical Report. International Commision on radiological protection.

ICRP, 2021. Use of dose quantities in radiological protection.

Ievdin, I.O., Khalchenkov, O.V., Kovalets, I.V., Raskob, W., Trybushnyi, D., Zheleznyak, M.J., 2012. Application of Decision Support System JRODOS for Assessments of Atmospheric Dispersion and Deposition from Fukushima Daiichi Nuclear Power Plant Accident. International Journal of Energy for a Clean Environment 13. Publisher: Begel House Inc.

Iosjpe, M., Karcher, M., Gwynn, J., Harms, I., Gerdes, R., Kauker, F., 2009. Improvement of the dose assessment tools on the basis of dispersion of the 99Tc in the Nordic Seas and the Arctic Ocean. Radioprotection 44, 531–536. Number: 5 Publisher: EDP Sciences.

Iserles, A., 2008. A First Course in the Numerical Analysis of Differential Equations. Cambridge Texts in Applied Mathematics. 2 ed., Cambridge University Press, Cambridge.

Ishimwe, A.P., Deleersnijder, E., Legat, V., Lambrechts, J., 2023. A split-explicit second order Runge–Kutta method for solving 3D hydrodynamic equations. Ocean Modelling 186, 102273.

Iwasa, Y., Aya, s., 1991. Predicting longitudinal dispersion coefficient in open-channel flows, Hing Kong. pp. 505–510.

Jonsson, B., Forseth, T., Ugedal, O., 1999. Chernobyl radioactivity persists in fish. Nature 400, 417–417. Publisher: Nature Publishing Group.

Kamidaira, Y., Uchiyama, Y., Kawamura, H., Kobayashi, T., Otosaka, S., 2021. A modeling study on the oceanic dispersion and sedimentation of radionuclides off the coast of Fukushima. Journal of Environmental Radioactivity 238-239, 106724.

Kawamura, H., Kobayashi, T., Furuno, A., In, T., Ishikawa, Y., Nakayama, T., Shima, S., Awaji, T., 2011. Preliminary numerical experiments on oceanic dispersion of 131I and 137Cs discharged into the ocean because of the Fukushima Daiichi nuclear power plant disaster. Journal of Nuclear Science and Technology 48, 1349–1356.

Kesserwani, G., Ghostine, R., Vazquez, J., Ghenaim, A., Mosé, R., 2008. Application of a second-order Runge–Kutta discontinuous Galerkin scheme for the shallow water equations with source terms. International Journal for Numerical Methods in Fluids 56, 805–821.

Kesserwani, G., Liang, Q., 2011. A conservative high-order discontinuous Galerkin method for the shallow water equations with arbitrary topography. International Journal for Numerical Methods in Engineering 86, 47–69.

Kesäniemi, J., Jernfors, T., Lavrinienko, A., Kivisaari, K., Kiljunen, M., Mappes, T., Watts, P.C., 2019. Exposure to environmental radionuclides is associated with altered metabolic and immunity pathways in a wild rodent. Molecular Ecology 28, 4620–4635.

Kitsikoudis, V., Becker, B.P.J., Huismans, Y., Archambeau, P., Erpicum, S., Pirotton, M., Dewals, B., 2020. Discrepancies in Flood Modelling Approaches in Transboundary River Systems: Legacy of the Past or Well-grounded Choices? Water Resources Management 34, 3465–3478.

Kobayashi, T., Nagai, H., Chino, M., Kawamura, H., 2013. Source term estimation of atmospheric release due to the Fukushima Dai-ichi Nuclear Power Plant accident by atmospheric and oceanic dispersion simulations: Fukushima NPP Accident Related. Journal of Nuclear Science and Technology 50, 255–264.

Kovalets, I.V., Robertson, L., Persson, C., Didkivska, S.N., Ievdin, I.A., Trybushnyi, D., 2014. Calculation of the far range atmospheric transport of radionuclides after the Fukushima accident with the atmospheric dispersion model MATCH of the JRODOS system. International Journal of Environment and Pollution 54, 101–109. Publisher: Inderscience Publishers.

Kryshev, I.I., 1995. Radioactive contamination of aquatic ecosystems following the Chernobyl accident. Journal of Environmental Radioactivity 27, 207–219.

Kärnä, T., Baptista, A.M., Lopez, J.E., Turner, P.J., McNeil, C., Sanford, T.B., 2015. Numerical modeling of circulation in high-energy estuaries: A Columbia River estuary benchmark. Ocean Modelling 88, 54–71.

Kärnä, T., Deleersnijder, E., de Brauwere, A., 2010. Simple test cases for validating a finite element unstructured grid fecal bacteria transport model. Applied Mathematical Modelling 34, 3055–3070.

Lacroix, G., Ruddick, K., Ozer, J., Lancelot, C., 2004. Modelling the impact of the Scheldt and Rhine/Meuse plumes on the salinity distribution in Belgian waters (southern North Sea). Journal of Sea Research 52, 149–163.

Lai, W., Khan, A., 2012a. Discontinuous galerkin method for 1d shallow water flows in natural rivers. Engineering Applications of Computational Fluid Mechanics 6, 74–86.

Lai, W., Khan, A.A., 2012b. Discontinuous Galerkin Method for 1D Shallow Water Flows in Natural Rivers. Engineering Applications of Computational Fluid Mechanics 6, 74–86.

Lambert, T., Bouillon, S., Darchambeau, F., Morana, C., Roland, F.A.E., Descy, J.P., Borges, A.V., 2017. Effects of human land use on the terrestrial and aquatic sources of fluvial organic matter in a temperate river basin (The Meuse River, Belgium). Biogeochemistry 136, 191–211.

Lambrechts, J., Hanert, E., Deleersnijder, E., Bernard, P.E., Legat, V., Remacle, J.F., Wolanski, E., 2008. A multi-scale model of the hydrodynamics of the whole Great Barrier Reef. Estuarine, Coastal and Shelf Science 79, 143–151.

Lax, P., 1973. Hyperbolic systems of conservation laws and the mathematical theory of shock waves. SIAM.

Leander, R., Buishand, A., Aalders, P., Wit, M.D., 2005. Estimation of extreme floods of the River Meuse using a stochastic weather generator and a rainfall–runoff model / Estimation des crues extrêmes de la Meuse à l'aide d'un générateur stochastique de variables météorologiques et d'un modèle pluie–débit. Hydrological Sciences Journal 50, null–1103.

Luxford, F., Stansby, P.K., Rogers, B.D., 2014. The importance of long wave reflections in tidal modelling on a continental shelf. Coastal Engineering Proceedings , 27–27Number: 34.

Maderich, V., Bezhenar, R., Tateda, Y., Aoyama, M., Tsumune, D., Jung, K.T., de With, G., 2018. The POSEIDON-R compartment model for the prediction of transport and fate of radionuclides in the marine environment. MethodsX 5, 1251–1266.

MIKE-11, 2021. A Modelling System for Rivers and Channels. URL: `https://manuals.mikepoweredbydhi.help/2021/Water_Resources/Mike_11_ref.pdf`.

Miyatake, H., Kawai, M., Yoshizawa, N., Suzuki, G., 2019. Estimation of internal dose from tap water after the Fukushima Daiichi Nuclear Power Station accident using newly obtained data. Journal of Radiation Research 61, 231–236.

Monte, L., Boyer, P., Brittain, J.E., Goutal, N., Heling, R., Kryshev, A., Kryshev, I., Laptev, G., Luck, M., Periañez, R., Siclet, F., Zheleznyak, M., 2008. Testing models for predicting the behaviour of radionuclides in aquatic systems. Applied Radiation and Isotopes 66, 1736–1740.

Monte, L., Boyer, P., Brittain, J.E., Håkanson, L., Lepicard, S., Smith, J.T., 2005. Review and assessment of models for predicting the migration of radionuclides through rivers. Journal of Environmental Radioactivity 79, 273–296.

Monte, L., Brittain, J.E., Gallego, E., Håkanson, L., Hofman, D., Jiménez, A., 2009. MOIRA-PLUS: A decision support system for the management of complex fresh water ecosystems contaminated by radionuclides and heavy metals. Computers & Geosciences 35, 880–896.

Monte, L., Periañez, R., Kivva, S., Laptev, G., Angeli, G., Barros, H., Zheleznyak, M., 2006. Assessment of state-of-the-art models for predicting the remobilisation of radionuclides following the flooding of heavily contaminated areas: the case of Pripyat River floodplain. Journal of Environmental Radioactivity 88, 267–288.

Morales-Hernández, M., Murillo, J., García-Navarro, P., 2013. The formulation of internal boundary conditions in unsteady 2-D shallow water flows: Application to flood regulation. Water Resources Research 49, 471–487.

Moriasi, D., Arnold, J., Van Liew, M., Bingner, R., Harmel, R., Veith, T., 2007. Model Evaluation Guidelines for Systematic Quantification of Accuracy in Watershed Simulations. Transactions of the ASABE 50.

Moukalled, F., Mangani, L., Darwish, M., 2016. The finite VOLUME method in computational fluid dynamics. volume 113. Springer.

Murakami, M., Oki, T., 2014. Estimated Dietary Intake of Radionuclides and Health Risks for the Citizens of Fukushima City, Tokyo, and Osaka after the 2011 Nuclear Accident. PLOS ONE 9, e112791. Publisher: Public Library of Science.

Neupane, P., Dawson, C., 2015. A discontinuous Galerkin method for modeling flow in networks of channels. Advances in Water Resources 79, 61–79.

NRC, 2006. Health risks from exposure to low levels of ionizing radiation: BEIR VII phase 2.

Onishi, Y., Kivva, S.L., Zheleznyak, M.J., Voitsekhovich, O.V., 2007. Aquatic Assessment of the Chernobyl Nuclear Accident and Its Remediation. Journal of Environmental Engineering 133, 1015–1023. Publisher: American Society of Civil Engineers.

Otto, L., Zimmerman, J.T.F., Furnes, G.K., Mork, M., Saetre, R., Becker, G., 1990. Review of the physical oceanography of the North Sea. Netherlands Journal of Sea Research 26, 161–238.

Park, S.U., Lee, I.H., Joo, S.J., Ju, J.W., 2017. Emergency preparedness for the accidental release of radionuclides from the Uljin Nuclear Power Plant in Korea. Journal of Environmental Radioactivity 180, 90–105.

Pereira, F., Nossent, J., Verwaest, T., Mostaert, F., 2016. Verlaging van de waterstanden in het Albertkanaal juli 2011. Technical Report WL2016A14_074_1. Hydraulic Engineering Laboratory. Antwerp.

Periáñez, R., Bezhenar, R., Brovchenko, I., Duffa, C., Iosjpe, M., Jung, K.T., Kim, K.O., Kobayashi, T., Liptak, L., Little, A., Maderich, V., McGinnity, P., Min, B.I., Nies, H., Osvath, I., Suh, K.S., de With, G., 2019. Marine radionuclide transport modelling: Recent developments, problems and challenges. Environmental Modelling & Software 122, 104523.

Periáñez, R., Cortés, C., 2023. A Numerical Model to Simulate the Transport of Radionuclides in the Western Mediterranean after a Nuclear Accident. Journal of Marine Science and Engineering 11, 169. Number: 1 Publisher: Multidisciplinary Digital Publishing Institute.

Periáñez, R., Min, B.I., Suh, K.S., 2021. The transport, effective half-lives and age distributions of radioactive releases in the northern Indian Ocean. Marine Pollution Bulletin 169, 112587.

Perret, E., Lang, M., Le Coz, J., 2022. A framework for detecting stage-discharge hysteresis due to flow unsteadiness: Application to France's national hydrometry network. Journal of Hydrology 608, 127567.

Pham Van, C., de Brye, B., Deleersnijder, E., Hoitink, A.J.F., Sassi, M., Spinewine, B., Hidayat, H., Soares-Frazão, S., 2016. Simulations of the flow in the Mahakam river–lake–delta system, Indonesia. Environmental Fluid Mechanics 16, 603–633.

Picano, E., Vano, E., 2011. The Radiation Issue in Cardiology: the time for action is now. Cardiovascular ultrasound 9, 35.

Prandle, D., Charnock, H., 1997. A modelling study of the mixing of 137Cs in the seas of the European Continental Shelf. Philosophical Transactions of the Royal Society of London. Series A, Mathematical and Physical Sciences 310, 407–436. Publisher: Royal Society.

Quarteroni, A., Sacco, R., Saleri, F., 2007. Principles of Numerical Mathematics, in: Numerical Mathematics. Springer, Berlin, Heidelberg, pp. 33–56.

Raskob, W., Landman, C., Trybushnyi, D., 2016. Functions of decision support systems (JRodos as an example): overview and new features and products. Radioprotection 51, S9–S11. Number: HS1 Publisher: EDP Sciences.

Reed, W.H., Hill, T.R., 1973. Triangular mesh methods for the neutron transport equation. Technical Report LA-UR-73-479; CONF-730414-2. Los Alamos Scientific Lab., N.Mex. (USA).

Reynaud, J.Y., Dalrymple, R.W., 2012. Shallow-Marine Tidal Deposits, in: Davis Jr., R.A., Dalrymple, R.W. (Eds.), Principles of Tidal Sedimentology. Springer Netherlands, Dordrecht, pp. 335–369.

Reynaud, J.Y., Witt, C., Pazmiño, A., Gilces, S., 2018. Tide-dominated deltas in active margin basins: Insights from the Guayas estuary, Gulf of Guayaquil, Ecuador. Marine Geology 403, 165–178.

van Rijn, L., 2013. Tidal phenomena in the Scheldt Estuary, part 2. Technical Report. Deltares.

Saint-Amand, A., Lambrechts, J., Thomas, C.J., Hanert, E., 2023. How fine is fine enough? Effect of mesh resolution on hydrodynamic simulations in coral reef environments. Ocean Modelling 186, 102254.

Schüz, J., Deltour, I., Krestinina, L.Y., Tsareva, Y.V., Tolstykh, E.I., Sokolnikov, M.E., Akleyev, A.V., 2017. In utero exposure to radiation and haematological malignancies: pooled analysis of Southern Urals cohorts. British Journal of Cancer 116, 126–133.

Selivanova, A., Hůlka, J., Kotík, L., Kuča, P., Rubovič, P., Malátová, I., Helebrant, J., Koc, J., Rulík, P., Vlček, O., 2023. Advanced simulation techniques for the transport of routine atmospheric discharges using the JRODOS system. Progress in Nuclear Energy 157, 104596.

Shchepetkin, A., McWilliams, J., 2005. The regional oceanic modeling system (ROMS): A split-explicit, free-surface, topography-following-coordinate oceanic model. Ocean Modelling 9, 347–404.

Siclet, F., Luck, M., Dortz, J., Damois, C., Ciffroy, P., Hendrickx, F., Courivaud, J.R., 2002. Radionuclides concentrations in the Loire river system resulting from routine discharges of five nuclear power plants: Assessment of dose to man. Radioprotection 37, 399–410.

Simonsen, M., Lind, O.C., Saetra, y., Isachsen, P.E., Teien, H.C., Albretsen, J., Salbu, B., 2019. Coastal transport of river-discharged radionuclides: Impact of speciation and transformation processes in numerical model simulations. Science of The Total Environment 669, 856–871.

Sobek, 2018. 1D/2D modelling suite for integral water solutions. URL: `https://www.deltares.nl/en/software/sobek/`.

Szymkiewicz, R., 2010. Numerical Modeling in Open Channel Hydraulics. volume 83. Springer Dordrecht.

Tan, W., 1992. Mathematical theory and numerical solution for a two-dimensional system of shallow-water equations. Elsevier.

Toro, E.F., 2009. Riemann Solvers and Numerical Methods for Fluid Dynamics: A Practical Introduction. Springer, Berlin, Heidelberg.

Tsabaris, C., Eleftheriou, G., Tsiaras, K., Triantafyllou, G., 2022. Distribution of dissolved 137Cs, 131I and 238Pu at Eastern Mediterranean Sea in case of hypothetical accident at the Akkuyu Nuclear Power Plant. Journal of Environmental Radioactivity 251-252, 106964.

Tsumune, D., Tsubono, T., Aoyama, M., Hirose, K., 2012. Distribution of oceanic 137Cs from the Fukushima Dai-ichi Nuclear Power Plant simulated numerically by a regional ocean model. Journal of Environmental Radioactivity 111, 100–108.

Tsuruta, H., Oura, Y., Ebihara, M., Ohara, T., Nakajima, T., 2014. First retrieval of hourly atmospheric radionuclides just after the Fukushima accident by analyzing filter-tapes of operational air pollution monitoring stations. Scientific Reports 4, 6717. Publisher: Nature Publishing Group.

Tu, J., Yeoh, G., Liu, C., Tao, Y., 2023. Computational fluid dynamics: a practical approach. Elsevier.

Tu, M., Hall, M.J., de Laat, P.J.M., de Wit, M.J.M., 2005. Extreme floods in the Meuse river over the past century: aggravated by land-use changes? Physics and Chemistry of the Earth, Parts A/B/C 30, 267–276.

UNSCEAR, 2020. Levels and effects of radiation exposure due to the accident at the Fukushima Daiichi Nuclear Power Station: implications of information published since the UNSCEAR 2013 Reports. United Nations Scientific Committee on the Effects of Atomic Radiation.

UNSCEAR, 2021. Levels and effects of radiation exposure due to the accident at the Fukushima Daiichi Nuclear Power Station: implications of information published since the UNSCEAR 2013 Report. Technical Report. United nations.

Vallaeys, V., Lambrechts, J., Delandmeter, P., Pätsch, J., Spitzy, A., Hanert, E., Deleersnijder, E., 2021. Understanding the circulation in the deep, micro-tidal and strongly stratified Congo River estuary. Ocean Modelling 167, 101890.

Van Liew, M., Arnold, J., Garbrecht, J., 2003. Hydrologic Simulation on Agricultural Watersheds: Choosing Between Two Models. Transactions of the American Society of Agricultural Engineers 46, 1539–1551.

Van Steenbergen, N., 2017. Low water in the Albert Canal:You've got to pump it up! URL: `https://publicwiki.deltares.nl/display/HydrologyMeuse/4th+symposium+on+the+hydrological+modelling+of+the+Meuse+basin?preview=/130387019/130387164/vanSteenbergen_Youvegottopumpitup.pdf`.

Vanderborght, J.P., Folmer, I.M., Aguilera, D.R., Uhrenholdt, T., Regnier, P., 2007. Reactive-transport modelling of C, N, and O2 in a river–estuarine–coastal zone system: Application to the Scheldt estuary. Marine Chemistry 106, 92–110.

Voitsekhovitch, O.V., Zheleznyak, M.J., Onishi, Y., 1994. Chernobyl nuclear accident hydrologic analysis and emergency evaluation of radionuclide distributions in the Dnieper River, Ukraine, during the 1993 summer flood. Technical Report PNL-9980. Pacific Northwest National Lab. (PNNL), Richland, WA (United States).

Vyzikas, T., 2014. Guide des bonnes pratiques : Application de modèles et codes numériques .

Wan, Z., Li, Y., Wang, X., An, J., Cheng, L., Liao, Y., 2022. Effect of ship-lock-induced surges on navigation safety in a branched lower approach channel system. Journal of Hydroinformatics 24, 481–496.

Wang, J., Baskaran, M., Cukrov, N., Du, J., 2022. Geochemical mobility of 137Cs in marine environments based on laboratory and field studies. Chemical Geology 614, 121179.

Wang, J., de Swart, H.E., Dijkstra, Y.M., 2021. Dependence of tides and river water transport in an estuarine network on river discharge, tidal forcing, geometry and sea level rise. Continental Shelf Research 225, 104476.

Ward, P.J., Renssen, H., Aerts, J.C.J.H., van Balen, R.T., Vandenberghe, J., 2008. Strong increases in flood frequency and discharge of the River Meuse over the late Holocene: impacts of long-term anthropogenic land use change and climate variability. Hydrology and Earth System Sciences 12, 159–175. Publisher: Copernicus GmbH.

Wauters, J., Madruga, M.J., Vidal, M., Cremers, A., 1996. Solid phase speciation of radiocaesium in bottom sediments. Science of The Total Environment 187, 121–130.

Wit, M.J.M.d., Warmerdam, P.M.M., Torfs, P.J.J.F., Uijlenhoet, R., Roulin, E., Cheymol, A., Deursen, W.P.A.v., Walsum, P.E.V.v., Ververs, M., Kwadijk, J.C.J., Buiteveld, H., 2001. Effect of Climate Change on the Hydrology of the River Meuse. Technical Report. Publisher: Dutch National Research Programme on Global Air Pollution and Climate Change. NRP.

Zeng, Y.h., Huai, W.x., 2013. Estimation of longitudinal dispersion coefficient in rivers. Journal of Hydro-environment Research 8.

Zerihun, Y.T., Fenton, J.D., 2007. A Boussinesq-type model for flow over trapezoidal profile weirs. Journal of Hydraulic Research 45, 519–528. Publisher: Taylor & Francis _eprint: https://doi.org/10.1080/00221686.2007.9521787.

Zheleznyak, M., Shepeleva, T., Sizonenko, V., Mezhueva, I., 1997. Simulation of Countermeasures to Diminish Radionuclide Fluxes from the Chernobyl Zone via Aquatic Pathways. Radiation Protection Dosimetry 73, 181–186.

Zheleznyak, M.J., 1998. The mathematical modelling of radionuclide transport by surface water flow from the vicinty of the chornobyl Nuclear Power Plant. Condensed Matter Physics 12, 37–50.

Zheleznyak, M.J., Demchenko, R.I., Khursin, S.L., Kuzmenko, Y.I., Tkalich, P.V., Vitiuk, N.Y., 1992. Mathematical modeling of radionuclide dispersion in the Pripyat-Dnieper aquatic system after the Chernobyl accident. Science of The Total Environment 112, 89–114.